Faculté des Sciences
Département de Physique - Unité de recherche CESAM
Group for Research and Applications in Statistical Physics

# Cooperative dynamics and self-propulsion of active matter at interfaces

Dissertation présentée par

Maxime Hubert

en vue de l'obtention du titre de
Docteur en Sciences
Année académique 2017-2018

# Abstract

Active particles, and more generally active matter, are known for their ability to move in a given medium by harnessing energy in their surrounding or by carrying their own energy reservoir. A large field of interest regarding active particles is their collective behaviour due to the interactions between individual components of the active system. Examples can be found in biology, medicine, microfluidic or chemistry. In this thesis, the role of individuals in active matter is investigated in two peculiar systems: walking droplets and magnetocapillary microswimmers. Each system lies at an liquid-air interface and relies on the deformation of the liquid surface in their dynamics.

Walking droplets are known to propel themselves thanks to the standing capillary waves they generate at each impact on the liquid interface. The persistence time of those waves can be controlled which allows to keep images of the droplet on the interface and to alter the particle motion. This is the memory of the walking droplets. Changing this persistence time allows to change the number of images of the droplet and to explore different dynamics. The limit of extremely large persistence time is considered in this manuscript. In free space, this unique wave memory dynamics allows to generate the first example of deterministic run and tumble dynamics widely encountered in biology. This behaviour finds its origin in the wavefield which traps temporarily the walking droplets. The properties of this run and tumble dynamics are shown to by directly related to the memory stored in the wavefield. If placed in an harmonic potential, the walking droplet is forced to continuously interact with this own wavefield. It is shown that the waves self-organise. In this case, the energy stored in the wavefield mimics an equipartition of energy as well as a minimisation principle.

Magnetocapillary microswimmers use the liquid interface in order to self-assemble and the liquid underneath in order to move thanks to hydrodynamic interactions and non-reciprocal deformation. This thesis models two different experimental microswimmers: the linear microswimmer better known as the Najafi-Golestanian microswimmer and the triangular magnetocapillary microswimmer. In each case, the non-reciprocal deformation required for the swimming dynamics is at the centre of the discussion. For the linear structure, non-reciprocity is produced by breaking the spatial symmetry of the swimmer. We also discuss the importance of the particles inertia in this low Reynolds dynamics. For the tri-

angular structure, a new swimming mechanism is highlighted where the particles rotation and the structure deformation act cooperatively to generate the translation of the swimmer along the interface. This findings constitute the first step towards the modelisation of larger structures and more efficient swimmers for application in microfluidic.

# Résumé

Les particules actives, où plus généralement la matière active, sont connues pour leur capacité à se déplacer en puisant de l'énergie dans leur milieu environnant ou bien en portant avec elles leur propre réservoir d'énergie. L'une des sources principales d'intérêt concernant les particules actives est leur comportement collectif, dû aux interactions entre les individus constituant la matière active. De nombreux exemples peuvent être donn'es allant de la biologie à la médecine, en passant par la microfluidique et la chimie. Dans cette thèse, le rôle des individus dans la dynamique de la collectivité est étudié au sein de deux systèmes: Les gouttes marcheuses et les micronageurs magnétocapillaires. Chacun de ces systèmes se déplace à une interface liquide/air et utilise la déformation qu'ils y induisent dans leur dynamique.

Les gouttes marcheuses se déplacent grâce aux ondes stationnaires d'origine capillaire qu'elles laissent sur la surface liquide à chacun de leur impact. Le temps de persistance de ces ondes est contrôlable et permet de garder sur la surface des "images" de la goutte sous forme de sources d'ondes. Ces ondes ont la propriété d'altérer la dynamique de marche de la goutte. Le nombre d'images est directement relié au temps de persistance de ces ondes et leur nombre permet d'explorer diverses dynamiques inédites. Il s'agit de la mémoire de la goutte, encodée sur l'interface. La limite d'un large temps de persistance, et donc d'un large nombre d'images, est au cœur de ce manuscrit. Dans un premier temps, l'accent est mis sur la dynamique en espace libre, où la goutte marcheuse produit une dynamique dite de "*run and tumble*", que l'on retrouve essentiellement en biologie et qui ici trouve sa source dans le piège temporaire que forment les ondes sous la goutte lors de son déplacement. Contrairement aux études existantes, les gouttes marcheurses constituent le premier exemple de "*run and tumble*" déterministe dont les propriétés sont directement reliées à la mémoire de la goutte. Ensuite, l'accent est mis sur la dynamique en espace confiné. Dans ce cas, les ondes sur la surface s'auto-organisent afin de reproduire une équipartition de l'énergie stockée dans l'interface ainsi qu'une principe de minimisation global de cette énergie.

Les nageurs magnétocapillaires utilisent la déformation de l'interface comme un moyen de s'auto-organiser. De plus le liquide sous l'interface est utilisé pour transmettre les interactions hydrodynamiques entre chaque composant du nageur. Les

recherches présentées dans ce manuscrit cherchent à modéliser deux systèmes différents: le nageur de Najafi et Golestanian, de structure linéaire, et le nageur triangulaire. Dans chaque cas, la condition de déformation non-réciproque nécessaire à la nage est au coeur de la discussion. Dans le premier système, cette condition est remplie en brisant la symétrie spatiale du nageur. Les effets de l'inertie des particules sont aussi mis en avant. Dans le second système, la nage de la structure est possible grâce à un mouvement de balancier du centre de masse dû à la déformation de la structure et à la rotation individuelle de chaque bille. C'est ce mouvement coopératif au sein de la structure qui est responsable de la nage. Les recherches présentées dans ce manuscrit constituent le premier pas vers la modélistion de structures plus complexes et plus efficaces pour des applications en microfluidique.

# Acknowledgments

*De nombreuses personnes m'ont aidé ou soutenu tout au long des six années de cette thèse de doctorat et je voudrais ici les en y remercier à ma manière.*

*Je voudrais tout d'abord remercier chacun des membres de mon jury; Prof. John Martin, Dr. Stéphane Dorbolo, Prof. Geoffroy Lumay, Prof. Ana-Sunčana Smith and Prof. Emmanuel Fort; d'avoir accepté de lire et d'évaluer ce travail. J'espère sincèrement que vous prendrez autant de plaisir à lire ce manuscrit et les recherches qui y sont résumées que j'en ai pris à réaliser ces travaux.*

*Bien sûr, je voudrais remercier mon promoteur, Prof. Nicolas Vandewalle. Merci infiniment à toi, pas seulement pour ces six années de doctorat, mais aussi pour les années d'études qui les ont précédées. C'est toi qui m'as amené au GRASP, qui m'as attiré vers la physique statistique et les dynamiques chaotiques, par ta manière bien à toi de transmettre ta passion de la physique. C'est toi qui m'as donné le goût de la recherche. Ç'a été plus qu'un plaisir que de travailler avec toi tout ce temps et j'espère plus que sincèrement que les années à venir me permettront encore de te courir sur les nerfs (et au passage de produire encore quelques bons articles).*

*Merci aussi à tous mes collègues; Floriane, Martin, Hervé, Martial, Eric, Alexis, Pauline, Sébastien, Sofiene, Jean, Lionel et Simon; pour les moments que j'ai pu vivre avec vous. Merci aux postdoc; Maryam, Guillaume, Florian et Felipe; pour votre aide. Merci également à Rémy, pour toute ta patience avec moi et pour tout ce que j'ai appris à tes côtés. Je voudrais remercier en particulier Galien et Boris, pour votre aide lors de ce doctorat et pour les moments passés avec vous. Merci Galien pour ces moments improbables en conférence à sillonner les autoroutes allemandes avec la pire techno que le monde ait pu produire ou encore pour les bons moments en Croatie. Merci Boris pour ... pour tout ce que la décence m'interdit de poser dans ce manuscrit. Merci aussi Charlotte, pour l'aide que tu m'as apportée lors de cette rédaction, mais surtout pour toute cette innocence pleine de chatons et de licornes que tu as amenée au bureau à ton arrivée. Puis, merci aux nouvelles recrues du labo; Joséphine, Ylona et Florence; pour l'ambiance que vous apportez déjà. Finalement, merci à Christophe, alias "M'sieur Becco" pour avoir su m'inspirer dans mon rôle d'enseignant, mais surtout pour m'avoir vendu du rêve comme personne lors de mes premières années en tant qu'étudiant. Tu as été un vrai modèle pour moi.*

*Merci ensuite à l'équipe de Paris. Merci Matthieu et merci Stéphane. Je ne pense pas que vous puissiez imaginer tout ce que vous avez pu m'apporter ces dernières anneés depuis mon stage à MSC. Au-delà des réunions improbables qui divergeaient sans cesse ou des pièges que se sont révélées être certaines de nos soirées, chaque fois que ce doctorat s'est révélé un peu difficile à vivre, vous avez su me donner le coup de boost qu'il me fallait pour continuer. Et puis, merci pour tout ce que j'ai appris à vos côtés. Je crois qu'il est temps de vous avouer que vous m'avez toujours impressionnés en tant que scientifiques. C'est pour moi un honneur de travailler avec vous et un plaisir de vous avoir pour amis. Finalement, merci infiniment Yves, pour ta bienveillance, pour ta gentillesse, pour tes conseils, pour avoir eu si rapidement confiance en ce que je pouvais produire et m'avoir donné confiance dans mes propres compétences. Jamais je n'aurai été aussi fier de ce travail sans ton aide et ton soutien.*

*Et puis il y a tous ceux qui m'ont fait marrer, m'ont accompagné, m'ont soutenu, en particulier ces deux dernières années. Tout d'abord merci à toute l'équipe de rôlistes; David, Christine, Pascal, Kly et Stéphane; avec qui j'ai pu passer nombre de mes soirées à défoncer du gobelin, à exploser du stormtrooper à grands coups de sabre laser et que j'ai exaspéré au-delà du possible lors de nos fabuleuses enquêtes. Merci à Camille et Yannik pour ces nombreuses soirées géniales qui ont fini par un peu trop de gin ou de whisky à chaque fois. Merci à toi "Princesse Valie" pour le scandale qu'est notre amitié et la bienveillance infinie qui est la tienne. Merci aussi à Julien et Aurélie, pour votre amitié et tous ces bons moments ensemble depuis de nombreuses années. Merci également à Youri, pour ces soirées de jeux pleines de mauvaise foi, pour les fous rires à l'appart', pour ton soutien. Et puis il y a ceux que je veux remercier de faire partie de ma vie; Xavier, Laura, Ariane et Manon. Et je voudrais adresser un merci tout particulier à Fanny, Pierre et Martin. Je ne pouvais souhaiter meilleurs amis que vous. Vous êtes tout bonnement géniaux, chacun d'entre vous. J'ai de la chance de vous compter auprès de moi.*

*Pour terminer, merci à ma famille, Papa et Maman, Quentin et Céline. Sans vous, je ne serais même pas ici.*

# Publications

## Bouncing droplets

Hubert M., Ludewig F., Dorbolo S. & Vandewalle N., *Bouncing dynamics of a spring*, Physica D, **272**, 1 (2014).

Hubert M., Robert D., Caps H. & Vandewalle N., *Resonant and antiresonant bouncing droplets*, Phys. Rev. E, **91**, 023017 (2015).

## Walking droplets

Filoux B., Hubert M. & Vandewalle N., *Strings of droplets propelled by coherent waves*, Phys. Rev. E, **92**, 041004 (2016).

Dubertrand R., Hubert M., Schlagheck P., Vandewalle N., Bastin T. & Martin J., *Scattering theory of walking droplets in the presence of obstacles*, New J. Phys., **18**, 113037 (2016).

Filoux B., Hubert M., Schlagheck P. & Vandewalle N., *Walking droplets in linear channels*, Phys. Rev. Fluids, **2**, 013601 (2017).

Hubert M., Labousse M. & Perrard S., *Self-propulsion and crossing statistics under random initial conditions*, Phys. Rev. E, **95**, 062607 (2017).

Hubert M., Perrard S., Labousse M., Vandewalle N. & Couder Y. *Memory-driven run and tumble deterministic dynamics*, Submitted.

Filoux B., Hubert M. & Vandewalle N. *Bragg's reflection for walking droplets in 1D crystals*, In preparation.

Hubert M., Perrard S., Labousse M., Vandewalle N. & Couder Y. *Statistical description of memory driven chaos*, In preparation.

## Numerical method

Hubert M. & Dubertrand R., *WKB approach to evaluate series of Mathieu functions in scattering problems*, Submitted.

## Magnetocapillary microswimmers

Grosjean G., Lagubeau G., Hubert M., & Vandewalle N, *Remote control of self-assembled magnetocapillary microswimmers*, Sci. Report, **91**, 023017 (2015).

Lagubeau G., Grosjean G., Darras A., Lumay G., Hubert M. & Vandewalle N. *Statics and dynamics of magnetocapillary bonds*, Phys. Rev. E, **93**, 053117 (2016).

Grosjean G., Hubert M. & Vandewalle N. *Realization of the Najafi-Golestanian microswimmer*, Phys. Rev. E, **94**, 021101 (2016).

Grosjean G., Hubert M. & Vandewalle N. *Magnetocapillary self-assemblies: Locomotion and micromanipulation along a liquid interface*, Adv. Col. Int. Sci.,**255**, 84 (2018).

Grosjean G., Hubert M., Collard Y., Pillitteri S. & Vandewalle N. *Surface microswimmers, harnessing the interface to self-propel*, Submitted.

Sukhov A., Ziegler S., Xie Q., Trosman O., Pande J., Grosjean G. , Hubert M., Vandewalle N., Smith A.-S. & Harting J., *Resonant motion of triangular magnetocapillary swimmers*, Submitted.

Grosjean G., Hubert M., & Vandewalle N. *Capillary assemblies in a rotating magnetic field*, In preparation.

Hubert M., Grosjean G., & Vandewalle N. *Swinging dynamics of magnetocapillary swimmer*, In preparation.

# Contents

# 1 Introduction

An active particle is characterised by its ability to drive itself far from equilibrium [7], either by carrying its own energy reservoir or by harvesting energy from its surrounding. As a result the active particle is able to move in its environment without external forces, contrarily to passive particles which rely on external potentials. Nature provides countless examples of active systems. The more intuitive are humans themselves. We harvest energy through the air we breath, the food we ingest and the water we drink. We store this energy into glucose and fat thanks to our organs. And finally, we use this energy by burning ATP when walking or running through muscular contraction. In this everyday example, our movement is possible due to the friction between our feet and the ground, allowing us to walk around. For animals, other moving strategies have been developed. Some birds and insects flap their wings and fly in the sky by propelling the air behind, relying only on gravity when decreasing their altitude [177, 163, 26, 164]. This flying dynamics is a direct consequence of Newton's third law of motion. By pushing the air downwards, the bird moves upwards by conservation of momentum. Still in the animal reign, fishes, aquatic mammals and cetaceans swim in rivers, seas and oceans by displacing water along their bodies. Basically, the strategy is the same as the one used by birds. Water is pushed backwards and the swimmer moves forwards [65]. Many dynamics can be observed depending on the fish morphology [161]. Other techniques can be found for water-walking arthropods or larvae. They can move at an interface by generating vortices thanks to their legs [84] or deform the interface and use capillary interactions to generate thrust

[83]. When looking at smaller scale, previously presented techniques may lose their efficiency and new ones are necessary. This is the case for micro-organisms such as bacteria or spermatozoon when swimming in biological fluids. Because of the important dissipation induced by viscosity at such scales, pushing water backwards does not provide significant thrust [149]. As a consequence, in order to swim, new strategies are developed. Bacteria such as *Escherichia coli* rotates an helical stiff flagellum for propulsion [10] while spermatozoon of most species use the whip-like motion of a flexible filament [107, 72]. Finally, the cellular and molecular level offers some examples. Cells use actin-myosin molecular motor for motion [108] and interactions between bacterial pathogen and actin filaments have also been observed [167]. Finally, enzymes processing DNA and RNA slide along the strands using the chemical energy associated to the polymerization process [78]. This list is certainly non-exhaustive but aims at giving an overview of the richness of the examples found in Nature.

Beyond biology, artificial active systems have been engineered. Transport technologies give the most intuitive examples and find their roots almost two centuries ago when thermodynamics emerged and first allowed for the transformation of fuel into mechanical work. Nowadays, robotics aims at developing always more efficient autonomous moving robots. Biomimetism gives clues about their realisation by getting inspiration from nature. Some of those robots aim at mimicking birds [66, 133, 30], sea serpents [34] or water striders [85]. At much smaller scale, self-propelled and autonomous systems constitute a major source of interest because of their potential applications in medicine and pharmaceutical engineering, from biohybrid systems assisting fertilisation and drug delivery [116, 115, 191] to fully artificial systems aiming at capturing and transporting pathogens [23, 126] and detect neurotoxins in liquid thanks to micromotors [166]. Numerous questions can be raised about their efficiency, their propulsion mechanism and the control one has on their motion. As a consequence, numerous models, either theoretical and experimental, aim at understanding the behaviour of active particles in hope of developing more efficient technologies. Some researches focus on Janus micromotors, particles with two or more distinct chemical or physical properties [7]. They have the ability to move thanks to light-triggered electrophoresis [102] or thanks to catalytic reactions in hydrogen peroxide $H_2O_2$ with partial platinum coating [62, 17]. For the sake of control, external fields are usually used to trig the self-propulsion. Those techniques can be sonic, electric or magnetic [186].

At the intersection between biology and technology, biohybrid microswimmer are designed. One can cite Dreyfus' microswimmer, made of a chain of magnetic colloids linked with DNA and attached to a red blood cell [45] or Nawroth's jellyfish made of rat cardiomyocytes and PDMS [125]. Beyond medical and biological applications, active particles are also observed when a system manages to harness energy from a mechanical vibration or from a field oscillation. For example, vibrobots achieve to move horizontally along a vertically shaken solid surface thanks to the deformation of their inclined "legs" [159]. Vertically vibrated disks with two "legs" of different materials have been seen to move horizontally using the different frictions and elastic deformations of those legs [41, 40]. The key for such a motion is the polar asymmetry of the particle which can be achieved by different means [192]. When dealing with liquid surface, the vertical shaking can sustain waves an active particle can use. This is the case of walking droplets which move by bouncing above the interface, propelled by the waves they create after successive impacts [33]. For a floating droplet, surface waves can be triggered on its surface therefore being propelled along the interface [49].

But one of the greatest interest about active particles is their collective dynamics. Many collective behaviours can be observed in nature such as flocks of birds [144, 193], schools of fishes [6, 187] or swarms of insects [5, 38, 13] and bacteria [79, 190, 81]. The phenomenon of active turbulence has been observed with microtubules [169] and with bacteria [118, 43, 39]. Spontaneous pattern formation arises with chemotactic bacteria [18]. One could also cite the observation of crystal structures using *Thiovulum majus* [140], an extremely fast moving bacteria or phase transition in 2D biofilms [184]. When dealing with motor proteins and solutions of actin filaments, pattern formation can also be seen [157, 96]. With humans, interactions between individuals lead to interesting questions about crowd motion [90] or the dynamics in traffic jam [95]. A more exhaustive review of collective behaviours in nature can be found in [181, 113]. Away from biological examples, artificial active systems also display collective dynamics. Vibrobots are able to produce self-organisation [159] and crystallisation [16]. Janus particles produce clusters despite their active nature [22, 70, 175]. Finally, mixing biologial materials and engineering, bacteria are used to powered micromotor in order to harness energy from their self-propulsion [183] A review about active systems collective dynamics can be found in [7].

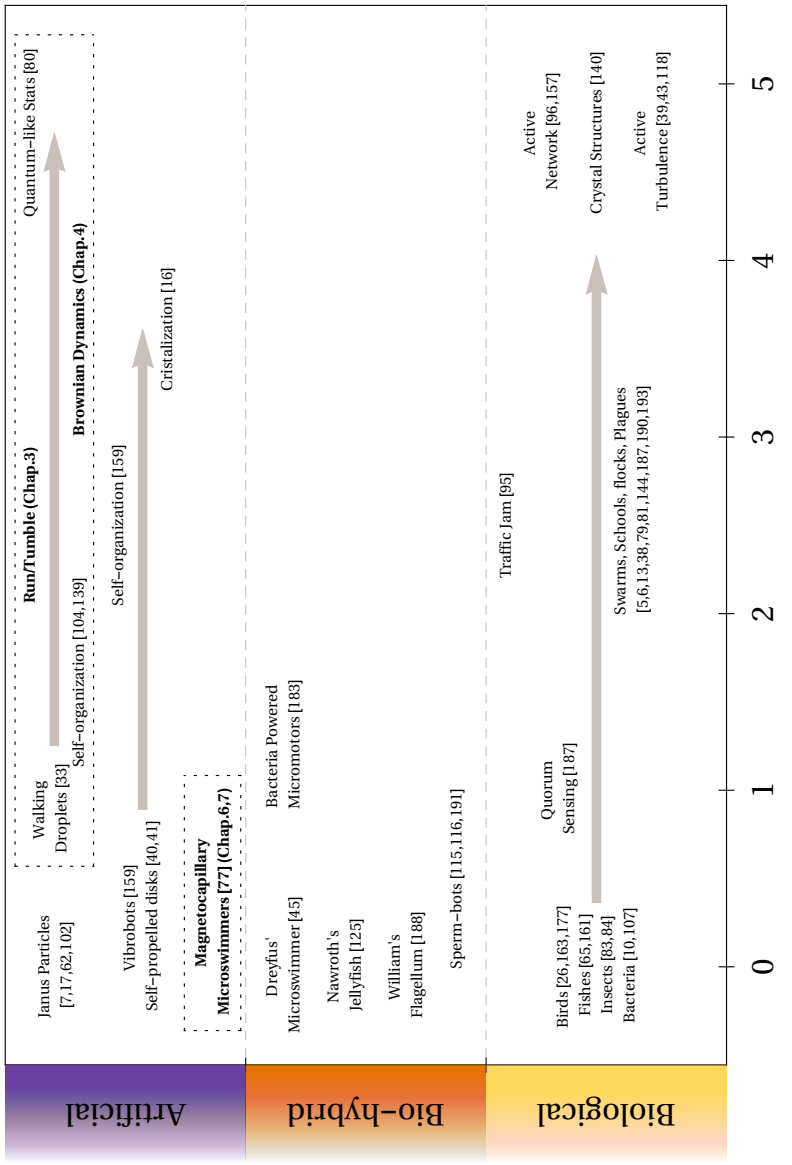


**Figure 1.1:** Overview of the richness of behaviours observed in active matter as a function of the number of individuals in the system. The systems considered in this manuscript are indicated with boxes. The specific dynamics considered in each chapter is highlighted in bold characters.

In such systems, individuals and interactions between individuals have a deep influence on the dynamics of the collectivity. Indeed, in schools of fishes, it has been shown experimentally using three-spine sticklebacks that the information about a threat or an obstacle propagates inside the school through quorum decision-making [187]. Another example is the collective motion in plagues of locusts. The driving mechanism in this case is the cannibalistic interactions between individuals [5]. Basically, a locust wants to feed on the preceding locust in the plague while running away from the following one. This highly inspiring driving mechanism results in migratory bands in the plague. If considering vibrobots [159], when put alone on a vibrated solid surface it only rotates and does not translate. But when another vibrobot is placed next to it, a translation of the pair can be seen as a result of their mutual interaction. Walking droplets also rely in the vibration of the liquid surface in order to achieve propulsion [33]. The vibration sustains the waves resulting from the impacts of the droplet. The result is many images of droplet kept on the interface [52] in the form of wave sources which drive it along the interface. Increasing the number of those images generates complex trajectories [139] and even chaotic dynamics [138]. Finally, as a last example, when dealing with swimming dynamics at very small scale, interaction between many individuals is often used as a way to circumvent the highly restricting *scallop theorem*. This is the case of magnetocapillary swimmers made of floating beads on liquid interface [111, 77, 75, 124, 71]. A brief overview of the behaviours observed in active matter as a function of the number of individuals in given in Fig. 1.1

In this manuscript, the question we raise is *how to generate an active propulsive mechanism from the collective interaction between passive individuals at an interface?* To investigate this question, we will consider two distinct systems: walking droplets [33] and magnetocapillary microswimmers [77]. Both systems have been shown to be able to move along an air-liquid interface when increasing the amount of individuals in the dynamics. The investigation run through this thesis is essentially based on numerical simulations and theory.

This manuscript is structured as follows. The first part is dedicated to the walking droplet dynamics. We explore the dynamics in the case of a large amount of individuals on the interface both in free space and in confining potentials. A short state of the art is given before investigating each geometry. The second part is dedicated to the magnetocapillary swimmer dynamics and investigates the

cooperative dynamics of the individuals on the interface in order to achieve a swimming dynamics. Both free space and confining potentials are considered in order to evidence different propulsion mechanisms. Before giving the result of the analysis, the state of the art is given. The last chapter of this manuscript gives the conclusions of this work and possible perspectives.

# Part I

# Walking droplets

# 2

# State of the art

*In recent years, an experiment has attracted lots of attention because of its peculiar dynamics mimicking behaviours usually found in quantum mechanics: the walking droplet experiment [19, 20]. The droplets involved in that study possess an unusual property. Their motion along an oscillating liquid surface is due to their interaction with the waves they create after each impact. Meanwhile, the waves sense the environment and allow the droplets to react to the presence of obstacles while moving. This symbiosis can be seen as a macroscopic wave-particle duality [147] and has led to the observation of numerous dynamics usually expected in the quantum world. As a few examples, let us cite the diffraction of particles [31, 46, 1, 148], the tunnel effect [51, 88, 123], the quantification of orbits in confined area and potentials [59, 128, 130], the quantification of observables [139, 104, 100] or even the intermittent dynamics between eigenstates in confining potentials [138, 100].*

## 2.1 The bouncing droplet experiment

The walking droplets experiment was originally conceived by Couder and his coworkers in order to prevent the coalescence of oil droplets in an oil reservoir [32]. The key idea is to shake the reservoir vertically. Thanks to the air layer between the droplet and the oil bath during impact, the drop bounce for a long time (typically minutes to hours) onto the surface. The air layer, by lubrication, exerts an upward force which can prevent coalescence. The vibration, if sufficiently strong, allows for the regeneration of the air layer between impacts, keeping the

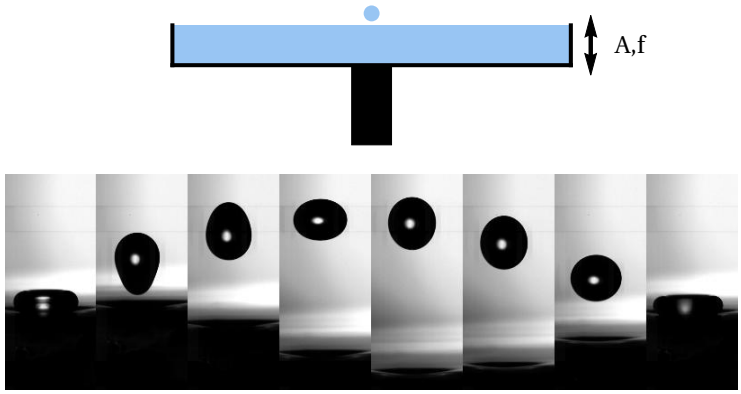


**Figure 2.1: (top)** Diagram of the bouncing droplet experiment. An oil droplet bounces onto an oil bath vertically shaken with an amplitude $A$ and a frequency $f$. **(bottom)** Snapshots of the bouncing droplet dynamics. The oil droplet never touches the surface underneath (oscillating black area) thanks to the air layer in between. The air layer is not visible here given its small thickness oscillating between $100\ \mathrm{nm}$ up to $10\ \mu\mathrm{m}$ [172]. The droplet has a radius $a = 0.76\ \mathrm{mm}$, a kinematic viscosity $\nu = 5\ \mathrm{cSt}$ while bouncing on a bath of kinematic viscosity $\nu = 1000\ \mathrm{cSt}$ oscillating at $f = 50\ \mathrm{Hz}$. Credit: Damien Robert, ULiege.

bouncing dynamics going. A schematic of the experiment is given in Fig.2.1 as well as an experimental snapshot of one period of the bouncing dynamics. The strength of the vibration is measured through its dimensionless acceleration noted $\Gamma$, which is defined by

$$\Gamma = \frac{4\pi^2 A f^2}{g}, \tag{2.1}$$

where $A$ and $f$ are the sinusoidal vibration amplitude and frequency, $g$ measures the gravity acceleration. One usually notes by $\gamma = 4\pi^2 A f^2$ the surface acceleration. In order to get some intuition, let us discuss the case of a completely inelastic ball. It would bounce continuously only if $\Gamma > 1$ [69], since no energy restoration is considered in this model. This condition corresponds to a surface acceleration $4\pi^2 A f^2$ greater than the gravity $g$. In this case, the ball cannot follow the surface motion because of gravity, the latter "falling down" with higher acceleration.

The case of the bouncing droplets dynamics is more complex to describe since the deformation of both the droplet and the oil surface has to be taken into account. The importance of deformations in the bouncing dynamics is quantified through the *Ohnesorge number* $\mathrm{Oh}$ [173, 89]. This number measures the importance of the viscous damping of oscillations relative to their restoring forces, namely inertia

and capillarity

$$\mathrm{Oh} = \frac{\eta}{\sqrt{\rho\gamma \mathrm{a}}} = \nu\sqrt{\frac{\rho}{\sigma \mathrm{a}}}, \tag{2.2}$$

where $\eta$ is the fluid dynamic viscosity, $\nu$ is the kinematic viscosity, $\sigma$ is the fluid-air surface tension and $a$ is the typical length scale of the dynamics. Typically, when considering the droplet one chooses its radius while, when considering the surface one chooses the radius of the impact area. Ohnesorge numbers lesser than one ($\mathrm{Oh} \ll 1$) corresponds to important oscillations of the system where elastic energy storage might affect the dynamics .This limit corresponds to large droplets with low viscosity, large density and surface tension. This is the case depicted in Fig.2.1. On the contrary, Ohnesorge numbers greater than one ($\mathrm{Oh} \gg 1$) lead to dynamics where deformations can be neglected. This case is usually found for highly viscous and small drops whose density and surface tension are relatively small.

Large Ohnesorge numbers for both the droplet and the bath ($\mathrm{Oh}_{\mathrm{drop}} \gg 1$ and $\mathrm{Oh}_{\mathrm{bath}} \gg 1$) correspond to the first experiments on bouncing droplets [32]. The case of deformable drops on rigid surface ($\mathrm{Oh}_{\mathrm{drop}} \ll 1$ and $\mathrm{Oh}_{\mathrm{bath}} \gg 1$) leads to the investigation of the droplet modes of deformation [44]. This regime also leads to the observation of resonant and antiresonant behaviours in the droplet bouncing dynamics [87]. This study allows the design of band-pass and band-stop filter selecting or suppressing a given size of droplet [89]. Finally, this regime leads to the observation of oil-water emulsions thanks to the bouncing dynamics and without contact from a external body [174]. The case of rigid droplets on deformable surface ($\mathrm{Oh}_{\mathrm{drop}} \gg 1$ and $\mathrm{Oh}_{\mathrm{bath}} \ll 1$) is the one leading to walking droplets.

Let us focus on this last regime. It has been studied by Couder and co-workers [147] and later intensively characterized by Bush and co-workers [189, 121, 122, 20]. Some observations can be made. The coalescence can be avoided for $\Gamma < 1$ as seen around $a = 0.4\ \mathrm{mm}$, contrarily to the completely inelastic ball because of the energy stored in the surface deformation. Above this coalescence threshold, it appears that different bouncing modes are encountered in the experiments as a function of the droplet radius $a$ and the dimensionless acceleration $\Gamma$. A summary of their experimental investigation is given in Fig.2.2. For the lowest values of $\Gamma$, the coalescence of the droplets is always observed (black shaded area). For

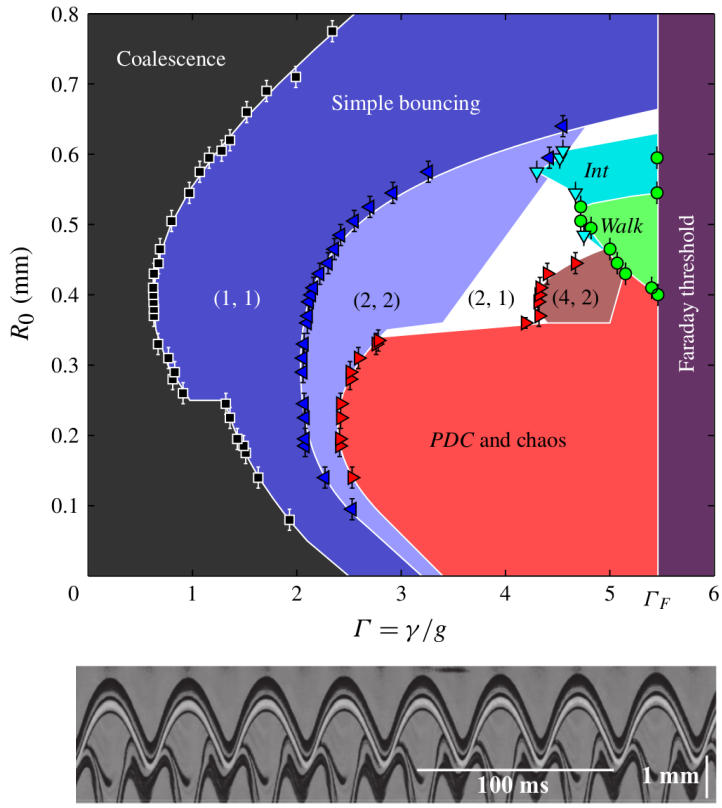


**Figure 2.2: (Top)** Experimental bouncing diagram showing the bouncing dynamics of a droplet of radius $a = R_0$ for a dimensionless acceleration $\Gamma$. For this figure, the forcing frequency $f$ is set to $60\text{Hz}$. The droplet and bath viscosity is $\nu = 50$ cSt. Each colour of the figure corresponds to a different dynamics. **(Bottom)** Spatio-temporal diagram illustrating the $(2, 1)$-bouncing mode. The upper curve corresponds to the droplet while the lower curve corresponds to the shadow it casts. One sees that the droplet bounces once while the surface oscillates twice. Diagram taken from [121]. Spatio-temporal diagram taken from [189].

higher acceleration, $(m, n)$-modes are reported. An $(m, n)$-mode corresponds to $n$ different bounces of the droplet while the surface oscillates $m$ times. After $p = LCM(m, n)$ surface periods of oscillation, $LCM$ being the Least Common Multiple of $m$ and $n$, the dynamics repeats. For example, the $(2, 1)$-mode corresponds to one bounce of the droplet meanwhile the surface oscillates twice. The bouncing period is therefore twice the forcing period of the interface. This mode is illustrated at the bottom of Fig.2.2. For the highest values of $\Gamma$, the Faraday instability is observed (purple shaded area). This instability, which leads to the spontaneous formation of standing waves on the liquid surface, is discussed

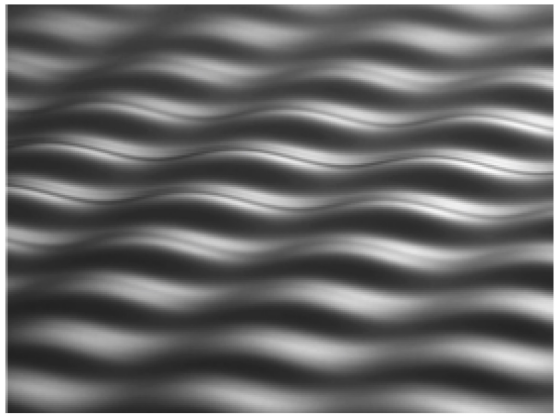

**Figure 2.3:** Side view of the Faraday instability. In this case, the instability shows a square symmetry. Credit: Lucie Domino, ESPCI.

in the next section. Between the $(2,1)$-mode and the Faraday instability lies the walking regime *Walk*. Other dynamics are also observed, such as a chaotic bouncing (*chaos*) resulting from a Period Doubling Cascade (*PDC*) [173] or intermittent walking dynamics (*int*). Those regimes are not of interest in the present discussion. Similar diagrams for other forcing frequencies can be found in [122].

One can observe from Fig.2.2 that the walking regime occurs near the Faraday instability. Indeed, bouncing droplets harness energy from the interface through Faraday waves emitted below the instability threshold to become walking droplets. The coupling mechanism between the droplet and the waves will be discussed after a short introduction to the Faraday instability.

## 2.2 The Faraday instability

The Faraday instability, first reported by Michael Faraday in 1831 [54], arises when a liquid surface is vertically shaken up to a threshold acceleration $\Gamma_F$. The result of this instability is the spontaneous formation of a sustained pattern of standing waves. The symmetry of the pattern is fixed by the geometry of the tank containing the liquid and also by the forcing acceleration [9]. An example of this instability is given in Fig.2.3.

Benjamin and Ursell [9] suggested a model for which the wave amplitude $\zeta(x,y,t)$

can be decomposed among a family of orthogonal eigenfunctions $\zeta_m(x, y)$ with

$$\zeta(x, y, t) = \sum_{m=0}^{\infty} a_m(t)\zeta_m(x, y). \tag{2.3}$$

The orthogonal eigenfunctions $\zeta_m(x, y)$ are chosen by the boundary conditions of the problem. As studied by Kumar [99], for fluid of low viscosity and infinite fluid depth, in the linear regime the amplitude $a_m(t)$ can be described by a damped angular Mathieu equation

$$\ddot{a}_m + 2\nu k^2 \dot{a}_m + \omega_0^2 \left(1 + \frac{\gamma k}{\omega_0^2} \cos(2\pi f t)\right) a_m = 0, \tag{2.4}$$

with the dispersion relation for gravito-capillary waves reading

$$\omega_0^2 = (2\pi f_0)^2 = gk + \frac{\sigma}{\rho} k^3, \tag{2.5}$$

where $k$ is the wavenumber associated to the mode $\zeta_m(x, y)$. The stability of each mode has been studied analytically in [99] and depends on the value of $\gamma$. The least stable mode, i.e. the one which appears first as the forcing acceleration $\gamma$ is increased, is the sub-harmonic mode $f_F = f/2$. Using Eq.(2.5), the Faraday frequency $f_F$ gives a wavenumber $k_F = 2\pi/\lambda_F$. The instability threshold for the least stable mode can be studied via Floquet analysis or via the two variables expansion method. It gives

$$\Gamma_F = \frac{2}{gk} \sqrt{\left(\omega_0^2 - \frac{1}{4}(2\pi f)^2\right)^2 + (2\pi\nu k^2 f)^2}. \tag{2.6}$$

Therefore, for $\Gamma < \Gamma_F$, the liquid surface remains still despite the vertical oscillation. For $\Gamma$ slightly above $\Gamma_F$, the surface deforms and standing waves appear spontaneously on the interface. The pattern of standing waves corresponds to the least stable mode fixed by Eq.(2.4), whose symmetry is given by the boundary conditions. For $\Gamma$ largely above $\Gamma_F$, multiple modes are triggered and a chaotic behaviour is expected. This last regime will not be discussed further in this manuscript.

## 2.3 From bouncing to walking

The relation between the Faraday instability and the bouncing dynamics comes from the resonance between each phenomenon [33]. Indeed, looking at Fig.2.2, one observes that close to the Faraday instability the droplet can bounce once during two oscillations, i.e. the $(2,1)$-mode, depending on its size. In other words, in this case, the bouncing frequency is half of the oscillation frequency and therefore matches the Faraday frequency $f_F = 1/\tau_F = 1/2f$. As a consequence, Faraday waves are triggered locally and below the theoretical threshold given by Eq.(2.6). Because the instability described by Eq.(2.4) corresponds to a Hopf supercritical bifurcation [52], perturbations of the interface triggered below the threshold, i.e. for $\Gamma < \Gamma_F$, decay over a time $\tau_M \propto \tau_F/\left(\Gamma_F - \Gamma\right)$. Note that this time can be significantly greater than the typical viscous time $\tau_V \propto 1/2\nu k^2$ arising from Eq.(2.4). This property allows the global wave field to reach high amplitudes since the damping time $\tau_M$ can be extremely large compared to the bouncing time $\tau_F$.

Finally, since the walkers sense their environment with their wavefield [31, 51], let us focus on its shape. In the case of walking droplets in large tanks, the emitted waves are cylindrical waves, as studied intensively by Eddi *et al.* in [52]. They considered the wavefield generated by the single impact of a steel bead on the liquid interface for different values of $\Gamma$ below the threshold. In this case, standing cylindrical waves were observed within a circle defined by the initial propagating wave front due to the impact. As expected and as already discussed above, when the interface is shaken vertically the standing waves created by the impact last longer. From all those observations, they model the wave created by a single impact $\zeta_i$ at position $\vec{r}_i$ and time $t_i$ as

$$\begin{aligned}\zeta_i\left(\vec{r},t;\vec{r}_i,t_i\right) =& \zeta_0 \cos\left(2\pi f_F(t-t_i)\right) J_0\left(k_F|\vec{r}-\vec{r}_i|\right) \\ &\times \exp\left(-\frac{t-t_i}{\tau_M}\right)\exp\left(-\frac{|\vec{r}-\vec{r}_i|}{\delta}\right), \end{aligned} \tag{2.7}$$

where $\zeta_0$ is the amplitude of the wave. The second factor accounts for the temporal oscillation of the wave. The third factor corresponds to the wave shape, here given by a cylindrical Bessel function of the first kind and zeroth order. The fourth factor is the temporal decrease of the wave amplitude linked to the threshold proximity. Finally, the last factor accounts for an empirical additional decrease of the wavefield with the distance from the wave source. This decrease is charac-

terized by the coefficient $\delta$ and was measured in some experiments [52]. Since the bouncing dynamics is periodic, the factor $\cos(2\pi f_F(t-t_i))$ is expected to always have the same value during the experiment. As a consequence, one usually drops this factor, defining $\zeta_0' = \zeta_0 \cos(2\pi f_F(t-t_i))$. For the sake of simplicity, the *prime* will be removed throughout this manuscript so that no misunderstanding occurs. The global wavefield made of the contribution of $N$ impacts on the surface therefore writes

$$\zeta(\vec{r},t) = \sum_{i=1}^{N} \zeta_0 J_0\left(k_F|\vec{r}-\vec{r}_i|\right) \exp\left(-\frac{t-t_i}{\tau_M}\right) \exp\left(-\frac{|\vec{r}-\vec{r}_i|}{\delta}\right). \quad (2.8)$$

This expression is said to be a *stroboscopic description* of the wavefield since it considers periodic successive instants of the dynamics.

Let us now focus on the walking mechanism. The amplitude of the global wave field is the key parameter that leads the dynamics from purely vertical to vertical and horizontal. This assertion can be proved via a simple model inspired by Protière *et al.* [147]. The droplet gets a kick of momentum coming from the slope of the emitted waves. Expressed as a force, this effect reads

$$\vec{F}_w = -C\vec{\nabla}\zeta(\vec{r},t), \quad (2.9)$$

where $C$ is a coupling constant which measures the intensity of the kick. Therefore, one can write down a Newton's equation for the droplet horizontal motion

$$m\ddot{\vec{v}} + \beta\vec{v} + C\vec{\nabla}\zeta(\vec{r},t) = 0, \quad (2.10)$$

where $m$ is the droplet mass and $\beta$ is a viscous damping coming from the friction between the droplet and the underlying air layer during impacts. Let us assume the droplet at the origin of the reference frame and assume a perturbation $\vec{r}$ of this position. All the previous impacts being located at the origin, the wavefield underneath the droplet writes

$$\zeta(\vec{r}) = \sum_{i=1}^{N} \zeta_0 J_0\left(k_F|\vec{r}|\right) \exp\left(-i\frac{\tau_F}{\tau_M}\right) \exp\left(-\frac{|\vec{r}|}{\delta}\right). \quad (2.11)$$

The sum in this expression runs over all previous impacts. Without any loss of generality, one can assume $\delta \to \infty$ and $N \to \infty$ and obtains for the wavefield

gradient

$$\vec{\nabla}\zeta(\vec{r}) = -\frac{\zeta_0 k_F}{1-\exp\left(-\frac{\tau_F}{\tau_M}\right)} J_1\left(k_F|\vec{r}|\right)\frac{\vec{r}}{|\vec{r}|}. \tag{2.12}$$

Finally, assuming a stationary speed, i.e. $\dot{\vec{v}} = \vec{0}$, and a motion along a straight line $\vec{r} = \vec{v}\tau_F$, one has the following transcendental equation

$$|\vec{v}| = \frac{C}{\beta}\frac{\zeta_0 k_F}{\left(1-\exp\left(-\frac{\tau_F}{\tau_M}\right)\right)} J_1\left(k_F\tau_F|\vec{v}|\right). \tag{2.13}$$

This equation shows a pitchfork bifurcation with the parameter $\tau_M$. This equation has two solutions depending on the amplitude of the right-hand size prefactor as shown in Fig.2.4. On the one hand, for $\tau_M \ll \tau_{M,c}$ the stable solution is $|\vec{v}| = 0$ (dashed purple line). On the other hand, for $\tau_M \gg \tau_{M,c}$, the zero-speed solution becomes unstable and one has, as the stable solution (plain orange line),

$$k_F\tau_F|\vec{v}| \simeq 2\sqrt{2}\sqrt{1-\frac{2\beta\left(1-\exp\left(-\frac{\tau_F}{\tau_M}\right)\right)}{C\zeta_0 k_F^2\tau_F}}. \tag{2.14}$$

For this expression, the expansion $J_1\left(k_F\tau_F|\vec{v}|\right) = k_F\tau_F|\vec{v}|/2 + \mathcal{O}(k_F\tau_F|\vec{v}|)^3$ was used. A finite value to the spatial damping $\delta$ only smooths the bifurcation and decreases the equilibrium speed for a given value of $\tau_M$. As a consequence of this bifurcation, the walking droplet begins to move along a straight line, only interrupted because of obstacles and external potentials.

One has a unique object to deal with. On the one hand, the walker can move horizontally along the interface thanks to the wave it creates by its successive impacts. The self-propulsion and the droplet energy harvest come from the sustained vertical vibration of the liquid surface. On the other hand, the wave shape is dictated by the geometry of the walker environment which allows to react to the presence of obstacles. This property is usually described as a macroscopic wave-particle duality [147]. A picture of a walker is given in Fig.2.5. The wavefield in the form of a horseshoe can be seen before the droplet.

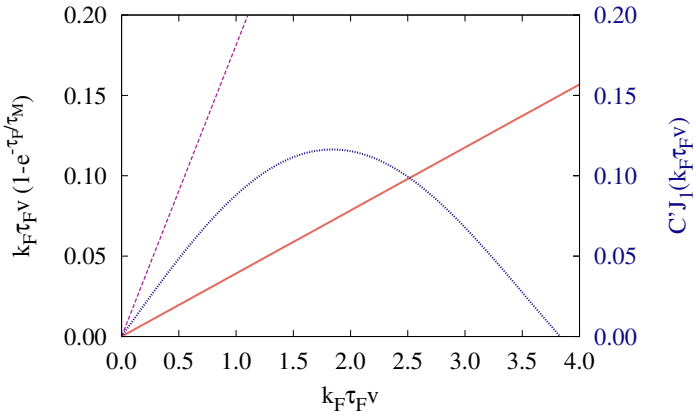


**Figure 2.4:** Illustration of Eq.(2.13) and the associated pitchfork bifurcation. The dashed and plain lines account to the function $(1-\exp(-\tau_F/\tau_M))\,k_F\tau_F|\vec{v}|$ for $\tau_M/\tau_F = 5$ (purple dotted line) and $\tau_M/\tau_F = 25$ (orange plain line). The blue dotted curve corresponds to $C' J_1(k_F\tau_F|\vec{v}|)$ where $C' = C\zeta_0 k_F^2\tau_F/\beta$ has been set to $C' = 0.2$. For $\tau_M/\tau_F = 5$ the blue dotted curve is only intercepted once which corresponds to the stable solution $|\vec{v}| = 0$. For $\tau_M/\tau_F = 25$ the blue dotted curve is intercepted twice. The previously stable solution $|\vec{v}| = 0$ has become unstable. The second intersection at $k_F\tau_F|\vec{v}| \simeq 2.5$ is the new stable solution. It changes with the value of $\tau_M/\tau_F$.

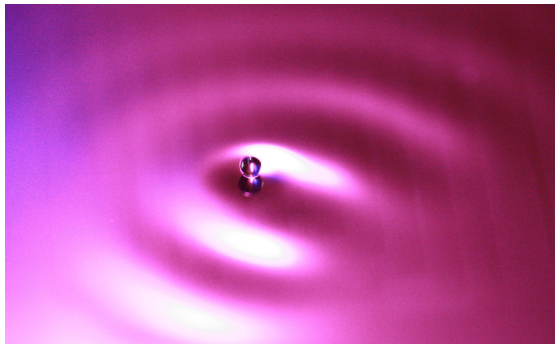

**Figure 2.5:** Walking droplet and its associated wave field. The waves are generated by the droplet by its successive impacts which are sustained by the oscillation of the surface. In return, the waves propel the droplets. Credit: Boris Filoux, ULiege.

## 2.4 Modelling the wavefield

Note that the shape of the wave field has been discussed in some studies. The wavefield description in Eq.(2.8) has been obtained from experimental investigation in free space by Eddi *et al* in [52]. In another study, in order to consider

obstacles and other geometries, Dubertrand *et al* [46] suggested to describe the walker global wavefield with Green functions, more specifically their imaginary part. In their framework, the wavefield due to a single impact is given by the differential equation

$$\left(\nabla^2 + k_F^2\right) G\left(\vec{r}, \vec{r}_i\right) = \delta\left(\vec{r} - \vec{r}_i\right), \tag{2.15}$$

and the field by

$$\zeta_i(\vec{r}) = -4\zeta_0 \mathrm{Im}\, G\left(\vec{r}, \vec{r}_i\right). \tag{2.16}$$

In Eq.(2.15), $\delta\left(\vec{r} - \vec{r}_i\right)$ is the Dirac delta and accounts for a single impact at position $\vec{r}_i$ and $G$ is the Green function. The differential operator $\left(\nabla^2 + k_F^2\right)$ selects only waves with a wavenumber $k = k_F$. They justify their hypothesis by considering the wavefield generated a single impact in free space and comparing this result to their model. They obtain

$$G\left(\vec{r}, \vec{r}_i\right) = -\frac{H_0^{(1)}\left(k_F|\vec{r} - \vec{r}_i|\right)}{4\mathrm{i}}. \tag{2.17}$$

The function $H_0^{(1)} = J_0 + \mathrm{i}Y_0$ is the Hankel function of first kind and zeroth order. When taking the imaginary part of this solution, one finds back the wavefield observed by Eddi *et al.*, namely cylindrical bessel functions. This approach has the great advantage to take into account the geometry of the experimental setup while being theoretically tractable in many situations. As a first example, in their article the authors considered the motion of walker through a single slit. The wavefield in this geometry is shown in Fig.2.6(a) in the case of Neumann boundary condition. In this case, the Green function is expressed with angular and radial Mathieu functions, usually encountered in situation showing an elliptical symmetry such as the single slit. This method gives the complex interference pattern before the slit, which gives rise to the scattering dynamics discussed in [46]. As a second example, one can focus on the wave pattern generated by the interaction with a semi-infinite line as depicted in Fig.2.6(b). Once again, one observes that interference pattern before the line as well as a shadow region beyond the line are produced by the model.

Other models have been proposed for the wavefield description. Oza *et al* suggested a continuous model based on an integro-differential equation [129]. The

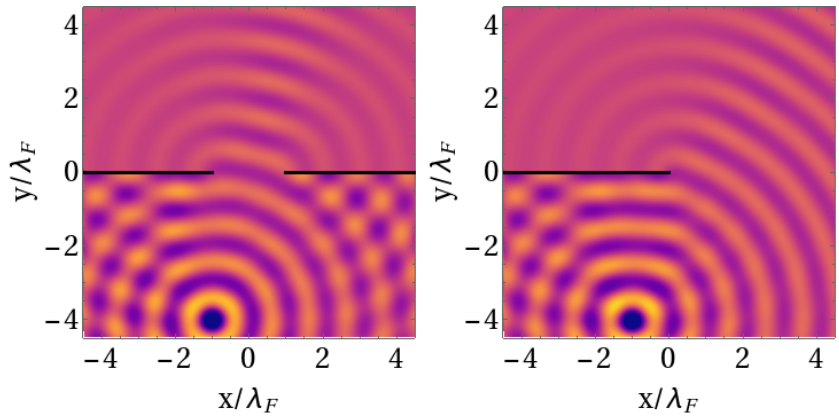


**Figure 2.6:** Wavefield generated by a single impact at coordinate $(x_0, y_0) = (-\lambda_F, -3\lambda_F)$ on a liquid surface based on the model of Dubertrand *et al.* **(Left)** Interaction with a single slit using Neumann boundary condition. The wavefield is obtained using the algorithm presented in [86] **(Right)** Interaction with a semi-infinite line with Neumann boundary condition. In each case, shadow regions are observed behind the obstacles while complex interference patterns arise before them.

wavefield is not only created by the successive impacts on the surface but integrated over the whole trajectory. This model has been the subject of intensive studies for its calibration [121, 122]. Another numerical model, suggested by Milewski *et al.* [119, 47], describes the waves directly through the Navier-Stokes equations. All models were shown to be able to reproduce experimental findings.

## 2.5 Path memory driven dynamics

Once a droplet is set into motion, the liquid surface keeps trace of the past trajectory of the particle. Indeed, all previous impacts generate standing waves which alter the long term dynamics, as seen from Eq.(2.11). This property is named the *wave-memory* of the walking droplet. Furthermore, the ratio $\tau_M/\tau_F = \mathrm{Me}$ is called the *memory*. This quantity measures the number of previous impacts which affect the droplet motion. In other words, thanks to the surface vertical oscillation approximately $\mathrm{Me}$ images of the droplets generate standing waves which alter its long term dynamics. The value of the memory $\mathrm{Me}$, and therefore the number of fictive immobile droplets on the surface, defines roughly three regimes:

1. The first regime appears for small memory, typically $\mathrm{Me} \lesssim 20$. In this limit,

the description of the wave interaction is made in the Frenet frame related to the droplet. In the tangential direction of the motion, the wavefield effect corresponds to a self-propulsive term. This limit was described by Labousse and Perrard in [103]. It is shown that the propulsion arising from the wavefield can be assimilated to a Rayleigh-type friction, i.e.

$$C\vec{\nabla}\zeta = \frac{m}{T_v}\vec{v}\left(\frac{|\vec{v}|^2}{V_0^2} - 1\right) \tag{2.18}$$

where $T_v$ is the relaxation time to the equilibrium velocity $V_0$. This type of nonlinear damping can be found in music when describing the motion of a clarinet reed [63] and in the description of self-propelled systems [152, 50]. This term leads to damping for $|\vec{v}| > V_0$ and is propulsive for $|\vec{v}| < V_0$. This model was later applied to the experiments made by Eddi *et al.* [51]. In this experiment, a walking droplet is compelled to interact with a submarine obstacle. Since the depth of the fluid layer influences the Faraday instability, the motion of the droplet above the obstacle is modified. They observed that the crossing dynamics of the droplet above the obstacle can only be described statistically with probability $\mathcal{P} \propto \exp\left(-cL/V_0^2\right)$, $L$ being the obstacle size and $c$ a constant. It was shown in [88] that this dynamics comes from an unknown statistics of impact angles which, because of the Rayleigh-type friction, gives the Boltzmann-like crossing probability. In the perpendicular direction of the motion, for slightly higher memory parameters, Bush *et al.* showed that the wavefield has the effect of an additional mass in the dynamics [21]. Indeed, they demonstrated that the force exerted by the wavefield is proportional to the acceleration of the walker which, once injected in the walker equation of motion, mimics an additional mass related to its velocity. Newton's equation for the walker reads

$$\frac{d}{dt}\underbrace{\left(m\gamma_B(|\vec{v}|)\vec{v}\right)}_{\vec{p}} + \beta(|\vec{v}|)\vec{v} = -\nabla U(\vec{r}), \tag{2.19}$$

where $\beta(|\vec{v}|)$ is a non-linear damping factor, similar to the one obtained by Labousse and Perrard for Eq.(2.18) and $U(\vec{r})$ accounts for external potentials. The factor $\gamma_B(|\vec{v}|)$ is the hydrodynamic boost factor and accounts for

the additional mass stored in the wavefield. It reads

$$\gamma_B(|\vec{v}|) = 1 + \frac{g\zeta_0 k_F^2 \tau_M^3}{2\tau_F \sqrt{1 + (k_F \tau_M |\vec{v}|)^2}^3}. \tag{2.20}$$

It is claimed in [21] that this boost factor tends to mimic the Lorentz factor encountered in special relativity.

2. The second regime appears for intermediate value of the memory $\mathrm{Me}$, roughly for $20 \lesssim \mathrm{Me} \lesssim 100$. In confined systems, this regime leads to the self-organisation of the wave sources on the liquid interface. A first example can be found in the paper of Perrard *et al.* [139]. In this article, the walking droplet is confined within an harmonic potential. The core of the droplet is made of ferrofluid and a magnet is placed above the liquid surface, mimicking a confining potential. Depending on the stiffness $k$ of the potential and the average velocity $V_0$ of the walker, different trajectories are observed: circle, lemniscates or trifolium. Those eigenstates are shown in Fig.2.7. As discussed in the same article, for those trajectories, the average radius $\langle|\vec{r}|\rangle$ (and therefore, the average energy $\langle U\rangle = k\langle|\vec{r}|\rangle^2/2$) as well as the average angular momentum $\langle L_z\rangle$ are quantified. Those trajectories and their properties were investigated by Labousse *et al.* [104]. They showed that the confining potential forces the walker to interact with sources emitted in the past. The interaction between the walking droplet and its past trajectory generates a self-organization of the wave sources in *pivotal points*, curving the overall trajectory. Furthermore, it has been shown that the overall dynamics of the walker and the symmetry of the trajectory were related to the minimization of field modes. Quantification also occurs for other confining systems. Quantified trajectory radii have been observed with Coriolis force [59] or, theoretically, with Coulomb potential [171]. Finally, without any confining potential, for sufficiently important wave amplitude, a circular motion can be made stable. In such a case, the centripetal force does not come from an external force field. Instead, it comes from the wave field created by the droplet. This leads to a *self-orbiting motion*, as studied in [105].

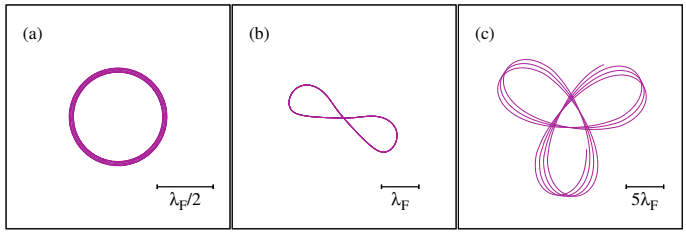


**Figure 2.7:** Eigenstates in an harmonic potential. **(a)** Circle, **(b)** Lemniscate, **(c)** Trifolium. For those trajectories, the average radius $\langle|\vec{r}|\rangle$ and the average vertical angular momentum $\langle L_z\rangle$ are quantified. The memory parameter ranges from $\mathrm{Me} = 15$ to $\mathrm{Me} = 100$. Those eigenstates have been obtained using the algorithm described in Appendix A.

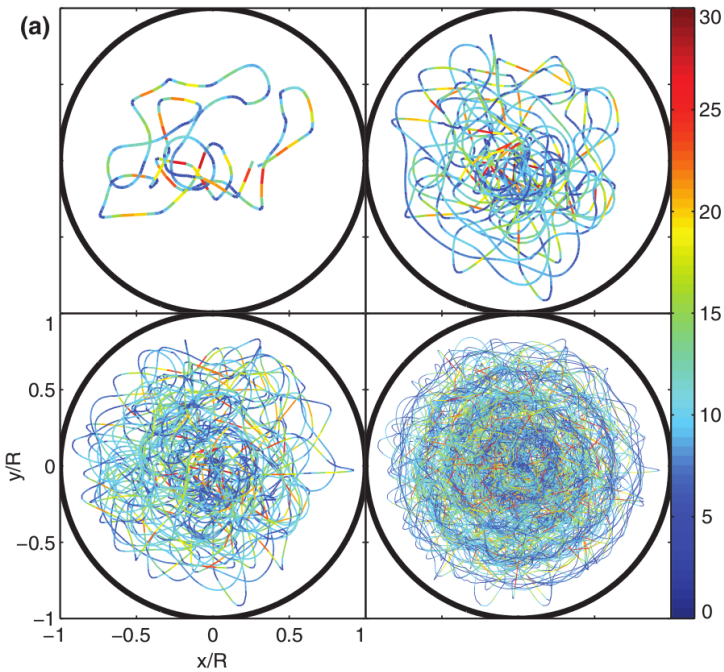


**Figure 2.8:** Overall trajectory of a walker in a circular corral for several acquisition time. The instantaneous speed of the walker is indicated from blue to red. The color bar indicates the speed in $\mathrm{mm/s}$. The radius of the corral is $R = 14.3\ \mathrm{mm/s}$. Alongside an oscillating density of presence in the radial direction, the speed is also shown to oscillate. Diagram taken from [80].

3. Finally, the last regime occurs for the high value of the memory $\mathrm{Me}$. In this limit, the dynamics becomes chaotic and ultimately leads to probabilistic

dynamics. The transition to chaos has been considered in a few articles. Perrard *et al.* focused on the case of a walking droplet in an harmonic potential [138]. They showed that for high memory, the dynamics oscillates randomly from an eigenstate to another, e.g. from a lemniscate to a circle. The transition to chaos was also studied by Tambasco *et al.* in the case of a walking droplet submitted to the Coriolis force [171]. The particle follows a period doubling cascade as the memory $\mathrm{Me}$ increases. The walking droplet, initially in a circular trajectory, begins wobbling to reach a chaotic motion. Yet, the study of the dynamics in the chaotic regime has been the subject of a only few studies, only focusing on the dynamics of a walker in circular and elliptic corrals, either experimentally [80], numerically [67, 68] or theoretically [150]. In this case, it is shown that the walker's overall trajectory can only be described statistically. The probability density function of the position relative to the center of the cavity $|\vec{r}|$ can be compared to the eigenmode of the cavity: the maxima and minima of the PDF match those of the least stable standing wave triggered by the successive impacts of the droplet on the liquid surface. The PDF of the speed $|\vec{v}|$ is also related to the eigenmodes of the cavity. This result is shown in Fig.2.8.

## 2.6 Conclusion

Walking droplets correspond to a new type of active matter, driven by the memory of this past. This memory is encoded in the surface with standing cylindrical waves which mimic many fictive immobile bouncing droplets. The persistence time of those standing waves, and therefore the number of images, is experimentally controlled through the vertical vibration of the interface. As a consequence, the walking droplets harvest energy thanks to the waves, which are maintained because of the vertical vibration. The continuous extraction of energy is only counterbalanced by the friction of the droplet with the underlying air layer.

In the following two chapters, the dynamics in the case of large memory parameter $\mathrm{Me}$ is explored. The question raised in this first part of the manuscript is *How this memory driven dynamics behave when a large amount of waves extend on the interface?* The dynamics in free space, where the droplet can flee away from its

waves, is explored in Chapter 3. The dynamics in a confining potential, where the droplet is forced to interact with its past, is investigated in Chapter 4.

*"The lesson of Lord Rayleigh's solution [regarding Random Walks] is that in open country the most probable place to find a drunken man who is at all capable of keeping on his feet is somewhere near his starting point."*

Karl Pearson, Nature, 10/08/1905

# 3

# Walkers in free space

*This chapter is dedicated to the analysis of the walking dynamics in the regime of high memory, in free space. We show that the high memory regime triggers a diffusive-like behaviour. The overall dynamics is shown to be made of ballistic phases interspersed by sudden changes in direction. This mimics a* run-and-tumble dynamics*, largely encountered in biology in the case of foraging animals and bacteria or in the case of proteins prospecting for a specific site along a DNA strain. We show that this diffusive dynamics is due to a Shil'nikov bifurcation leading to a chaotic evolution of the velocity. The resulting diffusive properties are investigated and discussed as a function of the memory of the system.*

The results presented in this chapter are summarized in the following article.

- Hubert M., Perrard S., Labousse M., Vandewalle N. & Couder Y., *Memory-driven run and tumble deterministic dynamics*, Submitted (arXiv:1807.02413).

## 3.1 Introduction

The walkers dynamics has been widely studied in the low and intermediate memory regime. Numerous examples have been discussed in the previous chapter. Yet, studies in the high memory regime are scarce and only considered peculiar

geometries [67, 68, 80, 156]. This observation finds two main explanations. On the one hand, experimentally, the memory parameter is subject to large incertitudes especially in the high memory regime. Since the memory parameter is related to the inverse to the distance to the Faraday threshold, i.e.

$$\mathrm{Me} \propto \frac{1}{\Gamma_\mathrm{F} - \Gamma}, \tag{3.1}$$

a small incertitude on $\Gamma$ leads to a large incertitude on $\mathrm{Me}$. Indeed, using logarithmic differentiation, one gets

$$\delta\mathrm{Me} \propto \mathrm{Me}^2 \delta\Gamma, \tag{3.2}$$

where the $\delta$'s correspond to the incertitudes on the memory and dimensionless acceleration. The incertitude on $\Gamma$ can arise from a leak of horizontality in the experimental set-up as well as from a too large experimental cell. In the later case, elastic deformations of the cell can be expected, spatially modifying the memory because of enhanced vertical vibrations. Indeed, the elastic oscillations of the cell superpose to the vertical forcing in this case. On the other hand, the results presented in this section show chaotic dynamics on a large spatial scale, with trajectories covering surfaces far more important than the area of existing experimental cells. As a consequence, size effects would be important in the experiments and cannot allow the study of the wave dynamics without boundary effects. Because of those two reasons, numerical simulation has been chosen over experiments in order to isolate the characteristics of a wave-memory.

The numerical scheme used to solve the walking dynamics corresponds to the one briefly described in [105], used in [105, 14, 59] and more extensively discussed in Appendix A. In a few words, the numerical scheme corresponds to an event-driven method which focus on the two peculiar instants: the droplet take-off and its landing on the surface. Because the algorithm is event-driven, the wavefield description follows the stroboscopic description seen in Eq(2.8). For further informations, the reader is invited to refer to Appendix A. In the following, the Faraday wavelength corresponds to $\lambda_F = 4.75\ \mathrm{mm}$ for a Faraday frequency $f_F = 40\ \mathrm{Hz}$. A time step in simulation corresponds to a bounce of the droplet on the surface, i.e. $\delta t_{simu} = 1/40\ \mathrm{s}$.

## 3.2 From a ballistic to a diffusive dynamics

As stated in Chapter 2, at low memory and in free space the walker is known to make a stable rectilinear motion [129]. Yet, numerically, when approaching $\mathrm{Me} = 150$, the rectilinear dynamics destabilizes and gives rise to an erratic and diffusive motion. In this section, we will describe the trajectory of the walker over the vibrating interface as the memory parameter $\mathrm{Me}$ changes in this high memory regime.

### 3.2.1 Trajectories for increasing memory parameter

The trajectories for increasing memory parameters $\mathrm{Me}$ are illustrated in Fig.3.1. In this figure, the walker evolves in free space, only submitted to its own wavefield without external forces. Note that despite all the trajectories are shown on the same plot, they have been obtained independently. Interactions between walkers are therefore non-existent. For each trajectory, only the memory is changed with $\mathrm{Me} = 15, 150$ and $1500$. The initial conditions are the same for each memory parameter. The dynamics has been integrated over $2.5\,10^5$ time steps, allowing visual comparison between each behaviour.

One observes on Fig.3.1 that for $\mathrm{Me} = 15$ (solid blue line), the dynamics indeed gives a rectilinear trajectory. This observation holds for memory parameters up to $\mathrm{Me} \approx 100$. When reaching $\mathrm{Me} = 150$ (solid purple line), the rectilinear trajectory is no longer observed. Instead, it shows sudden changes of direction. Long rectilinear motions alternate with re-orientation phases, leading to an overall diffusive process. The length of the rectilinear phase can reach hundreds of wavelengths, as seen from Fig.3.1. For this memory, one also observes that the walker covers a considerable area during its overall motion. Between $\mathrm{Me} = 100$ and $\mathrm{Me} = 150$, the transient dynamics shows the same diffusive process. But the walker eventually ends moving along a stable straight line. The closer the memory parameters is to $\mathrm{Me} = 150$, the longer this transient dynamics. For the highest memory considered in this figure, $\mathrm{Me} = 1500$ (solid orange line), the dynamics remains diffusive. The overall trajectory is more packed and the area covered by the walker is smaller than previously for $\mathrm{Me} = 150$. This is due to the smaller rectilinear parts of the dynamics, as seen in Fig.3.1. While not being shown here, even higher memories lead to even denser trajectories and even smaller covered areas.

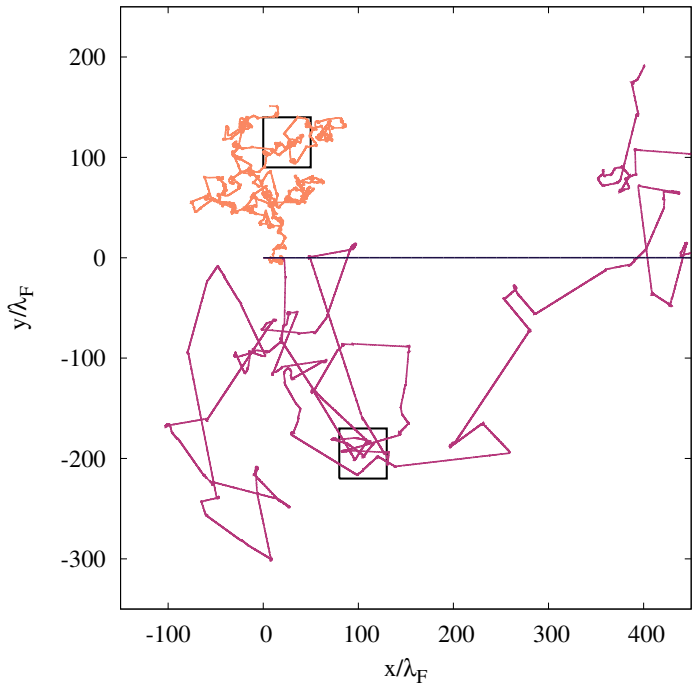


**Figure 3.1:** Numerical trajectories of a walker in free space for different memories over two decades: Dark blue $\mathrm{Me} = 15$, Purple $\mathrm{Me} = 150$ and Orange $\mathrm{Me} = 1500$. Each trajectory is obtained with the same initial conditions and integrated over $2.5\,10^5$ time steps. The squares correspond to the zooms in Fig.3.2(a) and (c).

Let us focus on the changes of direction in the trajectories in Fig.3.1. The result is given in Fig.3.2(a) and (c). This figure considers zooms on the trajectories for the two highest memories of Fig.3.1, i.e. $\mathrm{Me} = 150$ and $\mathrm{Me} = 1500$. One observes that during changes of direction, the walker wobbles in a small region before escaping in a random direction. As the memory increases, the walker wobbles more often, explaining the frequent changes of direction observed in Fig.3.1. Let us analyse the motion of the walker during this wobbling phase. Figure 3.2(b) zooms on a single wobbling phase for $\mathrm{Me} = 150$. Red arrows indicates the overall direction of motion while black arrows focus on three peculiar points of the trajectory. Point R (for Reflection) shows a sudden inversion of the direction of motion, from downwards to upwards, but the walker keeps moving along the same line. At point D (for Deviation), the walker changes its direction of motion

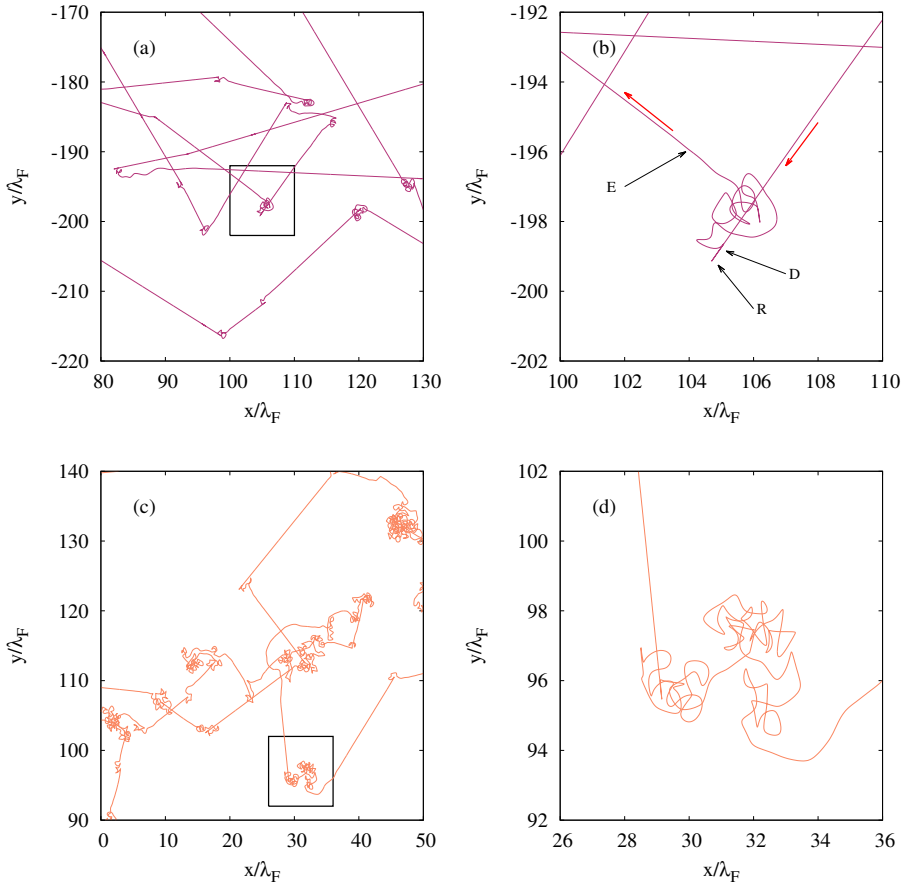


**Figure 3.2:** Zooms on the trajectories in Fig3.1 for $\mathrm{Me} = 150$ ((a) and (b)) and $\mathrm{Me} = 1500$ ((c) and (d)). The same data range has been considered along the $x$ and $y$ axis to allow comparison. Figures (a) and (c) focus on area of $50\lambda_F \times 50\lambda_F$. Figures (b) and (d) zoom on area of $10\lambda_F \times 10\lambda_F$, which correspond to the squares on Fig.(a) and (c). Red arrows on Fig.(b) give the direction of motion and black arrows give peculiar points of the dynamics: Reflection (R), Deviation (D), Escape (E).

and begins its wobbling motion. Finally, at point E (for Escape), the walker starts a new rectilinear trajectory, leaving the wobbling area. The same mechanism can be observed in Fig.3.2(d) which considers a memory $\mathrm{Me} = 1500$. The sole difference is the duration of the wobbling phase and the area covered during this phase.

This kind of dynamics reminds of the "Run and Tumble" dynamics widely encountered in biology. For example, the E. Coli bacteria has the same dynamics

when searching for nutriments [10]. Indeed, the bacteria alternates between linear motion (named the "run" phase) and short time erratic motion leading to a change of direction (named the "tumble" phase). The latter has a duration of a tenth of a second and occurs approximatively once per second for this bacteria [11]. This intermittent dynamics has been demonstrated to be especially efficient when "preys" are looking for specific "targets", either food, sexual partner or shelter. Therefore, this foraging strategy is also encountered in the case of wandering albatrosses [182]. Their rectilinear flights above the ocean are only interspersed with food foraging when the albatrosses dive into the ocean to catch fishes. The same dynamics can also be observed at the molecular level in the case of the interaction between DNA and a protein. The protein looks for a specific sequence along the DNA by alternating two distinct processes. The protein binds to a non-specific site of the strand via a weak electrostatic interaction and then slides along the DNA. At some point, the protein detaches and diffuses in the bulk in search of the specific sequence. Those two processes together have been proved to be two orders of magnitude more efficient than 3D diffusion alone [185]. More informations about intermittent search strategies in nature can be found in [8].

Nevertheless, models of intermittent search strategies are stochastic and follow a probabilistic description, not a deterministic one. The duration of both the run phase and the tumble phase is described using probability distribution functions [8, 4]. The case of the walker dynamics is deterministic since it follows the laws described in Chapter 2 and the algorithm described in Appendix A. None of them considers stochastic ingredients. Therefore, the walking droplet dynamics appears to be one dynamics, if not the only one, leading to the observation of a deterministic Run and Tumble dynamics. Furthermore, the properties of this deterministic Run and Tumble dynamics is seen to be controlled by the memory. By analogy with the studies of foraging animals, we will refer to the erratic phases as "tumbling phases" and to the rectilinear phases as "run phases". Since the walker evolves in free space, the only origin for this Run and Tumble dynamics can only come from the waves below the particle. As a consequence, we will study in the forthcoming section the wavefield beneath the walker as it comes closer to a R-point.

### 3.2.2 Wavefield structure

The walker being only compelled to interact with its own past, i.e. the waves on the surface, the chaotic-like trajectory and the subsequent diffusive dynamics can only arise because of the wavefield. In Fig.3.3, the dynamics of the wavefield is illustrated for a memory parameter $\mathrm{Me} = 150$. Each subplot corresponds to different instants of the dynamics around a R-point. The whole plot covers 35 bounces of the walker, each subplot being distant of 5 bounces. Note that the wavefield is only drawn along the direction of propagation of the walker for the sake of simplicity. The walker position relative to the wavefield is indicated by a black dot. Let us now describe the wavefield evolution. Before the R-point, the walker builds up its wavefield, increasing its amplitude. When comparing Fig.3.3(a) and Fig.3.3(e), the walker comes back to the same position relative to the wavefield: the walker appears both time at the bottom of the waves it creates. Yet, the global amplitude has increased. Because the amplitude increases and the wavelength $\lambda_F$ is fixed, the wave force $\vec{F}_w$ becomes more important. Between Fig.3.3(g) and Fig.3.3(h), the positive slope of the interface is able to completely stop the walker. Because it remains still above the interface, the walker accumulates impacts at the same position which in returns increases globally and significantly the wavefield amplitude. As a result, the walker moves backwards. The increase of the wavefield amplitude which eventually stops the walker is therefore the key to the wobbling motion. This behaviour contrasts with what is expected for a stable walk along the surface for lower memory parameters. Indeed, in such a case, the walker experiences always the same propulsive force since its position relative to its wavefield remains unchanged. An equilibrium is found between the kick of momentum provided by the wavefield and the average drag experienced during the surfing phase. This argument is discussed mathematically in Section 2.3. As a consequence, the wavefield keeps a constant amplitude and the wobbling phase cannot be started.

Let us try to understand how the wavefield amplitude increases. For this purpose, one needs to understand how the wavefield amplitude reacts to the relative position of two impacts. Two impacts which are distant of $n\lambda_F$, $n$ being an integer, generate waves that interfere constructively, resulting in an enhanced global amplitude. On the contrary, two impacts being distant of $(n + 1/2)\lambda_F$ interfere destructively, leading to a smaller global amplitude. As it can be deduced from Fig.3.3, the walker accelerates and decelerates relative to its wavefield. In par-

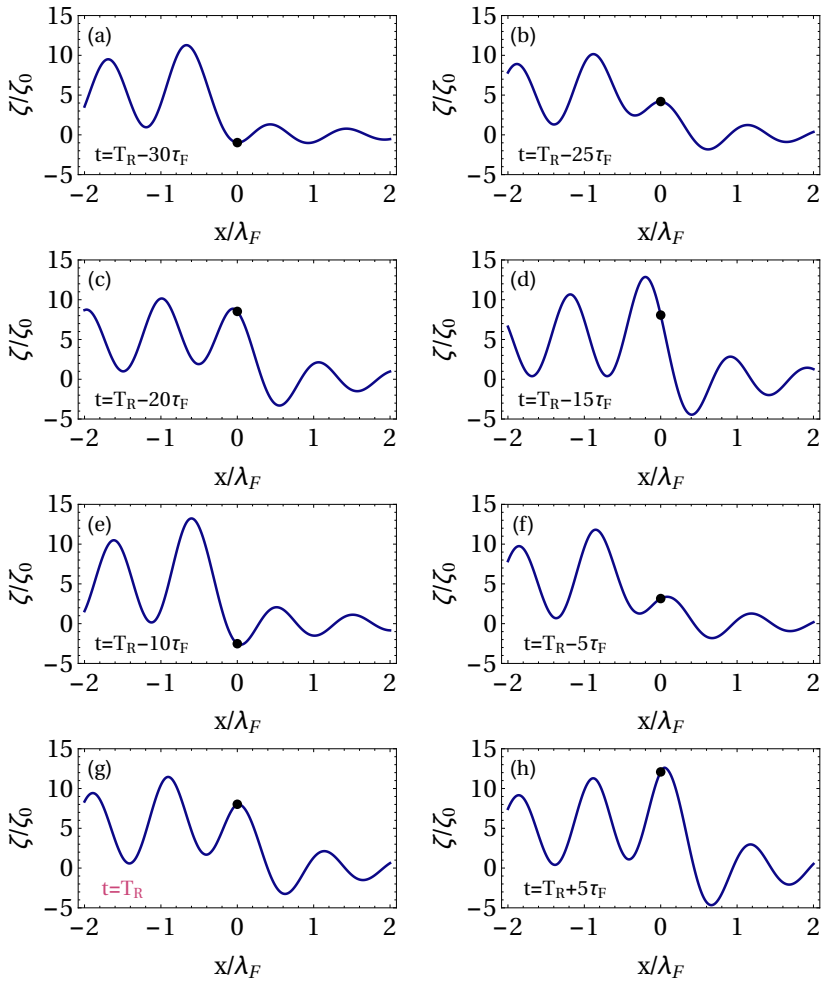


**Figure 3.3:** Time evolution of the wavefield near a R-point at $T_R = 456\tau_F$ for $\mathrm{Me} = 150$. Only the wavefield in the direction of propagation is depicted. The walker position is indicated by the black dot. The time is indicated on each subplot. At the instant $t = T_R$, the walker is not able to climb the wavefield it has created. While the walker remains almost motionless, the wavefield builds up underneath ($t = T_R + 5\tau_F$). The particle is then propelled in the opposite direction.

ticular, the walker spends a few period bouncing at the crest of its waves (see Fig.3.3(b,c)) while moving quickly when at the bottom (see Fig.3.3(d,e,f)). The density of impacts along the trajectory therefore oscillates with the Faraday wavelength. This assertion is proved with Fig.3.4. This figure shows the wavefield 16 bounces before the R-point discussed in Fig.3.3. Beside the wavefield, the density of impacts along the trajectory is displayed in purple. The darker the shade, the

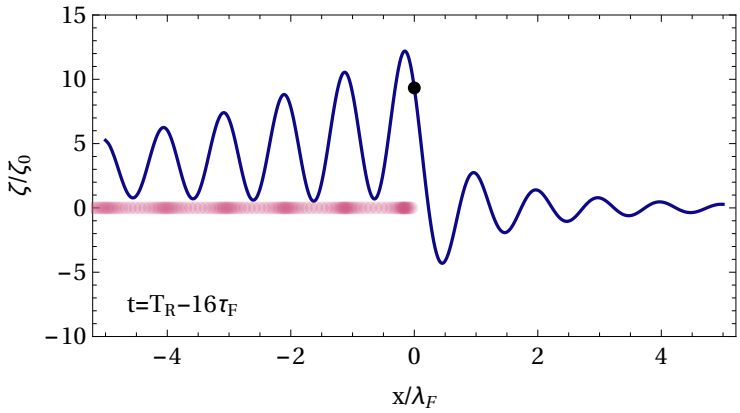


**Figure 3.4:** Wavefield under the walker at time $t = T_R - 16\tau_F$ for $\mathrm{Me} = 150$. The wavefield is only drawn along the rectilinear trajectory of the walker. The black dot gives the walker position on the wave field. The purple line gives the density of impacts on the surface along the trajectory. The more opaque the line is, the denser the sources distribution. One can see a resonance between the density oscillation and the wavefield structure, which explains the increase of amplitude observed in Fig.3.3.

more impacts can be found. It can be seen that when the walker sits at the crest of its wave more impacts can be found. On the contrary, on the bottom of the wavefield, fewer impacts are seen. Because dark shaded area are distant of $\lambda_F$, the global amplitude increases during the motion of the walker. A 2D visualisation is also given in Fig.3.5. The left part of this figure corresponds to the dynamics at $\mathrm{Me} = 50$ while the right part of this figure has been obtained for $\mathrm{Me} = 150$ 16 bounces before the R-point described previously. In the left side of Fig.3.5, the usual horseshoe pattern of the wavefield around the walker is recovered [52]. For the right side of this figure, modulation of the pattern behind the walker is seen, as a result of the oscillating density of impacts. There is therefore a resonance between the fluctuating velocity of the walker and the amplitude of the wavefield. The role of the memory in the amplifying process can be understood as follows. For low memory, the temporal damping of the waves is important. It means that even if the speed oscillated, the constructive interferences process would be limited thanks to the important temporal damping. On the other side, for high memory parameters, this temporal damping cannot limit the growth of the wavefield, ultimately leading to the reflection of the walker at a R-point. After the R-point, the has to interact with its own wavefield and the many images of its past. This acts as a trap which the walker eventually leaves.

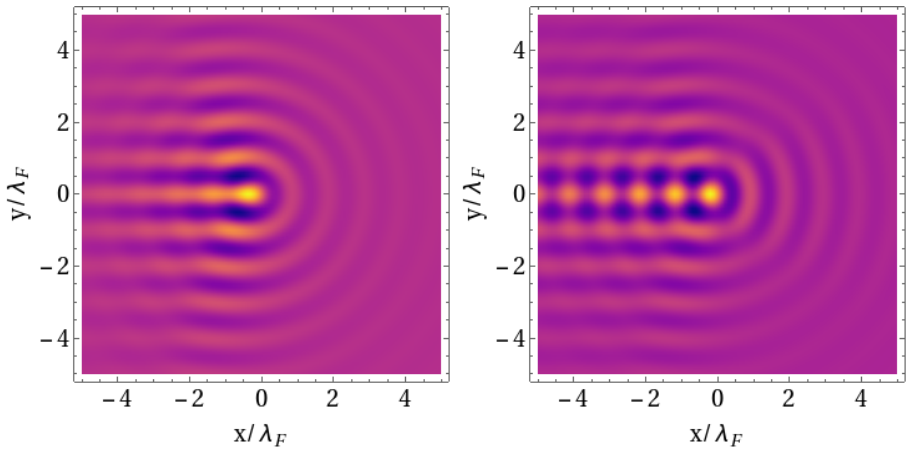


**Figure 3.5:** Comparison between the 2D wave field generated by a walker for different memory parameters $\mathrm{Me}$. **(Left)** $\mathrm{Me} = 50$ shown the wavefile for a stable rectilinear trajectory. A horseshoe pattern is visible. **(Right)** $\mathrm{Me} = 150$ shows the wavefield at $t = T_R - 16\tau_F$. Modulation are seen behind the walker.

We have shown in this section that a diffusive motion can be observed, which mimics a Run and Tumble motion. The memory parameter tunes this dynamics which finds its origin in the positive feedback between the fluctuating speed and the waveforce and increases the wavefield amplitude.

## 3.3 Chaotic evolution of the speed

It has been discussed in the previous section that the oscillating speed of the walker is the mechanism triggering the wobbling dynamics by increasing the wavefield amplitude. In this section, we will consider the time evolution of the walker speed and the chaotic dynamics which arises as the memory $\mathrm{Me}$ is increased.

### 3.3.1 Time series

Let us consider the time series describing the walker speed as the memory parameter $\mathrm{Me}$ is changed. Figure 3.6 shows the walker speed during the first thousand steps of the particle dynamics. Only the horizontal velocity is considered and it is obtained via an eleven points differentiation scheme based on the impact positions of the walker. The vertical bouncing dynamics is neglected. The memory parameters $\mathrm{Me}$ considered corresponds to the three memories investigated in

Fig.3.1. One observes that two distinct dynamics can be observed. For low memory parameters ($\mathrm{Me} \leq 100$), the walker speed is constant after a transient regime. This transient has a duration of a few tens of bounces and shows speed fluctuations. They are damped towards the equilibrium value. Note that the duration of the transient as well as the equilibrium speed is a function of the memory $\mathrm{Me}$: the higher $\mathrm{Me}$, the longer the transient and the higher the equilibrium speed. On the contrary high memory parameters ($\mathrm{Me} \geq 150$) lead to chaotic-like behaviours. For intermediate memory parameters ($\mathrm{Me} = 150$, see Fig.3.6(b)), the speed fluctuations are seen to increase slowly with time in comparison with high memory parameters ($\mathrm{Me} = 1500$, see Fig.3.6(c)). Furthermore, erratic fluctuations last longer for higher memory parameters (see Fig.3.6(c)) than for lower memory parameter (see Fig.3.6(b)). The transition from the increasing fluctuation part and the erratic fluctuation part arises when the walker speed reaches zero because of the high speed fluctuations. In between $\mathrm{Me} = 100$ and $\mathrm{Me} = 150$, the transient dynamics gives this increasing speed fluctuation. During a transient, erractic fluctuations arise. But after this transient the speed eventually reaches a equilibrium constant value. The closer the memory parameter is to $\mathrm{Me} = 150$, the longer this transient becomes. At $\mathrm{Me} = 150$, even after $10^7$ bounces, no decrease of the speed fluctuations is seen in simulation. Comparing the observations made regarding the trajectories and the speed time series allows the following conclusion. Rectilinear trajectories shorten likewise increasing speed fluctuations parts in the time series. The wobbling parts of the trajectories increase the same way chaotic speed evolution arises. As a consequence, the walker diffusive behaviour in real space must be triggered by a chaotic process in the velocity space of the walker. Especially, in the time series, the part where the speed fluctuations are seen to increase corresponds to the run phase while the chaotic evolution corresponds to the tumble phase.

It is worth noticing that fluctuations in time series, either damped (Fig.3.6(a)) or maintained Fig.3.6(b,c)), are common features of time delayed systems. As the result of an Hopf bifurcation [151, 53], this property is widely observed and also used in engineering in order to suppress unwanted oscillations in mechanical systems, e.g. for the cranes stabilisation when transporting loads [82] or for the anti-rolling motion of sailing ships [120]. Spontaneous oscillations are also observed in physiology with the Cheynes-Stokes respiration [112]. This is a disease where the patient's breathing "*is characterized by a crescendo-decrescendo pattern*

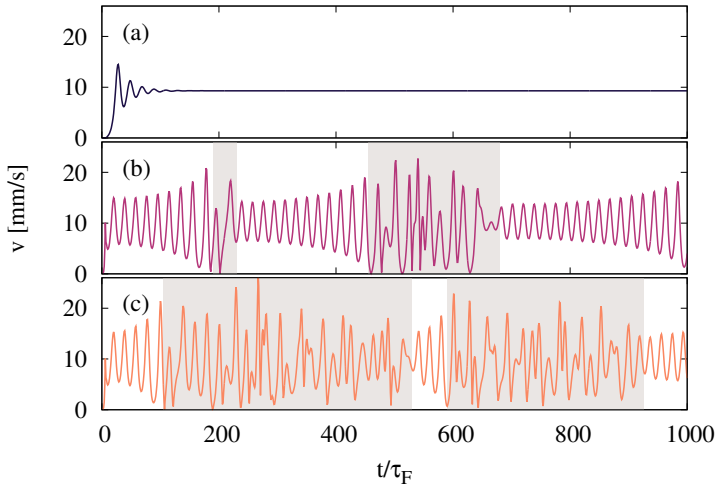


**Figure 3.6:** Speed as a function of time for the trajectories displayed in Fig.3.1: **(a)** $\mathrm{Me} = 15$, **(b)** $\mathrm{Me} = 150$, **(c)** $\mathrm{Me} = 1500$. The gray areas correspond to the tumble phases. Low memories lead to stable dynamics where initial velocity perturbations rapidly decrease towards the velocity equilibrium value. High memories give unstable dynamics with chaotic-like evolution. For $\mathrm{Me} = 150$ the perturbation grows exponentially over a period of a few hundreds of Faraday periods $\tau_F$. For $\mathrm{Me} = 1500$ the dynamics is mainly chaotic-like, with increasing and fluctuating perturbations arising over a few tenths of periods $\tau_F$.

*of hyperventilation alternating with apnea or hypopnea that occurs at the nadir of the crescendo-decrescendo pattern during sleep*" [93]. Nevertheless, the time delay in the walking droplet dynamics is implemented in a rather unique fashion. In all the examples cited above, the delay in the system is injected only once and the control parameter is the distance to the delay $\tau$. As an illustration, let us give the example found in most textbooks [151, 53]

$$\dot{x}(t) = -x(t-\tau), \tag{3.3}$$

where $\tau$ is the delay. It is at the opposite of the walking droplet dynamics where multiple delays are considered with a temporal distance $\tau_F$, as seen in Eq.(2.8). The walking droplet dynamics therefore defines a novel class of time delayed systems. Let us now describe the chaotic process observed in the velocity space.

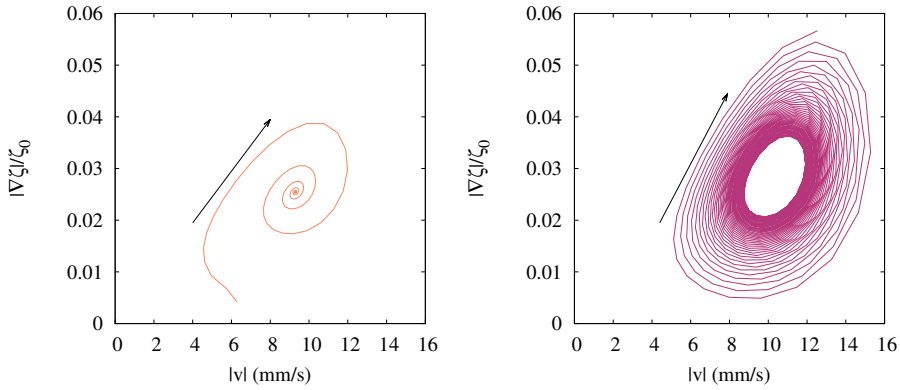


**Figure 3.7:** Flow in the $(|\vec{v}|, |\vec{\nabla}\zeta|/\zeta_0)$-space: **(a)** $\mathrm{Me} = 15$ and **(b)** $\mathrm{Me} = 150$. Low memory parameters give a stable fixed point at $(v^\star, \nabla\zeta^\star/\zeta_0) = (9.295, 2.544\,10^{-2})$. The flow in this case converges rapidly to this fixed point. The high memory case shows a unstable fixed point ejecting the flow outwards.

### 3.3.2 Shil'nikov chaos

When looking at Fig.3.6 and Fig.3.1, one sees that the memory parameter defines roughly two regimes. A first regime of decreasing speed fluctuations is observed for $\mathrm{Me} < \mathrm{Me_c}$ where the wave force reaches an equilibrium value. And a second regime of increasing oscillations, of both the speed and the wave force, joined to periods of erratic fluctuations for $\mathrm{Me} > \mathrm{Me_c}$. In this analysis, the critical memory parameter $\mathrm{Me_c}$ has yet to be defined. Since the chaotic process is triggered by the wavefield, we study the dynamics in the $(|\vec{v}|, |\vec{\nabla}\zeta|)$-space. The first regime for $\mathrm{Me} < \mathrm{Me_c}$ possesses a stable fixed point $(v^\star, \nabla\zeta^\star/\zeta_0) = (9.295, 2.544\,10^{-2})$ in the $(|\vec{v}|, |\vec{\nabla}\zeta|)$-plane, as illustrated in Fig.3.7(a) for $\mathrm{Me} = 15$. The speed here is expressed in $\mathrm{mm/s}$. The flow in the phase space spirals into the fixed point at a rate which decreases as the memory increases. Note that the position of this fixed point changes as the memory increases, especially for low memory. When the memory parameter $\mathrm{Me}$ crosses its critical value $\mathrm{Me_c}$, the flow spirals out of the fixed point, as observed from Fig.3.7(b) for $\mathrm{Me} = 150$. The eigenvalues at the unstable fixed point are imaginary, complex conjugate, with positive real parts. The flow does not reach a limit cycle after spiralling out. Instead, the walker enters a tumble phase where erratic fluctuations appear. This last behaviour is not shown in Fig.3.7 for the sake of clarity. Ultimately, at the end of a tumble phase,

the walker speed and the wave force are close to the value of the unstable fixed point. The flow spirals out of this fixed point again. The erratic phase can therefore be seen as a mechanism re-injecting the flow back at the vicinity of the fixed point, giving rise to a homoclinic orbit linking the fixed point to itself in a phase space of a much larger dimension.

A similar behaviour, a homoclinic orbit leading to chaotic dynamics, has been observed in many other systems. One can cite the Belousov-Zhabotinskii chemical reaction [2], an experimental illustration of the so-called *Brusselator* developed by Prigogine [146]. In [2], the Belousov-Zhabotinskii reaction is made using malonic acid $CH_2(COOH)_2$, sodium bromate $NaBrO_3$ and cerium sulfate $Ce_2(SO_4)_2$ continuously mixed in heated sulphuric acid $H_2SO_4$. Each chemical is injected with three feed lines into the reactor at a given flow rate, which is the control parameter of the experiment. The authors showed that the concentration of ceric ions $Ce^{4+}$ in solution oscillates and those fluctuations increase strongly with time before dropping to zero and starting again. This behaviour is shared with the walking droplet dynamics. The authors demonstrated that this chaotic behaviour originates from a Shil'nikov-type bifurcation, which describes the homoclinic orbits that departs from a saddle point and returns to itself after an infinite period [117].

In order to illustrate the Shil'nikov bifurcation and the subsequent homoclinic chaos, let us consider the Rössler model [154]. It is defined as follows

$$\begin{cases} \dot{x} = -y - z, \\ \dot{y} = x + ay, \\ \dot{z} = b + z(x - c), \end{cases} \tag{3.4}$$

where $a$, $b$ and $c$ are constant. This system is shown to exhibit a Shil'nikov bifurcation for $a = 0.18$, $b = 0.2$ and $c = 15$ [3], leading to a homoclinic chaos as depicted in Fig.3.8. The system shows two fixed points

$$\vec{x}^{\star}_{\pm} = (ap_{\pm}, -p_{\pm}, p_{\pm}) \quad \text{with} \quad p_{\pm} = \frac{c \pm \sqrt{c^2 - 4ab}}{2a}. \tag{3.5}$$

Figure 3.8 focuses on $\vec{x}^{\star}_{-}$ and on the flow around this fixed point. Given the small values of $a$ and $b$ compared to $c$, $\vec{x}^{\star}_{-} \approx \vec{0}$. In Fig.3.8, the flow spirals out

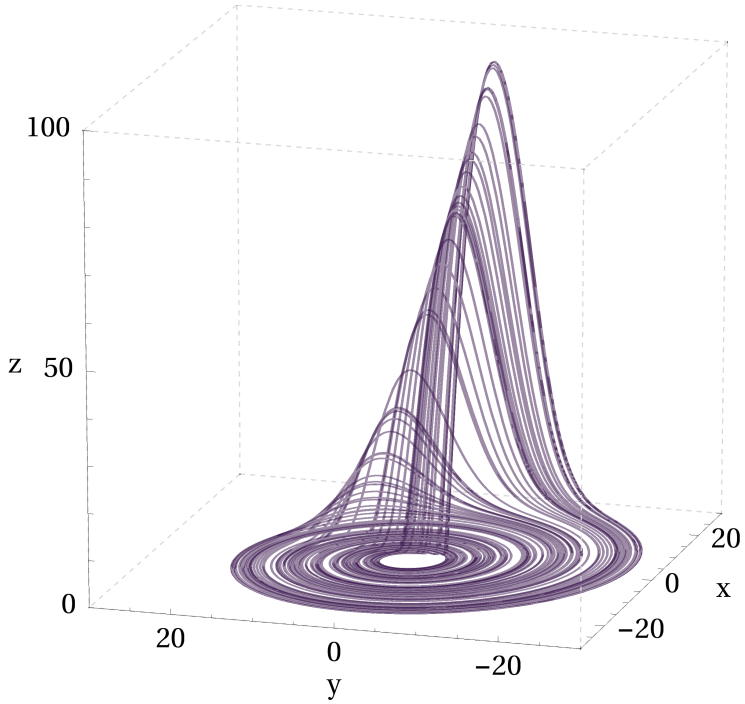


**Figure 3.8:** Chaotic attractor for the Rössler model with parameters $a = 0.18$, $b = 0.2$ and $c = 15$. The fixed point $\vec{x}^{\star}_{-}$ near $\vec{0}$ is unstable in the $(x, y)$-plane and stable in the $z$-direction. The flow spirals out of in the $(x, y)$-plane before jumping in the $z$ direction.

of the fixed point in the $(x, y)$-plane. Once reaching large values of $x$ and $y$, the flow jumps vertically in the $z$ direction and is reinjected near the stable fixed points. The two time scales associated with the two phenomena, the spiralling divergence out of the fixed point and the reinjection at the center, are largely different. Indeed, linear analysis at the fixed point gives the following eigenvalues for each direction $\lambda_{x,y} \approx 9\,10^{-2} \pm 1i$ and $\lambda_z \approx -15$ for $a = 0.18$, $b = 0.2$ and $c = 15$. Since the rate of divergence and convergence is given by the real part of those eigenvalues, one sees that the time scale associated with the two processes differs from more than two orders of magnitude. The ratio of the two time scales $\nu = |\mathrm{Re}\,\lambda_\mathrm{z}/\mathrm{Re}\,\lambda_\mathrm{x,y}|$ defines the *saddle index* of the fixed point, which in our case gives $\nu \gg 1$.

With those definitions, one could discuss the condition required to observe a Shil'nikov-type homoclinic chaos. The following theorem is adapted from [165]

and is given without proof.

Theorem 1 *Given the third-order automonous system*

$$\frac{d\vec{x}}{dt} = \psi(\vec{x}), \quad t \in \mathbb{R}, \quad \vec{x} \in \mathbb{R}^3,$$

*where $\psi$ is a $\mathcal{C}^2$ vector field on $\mathbb{R}^3$. Let $\vec{x}^\star$ be an equilibrium point for this ODE and let suppose the following*

- *the equilibrium point is a saddle focus whose characteristic eigenvalues defines a saddle index $\nu > 1$,*
- *there exists a homoclinic orbit based at $\vec{x}^\star$.*

*Then, the system exhibits homoclinic chaos.*

Clearly, the Rössler system satisfies the condition of this theorem, rationalizing the chaos one observes. Note that this type of chaos is also observed in other systems: in Chua's circuit [117], in the Rosenzweig-MacArthur food chain model [101], and in the well-known Lorenz model for peculiar values of its parameters [162].

Let us study the walking droplet dynamics under this perspective. We need a 3D-phase space to apply the Shil'nikov theorem. The $(|\vec{v}|, |\vec{\nabla}\zeta|)$-plane illustrated in Fig.3.7 gives the unstable part of the phase space. In order to complete the phase space, one needs a variable that brings the flow back to the unstable plane of the phase space. Empirically, we choose as the third axis of the phase space the $\dot{\theta}$-axis, describing the change of orientation $\theta$ of the velocity vector in real space. Indeed, as seen from Fig.3.1, during the run phase of the dynamics, the orientation of the velocity remains constant, the trajectory being rectilinear and this gives $\dot{\theta} = 0$. Furthermore, after a tumble phase, the walker is always seen in a rectilinear phase, which indicates the existence of an homoclinic loop in the $(v, \nabla\zeta/\zeta_0, \dot{\theta})$-space. As a consequence, the flow is expected to spiral out of the saddle focus $(v^\star, \nabla\zeta^\star/\zeta_0, 0)$ along the $(\dot{\theta} = 0)$-plane and to converge back to the saddle focus along the $\dot{\theta}$-axis. This assertion is proved thanks to Fig.3.9 which shows the flow in the $(|\vec{v}|, |\vec{\nabla}\zeta|, \dot{\theta})$-space during a run-phase for a walker with a memory parameter $\mathrm{Me} = 150$ during 3000 bounces. The run phase is shown in orange and the tumble phases in purple. Both the early instants of the

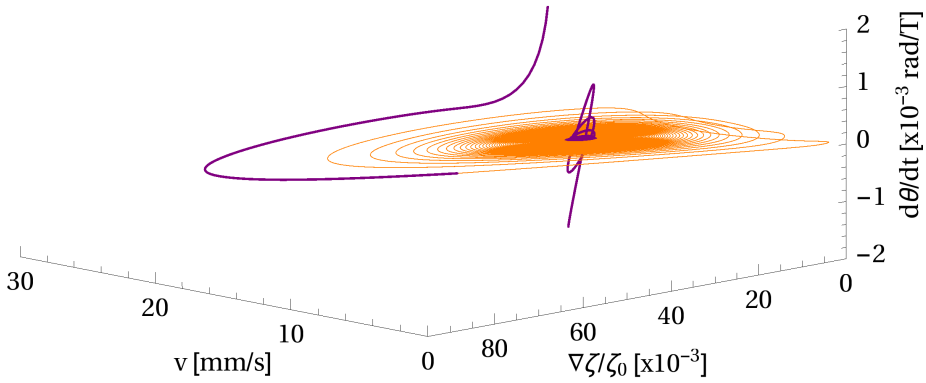


**Figure 3.9:** Flow in the $(|\vec{v}|, |\vec{\nabla}\zeta|, \dot{\theta})$-space around the unstable saddle focus for $\mathrm{Me} = 150$. The run phase is shown in orange and the tumble phases in purple. Both the early instants of the folliwing run phase and the later instants of the previous one are shown. The flow in injected near the saddle focus from below the $(\dot{\theta} = 0)$-plane. The flow then spirals outwards in this plane before distabilizing and being ejected out of the plane. The dynamics is shown over 3000 bounces.

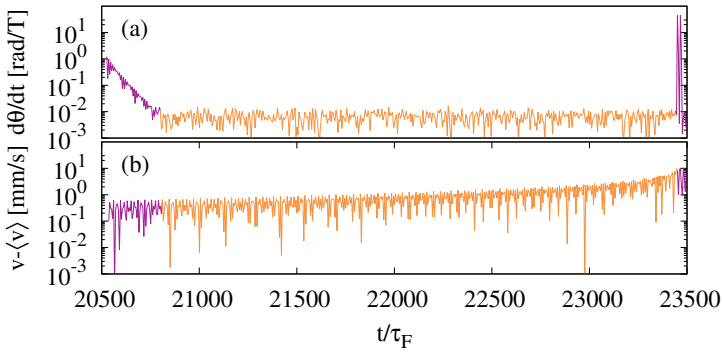


**Figure 3.10:** Fluctuations around the saddle focus along the $\dot{\theta}$ direction (a) and along the $|\vec{v}|$ direction (b). The fluctuations are given in logarithmic scale in order to evidence exponential decrease/increase around the saddle focus. The colour code used is the same as in Fig.3.9: Orange accounts for the run phase and purple for the tumble phases. Those time series corresponds to the same flow depicted in Fig.3.9.

following run phase and the later instants of the previous one are shown. The flow in injected near the saddle focus from below the $(\dot{\theta} = 0)$-plane. The flow then spirals outward in this plane before destabilizing and being ejected out of the plane. In order to conclude about the existence of a Shil'nikov type chaos, one

has to measure the saddle index of the saddle focus. For this purpose, we have plotted in Fig.3.10 the time series relative to $\dot{\theta}$ and $(|v| - \langle v \rangle)$, $\langle v \rangle$ being the average speed expected to give a good approximation of the saddle focus position. Similarly to Fig.3.9, the run phase is drawn in orange and the tumble phases in purple. For each plot, semi-logarithmic scale has been used along the vertical axis in order to evidence exponential evolution and to extract Lyapunov exponents. Along the $\dot{\theta}$ direction (Fig.3.10(a)), one has $\mathrm{Re}\,\lambda_{\mathrm{z}} \approx -1.535\,10^{-2}\ T^{-1}$ and in the $(|\vec{v}|, |\vec{\nabla}\zeta|)$-plane (Fig.3.10(b)), one has $\mathrm{Re}\,\lambda_{\mathrm{x,y}} \approx 8.53\,10^{-4}\ T^{-1}$. Given the definition of the saddle index, it yields $\nu \approx 18$ which indicates indeed a Shil'nikov type chaos thanks to theorem 1.

We have seen in this section that the chaotic dynamics in the velocity space is due to a Shil'nikov-type chaos. This chaos is due to a homoclinic bifurcation linking a saddle focus to itself in the $(|\vec{v}|, |\vec{\nabla}\zeta|, \dot{\theta})$-space. The flow spirals out of the saddle focus along the $(|\vec{v}|, |\vec{\nabla}\zeta|)$-plane and eventually is ejected out of this plane once $|\vec{v}|$ has reached zero. After some time, the flow is injected back near the saddle focus and the dynamics repeats. The first part of this process corresponds to the run phase while the reinjection process corresponds to the tumble phase. As a consequence, the diffusive process observed in the real space comes from a chaotic process in the velocity space. Given this conclusion, let us analyse the diffusive dynamics from a statistical description.

## 3.4 Large scale diffusion

Let us focus on the trajectories and their statistical description. The overall dynamics of the walker is made of two contributions: run stages when the walker travels along a straight line with a fluctuating speed around a constant mean and tumble stages when the walker remains in a small region of the plane because of erratic fluctuations of the velocity trapped into its own waves. For increasing memory parameters $\mathrm{Me}$ the duration of the run stages decreases and tumble stages appears more frequently. Let us describe statistically each process before studying the walker mean squared displacement and diffusive properties.

### 3.4.1 Statistical description of the dynamics

The run and tumble stages of the dynamics are detected thanks to the instantaneous curvature of the trajectory

$$\mathcal{C}(t) = \frac{|\dot{x}(t)\ddot{y}(t) - \dot{y}(t)\ddot{x}(t)|}{(\dot{x}^2(t) + \dot{y}^2(t))^{3/2}}. \tag{3.6}$$

The instantaneous velocity and acceleration are obtained via an eleven points differentiation scheme based on the impact positions of the walker. The walker is considered to be in a run stage if $\mathcal{C}(t) < |\lambda_F^{-1}|$ during at least 50 bounces. By tracking the value of the curvature during the simulation, the duration of each run stage can be computed. We focus on the Probability Distribution Function (PDF) of the time spent in the run stage, namely $\Delta T_{run}$. The tumble phase will be discussed later in this section. Figure 3.11 gives the PDF of $\Delta T_{run}$ for a memory parameter $\mathrm{Me} = 150$ and $\mathrm{Me} = 1500$. Thanks to the logarithmic scale, the PDF is seen to follow an exponential distribution

$$\mathcal{P}(\Delta T_{run}) \sim \exp\left(-\Delta T_{run}/\tau_{run}\right), \tag{3.7}$$

where $\tau_{run}$ is the average time spent in the run stage. The average time $\tau_{run}$ is seen to decrease significantly with the memory parameter. It is interesting to note that this probability distribution cancels the existence of Levy flights in the dynamics usually considered for the statistical description of Run and Tumble dynamics [8]. Indeed, the Levy flight PDF is given by the power law $\mathcal{P}(d_{run}) \sim d_{run}^{-\alpha}$ where $d_{run}$ is the distance travelled during a run stage and $\alpha$ is a positive real number such as $1 < \alpha < 3$.

Memory is seen to alter the PDF in Fig.3.11. Figure 3.12 gives the average time in the run phase $\tau_{run}$ as a function of the memory parameter. A double logarithmic scale has been used. One sees that $\tau_{run}$ is indeed decreasing as $\mathrm{Me}$ increases. Furthermore, $\tau_{run}$ diverges near a peculiar value $\mathrm{Me_c}$ below which no tumbling phase is seen. One therefore has an infinitely long run phase, i.e. the stable rectilinear trajectory expected for low memory. Beyond the singularity, $\tau_{run}$ decreases as a power law, as illustrated in the inset of Fig.3.12. In this inset, the inverse value of $\tau_{run}$ is displayed as a function of $(\mathrm{Me} - \mathrm{Me_c})$, in double logarithmic scale to evidence the power law. The value of $\mathrm{Me_c}$ has been obtained by fitting the data with the function $c(x - \mathrm{Me_c})^{\mathrm{b}}$ and gives $\mathrm{Me_c} = 146.41 \pm 6.44$. The exponent

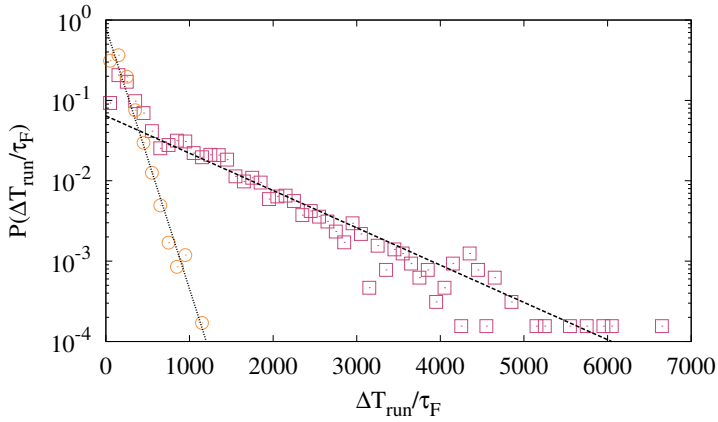


**Figure 3.11:** Probability to find a run stage of duration $\Delta T_{run}$ in the walker dynamics for memory parameter $\mathrm{Me} = 150$ (purple squares) and $\mathrm{Me} = 1500$ (orange circle). Logarithmic scale has been used along the $y$-axis, data have been acquired over a trajectory of $4.5\,10^6$ bounces. Solid lines give the fit by a exponential probability distribution $\mathcal{P}(\Delta T_{run}) \sim \exp\left(-\Delta T_{run}/\tau_{run}\right)$.

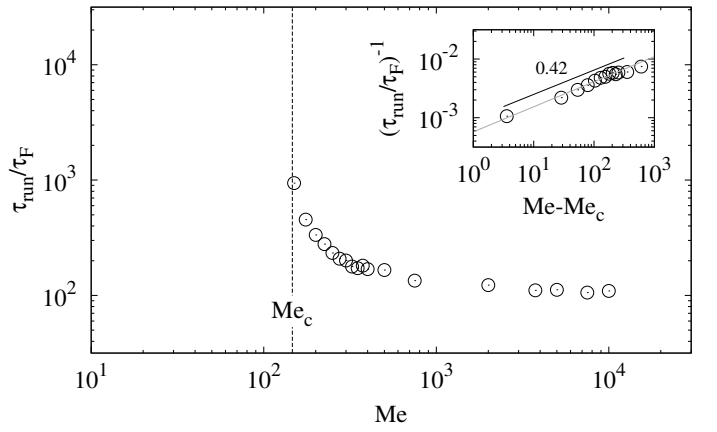


**Figure 3.12:** Average time spent in the run stage $\tau_{run}$ as a function of the memory parameter $\mathrm{Me}$. Double logarithmic scale has been used. The vertical dashed line gives the value of the critical memory parameter $\mathrm{Me_c} = 146.41 \pm 6.44$ giving the appearance of a tumbling motion. **(Inset)** Focus near the critical memory parameter $\mathrm{Me_c}$ in order to prove the power law dependence between $\mathrm{Me}$ and $\tau_{run}$. The solid gray line gives the power law $\tau_{run} \propto (\mathrm{Me} - \mathrm{Me_c})^b$ where $b = 0.42 \pm 0.09$.

of the power law is found to be $b = 0.42 \pm 0.09$ such as, near the singularity one

has

$$\tau_{run} \propto (\mathrm{Me} - \mathrm{Me_c})^{-0.42} . \tag{3.8}$$

We therefore possess the critical memory parameter triggering the chaotic process and diffusive dynamics. It is worth noticing that this analysis is hard to perform on the tumble phase. Indeed, one cannot use the complement of the run phase definition, namely a tumble phase defined by $\mathcal{C}(t) > |\lambda_F^{-1}|$. Indeed, the curvature of the trajectory varies a lot during the tumble phase and even vanishes for a few bounces. As a consequence, the algorithm detects a short term run phase and the tumble phases are measured as being shorten than what they really are. As a consequence, we have limited ourselves to the study of the run stage only.

The overall dynamics can be shown to be isotropic. In other words, there is no correlation between the angle at which the walker enters and leaves a tumble stage. This is proved by Fig.3.13 which shows the PDF of the difference between the outward angle $\theta_1$ and inward angle $\theta_2$ for the same tumble stage in the dynamics. One observes that the PDF is given by a uniform distribution, namely

$$\mathcal{P}(\theta_1 - \theta_2) \sim \mathcal{U}(0, \pi) . \tag{3.9}$$

This distribution is independent of the memory parameter value. A natural consequence of this result is that the walker diffuses in space uniformly without following a peculiar direction. In statistical terms, it means that the PDF describing the position of walker $\vec{r}$ has a zero mean value like a random walk. In physical terms, it means that the walker has no drift velocity when diffusing.

### 3.4.2 Diffusive dynamics

Finally, we consider the Mean Squared Displacement (MSD) of the walker. Statistically, this corresponds to the second moment of the $\vec{r}(t)$ distribution and measures the spreading of the distribution around its mean as a function of time. Since the first moment of this distribution is equal to zero, this is also the square of the standard deviation of the distribution. Mathematically, it is defined as

$$\langle \vec{r}(t)^2 \rangle = \frac{1}{N} \sum_{p=1}^{N} \left| \vec{r}(p\tau_F) - \vec{r}\left((p+t)\tau_F\right) \right|^2 , \tag{3.10}$$

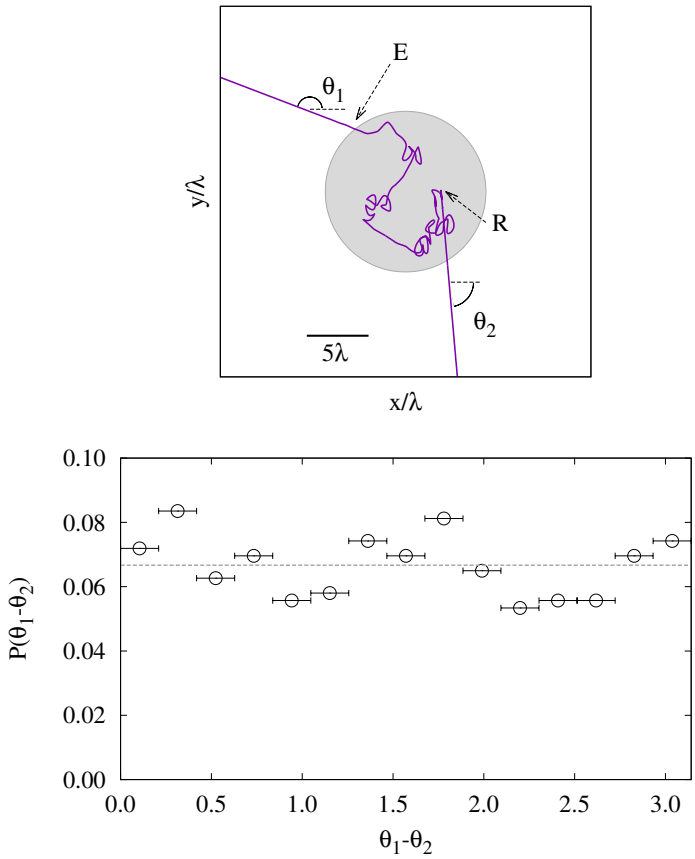


**Figure 3.13: (Top)** Schematic representation of the angle $\theta_1$ and $\theta_2$ of a tumbling phase. **(Bottom)** PDF of $\theta_1 - \theta_2$ for a memory parameter $\mathrm{Me} = 150$ showing a nearly uniform distribution in the interval $[0, \pi]$. Black points corresponds to simulations with the errorbars giving the size of a class of the histogram, 15 classes have been considered. The solid line gives the expectency for a uniform distribution. Data have been acquired over a trajectory of $5\,10^5$ bounces.

where $N$ is the number of positions considered in the sum. Two limit cases can be distinguished. If $\langle \vec{r}(t)^2 \rangle \propto t^2$, ballistic behaviour is obtained. If $\langle \vec{r}(t)^2 \rangle \propto t$ the dynamics is said to be diffusive. In between those two limits, the dynamics is said to be super-diffusive. Figure 3.14 shows the walker MSD for several memory parameters as a function of time in double logarithmic scale. Power laws are observed, as expected. Two behaviours can be observed depending on the memory parameter of the walker. For low memory parameters, $\mathrm{Me} = 100$ in Fig.3.14,

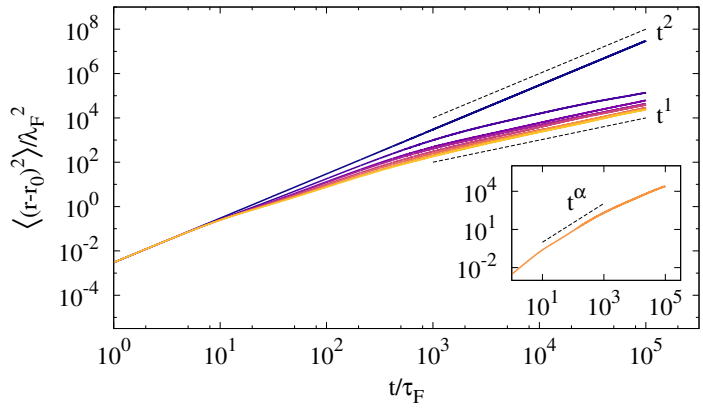


**Figure 3.14:** Mean squared displacement as a function of the time in double logarithmic scale. The different colors correspond to different memory parameters. From the darkest blue to the lightest yellow: $\mathrm{Me} = 100, 200, 375, 500, 1000, 2000, 5000, 10000$. Data have been acquired over $2.5\,10^6$ bounces of the walker. Ballistic behavior is observed for small time scale. Diffusive behavior is observed for long time scale. **(Inset)** Focus on the intermediate time scale. Superdiffusive behavior is seen for $10^1 < t < 10^3$ with a stable exponent. This exponent is seen to vary only due to the memory parameter $\mathrm{Me}$ as seen in Fig.3.15.

ballistic behaviour is observed for all time scales. For higher memory parameters, three regimes have to be distinguished depending on the time scale one considers. For small time scales ($t/\tau_F < 10$), ballistic dynamics is observed. But contrarily to low memory dynamics, for higher memory parameters super-diffusive behaviour arises with $\langle \vec{r}(t)^2 \rangle \propto t^\alpha$ for intermediate time scales ($10 < t/\tau_F < 10^3$). The exponent $\alpha$ is seen to depend on $\mathrm{Me}$ as depicted in Fig.3.15. For longer time scale ($t/\tau_F > 10^3$), the dynamics is diffusive without influence of the memory parameter. Let us discuss those results. The ballistic behaviour obtained for low memory parameters corresponds to the rectilinear trajectory shown in Fig.3.1. Thanks to Eq.(3.10), for a steady velocity $\vec{v}_0$, the MSD is $\langle \vec{r}(t)^2 \rangle = |\vec{v}_0|^2 t^2$ which rationalise this observation. For higher memory parameters, the appearance of the tumbling dynamics leads to a diffusive behavior for long time scales, as expected. Yet, short time scales give ballistic behaviour. When comparing this time scale to the distance travelled by the walker using $\Delta x = \langle v \rangle 10\tau_F$, one sees that it corresponds to half a Faraday wavelength. This means that the walker does not change its direction of motion below this distance. This result joins the observations made by Labousse *et al* [105] in their experimental and numerical studies of

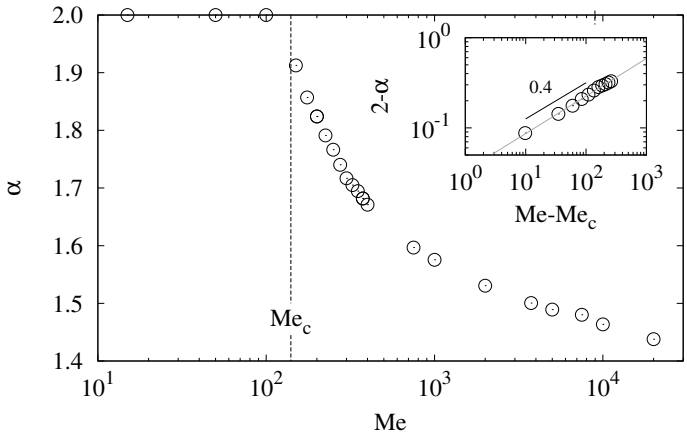


**Figure 3.15:** Exponent of the MSD for intermediate time scales as a function of the memory, in logarithmic scale along the $x$-axis. The dashed line gives the critical value of the memory parameter $\mathrm{Me_c}$ above which diffusion is seen. Above $\mathrm{Me_c}$, the diffusion exponent is seen to decrease as a power law with the memory parameter. **(Inset)** Evidence of the power law above $\mathrm{Me_c}$. The exponent is shown to change as $2-\alpha \sim (\mathrm{Me}-\mathrm{Me_c})^{-0.415}$ near the critical point.

self-orbiting motion. In their article, they shown that the walker is capable of self-trapping because of its wavefield. The walker begins orbiting along trajectories of quantified radii. The shortest possible radius is given by the first zeroth of $J_0$ and corresponds to $0.38\lambda_F$. Furthermore, they showed that for high memory and chaotic-like trajectories, the overall motion of the walker is made of loops reminiscent of the self-trapping dynamics. Those observations rationalise the ballistic motion of the walker for small time scales.

The intermediate time scale dynamics dynamics is quantified in Fig.3.15. This figure shows the exponent $\alpha$ of the superdiffusive dynamics as a function of the memory parameter in semi logarithmic scale along the x-axis. Two regimes can be seen, separated by a critical memory parameter $\mathrm{Me_c}$. Below $\mathrm{Me_c}$, ballistic behaviour is seen with $\alpha = 2$. This result corresponds to the ballistic dynamics for low memory. Above $\mathrm{Me_c}$, the exponent decreases from $\alpha = 2$ to $\alpha \simeq 1.4$ for the highest memory. Note that Note that the exponent seems to decrease beyond this value for even higher memory parameters. Similar exponents can be observed for the self-avoiding random walk where the particle avoids places it already has visited. The walking droplet can be seen as a kind of self-avoiding random walker since it is propelled by its past position and only interacts with

past positions when trapped in its wavefield.

The transition between the two regimes in Fig.3.15 has been studied by considering the evolution of $\alpha$ around $\mathrm{Me_c}$. The inset of Fig.3.15 gives, in double logarithmic scale, the evolution of $2-\alpha$ as a function of $\mathrm{Me}-\mathrm{Me_c}$. One has a power law given by

$$2-\alpha \propto (\mathrm{Me}-\mathrm{Me_c})^{0.415}\,, \tag{3.11}$$

with $\mathrm{Me_c} = 140.18 \pm 5.75$. The exponent of the power law $b = 0.415 \pm 0.047$. This critical memory parameters and the exponent of the power law are close to the ones obtained for the average time spent in the run phase. This observation indicates that the evolution of the run stage with memory drives the evolution of the superdiffusive dynamics. Nevertheless, its origin requires further investigations.

Similar dynamics have been observed in other systems tuned by memory. An interesting example is given by non-markovian random walks. Schütz and Trimper [160] suggested the following model. The walker position $x_{t+1}$ is related to the previous position $x_t$ by

$$x_{t+1} = x_t + \sigma_{t+1}, \tag{3.12}$$

where $\sigma_{t+1} = \pm 1$. The exact value of $\sigma_{t+1}$ is chosen within the memory of the system. This memory is made of the vector $\vec{\sigma} = (\sigma_1, \sigma_2, \ldots, \sigma_t)$ containing all the previous values of $\sigma$. An integer $j$ is chosen in the interval $\{1, t\}$ with a uniform probability, i.e. $j \sim \mathcal{U}(1,t)$, and one has

$$\sigma_{t+1} = \begin{cases} \sigma_t & \text{with probability } p, \\ -\sigma_t & \text{with probability } 1-p. \end{cases} \tag{3.13}$$

Therefore, memories can be remembered wrong with a probability $1-p$. Depending on the value of $p$, two dynamics are observed. For $p < 3/4$, the dynamics is diffusive with $\langle x_t^2 \rangle \propto t$. For $p > 3/4$, anomalous diffusion arises with $\langle x_t^2 \rangle \propto t^{4p-2}$. The peculiar case $p = 1$ gives a ballistic dynamics since the same choice $\sigma$ is made at each iteration of the model. Despite showing anomalous diffusion and including memory, the anomalous diffusion observed comes from the wrongness of the memories. An extension of this model has been proposed by Cressoni *et al* [36, 57, 37, 35] in which only a fraction $f < 1$ of the whole

memory $\vec{\sigma}$ is conserved. The choice for $\sigma_{t+1}$ is therefore restricted to the interval $\{1, \lfloor ft\}$, where $\lfloor$ refers to the integer part. In this example, $f$ would play the same role as $\mathrm{Me}$ in the walking droplet dynamics. As a function of both $p$ and $f$, different diffusive mechanisms are seen. Small values of $f$ favours anomalous diffusion while large values of $f$ leads to normal diffusion. Those properties relate to the observations made for the walkers as the memory parameter varies. Indeed, low $\mathrm{Me}$ gives ballistic dynamics and high $\mathrm{Me}$ gives diffusion. An exhaustive list of the effects of $f$ on the dynamics is beyond the scope of this manuscript. A complete description of the dynamics in the $(p, f)$ parameters space can be found in [36]. It is worth noticing that, contrarily to the walking droplet case, this dynamics is stochastic for $p \neq 1$ since the memory is randomly altered.

Memory effects and diffusive dynamics were also studied by Freund and Grassberger in [60] with their *Red queen's walk*. Similarly to the walking droplets dynamics, they encoded the memory within a 2D field and diffusion is observed. Very small time scales leads to super diffusion while normal diffusion is observed for long time scales, similarly to a true self-avoiding walk. Surprisingly, it is worth noticing that this model is deterministic and yet gives anomalous diffusion and normal diffusion for different time scale. Further comparisons could therefore be interesting.

## 3.5 Conclusion

We showed in this chapter that a walker may move above the surface in straight line or mimicking a run and tumble dynamics depending on its memory. Low memory parameters give a ballistic motion as described in previous works. High memory parameters give the newly observed diffusive motion. This new behaviour finds its roots in the wavefield generated by the walker. Beyond a critical value $\mathrm{Me}_\mathrm{c}$, the wavefield has the ability to reflect the walker in the opposite direction, forcing the walker to interact with its own past wavefield. As a consequence, the walker begins an erratic motion in a closed region of the surface, trapped by those waves. After a few tens of bounces, the walker eventually evades the trap and begins a new rectilinear part of this dynamics before being reflected again. This process can also be studied from the speed point of view. Ballistic phases show a fluctuating speed with increasing fluctuations. When the fluctuations get

the walker to stop, the erratic phase of the dynamic is triggered. The walker speed is shown to evolve chaotically. The underlying chaotic process can be described by a Shil'nikov bifurcation, giving birth to a homoclinic chaos in the $(|\vec{v}|, |\vec{\nabla}\zeta|, \dot{\theta})$-space. The overall consequence of this chaotic dynamics is the diffusion of the walker. At small time scale, ballistic dynamics is observed and for large time scale, diffusion is seen. In between, anomalous diffusion arises with an exponent for the mean squared displacement decreasing with the memory parameter $\mathrm{Me}$. Therefore, we relate the microscopic properties of the dynamics (the memory $\mathrm{Me}$) to the macroscopic properties of the diffusion (the exponent $\alpha$ of the mean squared displacement).

The most striking result is that the run and tumble dynamics one observes is deterministic. So far, models for this dynamics are stochastic and the duration or length of the run phase is chosen randomly. Typically, its duration follows a Lévy distribution or exponentials distribution [8]. In our case, the run and tumble dynamics comes from a set of deterministic rules as seen in Chapter 1 with Eqs.(2.10) and (2.11) or in Appendix A. To our knowledge, this is the first example of a deterministic approach of the run and tumble dynamics. Moreover, the diffusive process is obtained only with one particle in free space, without inclusion of obstacles, as in the Lorentz gas model [42]. The diffusive dynamics is only obtained via the nonlinear interaction of the walker with its past, through the wavefield it generates. The images of the past positions of the walker mimic as many interacting particles, allowing the walker to reach the thermodynamic limit usually required to observed this kind of dynamics.

# 4

# Walkers in harmonic potentials

*The walkers' dynamics in free space allows the particle to leave the trap the waves create. In other words, the walker escapes the trap of its own memory, leading to the diffusive dynamics discussed in the previous chapter. Therefore, interactions with the wave trap are time-limited. We ask the question of the continuous interaction between the walker and its memory by placing it in harmonic potentials of various stiffness, namely in region of space where its potential energy writes*

$$U(\vec{r}) = \frac{m\omega^2}{2}|\vec{r}|^2, \tag{4.1}$$

*$\omega = 2\pi f$ being the angular frequency and $f$ the frequency of the potential, $m$ being the walker mass. As stated in the introduction, the walker dynamics in harmonic potential has already been largely studied in the low memory regime and in the intermediate memory regime. Especially, the latter study has demonstrated that the walker follows stable trajectories at intermediate memory parameters. These eigenmodes quantify the average potential energy and average kinetic momentum. At the edge of chaotic dynamics, Perrard* et al. *showed that the walker erratically alternates between one eigenstate to another. Nevertheless, to our knowledge, there is no extensible study of the walker dynamics in the high memory limit.*

*The particle trajectory and velocity is described in the first part of this chapter, from a statistical point of view. We show that the memory acts as a thermal bath whose properties are tuned via the memory parameter* $\mathrm{Me}$*. A Fokker-Planck equation is*

*used to compute an equivalent temperature tuned by the memory. The wave dynamics is presented in the second half of the chapter. The waves are described thanks to Graff's addition theorem which allows for an efficient computation of the energy. We show that the time correlation of the walker dynamics leads to two major properties: equipartition of energy within the different wave modes and a global energy minimisation process which keeps a relatively low energy compared to uncorrelated dynamics.*

## 4.1 Particle dynamics statistical description

We first focus on the particle dynamics for various values of the memory parameter $\mathrm{Me}$ and frequency of the confining potential $f$. The statistical description follows.

### 4.1.1 Trajectories in harmonic potentials

Once immersed within an harmonic potential, the walker remains in an enclosed region of space. Depending on the value of the frequency $f$ and the value of the memory parameter $\mathrm{Me}$, the confinement is expected to be more or less efficient. Let us begin with a description of the dynamics for increasing memory parameters. In Fig.4.1, a walker is immersed in an harmonic potential with a natural frequency $f = 100\ \mathrm{mHz}$. The memory parameters investigated are $\mathrm{Me} = 10$ (a), $\mathrm{Me} = 89$ (b) and $\mathrm{Me} = 250$ (c). Increasing the memory increases the complexity of the dynamics. Low memory parameters give a circular trajectory. This limit was studied by Labousse and Perrard [103] and later by Bush *et al* [21]. The intermediate memory parameters lead to the self-organisation of sources on the interface [104]. As a consequence, the trajectory can be different from a circle and other eigenstates can be observed [139]. In the dynamics illustrated in Fig.4.1(b), a trifolium is seen. Finally, for high memory parameters, the dynamics becomes chaotic with features similar to the dynamics explored in the previous chapter. Nevertheless, because of the harmonic potential, the walker is compelled to remain in a close region of space. This is the regime of interest in this chapter.

Let us now study the effect of the frequency on the walker dynamics. Figure 4.2 shows the influence of the frequency $f$ on the dynamics for a walker in the very high memory regime, i.e. $\mathrm{Me} = 1000$. Two frequencies are considered: $f = 100$ $\mathrm{mHz}$ and $f = 250\ \mathrm{mHz}$. The left-hand side of this figure shows the trajectory

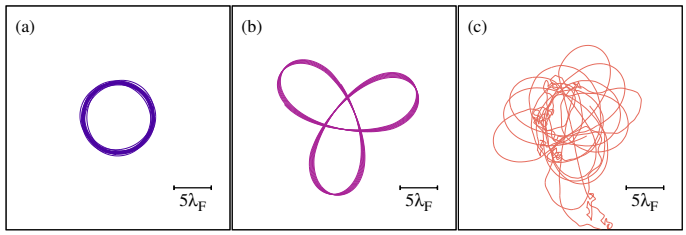


**Figure 4.1:** Trajectories within an harmonic potential for increasing memory parameters and for a fixed natural frequency $f = 100$ mHz. **(a)** $\mathrm{Me} = 10$, **(b)** $\mathrm{Me} = 89$ and **(c)** $\mathrm{Me} = 250$. Each trajectory displayies $10^4$ bounces.

over $10000$ steps (resp. $25000$ steps) for the frequency $f = 250$ mHz (resp. $f = 100$ mHz). Two different simulation times have been considered in order to have the same coverage within the harmonic potential despite having different confinement. Note that the scale of each sub-plot is different. The trajectories appear to be chaotic in each case, and made of succession of sharp changes of direction, loops and even reminiscence of the eigenstates observed in the same harmonic potential for much lower memories. Excursions in region of high potential energy is also observed, especially in the low frequency case. Large loops left the center of the potential and reach distance up to $15\lambda$. Finally, the walker tends to remain at the center of the potential, barely travelling away. Given the chaotic evolution of the position, we discuss the dynamics from a statistical point of view. The right-hand side of Fig.4.2 gives a heat map of the probability to find the walker at a given position in the long term dynamics. Simulation times are $2.5\,10^5$ steps for $f = 250$ mHz and $10^6$ steps for $f = 100$ mHz. Once again, the scale of each figure is not the same since the confinement varies. One sees that both figures are almost identical and axis-symmetric, only differing from each other by small details. This last observation points out that a common description lies in the dynamics.

In order to evidence a common feature in the dynamics, we consider the Probability Distribution Function (PDF) in the physical space $\mathcal{P}(\vec{r})$ and the PDF in the velocity space $\mathcal{P}(\vec{v})$. The corresponding results are given in Figs.4.3 and 4.4. We investigate different frequencies at the given memory parameter $\mathrm{Me} = 2500$. For Fig.4.3, the results show Maxwell-Boltzmann distribution with a mean value and standard deviation directly related to the stiffness of the harmonic potential. The

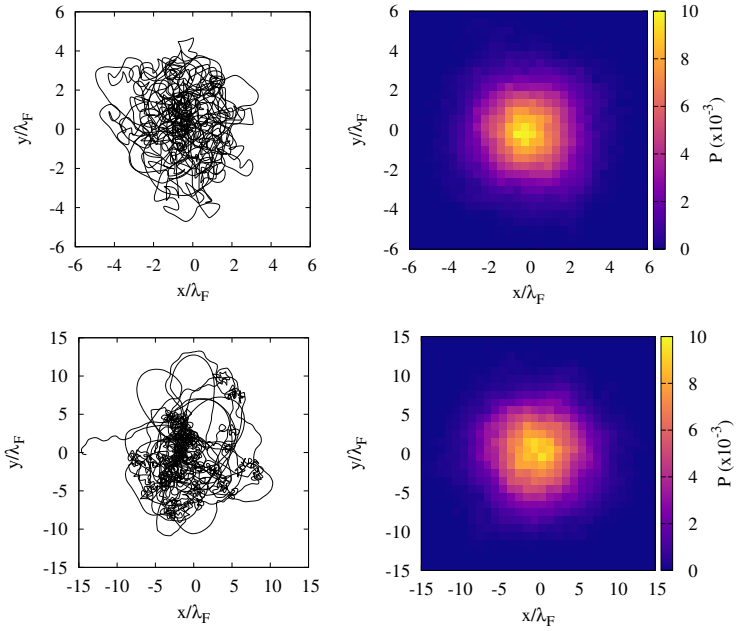


**Figure 4.2:** Trajectories within an harmonic potential for several confinement in the high memory regime with $\mathrm{Me} = 1000$. **(Top)** $f = 250$ mHz, **(Bottom)** $f = 100$ mHz. **(Left)** Trajectories followed by the walker. **(Right)** Probability density function displaying the probability $\mathcal{P}(\vec{r})$ to find the walker at a given position. Note that the scale along each direction is not the same for $f = 250$ mHz and $f = 100$ mHz. As a consequence, the time of simulation for each confinement is different in order to have the comparable statistics.

larger the frequency, the larger the area covered by the walker. The inset of this figure shows the same PDF but as a function of the potential energy of the walker at position $\vec{r}$, namely $U(\vec{r}) = m\omega^2|\vec{r}|^2/2$, in semi-logarithmic scale. One sees that the PDF writes

$$\mathcal{P}(\vec{r}) \sim \exp\left(-\beta U(\vec{r})\right), \tag{4.2}$$

where $\beta$ is related to the standard deviation $\sigma$ of the distribution. Note that an unitary mass has been considered. This last formula indeed gives the Maxwell-Boltzmann distribution when focusing on $\mathcal{P}(|\vec{r}|)$. One has

$$\mathcal{P}(|\vec{r}|) \sim \omega^2|\vec{r}| \exp\left(-\frac{\beta\omega^2|\vec{r}|^2}{2}\right). \tag{4.3}$$

Even though only one memory parameter is displayed here, coefficient $\beta$ depends

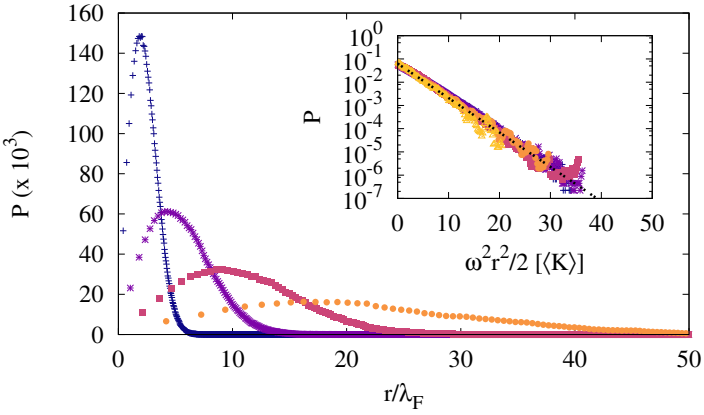


**Figure 4.3:** Walker dynamics statistical description: probability distribution function in the physical space. The probability $\mathcal{P}(|\vec{r}|)$ is given for several frequencies for the memory parameter $\mathrm{Me} = 2500$. From left to right $f = 250$ mHz, $f = 100$ mHz, $f = 50$ mHz and $f = 25$ mHz. **(Inset)**: Probability distribution function as a function of $\omega^2|\vec{r}|^2/2$ in logarithmic scale along the $y$-axis for several frequencies ranging from $f = 250$ mHz to $f = 10$ mHz. The dashed black line accounts for the scaling $\mathcal{P}(\vec{r}) \sim \exp(-U(\vec{r}))$ where $U(\vec{r})$ is defined by Eq.(4.1).

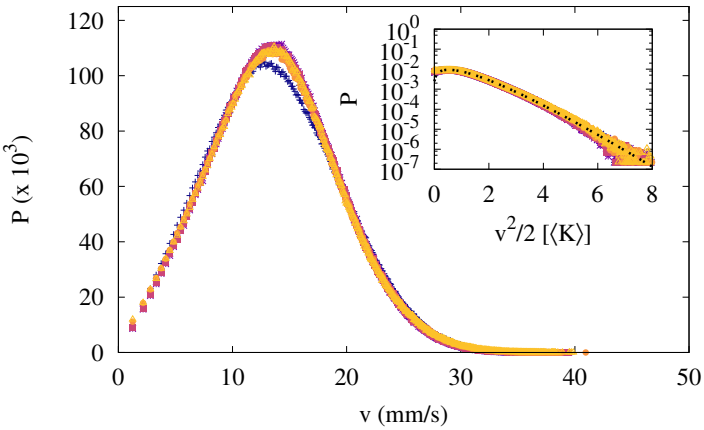


**Figure 4.4:** Walker dynamics statistical description: probability distribution function in the velocity space. The probability $\mathcal{P}(|\vec{v}|)$ is given for several frequencies for the memory parameter $\mathrm{Me} = 2500$. Frequencies investigated ranges in the interval $f \in [10, 250]$ mHz. The probability distribution function is shown to be mostly independent from the frequency of the harmonic potential. **(Inset)**: Probability distribution function as a function of $|\vec{v}|^2/2$. All data have the same statistics but this one is not given by a Gaussian distribution. The dashed black line accounts for the scaling $\mathcal{P}(\vec{v}) \sim \exp(\gamma|\vec{v}|^2 - \delta|\vec{v}|)$.

slightly on $\mathrm{Me}$ which indicates that the memory plays the role of temperature. Let us now focus on the PDF associated with the speed of the walker $\mathcal{P}(\vec{v})$. Once again Maxwell-Boltzmann-like distribution are observed. Contrarily to the previous investigation, the frequency has merely no effect on $\mathcal{P}(\vec{v})$. In the inset of Fig.4.4, the same probability is plotted as a function of the kinetic energy $K = m|\vec{v}|^2/2$ in semi-logarithmic scale. This time, one observes that the PDF differs from a simple exponential law, since a maximum is observed away from $K = 0$. The maximum in the PDF describing the kinetic energy find its source in the propulsion mechanism of the walker. Indeed, the particle harness energy from the oscillation of the surface through the Faraday waves emitted by the drop. Thanks to this mechanism the walker is an active particle, moving without external forces. In the low memory regime, the propulsion can be modelled with a non-linear Rayleigh friction. As described in [152], propulsive mechanisms give a global maximum in $\mathcal{P}(\vec{v})$ which differs from zero.

### 4.1.2 Stiff harmonic potentials

In the previous section, the natural frequencies investigated were rather low compared to experimental values in previous studies ($f \approx 1\,\mathrm{Hz}$ in the stiffest potential investigated in [139], assuming a speed of $10\ \mathrm{mm/s}$). Let us take a look at the dynamics in stiff harmonic potentials in the high memory regime. Figure 4.5 gives the trajectory (a,b), the PDF of the position (c) and the PDF of the velocity (d) for a walker in an harmonic potential with a natural frequency $f = 1\ \mathrm{Hz}$ for $\mathrm{Me} = 1000$. Even though the dynamics could look similar to the low frequency regime, Figs.4.5(c) and (d) show some deviations to the results shown in Figs.4.3 and 4.4. Indeed, in the inset of each figure, the PDFs $\mathcal{P}(\vec{r})$ and $\mathcal{P}(\vec{v})$ for the low frequency regime are indicated with a dashed line. The results for the high frequency regime are given with black dots. One observes that for $\mathcal{P}(\vec{r})$, compared to the low frequency case, the PDF in the high frequency case decreases with a lower slope for small distances and drops with a higher slope for large distances. Regarding the $\mathcal{P}(\vec{v})$, small deviations are seen between each curve especially for high kinetic energy. The high frequency case is seen to display more often large values of $|\vec{v}|$ than the low frequency case.

In this chapter, we will only focus on the low frequency case where such deviations are not seen in the PDFs. We will therefore restrict ourselves to frequency

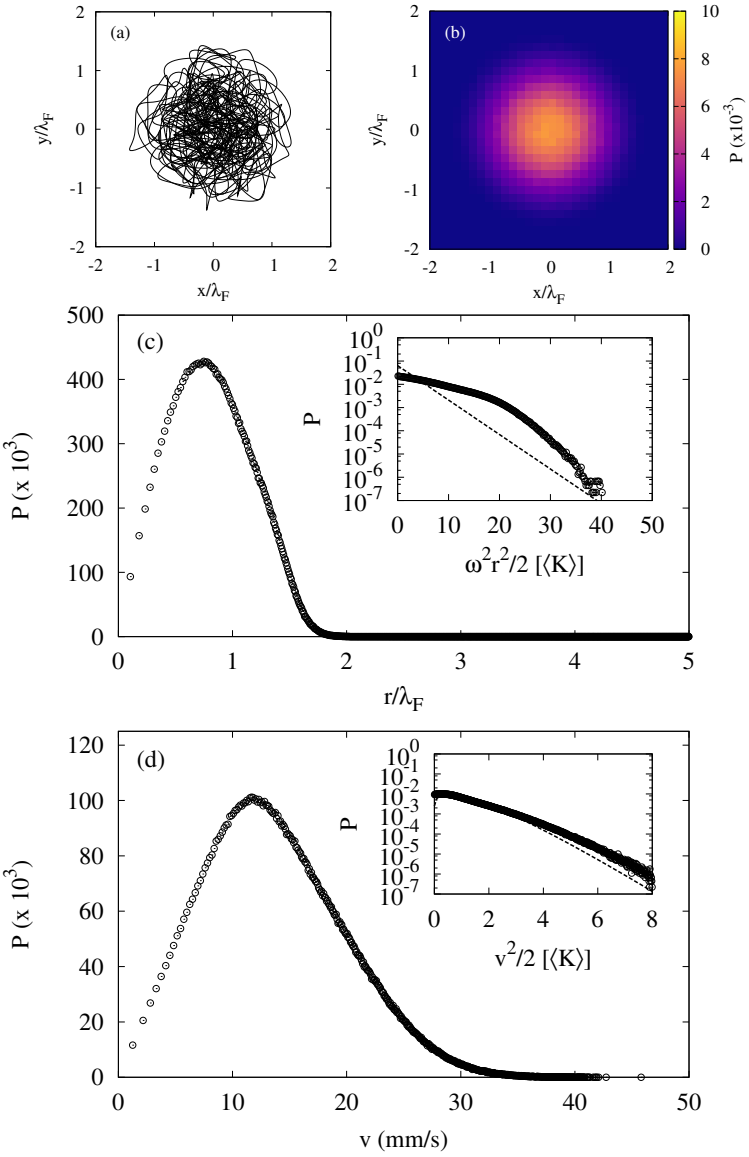


**Figure 4.5:** Statisical description of a walker in a stiff harmonic potential with $f = 1$ Hz. The memory parameter is set to $\mathrm{Me} = 1000$. **(a)** Walker trajectory within the potential during 5000 bounces. **(b)** Heat map giving of the walker position in the potential. **(c)** PDF for the position to the center $|\vec{r}|$. **(Inset)**: PDF as a function of the potential energy $U(\vec{r})$. **(d)** PDF for the speed $|\vec{v}|$. **(Inset)**: PDF as a function of the kinetic energy $K$. The dotted lines correspond to the result in Fig.4.4

lower than $f \leq 0.25$ Hz. Note that stiffer harmonic potentials ($f > 5$ Hz) lead to unstable numerical simulations. Furthermore, because of numerical limitations, frequencies lower than $f = 10$ mHz have not been studied extensively. Nevertheless similar dynamics are still observed in this limit.

In the following section, we discuss further the analogy between the memory parameter and a measure of the temperature of the surface. We will also discuss the shape of the PDF related to the speed of the walker through a mean field approach.

### 4.1.3 Model "à la Langevin"

In order to understand the statistical observations made in the previous section, we focus on the force the wavefield exerts on the particle $\vec{F}_w = -\vec{\nabla}\zeta$. Especially we consider the statistical properties of the components of this force, namely $F_{w,x} = \vec{F}_w.\vec{e}_x$ and $F_{w,y} = \vec{F}_w.\vec{e}_y$ in a cartesian coordinate system $(\vec{e}_x, \vec{e}_y)$ fixed in the laboratory. Since the dynamics in the harmonic potential does not show preferential direction as the walker moves along the interface, the same properties are expected for each component. We therefore focus only on $F_{w,x}$. We study the wavefield force from three different points of view: (i) with time series, (ii) with probability distribution functions, and (iii) with the absolute correlation function.

Time series relative to $F_{w,x}$ are shown in Fig.4.6 for an harmonic potential at frequency $f = 100$ mHz and memory parameters $\mathrm{Me} = 25$, $\mathrm{Me} = 250$ and $\mathrm{Me} = 2500$. In the case of the lowest memory parameter, the time series shows an oscillating value of the force $F_{w,x}$, with a period of a few hundreds of Faraday periods. The intermediate memory regime leads to a situation where global oscillations are still observed but superposed with erratic fluctuations. Finally, at high memory parameters, an overall noisy time series is observed. The previously observed oscillations have disappeared in this limit. The oscillating time series observed for low memory can be easily understood when looking at the trajectory of the walker. As it has been shown in Fig.4.1(a), in harmonic potentials and low memory, the trajectory of the walker is a circle. In the case of $f = 100$ mHz, the radius of the trajectory is approximately of $5\lambda_F$. For a speed of approximately $10$ mm/s, it gives a period of revolution of $15$ s or $600$ bounces, which corresponds to the observations in Fig.4.6(a). The force exerted by the wavefield along the

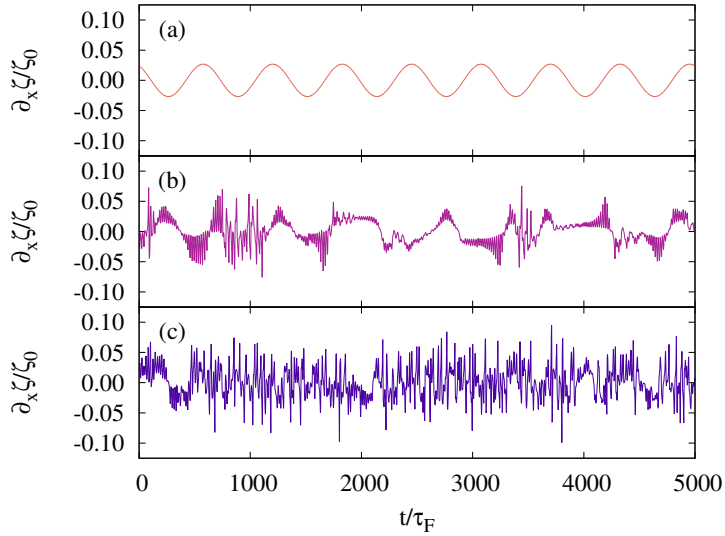


**Figure 4.6:** Time series of the force $F_{w,x} = -\partial_x \zeta(\vec{r})$ exerted by the wavefield on the walker for different memory parameters and at the frequency $f = 100$ mHz. **(a)** $\mathrm{Me} = 25$, **(b)** $\mathrm{Me} = 250$, **(c)** $\mathrm{Me} = 2500$. As the memory parameter is increased, coherence disappears in the time series, which become more and more chaotic.

$x$-direction therefore oscillates with a period equal to the period of revolution around the centre. For the intermediate memory parameters, bursts intersperse with slow oscillations, reminding of the chaotic behaviour observed in the previous chapter. Indeed, the global orbital motion is conserved as evidence by the slow oscillations of the force. But short-term erratic fluctuations are observed because of "traps" created in the wavefield as seen in Fig.4.1(c). The behaviour at high memory shows only chaotic fluctuations. Indeed, no correlation can be seen in this random-like time series, mimicking some noise in the dynamics. In order to characterise this noise, we focus firstly on the PDF of $F_{w,x}$.

Figure 4.7 shows the PDF of $F_{w,x}$ for the same memory parameters investigated in Fig.4.6 and the same frequency $f = 100$ mHz. The case of low memory gives an arcsine distribution. This one can easily be understood since the values of $F_{w,x}$ arise from a sine-like function. This distribution is bounded by the two values defining the maximum and minimum of the time series. For high memory parameters, the distribution is a Gaussian, centred around zero. The case of intermediate memory shows features of both limits. Three local maxima appear.

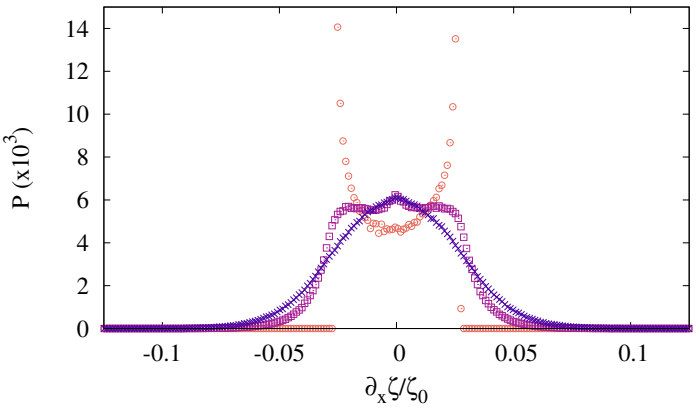


**Figure 4.7:** Probability Distribution Function (PDF) of $F_{w,x} = -\partial_x \zeta(\vec{r})$, for the memory parameters investigated in Fig.4.6 and a frequency $f = 100$ mHz. (Orange circles) $\mathrm{Me} = 25$, (purple squares) $\mathrm{Me} = 250$, (blue crosses) $\mathrm{Me} = 2500$. The PDF is shown to evolve from an arcsine distribution at low memory parameter to a gaussian distribution at high memory parameter. In between, the PDF shows feature of both distribution.

One at the center, which corresponds to the maximum of the high memory case and two on the sides which correspond to the two maxima of the arcsine distribution. Furthermore, the sharp cut-off of the arcsine distribution is smoothed, giving a Gaussian-like tail to the distribution.

In order to end the statistical description of the time series depicted in Fig.4.6, we focus on the absolute autocorrelation function of those signals. The absolute autocorrelation function is given by the following formula

$$C_x(t) = \frac{1}{N} \sum_{p=1}^{N} x\left((p+t)\tau_F\right) x\left(p\tau_F\right), \tag{4.4}$$

which is the discrete convolution of the time series with itself. Note that the absolute autocorrelation gives a function which is centred around the mean value of $F_{w,x}$ and is not normalized to one. The corresponding results are shown in Fig.4.8(a,b,c). The same memory parameters as well as the same frequency as Fig.4.6 are considered. The case of low memory shows an oscillating autocorrelation with the same period as the corresponding time series. This result can be understood by computing the convolution of a cosine function with itself, which

gives back another cosine function with the exact same frequency. For intermediate and high memory parameters, temporal decorrelation is observed. This decorrelation appears faster with high memory parameters. The case of intermediate values of $\mathrm{Me}$ shows exponentially decreasing and oscillating autocorrelation while for high values of $\mathrm{Me}$ one has a peak whose extension does not go beyond a hundred Faraday periods. For even high memory parameters, this peak width decreases up to about ten periods. This loss of temporal correlation is concomitant with the appearance of noisy fluctuations in the time series. In this last case, if one rescales the time $t$ by the memory time $\tau_M$, this peak finally reduces to a Dirac delta.

All those observations allow us to conclude that the inclusion of memory in the dynamics can be reduced to an uncorrelated, Gaussian distributed signal, i.e. a white noise. This type of noise is the very basics of the description of Markovian processes, which appear in statistical physics in the mathematical discussion of random walks and diffusion [136], in finance when describing a market dynamics [134] or in population biology [137] and foraging strategies [28, 182]. Nevertheless, Markovian processes are considered memoryless since the event at time $t+1$ is completely uncorrelated to the event at time $t$. This consideration is appealing for two major reasons. Firstly, the walker dynamics is driven by memory. The walker can walk on the interface solely because of its previous impacts. Removing the memory from the dynamics only gives a vertically bouncing droplet. The dynamics is therefore non-Markovian. Secondly, the decorrelation observed appears when the memory is increased. This means that adding more souvenirs of the trajectory in the dynamics mimics a white noise and gives a chaotic evolution. The temporal decorrelation appears when it is least expected. It worth reminding that this dynamics is deterministic and this artificial white noise is exactly the same for the same initial conditions.

The following results may lead to a curious conclusion. Indeed, in the cartesian coordinate system, the statistics regarding $\vec{F}_w$ mimics the properties of a white noise. Nevertheless, the walker is propelled by its previous impact. Therefore, the correlation in the dynamics must be seen somewhere. In order to evidence the properties of the memory stored in the interface, we focus on the component of the wave force in the Frenet frame associated to the particle. The force decomposes into two components, $F_{w,t}$ and $F_{w,n}$ which are the components

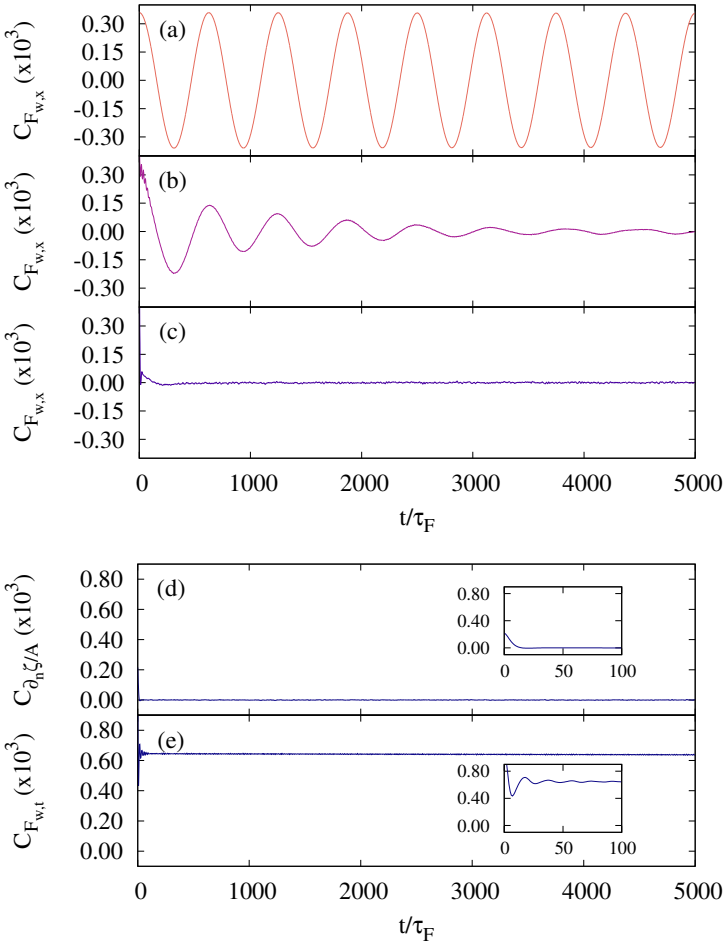


**Figure 4.8:** Absolute autocorrelation function for the force exerted on the walker: **(a,b,c)** $F_{w,x}$ the force along the $x$-direction **(d)** $F_{w,t}$ the force along the tangential direction **(e)** $F_{w,t}$ the force along the normal direction. **(a)** $\mathrm{Me} = 25$, **(b)** $\mathrm{Me} = 250$ and **(c,d,e)** $\mathrm{Me} = 2500$. **(Inset)**: Focus on the early instant of the autocorrelation functions. The $y$-axis in the inset is the same as in the main plot.

tangent and normal to the trajectory respectively. They define as

$$F_{w,t} = \vec{F}_w . \frac{\vec{v}}{|\vec{v}|}, \tag{4.5}$$

$$F_{w,n} = \left| \vec{F}_w - F_{w,t} . \frac{\vec{v}}{|\vec{v}|} \right|. \tag{4.6}$$

Figure 4.8(d,e) shows the correlation function for those two components of the

force. The inset of each plot focuses on the early instants of the correlation function. One sees that the correlation function for the normal component is equal to zero for $t > 10\tau_F$. On the contrary, for the tangential component, a non-zero value is obtained with fluctuations in the early instants. The fluctuation has a period of about ten bounces. This is where the correlation in the walking dynamics is seen, in the tangential direction of the trajectory. It is also interesting to focus on the period of the early oscillations. Assuming a speed of approximately $10$ $\mathrm{mm/s}$, it gives $2.5$ $\mathrm{mm}$ which is half a Faraday wavelength. Those oscillations are thus associated with the wavy nature of the memory and remain of the fluctuating waveforce studied in the previous chapter.

All those observations allow for a mean field approach of the problem. We reduce the effect of the wavefield to a white noise $\vec{\eta}(t)$ and the correlation in the tangential direction to a non-linear damping factor $\phi(|\vec{v}|)$ of propulsive nature. As a consequence, one can write the following Langevin equation for the walker:

$$\dot{\vec{v}} + \phi(|\vec{v}|)\vec{v} + \omega^2\vec{r} = \vec{\eta}(t). \tag{4.7}$$

The white noise $\vec{\eta}(t)$ has the following properties

$$\langle\vec{\eta}(t)\rangle = 0, \tag{4.8}$$

$$C_\eta(t) = 2D\delta(t). \tag{4.9}$$

The PDF $\mathcal{P}(\vec{r},\vec{v})$ associated to this Langevin equation is known to be a solution of the following Fokker-Planck equation [152, 25]

$$\frac{\partial\mathcal{P}}{\partial t} + \vec{v}\,\vec{\nabla}_r\mathcal{P} - \omega^2\vec{r}\,\vec{\nabla}_v\mathcal{P} = \vec{\nabla}_v\left(\phi(\vec{v})\vec{v}\,\mathcal{P} + D\vec{\nabla}_v\mathcal{P}\right), \tag{4.10}$$

where $\vec{\nabla}_r$ and $\vec{\nabla}_v$ correspond to the nabla operator in physical and velocity space respectively. Observations made from Fig.4.3 as well as theory regarding self-propelled systems [152, 170] suggest the following empirical solution

$$\mathcal{P}(\vec{r},\vec{v}) = \mathcal{N}\exp\left(-\frac{\beta\omega^2|\vec{r}|^2}{2}\right)\exp\left(-\frac{\Phi(\vec{v})}{D}\right) \tag{4.11}$$

where $D$ is a diffusion coefficient, $\mathcal{N}$ a normalisation constant and $\beta^{-1}$ the equivalent thermal energy. The function $\Phi(\vec{v})$ corresponds to the potential energy in

the velocity space, related to the non-linear damping $\phi(|\vec{v}|)\vec{v}$. One has

$$\Phi(\dot{\vec{r}}) = \int_0^{\vec{v}} \phi(\vec{u})\vec{u}\, d\vec{u}. \tag{4.12}$$

Note that the solution given in Eq.(4.11) cannot lead to a detailed balance from the Fokker-Planck equation [25]. Indeed in the case of active brownian particles trapped in a harmonic potential, entropy production has to be considered and, as a consequence, fluctuation-dissipation relations have to be modified.

Note that, thanks to Eq.(4.11), Fig.4.4 gives the shape of the potential in velocity space. Indeed, by fitting the PDF on this figure, one can access $\Phi(\vec{v})$. From the literature, two models of self-propulsion has been considered. The first model, which corresponds to the Rayleigh friction [152, 103], gives

$$\phi(\vec{v}) = -\phi_0|\vec{v}|\left(1 - \frac{|\vec{v}|^2}{v_0^2}\right) \quad \rightarrow \quad \Phi(\vec{v}) = \frac{\phi_0|\vec{v}|^2}{2}\left(\frac{|\vec{v}|^2}{2v_0^2} - 1\right). \tag{4.13}$$

The second model, which is a harmonic potential in velocity space around a non-zero value [152], gives

$$\phi(\vec{v}) = \phi_0\left(|\vec{v}| - v_0\right) \quad \rightarrow \quad \Phi(\vec{v}) = \frac{\phi_0}{2}\left(|\vec{v}| - v_0\right)^2. \tag{4.14}$$

Each model has been tested and fitted on numerical data. The one minimizing the $\chi^2$ value is always the latter. This result is illustrated in the inset Fig.4.4 with the black dotted line. One can observe that this model indeed reproduces correctly the PDF. This is surprising since the former model is the one corresponding to the low memory regime analysis performed by Labousse and Perrard [103].

Given the result of Eq.(4.10), let us analyse deeper the PDF given in Fig.4.3 by considering the inverse value of the coefficient $\beta$. By analogy with statistical physics, this coefficient would play the same role as the thermal energy $K_BT$ and would henceforth be referred to as the *effective temperature*. Figure 4.9 gives the effective temperature $\beta^{-1}$ as a function of the memory parameter in double logarithmic scale in order to evidence power laws. The analysis has been performed over two orders of magnitude of memory parameters. Different frequencies have been considered, from $f = 10$ mHz up to $f = 250$ mHz. One sees that all

frequencies collapse on the same line, with the exception of the case $f = 250$ $\mathrm{mHz}$ which is slightly above the others and increases more significantly at high memories. The power law has an exponent $b = 0.096 \pm 0.021$, where the uncertainty corresponds to a $95\%$ confidence interval given by the fitting algorithm. The power law has been fitted considering all five frequencies. It is worth noticing that $\beta^{-1}$ also measures the width of the PDF $\mathcal{P}(\vec{r})$. Figure 4.9 shows that the PDF does not widen much as the memory increases. One could have expected a more important exponent $b$ for the power law. For example, one could have thought that the effective temperature could have scaled as $\beta^{-1} \propto \mathrm{Me}$. Indeed, the active property of the walker comes from the wavefield, more specifically from the waveforce $\vec{F}_w$. Assuming that each impact on the surface generates waves that add up together, one has $|\vec{F}_w| \propto \mathrm{Me}$ since the wavelength is fixed. As a consequence, the driving mechanism having an efficiency increasing linearly with the memory parameters, the effective temperature could have behaved in the same way. Given the measures value of the exponent, another ingredient has to be taken into account. This could come from the wavy nature of the reservoir. Indeed, on the interface, standing waves arising from previous impacts could interfere destructively, leading in a relatively small overall amplitude.

In this section, we studied the dynamics of a walker trapped in an harmonic potential from a statistical point of view. We show that, in the limit of small frequencies, i.e. large potentials, the walker dynamics can be described by the tools of non-equilibrium statistical physics. Indeed, the probability distribution function regarding the position $|\vec{r}|$ of the walker can be described by $\mathcal{P}(\vec{r}) \sim \exp(-\beta U(\vec{r}))$. The PDF for the speed $|\dot{\vec{r}}|$ can be described by $\mathcal{P}(\vec{v}) \sim \exp(-\Phi(\vec{v})/D)$. We show that the coefficient $\beta$ increases with the memory and plays the role of an effective temperature. The rather slow increase of the effective temperature with the memory can come from the wavy nature of the noise. Adding wave sources on the surface does not necessary leads to an equal increase of the wave field amplitude because of interference effect. The velocity potential $\Phi(\vec{v})$ has been shown to be correctly approximated by $\phi_0(|\vec{v}| - v_0)^2/2$. It is worth noticing that the time correlation which appears in the dynamics is completely absent from this description. Indeed, when studying the wave force applied to the droplet, one observed that the inclusion of memory break the time correlation in the time series. As a consequence, the wave force acts as a thermal noise in the dynamics. In order to go beyond this mean field approach, we suggest to study the wavefield

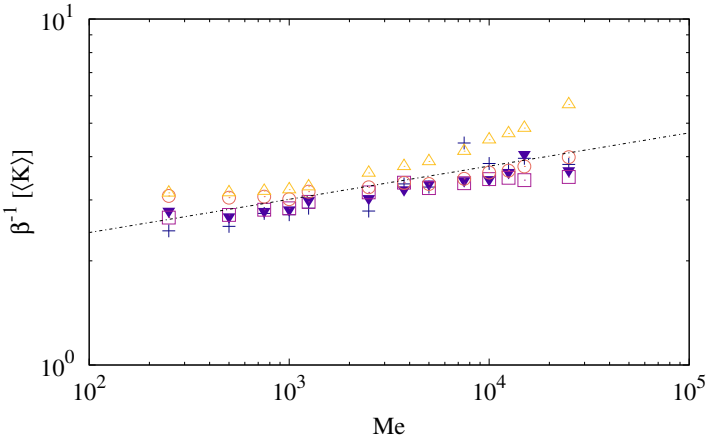


**Figure 4.9:** Evolution of the effective temperature $\beta^{-1}$ as a function of the memory in double logarithmic scale. Coefficient $\beta$ has been obtained fitting the PDF given in Fig.4.3 for memory parameters ranging from $\mathrm{Me} = 250$ to $\mathrm{Me} = 25000$ for different frequencies: Crosses $f = 0.010$ Hz, reverse triangles $f = 0.025$ Hz, squares $f = 0.050$ Hz, circles $f = 0.100$ Hz, triangles $f = 0.250$ Hz. The black dashed line accounts for a fitted power law with exponent $b = 0.096 \pm 0.021$, where the uncertainty corresponds to a $95\%$ confidence interval given by the fitting algorithm.

dynamics and the influence of time correlation.

This mean field approach cannot evidence time correlation within the walker dynamics. Indeed, neither the PDF (regarding the position, velocity or force) nor the correlations functions can distinguish the walker from an active Brownian particle. Nevertheless, some questions are raised, especially regarding the evolution of $\beta^{-1}$ as a function of the memory $\mathrm{Me}$. To investigate further the dynamics, we will know focus on the wave dynamics in order to understand how the propulsive mechanism is affected by the memory.

## 4.2 Wave dynamics statistical description

As it has been seen in the last section, despite increasing significantly the number of images on the surface, and therefore the number of standing waves, the PDF describing both the position and the velocity of the particle does not change as much as one could have expected. In order to understand the results presented in the previous section, we focus on the waves dynamics, especially from a statistical

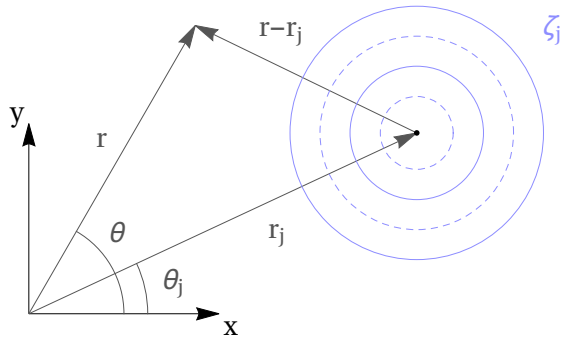


**Figure 4.10:** Graff's addition thereom illustrated. The surface elevation $\zeta_j(\vec{r})$ due to a single impact at $\vec{r}_j$ is expressed around the center of the harmonic potential which defines the origin of ther reference frame.

point of view. Before considering the description, we first introduce the tools required for this investigation.

### 4.2.1 Graff's addition theorem

The wave description can be challenging especially in the high memory regime where the number of impacts considered is tremendous. The cylindrical symmetry of the harmonic potential gives us the possibility to reduce this difficulty, by using Graff's addition theorem. This theorem allows to express Bessel functions $J_n$ from one reference point to another reference point. In our case, waves would be no longer expressed around the impact point but around the center of the harmonic potential. Since we are only interested in the Bessel function of zeroth order $J_0$, we will not consider the general expression of the theorem but only apply it for this peculiar Bessel function.

Let us consider an impact at coordinate $\vec{r}_j$ and study the resulting surface deformation at coordinate $\vec{r}$, as depicted in Fig.4.10. For the sake of simplicity, the origin of the reference frame is set at the center of the harmonic potential. The vectors $\vec{r}$ and $\vec{r}_j$ define respectively the angles $\theta$ and $\theta_j$ with the $x$-axis. The interface elevation $\zeta_j(\vec{r})$ is given by

$$\zeta_j\left(\vec{r}\right) = \zeta_0 J_0(k_F|\vec{r} - \vec{r}_j|). \tag{4.15}$$

Graff's addition theorem allows to express $\zeta_j(\vec{r})$ in terms of the distances $|\vec{r}|$ and

$|\vec{r}_j|$ to the origin. The surface elevation writes

$$\zeta_j\left(\vec{r}\right) = \zeta_0 \sum_{p=-\infty}^{\infty} J_p(k_F|\vec{r}|)J_p(k_F|\vec{r}_j|)\exp\left(ip\left(\theta-\theta_j\right)\right), \tag{4.16}$$

$i$ being the imaginary unit. The functions $J_p$ are the cylindrical Bessel functions of first kind and p-th order. For a collection of $N$ impacts $\vec{r}_j$, the total wavefield writes

$$\begin{aligned}\zeta\left(\vec{r}\right) &= \zeta_0 \sum_{j=1}^{N}\sum_{p=-\infty}^{\infty} J_p(k_F|\vec{r}|)J_p(k_F|\vec{r}_j|)e^{ip(\theta-\theta_j)} \\ &= \zeta_0 \sum_{p=-\infty}^{\infty} \underbrace{\left(\sum_{j=1}^{N} J_p(k_F|\vec{r}_j|)e^{-ip\theta_j}\right)}_{a_p} J_p(k_F|\vec{r}|)e^{ip\theta}\end{aligned} \tag{4.17}$$

Note that, when considered, memory effects appear in the $a_p$ coefficients. In this case, the amplitude writes

$$a_n = \sum_{j=1}^{N} J_p(k_F|\vec{r}_j|)\exp(-ip\theta_j)\exp\left(-\frac{j}{\mathrm{Me}}\right). \tag{4.18}$$

The functions $J_p(k_F|\vec{r}|)e^{ip\theta}$ correspond to the eigenmodes of the decomposition while the coefficients $a_p$ correspond to their amplitude. Note that both eigenmodes and amplitudes are complex quantities. The real part of the eigenmodes $J_p(k_F|\vec{r}|)e^{ip\theta}$ are illustrated in Fig.4.11 for several values of $p$. The imaginary part is obtained by a counterclockwise-$\pi/2p$ rotation in the $(x, y)$-plane. A given mode shows $p$ nodal lines. Furthermore, as the index $p$ increases, a flat area appears at the center of the mode. This is a direct consequence of the relation between the Bessel functions $J_p$ and their derivatives around zero. The $k$-th derivative $J_p^{(k)}$ can be related to all $J_m$ with $p-k \leq m \leq p+k$ with

$$J_p^{(k)}(0) = \frac{1}{2^k}\sum_{m=0}^{k}(-1)^m\binom{k}{m}J_{p-k+2m}(0) \tag{4.19}$$

Since all $J_m(0) = 0$ for $m > 0$, the derivative $J_p^{(k)}$ vanishes for $k < p$. The

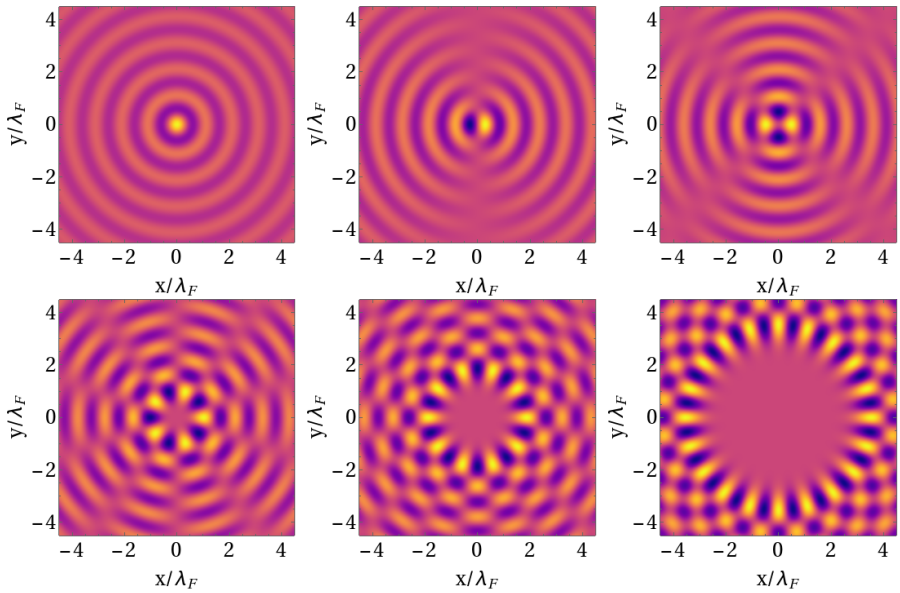


**Figure 4.11:** Eigenmodes used in Graff's addition theorem. From left to right, from top to bottom: $p = 0, 1, 2, 5, 10, 20$. Only the real part has been plotted, imaginary part are obtained by a counterclockwise-$\pi/2p$ rotation in the $(x, y)$-plane. One observes that the eigenmodes possess $p$ nodal lines and have a wavelength equals to the Faraday wavelength. As the index $p$ increases, a flat area is observed around the origin.

first non-vanishing derivative is encountered for $k = p$, since appears $J_0(0) = 1$. This result means that, for increasing value of $p$, even more derivatives at zero vanish. As a consequence, the function $J_p$ flattens more around zero as $p$ increases. In another words, one can show that the radius of the flat area increases linearly with $p$. Therefore, impacts close to the center of the harmonic potential do not trigger high order eigenmodes since $a_p = \sum_{j=1}^{N} J_p(k_F|\vec{r}_j|)e^{-ip\theta_j}$. Because the walker trajectory is confined due to the harmonic potential, another consequence is that not all eigenmodes are triggered along the walker trajectory. Only a limited amount of eigenmodes has to be considered in the description of the global wavefield, significantly decreasing its complexity. Therefore, one can substitute the knowledge of a few tens of eigenmodes to the knowledge of all the previous positions of the walker. Even for an infinitely large amount of wave sources, only a finite number of eigenmodes is required to describe the wavefield.

From the definition of the eigenmode amplitude in Eq.(4.17), one can understand how a given eigenmode becomes relevant in the wavefield description. An impact

in the yellow parts of the figure displayed in Fig.4.11 increases the corresponding eigenmode amplitude. On the contrary, an impact in blue parts of Fig.4.11 decreases the amplitude of the corresponding eigenmode. Finally, an impact in the pink areas does not change the amplitude of the corresponding mode.

### 4.2.2 Energy of the wave field

Graff's addition theorem gives us a handy way to compute the wavefield energy arising from the deformation of the interface. The energy $E$ defines as follows

$$E = \int_0^{\infty} \int_0^{2\pi} \zeta(\vec{r})^2 r dr d\theta. \tag{4.20}$$

Using the addition theorem, it yields

$$\frac{E}{\zeta_0^2} = \int_0^{\infty} \int_0^{2\pi} \sum_{p=-\infty}^{\infty} \sum_{p'=-\infty}^{\infty} a_p a_{p'} J_p(k_F|\vec{r}|) J_{p'}(k_F|\vec{r}|) e^{i(p+p')\theta} r dr d\theta. \tag{4.21}$$

The integration over the azimuthal coordinate greatly simplifies this integrand since

$$\int_0^{2\pi} e^{i(p+p')\theta} = 2\pi\delta(p+p'), \tag{4.22}$$

where $\delta$ is the Kroenecker symbol. The expression of the energy reduces to

$$\frac{E}{\zeta_0^2} = 2\pi \int_0^{\infty} \sum_{p=-\infty}^{\infty} a_p a_{-p} J_p(k_F|\vec{r}|) J_{-p}(k_F|\vec{r}|) r dr. \tag{4.23}$$

Since $J_p(x) = (-1)^p J_{-p}(x)$, one has

$$a_p = (-1)^p a_{-p}^{\dagger}, \tag{4.24}$$

where † denotes the complex conjugate. As a consequence, the wave energy expression reduces to

$$\frac{E}{\zeta_0^2} = 2\pi \sum_{p=-\infty}^{\infty} |a_p|^2 \int_0^{\infty} J_p(k_F|\vec{r}|)^2 r dr. \tag{4.25}$$

The integral in this expression does not converge. Indeed, as solution of the Helmholtz equation, all the $J_p(x)$ scale as $x^{-1/2}$ because of energy conservation. More specifically, for large arguments, the Bessel functions can be approximated by

$$J_p(x) \simeq \sqrt{\frac{2}{x\pi}} \cos\left(x - \frac{p\pi}{2} - \frac{\pi}{4}\right). \tag{4.26}$$

Therefore, the integrand scales as $J_p(k_F|\vec{r}|)^2 r \sim 1$ which leads to a divergent integral. One elegant solution is to integrate up to a given radius $R$ and to normalize the result by the diameter of the corresponding circle of integration. To integrate on all position, the limit $R \to \infty$ is used. This approach gives

$$\lim_{R\to\infty} \frac{1}{2R} \int_0^R J_p(k_F|\vec{r}|)^2 r dr = \frac{1}{2\pi}. \tag{4.27}$$

This relation implies that all eigenmodes have the same energetic cost since the final result does not depend on $p$. Finally, the energy writes

$$\frac{E}{\zeta_0^2} = \sum_{p=-\infty}^{\infty} |a_p|^2. \tag{4.28}$$

A last simplifcation can be made using Eq.(4.17). The sum over $p$ can be reduced to $p \in [0, \infty[$ instead of $p \in ]-\infty, \infty[$ since $a_p$ and $a_{-p}$ share the same modulus. It yields

$$\frac{E}{\zeta_0^2} = |a_0|^2 + 2\sum_{p=1}^{\infty} |a_p|^2. \tag{4.29}$$

We have now an efficient way to measure the wave energy as a superposition of central eigenmodes $J_p(k_F|\vec{r}|)e^{ip\theta}$. All the $a_p$ are stored in a double-infinite vector $\vec{a} = (\dots, a_{-p}, \dots, a_{-1}, a_0, a_1, \dots, a_p, \dots)$ which describes exactly the state of the interface at each instant. The modulus of this vector gives the energy stored in the interface. In particular, the value of $|a_p|^2$ gives the energy stored in the eigenmode of index $p$.

It is worth noticing that this approach does not consider the spatial damping $\exp(-|\vec{r} - \vec{r}_j|/\delta)$ included in the wavefield description in Eq.(2.8). Nevertheless, two reasons have led us to consider Graff's theorem in this study. First, without Graff's theorem, the wave energy computation is extremely costly from a numer-

ical point of view. Indeed, one needs to integrate $\zeta^2(\vec{r})$ over a vast area (typically, seven times the area covered by the walker [14]). Because a statistical description is needed, this integration needs to be repeated several millions times for each set of parameters. The numerical resources available for this study were not sufficient for such a massive computation. Secondly, again because of numerical resources, the wavefield dynamics has been described for two confinement only: $f = 100$ $\mathrm{mHz}$ and $f = 250$ $\mathrm{mHz}$. In such case, considering the value $\delta = 2.5\lambda_F$ (see parameters in Appendix A), the walker is confined in a region of space where the wave sources still affect its trajectory (see Fig.4.2) and therefore $\delta$ is not expected to affect much the results obtained.

### 4.2.3 Statistical description

We first illustrate the instantaneous wavefield underneath the walker in Fig.4.12 for $\mathrm{Me} = 1000$ and $f = 100$ $\mathrm{mHz}$. Since the wavefield is made with the superposition of numerous wave sources located along the trajectory of the walker, the previous positions are indicated with black vanishing points. The more opaque points correspond to the more intense wave sources. Given Graff's theorem, we can now study the walker wave dynamics.

Let us begin with the time series of the eigenmode amplitude $|a_p|$ and their evolution as the memory parameter increases. Figure 4.13 gives the time series for the modulus of $a_0$, $a_{20}$ and $a_{40}$ for a walker with a memory parameter $\mathrm{Me} = 25$ and $2500$ and immersed in an harmonic potential of natural frequency $f = 100$ $\mathrm{mHz}$. The case of $\mathrm{Me} = 25$ gives constant values of the amplitudes which decreases with $p$. On the contrary, the case of $\mathrm{Me} = 2500$ gives erratic signals. Yet, in the latter case, amplitude of fluctuations and average value decrease with $p$. Both behaviours can be understood when considering the trajectory of the walker in each case. For $\mathrm{Me} = 25$, the walker moves along a circular trajectory with a fixed radius. As a consequence, given the definition of the $a_p$, they only have a single constant value. And since the Bessel functions $J_p$ becomes flatter and flatter near zero for increasing values of $p$, the constant value of $a_p$ decreases. For $\mathrm{Me} = 2500$, the chaotic aspect of the trajectory reflects in the eigenmode amplitudes.

In order to characterize the chaotic time series in Fig.4.13, we consider their sta-

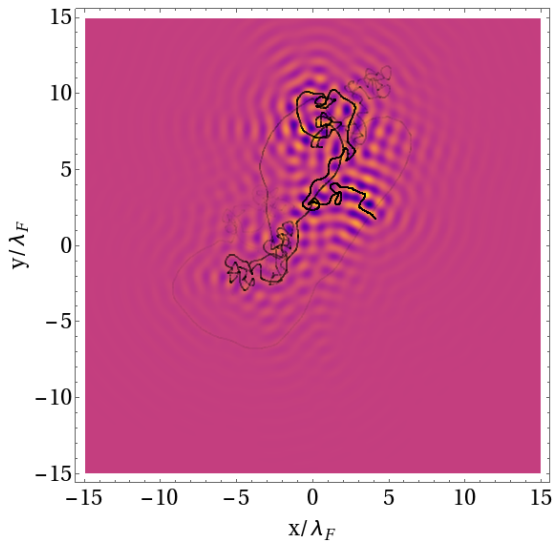


**Figure 4.12:** Instantaneous wavefield underneath the walker for $\mathrm{Me} = 1000$ and $f = 100$ mHz. The vanishing black line corresponds to the past trajectory of the walker. The opacity of the trajectory gives the intensity of the corresponding wave sources, the more opaque being the more intense.

tistical properties. In Fig.4.14, the probability distribution function of $|a_p|^2$ are given in semi logarithmic scales for the memory parameter $\mathrm{Me} = 2500$ and for an harmonic potential with natural frequency $f = 100$ mHz. This figure only displays the PDF for $p = 0, \ldots, 7$. One observes an exponential distribution for each value of $p$. Similar distributions are also seen for higher values of $p$. As a consequence, the eigenmode amplitudes $|a_p|$ should follow a Gaussian distribution. Note that the choice of considering the modulus of $a_n$ is justified by the fact that the real and imaginary parts of the amplitude show the same distribution. One sees that the value of $p$ does not significantly change the distribution, put aside the case $p = 0$. This result can be appealing. Indeed, given the axis-symmetry of the trajectory and given the definition of $a_p$, one might think that $a_p^{\mathrm{rms}} = 0$ for $p > 0$. Nevertheless, because of the factor $\exp(-j/\mathrm{Me})$ in the definition of the amplitude, the spatial symmetry is broken. As a consequence, $a_p^{\mathrm{rms}} \neq 0$. Yet, the PDFs are narrower in the case $p > 0$ than the case $p = 0$.

Let us now characterize the PDFs shown in Fig.4.14. Especially, the $a_p$ following a Gaussian distribution, we only need to focus of the standard deviation of the distribution. An indirect way to obtain this value is to consider the root mean

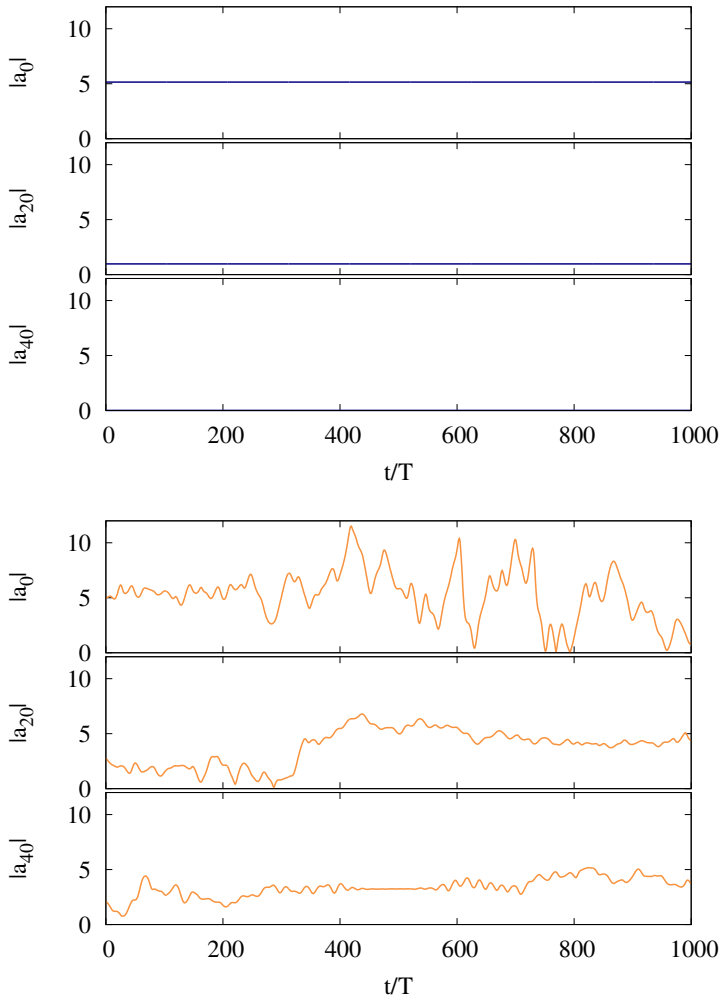


**Figure 4.13:** Modulus of the eigenmode amplitude $a_p$ as a function of time for differens values of $p$ and different values of the memory parameter $\mathrm{Me}$. The harmonic potential has a natural frequency $f = 100$ mHz. **(Blue)** $\mathrm{Me} = 25$, **(Orange)** $\mathrm{Me} = 2500$. From top to bottom: $p = 0$, $p = 20$ and $p = 40$.

squared value of $a_p$ for a given simulation. Given the PDF of $|a_p|^2$ in Fig.4.14, one has

$$\mathcal{P}(a_p) = \frac{1}{2\pi\sigma_p^2} \exp\left(-\frac{|a_p|^2}{2\sigma_p^2}\right), \tag{4.30}$$

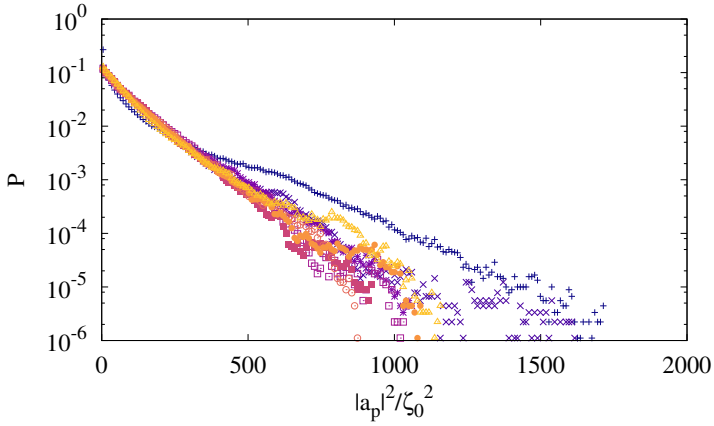


**Figure 4.14:** Probability Distribution Function for $|a_p|^2$ for a memory parameter $\mathrm{Me} = 2500$ and a frequency of harmonic potential $f = 100$ mHz. Logarithmic scale along the $y$-axis has been used. From dark blue to yellow: $p = 0, \ldots, 7$. Exponential distribution can be seen leading to a Gausssian distribution of the amplitudes $|a_p|$.

which gives

$$a_p^{\mathrm{rms}} = \sqrt{\langle |a_p|^2 \rangle}, \tag{4.31}$$

$$= \sqrt{\int_{\mathbb{R}^2} \frac{|a_p|^2}{2\pi\sigma_p^2} \exp\left(-\frac{|a_p|^2}{2\sigma_p^2}\right) da_p}, \tag{4.32}$$

$$= \sqrt{2}\sigma_p. \tag{4.33}$$

The value of $a_p^{\mathrm{rms}}$ is given in Fig.4.15 for memory parameters ranging from $\mathrm{Me} = 200$ to $\mathrm{Me} = 10000$ and for frequencies $f = 100$ mHz and $f = 250$ mHz. A few observations can be made. First, one observes that in the case of each frequency investigated, the root mean squared values of $a_p$ shows a Gaussian-like profile. Especially, from this figure, one can conclude that the eigenmodes $a_p$ of lower index $p$ have the largest PDF, since $a_p^{\mathrm{rms}}$ has the largest value. Second, small frequencies $f$ are shown to activate more eigenmodes than large frequencies $f$ since the Gaussian-like profile seen in Fig.4.15 is wider in the former case than in the latter case. Third, one observes that as the memory parameter $\mathrm{Me}$ increases, more eigenmodes are solicited since the Gaussian profile becomes wider. For example, considering the case $f = 250$ mHz, the Full Width at Half Maximum (FWHM) of the Gaussian-like profile goes from $p = 15$ for $\mathrm{Me} = 200$ up to

$p = 30$ for $\mathrm{Me} = 10000$. Fourth, the $a_p^{\mathrm{rms}}$ are shown to increase only slightly with the memory parameter when $p$ is relatively small. For example, boosting the memory parameter from $\mathrm{Me} = 200$ to $\mathrm{Me} = 10000$ for $f = 100\ \mathrm{mHz}$ does not even double the value of $a_0$. On the contrary, the same boost for $\mathrm{Me}$ increases more than ten times the value of $a_{100}$. A non-linear increase is therefore observed. Fifth, the $a_p^{\mathrm{rms}}$ has the same order of magnitude for each frequency investigated, with $a_0^{\mathrm{rms}} \approx 8$ in each case. Sixth, in the case $f = 100\ \mathrm{mHz}$, the lowest memory parameter gives a different profile. Indeed, since the case $\mathrm{Me} = 200$ does not trig a fully chaotic regime, the associated PDF shows reminiscence of lower memory dynamics. Let us explain and interpret some of those observations. The large Gaussian-like profiles observed for $a_p^{\mathrm{rms}}$ at low frequency $f$ can be explained via the area covered by the walker overall trajectory. As stated in the end of Section 4.2.1, eigenmodes of high order $p$ are only triggered for large values of $k_F|\vec{r}|$, and therefore vast trajectories, given the mathematical properties of the Bessel function $J_p$. Since the area covered by the walker is larger in low frequency harmonic potentials, more eigenmodes are required in the wavefield description. Interestingly, the case $f = 250\ \mathrm{mHz}$ requires approximatively 40 modes against 100 for $f = 100\ \mathrm{mHz}$. The ratio of modes required changes as the ratio of frequency involved. Regarding the eigenmodes triggered as the memory increases, the vast area covered by the walker cannot explain such an increase. Indeed, Fig.4.9 which gives the effective temperature of the bath, also gives the standard deviation of $\mathcal{P}(\vec{r})$. One sees in Fig.4.9 that the standard deviation does not even double from $\mathrm{Me} = 200$ to $\mathrm{Me} = 10000$, while the FWHM for $f = 250\ \mathrm{mHz}$ in Fig.4.15 doubles for the same variation. Finally, one might think that the amplitude of the eigenmodes would increase linearly with the amount of standing wave sources on the interface. But, as stated before, the increase is not so significant. The $a_p$ statistical description therefore raises some questions that are difficult to answer with the results actually available. Before giving us new insight in the following section, we discuss the energy stored in the wavefield.

Having described the statistical properties of the eigenmodes and their associated amplitude, let us now consider the energy of the wavefield. The time series for the $a_p$ being chaotic and given the relation defining the energy $E$ in Eq.(4.29), the wavefield energy time series is also chaotic. As a consequence, we will study its statistical properties. Figure 4.16 gives the PDF of the wavefield energy as a function of the memory parameter $\mathrm{Me}$ for a walker immersed in an harmonic potential of stiffness $f = 100\ \mathrm{mHz}$. The PDF are given in semi logarithmic scale

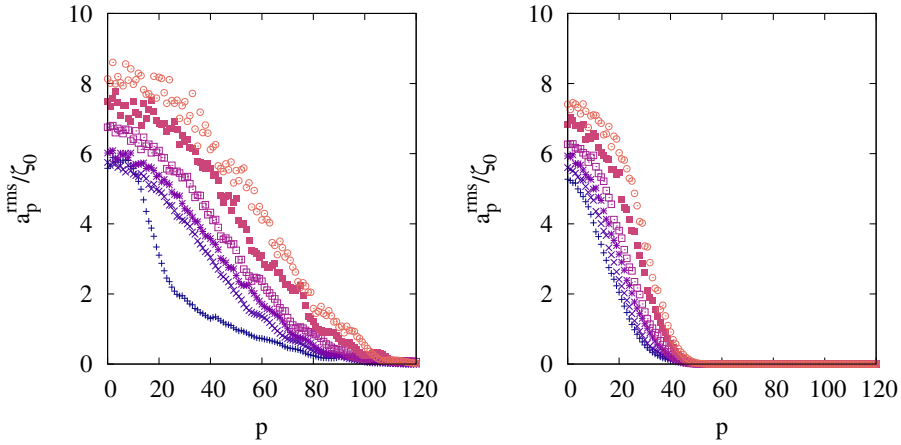


**Figure 4.15:** Average value of the modulus of the eigenmode amplitude as a function of $p$, for several values of the memory parameter and frequency of the harmonic potential. **(Left)** $f = 100$ mHz, **(Right)** $f = 250$ mHz. From blue to orange, $\mathrm{Me} = 200, 500, 1000, 2000, 5000, 10000$. Statistics are obtained over $2.25\,10^6$ bounces.

along the $y$-axis. This figure shows that, as the memory parameter increases, the distribution shifts towards high energy while becoming wider. This figure also shows that the PDF can be approximated by a Gamma distribution. In the case of higher frequency $f$ (not shown here), the energy distribution is only narrower and shows a smaller mean value. This can be understood by considering Fig.4.15. Smaller frequencies require less eigenmodes in the description of the wavefield compared to larger harmonic potentials. As a consequence, less terms are considered in Eq.(4.29). Since, the $a_p^{\mathrm{rms}}$ has the same order of magnitude for small index $p$ for each frequency, this rationalizes the observation.

Finally, we study the influence of the memory parameter on the average energy of the wavefield. This last analysis is given in Fig.4.17, in double logarithmic scale for the two frequencies investigated in this section. Power laws are observed. The exponent for those power laws are $b = 0.380 \pm 0.021$ for $f = 100$ mHz and $b = 0.335 \pm 0.021$ for $f = 250$ mHz. The errors are given by the fitting algorithm and correspond to an interval of confidence of 95% on the resulting value.

The results of this section, regarding the $a_p$ and $E$ statistical description, raise some questions that the mean field analysis in Section 4.1 cannot answer. Indeed, the rms value of $a_p$ are seen to change with the memory in a way that the

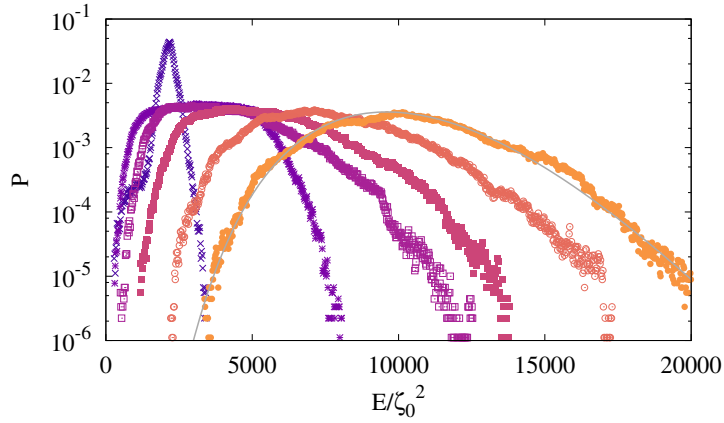


**Figure 4.16:** Probability Distribution Function for the energy stored in the wavefield for a walker in a harmonic potential of stifness $f = 100$ mHz. Logarithmic scale is used along the y axis. From blue to orange: $\mathrm{Me} = 200, 500, 1000, 2000, 5000, 10000$. The solid gray line corresponds to a fit using a Gamma distribution. Statistics are obtained over $2.25\,10^6$ bounces.

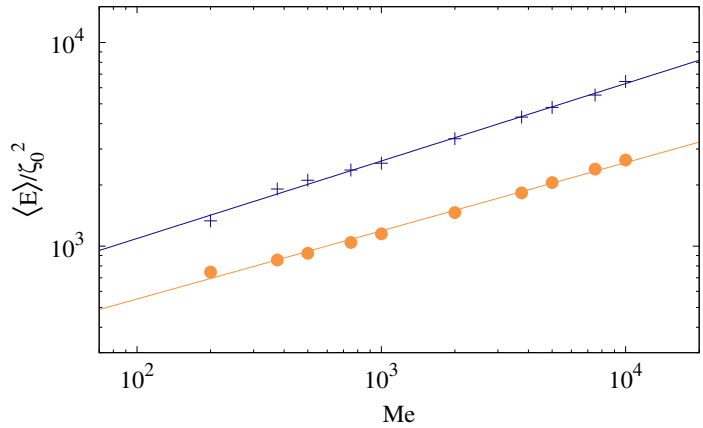


**Figure 4.17:** Average energy stored in the wavefield as a function of the memory, in double logarithmic scale, for $f = 250$ mHz (orange points) and $f = 100$ mHz (blue crosses). Exponents for the power laws are $b = 0.38$ ($f = 100$ mHz) and $b = 0.33$ ($f = 250$ mHz). Statistics are obtained over $2.25\,10^6$ bounces.

statistical description for the walker cannot justify. As a consequence, the increase of energy stored in the wavefield with the memory cannot be explained. But an ingredient has been forgotten in our argumentation: the correlation along the walker trajectory. Therefore, in the following section, we will build a model

without time correlation in order to evidence the missing mechanism and find some explanation for the $a_p$ and $E$ statistical dynamics.

### 4.2.4 Wave dynamics without temporal correlation

In order to have some intuition of the dynamics of the wavefield generated by a walker, let us create the model of a randomly generated wavefield. It will give us a point of comparison with the previous analysis. Indeed, such a randomly generated wavefield breaks all the possible spatial correlation between successive wave sources. Here is how the model is built. Statistically, we know the distribution of impacts of a walker on the surface from Fig.4.3. As a consequence, one also knows the distribution of waves sources on the interface. From the knowledge of the statistics, we suggest to create a wavefield made of ramdomly chosen sources on the interface. Mathematically, it builds as follows. Given the distribution $\mathcal{P}(\vec{r})$ describing the walking droplet positional statistic, a collection $\{\vec{s}\}$ of $N$ random positions is considered with the $j^{\text{th}}$ item of the collection given by

$$\vec{s}^{(j)} \sim \exp\left(-\beta U(\vec{s})\right), \tag{4.34}$$

$U$ being given by Eq.(4.1) and $\beta$ by Fig.4.9. The last item in the collection is assumed to be the oldest regarding to the temporal damping of the waves. The wavefield is therefore given by

$$\zeta\left(\vec{r},t\right) = \zeta_0 \sum_{p=-\infty}^{\infty} b_p(t) J_p(k_F|\vec{r}|)\exp(ip\theta), \tag{4.35}$$

with

$$b_p(t) = \sum_{j=1}^{N} J_p(k_F|\vec{s}_j|)\exp(-ip\theta_j)\exp\left(-\frac{j}{\mathrm{Me}}\right), \tag{4.36}$$

where the symbol $b_p$ is the uncorrelated wave amplitude, as opposed to the correlated case $a_p$. For the following analysis, two cases have been considered. We have taken the distribution of impacts for $f = 100$ mHz and $f = 250$ mHz for a memory parameter $\mathrm{Me} = 1000$ as calibrations for this study. Those two cases allow to investigate the effects of the stiffness of the harmonic potential on the random wavefield dynamics. Note that, because of the small effects of the memory on the width of the impacts distribution (see Fig.4.9), considering only the case $\mathrm{Me} = 1000$ does not significantly change the results presented here

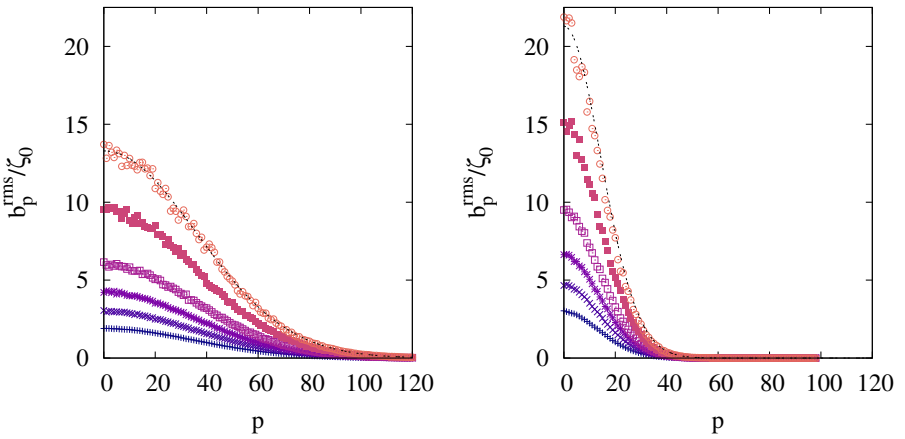


**Figure 4.18:** Average value of the modulus of the eigenmode amplitude for a randomly created wavefield as a function of $p$, for several values of the memory parameter and different calibrations. Impacts distribution calibrated with the walker dynamics for **(Left)** $f = 100$ mHz, **(Right)** $f = 250$ mHz. From blue to orange, $\mathrm{Me} = 200, 500, 1000, 2000, 5000, 10000$. Statistics are obtained over $2.25\,10^6$ bounces. As the memory parameter is increased, only the average values increases.

below.

Since the wave sources are picked up randomly, the time series associated to the $b_p$ are stochastic and need to be described statistically. Their distribution is Gaussian, likewise the walker dynamics presented in Fig.4.14 and therefore they do not need further illustration. We analyse the width of those Gaussian distributions by considering the root mean squared value of the amplitude $b_p$, namely $b_p^{\mathrm{rms}}$. The corresponding results are given in Fig.4.18 for memory parameters ranging from $\mathrm{Me} = 200$ to $\mathrm{Me} = 10000$ and for the two calibrations presented above. This figure corresponds to Fig.4.15, but in the case of a random wavefield. Several observations can be made. Some of them differ from the dynamic of the wavefield created by a walker. The curve describing the evolution of $b_p^{\mathrm{rms}}$ is similar to the case of the walker, for the two calibrations. Yet, in the case of the random wavefield, the curve does not get larger as the memory increases. Only the overall amplitude increases, identically for all index $p$. In the case of a random wavefield, the value of $b_p^{\mathrm{rms}}$ can be computed exactly, since two impacts on the surface are

independent. Knowing the distribution $\vec{s}^{(i)} \sim \exp(-\beta U(\vec{s}))$, one has

$$\begin{aligned}\langle |b_p|^2 \rangle &= c \int_0^\infty |\vec{r}| J_p\left(k_F |\vec{r}|\right)^2 \exp\left(-\frac{|\vec{r}|^2}{2\sigma^2}\right) d|\vec{r}|. \\ &= c\,\sigma^2 \exp\left(-k_F^2\sigma^2\right) I_p\left(k_F^2\sigma^2\right), \end{aligned} \tag{4.37}$$

where $\sigma$ is the standard deviation of the PDF $\mathcal{P}(\vec{s})$ and $I_p$ is the modified Bessel function of second kind and $p$-th order. There is only one unknown parameter, the proportionality coefficient $c$. This expression can be fitted on the numerical results in Fig.4.18. The fit is given with the black curve in the case of the largest memory parameters displayed. As one can see, Eq.(4.37) fits correctly the data. The same observation can be made for all memory parameters and frequencies investigated. Equation (4.37) also justifies that the width of the curve in Fig.4.18 does not change with the memory parameter. Indeed, once $\sigma$ is known, the width cannot change.

The lower frequencies required more eigenmodes for the description of the wavefield, similarly to the wavefield generated by a walker. Nevertheless, as seen when looking at the $y$-axis of each plot in Fig.4.18, the value of $b_p^{\mathrm{rms}}$ are different for the two dynamics. For $f = 100$ mHz, $b_0^{\mathrm{rms}} \approx 14$ while for $f = 250$ mHz, $b_0^{\mathrm{rms}} \approx 24$. This result also contrasts with the walker dynamics, where results were almost identical. Furthermore, the effect of the memory is also different in the walker and in the random case. In Fig.4.18, the Gaussian profile one observes only increases in amplitude while in Fig.4.15 the Gaussian profile gets wider as the memory parameter is increased. Finally, the increase of amplitude arising in the random wavefield dynamics is much more important than the one observed in the case of a walker.

The energy $E$ of the wavefield can also be studied and requires a statistical description as well. The probability distribution function of the energy is given in Fig.4.19 for the calibration at $f = 100$ mHz and for several memory parameters ranging from $\mathrm{Me} = 200$ to $\mathrm{Me} = 10000$. The PDF for a random wavefield appears to be similar to the one obtained for the walkers. Indeed, as seen in the figure, the gamma distribution also fits the PDFs correctly. Nevertheless, for a random wavefield, the PDFs are narrower and the average value of the wavefield energy increases much more with the memory. This last assertion can be proved

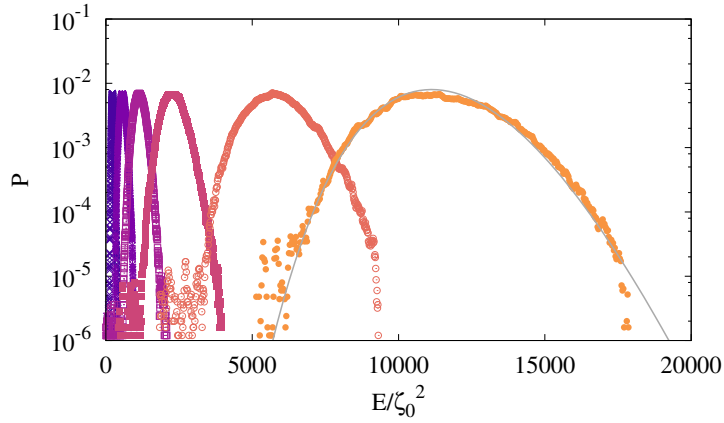


**Figure 4.19:** Probability distribution function for the energy stored in the randomly created wavefield for an impact distribution calibrated with $f = 100$ Hz. Logarithmic scale is used along the y axis. From blue to orange: $\mathrm{Me} = 200, 500, 1000, 2000, 5000, 10000$. The solid gray line corresponds to a fit using a Gamma distribution. Statistics are obtained over $2.25\,10^6$ bounces.

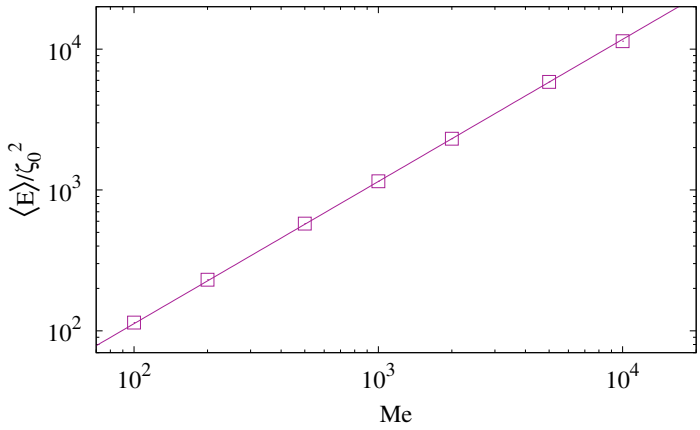


**Figure 4.20:** Average energy stored in the randomly created wavefield as a function of the memory, in double logarithmic scale. Each calibration ($f = 0.100$ Hz and $f = 0.250$ Hz) gives the same result. One has a linear increase of the energy with the memory parameter. Statistics are obtained over $2.25\,10^6$ bounces.

by analysing the average value of the wavefield energy as a function of the memory, as given in Fig.4.20. In this case, a linear increase is observed, contrarily to Fig.4.17.

We can explain this behaviour as follows. For the sake of simplicity, let us consider a 1D system where a collection of $N$ sources $\{s^{(j)}\}$ is located randomly and uniformly in the interval $[0, \lambda_F]$. The wavefield writes

$$\zeta(s, \{s^{(j)}\}) = \sum_{j=0}^{N-1} \underbrace{\zeta_0 \cos\left(\frac{2\pi}{\lambda_F}(s - s_j)\right) \exp\left(-\frac{j}{\mathrm{Me}}\right)}_{\zeta_j}. \tag{4.38}$$

The average energy is given by

$$\langle E \rangle = \frac{1}{\lambda_F^N} \int_0^{\lambda_F} \dots \int_0^{\lambda_F} \zeta(s, \{s^{(j)}\})^2 ds^{(1)} \dots ds^{(N)}, \tag{4.39}$$

$$= \frac{1}{\lambda_F^N} \int_0^{\lambda_F} \dots \int_0^{\lambda_F} \sum_{j=0}^{N-1} \sum_{k=0}^{N-1} \zeta_j \zeta_k \, ds^{(1)} \dots ds^{(N)}. \tag{4.40}$$

Since the impacts are uncorrelated, the product $\zeta_j \zeta_k$ gives the Dirac delta $\delta(j-k)$ and it yields

$$\langle E \rangle = \frac{\zeta_0^2}{2} \sum_{j=0}^{N-1} \exp\left(-\frac{2j}{\mathrm{Me}}\right), \tag{4.41}$$

$$= \frac{\zeta_0^2}{2} \frac{1 - \exp\left(-\frac{2N}{\mathrm{Me}}\right)}{1 - \exp\left(-\frac{2}{\mathrm{Me}}\right)}. \tag{4.42}$$

In the last line, the result regarding geometric series was used. Finally, assuming $N \to \infty$ and $\mathrm{Me} \gg 1$, one has

$$\langle E \rangle = \mathrm{Me} \frac{\zeta_0^2}{4} + \mathcal{O}\left(\mathrm{Me}^{-2}\right). \tag{4.43}$$

Therefore, the energy scales linearly with the memory.

With all the results regarding the randomly generated wavefield, let us compare the uncorrelated case with the walker case.

### 4.2.5 Comparison

In the beginning of this chapter dedicated to the statistical description of the particle dynamics, we conclude that a mean field approach cannot distinguish a walker from a thermally activated particle. Indeed, the time correlation which is at the root of the walker dynamics completely disappear. The walker therefore mimics a Brownian active particle, which is assumed to have a markovian dynamics. Nevertheless, this conclusion is no longer valid when considering the wavefield and its statistical properties. The two model considered, i.e. the walker wavefield and the randomly generated wavefield, show distinct behaviours despite being built on the same PDF $\mathcal{P}(\vec{r})$. Let us discuss the effect of the time correlation in the wavefield dynamics.

The first difference appears when considering the rms value of $a_p$ and $b_p$, namely Figs.4.15 and 4.18. Both show a Gaussian-like profile but their evolution with $\mathrm{Me}$ differs. In the walker case, this profile essentially widens with only a slight increase of amplitude. On the contrary, the random case shows only an increase of amplitude without widening the profile. The difference can only come from coherence within the walker dynamics. Looking back at Fig.4.2, one sees that the walker make large loops far from the center of the potential. Such a motion has two consequences. Firstly, because the walker moves away from the center, it excites high index eigemodes with a large number of impacts. Secondly, while moving away from the center, low index eigenmodes are only slightly excited and can relax towards zero. The overall effect is a coherent injection of energy in eigenmodes of large index. As a consequence, distributions $\mathcal{P}(a_p)$ widen for $p \ll 1$ and the corresponding rms values $a_p^{\mathrm{rms}}$ increase. On the contrary, for low index eigenmodes, the injection of energy is limited.

One can also discuss this observation from a dynamical point of view. Let us imagine that, at some point during the walker motion, low index eigenmodes would have an very high amplitude (which would indicate large value of $a_p^{\mathrm{rms}}$). This situation would correspond to a pump at the centre of the confining region. Because the walker is driven by the slope of the wavefield, it would move in opposite direction of the gradient of the wave, namely away from the center. This is how the loops observed in Fig.4.2 arise. Therefore, the energy tends to be injected equally in all eigenmodes in order to limit their amplitude. This tendency to limit the growth of a given mode has already been observed in the intermediate mem-

ory regime when discussing quantified trajectory in harmonic potentials [139, 104].

Beside this limited storage of energy in each eigenmode, interferences arise. Indeed, looking at Figs.4.17 and 4.20, one sees that the energy increase is limited in the walker case compared to the random case. The former gives $\langle E \rangle \propto \mathrm{Me}^{0.38}$ for $f = 100\ \mathrm{mHz}$ while the latter gives $\langle E \rangle \propto \mathrm{Me}$. Destructive interferences appear along the path in order to limit the amplitude of the wavefield. This last property mimics a minimisation principle of the energy stored in the wavefield.

As a consequence, correlations along the path of the walker tend to inject energy equally in all modes, a way to mimic an equipartition theorem for the wavefield, and also tend to organize the wave sources in order to favour destructive interferences in the wave dynamics. Given those two observations, one could develop a more precise model of the confined walker dynamics in the high memory regime.

## 4.3 Conclusion

This chapter has been dedicated to the investigation of the continuous interaction of the walker with its wavefield in an harmonic potential. Both the effect of the memory and the stiffness of the potential were investigated. In such a confinement, the walker is seen to behave like a thermally activated Brownian particle. Indeed, the wavefield it creates mimics a thermal bath. The noise this thermostat generates can be well approximated by a white noise, i.e. Gaussian-distributed and uncorrelated in time. We have shown that the addition of memory in the dynamics increases the effective temperature of this thermostat but also removes the correlation in the dynamics. In order to understand this apparent paradox, the dynamics of the wavefield has been considered. The organisation of the wave sources on the interface tend to spontaneously mimic an equipartition of energy in the different wave mode available. Furthermore, destructive interferences arise along the walker trajectory in order to limit the amplitude of the global wavefield. As a consequence, the limited increase of the effective temperature with the memory parameter comes from this minimisation principle. Indeed, by promoting destructive interference, the increase of amplitude of the wavefield is limited.

This last conclusion can also be applied to the previous chapter, in the case of the run and tumble dynamics. Indeed, we have seen that the walker is trapped in its

wavefield during a tumble phase but eventually escapes. Considering the wave trap dynamics under the perspective of the minimisation principle, one can now understand how the walker escape the trapping area. Indeed, promoting destructive interferences decrease the wavefield and opens a way out for the particle.

Some questions can be asked regarding the statical description of the walker dynamics in confining potential. One of them is the entropy of the system. Indeed, The Fokker-Planck equation for the walker is know to lead to entropy production once the active particle is trapped in an harmonic potential. It would therefore be interesting to study further this particle dynamics and the wave dynamics by taking entropy production into account.

# Part II

# Magnetocapillary microswimmers

# 5
# State of the art

*From the movie "Fantastic Voyage" to Richard Feynman's seminal talk "There's Plenty of Room at the Bottom" where he suggested that in the future one would "swallow the surgeon"* [58] *, people have always fantasised about nanoscale technologies and their applications in medical fields. Today technologies are not far from those wonders: biohybrid microp*ropellers *have been designed in order to circumvent and treat fertility issues with so-called "spermbots"* [116, 115, 191]*, micro/nanomotors are used to track cancer cells and also used for drug delivery* [61, 191]*, magnetic colloids can be used to trigger the apoptosis of cancer cells* [109] *and micromotors have also been used to capture and transport* [92] *of bacterium* [23] *and anthrax spores* [126]*. Before realising such experiments, one needs to understand the motion and dynamics of microscopic and nanoscopic devices. In particular, in this second part of the thesis, we will focus on microswimmer, i.e. meso/microscopic structures and objects which can deform and move into fluids thanks to hydrodynamic interactions* [149, 107]*. Recent experiments have shown that magnetically-powered microswimmers could be created using millimetric magnetic beads on air/water interfaces* [111, 77, 75, 76, 74, 168].

## 5.1 Low Reynolds number swimming strategies

Large mammals like cetaceans and fishes use a different swimming strategy than "small organisms" such as bacteria or sperms to move themselves into a fluid. Indeed, in the former case, the animal relies on inertia to propel itself into the fluid [65]. The beating motion of its fins or flippers pushes the water backwards.

Thanks to Newton's third law, the animal moves in the opposite direction of the propelled fluid. This dynamics also corresponds to the strategies used by humans, such as breaststrokes or crawl, to swim. In the case of bacteria or sperms, the effect of viscous damping relative to inertia does not allow the organism to use similar strategies. Let us consider a numerical example. An Escherichia Coli bacterium of effective radius $a$ moving at speed $v$ within a fluid of viscosity $\eta$ will experience in first approximation a drag force of intensity $\vec{F_d} = -6\pi\eta a\vec{v}$. Considering inertia, Newton equation for this bacterium gives the typical coasting time and distance $\tau = 2a^2\rho/9\eta$ and $\Delta x = v\tau$, $\rho$ being the bacteria density. Considering $a = 1\ \mu\mathrm{m}$, $v = 30\ \mu\mathrm{m/s}$, $\eta = 10^{-3}\ \mathrm{Pa.s}$ and $\rho \sim 10^3\ \mathrm{kg/m^3}$, one has a coasting time $\tau \sim 10^{-7}\ \mathrm{s}$ and distance $\Delta x \sim 10^{-11}\ \mathrm{m}$. As a consequence, the bacteria cannot rely on the inertia of the fluid, alike fishes or aquatic mammals. The effect of viscosity is too important and stops the bacteria almost instantaneously. Instead, their swimming dynamics rely on the concept of non-reciprocal deformation.

### 5.1.1 Stokes equation and the Scallop theorem

The equation describing locally the dynamics of a fluid is given by the Navier-Stokes equation

$$\rho\frac{\partial\vec{u}}{\partial t} + \rho\left(\vec{u}.\vec{\nabla}\right)\vec{u} = -\vec{\nabla}p + \eta\Delta\vec{u} \tag{5.1}$$

where $\rho$ is the fluid density and $\eta$ its dynamic viscosity, $\vec{u}$ is the local flow velocity and $p$ the local pressure. In the special case of swimming, the pressure field $p$ arises from the deformation of the swimmer while $\vec{u}$ is the flow induced by dynamics. Note that no external volume forces are considered for a swimmer since it is expected that a swimmer only rely on its deformation to achieve propulsion. This equation can be greatly simplified when considering small obstacles or objects into a flow of small magnitude. Indeed, assuming that the object has a typical length $L$ and the flow a typical speed $U$ aside assuming a stationary flow, one can write

$$\frac{\rho UL}{\eta}\left(\vec{u}'.\vec{\nabla}'\right)\vec{u}' = -\frac{L}{\eta U}\vec{\nabla}'p + \Delta'\vec{u}' \tag{5.2}$$

where primed variables correspond to dimensionless quantities. The prefactor in the left-hand side of the equation defines the *Reynolds number* $\mathrm{Re}$ as

$$\mathrm{Re} = \frac{\rho \mathrm{UL}}{\eta} \tag{5.3}$$

which measures the relative effect of inertia and viscosity. For example, let us consider the swimming dynamics of a human and a bacteria. For a human, $L \sim 1$ $\mathrm{m}$, $U \sim 10^{-1}$ $\mathrm{m/s}$, $\rho = 10^3$ $\mathrm{kg/m^3}$ and $\eta = 10^{-3}$ $\mathrm{Pa.s}$, the Reynolds number is of the order of $\mathrm{Re} \sim 10^5$. This result indicates that inertia greatly overcomes viscosity in the flow dynamics. This corresponds to the intuition of pushing water backward when swimming breaststrokes. For a bacteria in water, $L \sim 10^{-6}$ $\mathrm{m}$ with $U \sim 10^{-5}$ $\mathrm{m/s}$. As a consequence, the Reynolds number scales as $\mathrm{Re} \sim 10^{-5}$ which leads to a dynamics dominated by viscosity. This result also corroborates the intuition developed earlier in this section: bacteria cannot rely on inertia. As a consequence, Eq.(5.2) reduced to the Stokes equation in the limit $\mathrm{Re} \to 0$, which in dimensioned form writes

$$\eta \Delta \vec{u} = \vec{\nabla} p \tag{5.4}$$

The Stokes equation has two important properties: it is rate-independent and time-reversible. The rate independence arises from the observation that no explicit time dependence can be seen in Eq.(5.4). There is no advantage for the swimmer to deform rapidly ($\partial p/\partial t \gg 1$) compared to slow deformations ($\partial p/\partial t \ll 1$). Indeed, whatever the rate of deformation, the flow $\vec{u}$ would be the same over a deformation sequence and so will be the swimming speed. This observation strongly contrasts with the intuition one has when swimming at high Reynolds number. In this case the strokes rate has an influence on the flow generated. The second property, the time reversibility observed in Eq.(5.4), says that if one reverses the deformation sequence of the swimmer ($p \to -p$) one obtains the opposite flow ($\vec{u} \to -\vec{u}$). This observation leads to the concept of reciprocal and non-reciprocal motion. If a sequence of deformation is identical to itself when read backward (i.e. like a palindrome) then the deformation is said to be reciprocal. Such a sequence cannot lead to a net motion along the fluid because of the time reversibility of the Stokes equation. Indeed, imagine decomposing the deformation sequence in two halves. The first half of the deformation sequence would produce a flow. But because of time reversibility, the second half would

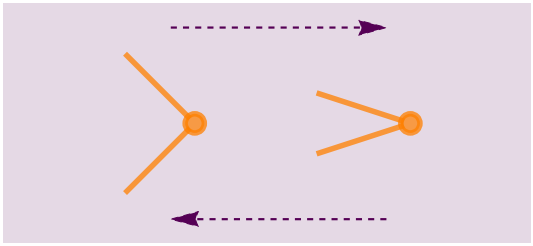

**Figure 5.1:** Illustration of the swimming strategy of a scallop. The scallop swims into water at high Reynolds number by closing and opening its shell at different rates. This strategy is unefficient at low Reynolds number since this motion is reciprocal and since low Reynolds swimming strategies cannot rely on the rate of deformation to change the flow one produces.

cancel the effect of the former. On the opposite, a non-reciprocal deformation, i.e. which breaks the time reversibility of the sequence, can create a net flow and therefore gives rise to a swimming dynamics. Let us give an example illustrating each property. Figure 5.1 provides a schematic of a scallop (or a mussel if one want to discuss this picture the Belgian way). Scallops are known to move into water at high Reynolds number by closing and opening their shell at different rate. This deformation is described by a sole degree of freedom and cannot lead to a motion at low Reynolds number because of time reversibility. One could think that closing and opening the shell at different rate would work. This strategy indeed works at high Reynolds number. They close their shell rapidly, expelling water at high velocity therefore moving the opposite direction. The shell opening is made slowly in order to generate a flow of small intensity and therefore minimizing an opposite thrust. At low Reynolds number, each displacement of the shell would generate the same flow. As a consequence, the closing of the shell cancels the opening and the scallop remains immobile at low Reynolds number.

More generally, deformation relying on one degree of freedom cannot lead to any efficient swimming strategy at low Reynolds number. Named by Purcell [149], the *scallop theorem* states that since the rate of deformation does not matter at least two degrees of freedom are mandatory to observe a object swimming at low Reynolds number. In his paper [149], Purcell gave an example of a functioning microswimmer. Imagined as the extension of a scallop, his *three link swimmer* is made of two hinges and three rigid rods as depicted in Fig.5.2(a) and (b). This model mimics the propulsion mechanism of a flagella or a sperm. The deforma-

tion of this swimmer is described by the two angles $\theta_1$ and $\theta_2$ which measures the relative position of each arm. This model has therefore two degrees of freedom and may be expected to swim for a non-reversible deformation. Fig.5.2(a) gives the non-reciprocal deformation. The arms move in the sequence *right* $\rightarrow$ *left* $\rightarrow$ *right* $\rightarrow$ *left* which is not a palindrome and which is therefore non-reciprocal. Note that the direction of swimming can also be guessed. Indeed, this sequence depicts a wave travelling from left to right with the swimmer catching only half a wavelength of it. Because momentum would be given to the liquid in the direction of the propagating wave, the swimmer travels from right to left. As a comparison, a reciprocal deformation of the swimmer is provided in Fig.5.2(b). The arms move according to the sequence *right* $\rightarrow$ *left* $\rightarrow$ *left* $\rightarrow$ *right* which is reciprocal. The ability to swim can easily be described in a phase space constructed with the different degrees of freedom. Figures 5.2(c) and (d) show that a non-reciprocal deformation corresponds to an open cycle in the deformation space. On the contrary, a reciprocal deformation does not show any cycle.

### 5.1.2 Models for microswimmers

During last decades, lots of efforts have been made to model and craft microswimmers. Regarding modelisation, lots of energy has been dedicated to the understanding of the swimming strategy of microorganisms. One can cite the work of Gray and Hancock regarding the propulsion of sea-urchin spermatozoa [72]. They considered waves propagating along the flagellum of the spermatozoon and the subsequent locomotion. More recently, Farutin *et al* modelled the motion of *Eutreptiella gymnastica* known to swim by deforming its body. In their study, they considered a sphere whose deformation is described as a sum of axisymmetry spherical harmonics $Y_{l,0}$ and showed that the swimming velocity is linearly proportional to the excess area, which is related to the amplitude of the spherical harmonics in the deformation [55]. Theoretical researches have also focused on the minimal model leading to a swimming motion, following the idea of Purcell and his three link swimmer. By far, the most known model is the one studied by Najafi and Golestanian [124, 71]. This model is originally made of three beads placed along a line and linked by two arms as depicted in Fig.5.3. The arm length changes through time in a periodic fashion. Being one dimensional, this model allows an easier analytical investigation of this swimmer. In particular, it has been shown [71] in the case of a continuous deformation that non-reciprocity is well

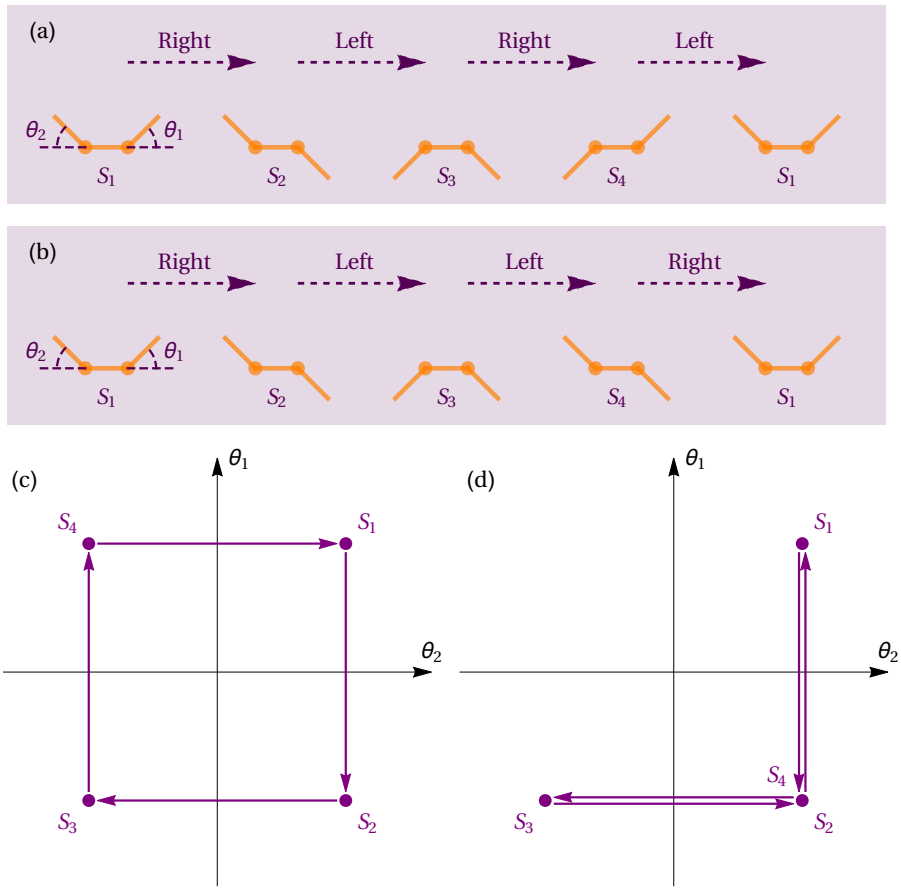


**Figure 5.2: (a)** Non-reciprocal deformation of the Purcell three link swimmer. The sequence leads to a swimming motion going from right to left. **(b)** Reciprocal deformation. **(c)** Cycle in the $(\theta_1, \theta_2)$ phase space for a non-reciprocal deformation. The enclosed area is known to be proportionnal to the distance travelled during a cycle. **(d)** Cycle in the $(\theta_1, \theta_2)$ phase space for a reciprocal deformation.

achieved when the arm oscillations are in quadrature of phase. The velocity of this swimmer scales as

$$\mathcal{V} = \frac{\kappa}{2}\omega A_1 A_2 \sin(\Delta\phi) \tag{5.5}$$

where the $A$'s are the amplitude of deformation, $\omega$ the angular frequency of deformation and $\Delta\phi$ the relative phase shift between the arm oscillations. The phase shift is here a measure of the non-reciprocity of the deformation. The constant

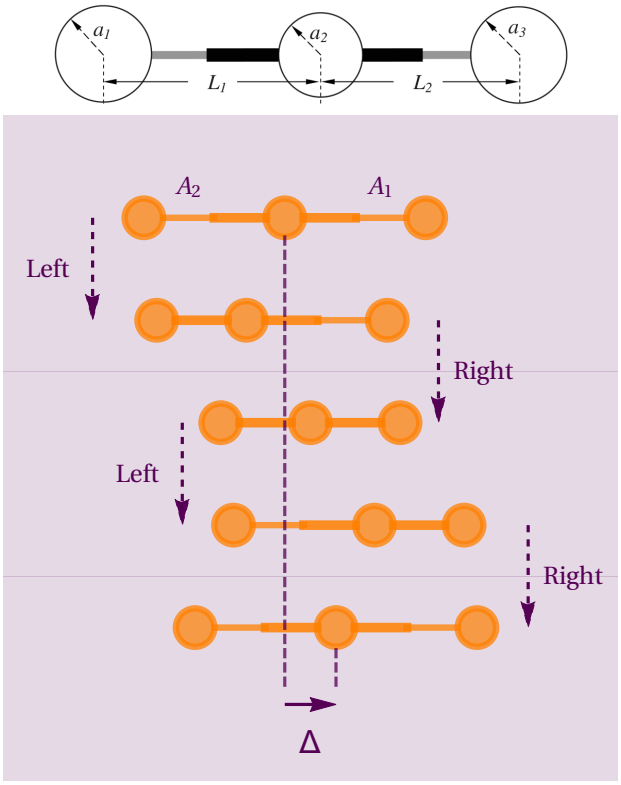


**Figure 5.3: (Top)** Schematic representation of the Najafi-Golestanian swimmer. Three spheres of respective radii $a_1$, $a_2$ and $a_3$ are linked together by two arms of variable lengths $L_1(t)$ and $L_2(t)$. **(Bottom)** Sequence of deformation of the Najafi-Golestanian swimmer. The arms deform according to the sequence *left* → *right* → *left* → *right* which is non-reciprocal, leading to an overall displacement $\Delta$ at the and of one cycle.

$\kappa$ accounts for the geometry of the swimmer and has been extensively studied in [132]. It is worth noticing that the quantity $A_1 A_2 \sin(\Delta\phi)$ corresponds to the area enclosed by the swimmer deformation in the phase space made by both axes $(A_1, A_2)$. Nevertheless, this model is kinematic. The arms deformation is known a priori without considering the energetic cost of such a deformation neither its dynamical origin. This model has known numerous extensions due to its analytical tractability. For example, Pande *et al* [131, 142] adopted a more dynamical approach. Instead of assuming the deformation of the swimmer, they considered knowing the forces acting at each instant. The link between the beads is not due to length-varying rods but due to springs. In this framework, they showed that

the speed of the swimmer may still be expressed as Eq.(5.5) but with parameters $A_1$, $A_2$ and $\Delta\phi$ depending on the forces and spring considered. Note that this model was also studied numerically via Lattice-Boltzmann simulations [141]. The Najafi-Golestanian model has also been extended to a two-dimensional analysis. Earl *et al* [48] considered a triangular geometry, where the two oscillating arms of the swimmer are separated by an angle $\theta$. Such a swimmer is shown to make circular motion during its cycle of deformation.

Beside theoretical investigations, lots of efforts have been made in realising experimentally microswimmers. In 2005, Dreyfus *et al* [45] realised a microswimmer with micrometric superparamagnetic colloids linked together with double strained DNA. The result is a flagellum reacting to time-dependent magnetic fields. This flagellum was attached to a red blood cell for a spermatozoon-like microswimmer. The result was a biohybrid microswimmer. For magnetic fields of around $10\ \mathrm{mT}$ and frequency of $10\ \mathrm{Hz}$, this swimmer could reach speed up to $15\,10^{-3}\ L/T$ where $L$ is the swimmer length and $T$ is the period of the time-dependent magnetic field. This experiment was studied theoretically one year later by Gauger *et al* [64] and by Roper *et al* [153]. In 2013, Williams *et al* also considered spermatozoon-like swimmer [188]. Their difference with the experiments of Dreyfus *et al* was the use of synthetic material alongside biological one. The flagellum and head of the swimmer was made of PDMS while the deformation the flagellum is made using cardiomyocytes on precise areas of the flagellum. The use of biological material removed the necessity of magnetic fields to generate the non-reciprocal deformation. Non-reprocity can also be achieved using the proximity to an interface. In such case, the position of the swimmer relative to the interface changes the viscous drag. As a consequence, swimming dynamics can be obtained with a swimmer with one degree of freedom. For example, such a swimmer was obtained by Tierno *et al* [176] with two paramagnetic colloidal particles of different radii in a precessing magnetic field.

Recently, a new experiment developed in our lab and involving magnetic material has attracted lots of attention [178, 179, 111, 106, 77, 75]. It consists in millimetric ferromagnetic beads trapped at an air-water interface as depicted in Fig.5.4. Since those particles are made of a metallic alloy, they float thanks to their wetting properties instead of buoyancy. The capillary attraction between those beads, the so-called *Cheerios effect* [180], is counterbalanced by dipole-dipole magnetic

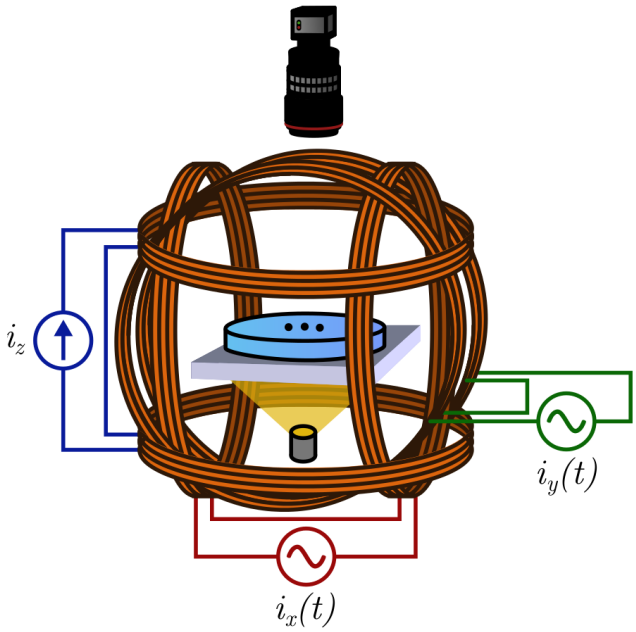


**Figure 5.4:** Schematic of the magnetocapillary swimmer experiment. Magnetic beads (in black) float at the air-water interface thanks to their wetting properties in a square tank filled with water. Three sets of Helmholtz coils generate magnetic fields. The horizontal pair generates a vertical and constant field in order to counterbalance the capillary attraction through dipole dipole repulsion. An equilibrium position can be obtained and is fully controllable. The vertical pairs of coils generate time dependent fields which deforms the structure. Images are taken from the top and the experiment is lit from below. Credit: Galien Grosjean, ULiege.

repulsion. Indeed, the horizontal coils depicted in Fig.5.4 induce magnetic dipoles and therefore dipole-dipole repulsion. This experimental set-up has been used to study the self-assembling dynamics of these beads [178, 179]. In particular, triangular and linear structures can be obtained [27]. Using horizontal time-dependant magnetic field, it has been shown that non-reciprocal motion can be achieved with those structures. The linear structure has led to the experimental realization of the Najafi-Golestanian microswimmer, as shown in Fig.5.5(top). The triangular structure is shown to be the most efficient in terms of speed [77, 75]. It is pictured in Fig.5.5(bottom).

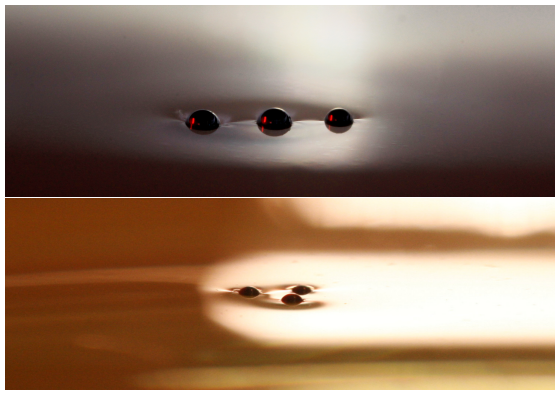

**Figure 5.5: (Top)** Picture of the experimental realization of the Najafi-Golestanian microswimmer using millimetric ferromagnetic beads at an air-water interface. The linear structure is obtained thanks to a strong horizontal magnetic field which keeps a stable alignment. **(Bottom)** Picture of the triangular swimmer. For each picture, the beads diamater is 500 $\mathrm{mm}$. Credit: Galien Grosjean, ULiege

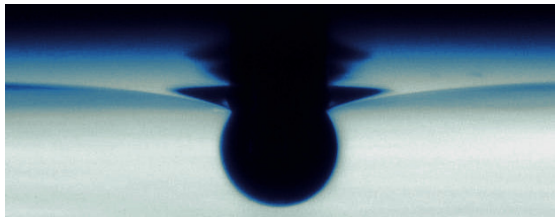

**Figure 5.6:** Picture illustrating the suspension of one bead at the air-water interface because of the partial wetting of the beads. One sees that, at the contact line and given the wetting angle, capillary forces pull the particle upward, preventing it to drown in the water. Nonetheless, most of the particle is underwater. Finally, one can see the important deformation of the interface due to the weight of the particle. This curvature is the key to the ``Cheerios effect''. Credit: Galien Grosjean, ULiege

## 5.2 Magnetocapillary microswimmer

Let us focus more deeply on this experiment. We will first describe the static case, where the magnetic fields are constant before illustrating the dynamics in the case of time-dependent magnetic fields.

### 5.2.1 Static magnetic fields - Self-organisation

As it can be seen in Fig.5.5, the beads used seem to float on the surface, without touching each other while remaining at a given constant interdistance. This

equilibrium is due to the self-organisation of the beads on the interface thanks to two effects: the capillary interactions between the beads which are mediated by the liquid-air interface curvature and the dipole-dipole magnetic interaction due to the magnetization induced by the coils.

Let us describe the self-assembling process by considering the attractive force of the experiment, the so-called "Cheerios effect". This force, nicknamed after the famous brand of cereals, originates from the curvature of the liquid interface. Indeed, the beads in the experiments are made of an alloy of chrome and steel with a density of $\rho_b = 7830\ \mathrm{kg/m^3}$. Yet, due to the small size of the beads, ranging from $2a = 397\ \mu\mathrm{m}$ to $2a = 1\ \mathrm{mm}$ in diameter, they can be trapped at the air water interface while being denser than water. This apparent floatability comes from the partial wetting of the beads. The capillary forces prevent particles from drowning. This property is pictured in Fig.5.6, one observes that most of the volume is immersed in water. The interface is significantly deformed because of the bead weight. Indeed, its weight pulls the interface downwards which deforms in return.

As stated before, this curvature of the interface is key to the "Cheerios effect". For the sake of intuition, imagine another particle, identical to the first one, suspended at the interface in its vicinity. Because of the curvature created by the former, the latter will slide along the interface and fall into the depression. This results in an attraction between each particle, mediated by the overall curvature. A complete demonstration of the resulting force can be found in [180, 135, 98]. The surface profile due to one bead can be expressed in terms of a Poisson equation expressing the pressure balance at the interface. One has

$$\sigma \nabla^2 h = \rho g h, \tag{5.6}$$

where $h$ is the height of the interface. This equation expresses the balance between the capillary interaction due to the curvature and the hydrostatic pressure caused by the deformation [180]. Given the axis-symmetry of the problem, one can express the Laplacian in cylindrical coordinate, which gives

$$\frac{\partial^2 h}{\partial r^2} + \frac{1}{r}\frac{\partial h}{\partial r} = \frac{\rho g}{\sigma} h. \tag{5.7}$$

Solutions of this equation are the modified Bessel function of the first kind $K_0$

and of the second kind $I_0$. Since one expects that $h \to 0$ for $r \to \infty$, the final solution is only expressed in terms of $K_0$. Therefore, one has [135]

$$h(r) = -qK_0\left(\frac{r}{l_c}\right) \tag{5.8}$$

where $l_c = \sqrt{\sigma/g\rho_f}$ is the capillary length and $q$ is called the capillary charge and depends on the boundary conditions along the particle. It writes

$$q = \frac{1}{6}\frac{a^3}{l_c^2}\left(2 - 4\frac{\rho}{\rho_f} + 3\cos\alpha - \cos^3\alpha\right) + \mathcal{O}\left(\frac{a^4}{l_c^3}\right), \tag{5.9}$$

where $\alpha_i$ is the three-phase contact line angle on the beads [24, 135, 97]. Note that $q$ scales as a length and can be extended to particles of any shape. In the $q$ expression, the density of the air has been neglected compared to the bead density $\rho$ and water density $\rho_f$. The $q$'s can either be positive or negative depending on the curvature of the interface created by the floating objects, namely, depending on the value of $\alpha_i$ and the ratio $\rho/\rho_f$. A positive sign ($q > 0$) corresponds to an object deforming the air-water interface downwards, in the same way than the metallic beads previously introduced. In the contrary, a negative sign ($q < 0$) corresponds to an upward curvature of the interface. An example would be an air bubble trapped beneath the air-water interface. Those quantities have been defined by analogy with interacting electric charges through the Coulomb potential. Indeed, the capillary interaction potential is obtained by multiplying the capillary charge $q$ by the deformation induced by the neighbouring bead. For two objects labelled $i$ and $j$ whose inter-distance reads $\vec{r}_{ij}$, one has [98]

$$\begin{aligned} U_c(\vec{r}_{ij}) &= 2\pi\sigma q_i h_i(\vec{r}_{ij}), \\ &= -2\pi\sigma q_i q_j K_0\left(\frac{|\vec{r}_{ij}|}{l_c}\right). \end{aligned} \tag{5.10}$$

The factor $2\pi$ comes from geometric arguments and the factor $\sigma$ appears as a link between the energy $U_c$ and the deformation $h_i$ induced by the bead $i$. Note that this expression has been obtained using the superposition principle. The depletions created by each bead are assumed to be independent. This is not the case for particles close to each other. Indeed, the curvature of the interface should be a solution of Eq.(5.7) and the superposition principle is shown to be valid for large interdistance only. For close particles, other techniques are required.

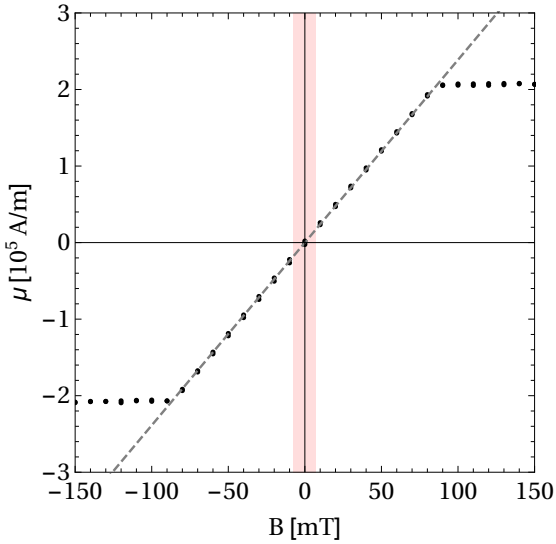


**Figure 5.7:** Magnetisation curve for beads with a diameter $D = 500\ \mu\mathrm{m}$, giving the magnetic dipole $\mu$ as a function of the magnetic field magnitude $B$. Black points correspond to experimental measurements made by Silhanek and his team at Liège University. The gray dashed line accounts for the paramagnetic approximation of the beads magnetization. The shaded area corresponds to the range of experimental values being far from the magnetic saturation.

As a consequence, once trapped at the interface, two or more beads with the same capillary charge attract. One needs another mechanism to intervene in order to maintain a stable equilibrium configuration. In this experiment, repulsive dipole-dipole interactions are used as the stabilizing force. Indeed, as stated at the beginning of the previous section, the beads are made of an alloy of chrome and steel which confers them a strong magnetic susceptibility. As a consequence, once placed within magnetic fields, those beads posses a magnetic dipole and therefore interact through magnetic dipole-dipole interaction. Two beads with dipole $\vec{\mu}_i$ and $\vec{\mu}_j$ and interdistance $\vec{r}_{ij}$ have an interaction potential given by

$$U_m(\vec{r}_{ij}) = \frac{\mu_0}{4\pi}\left(\frac{\vec{\mu}_i.\vec{\mu}_j}{|\vec{r}_{ij}|^3} - \frac{3\,(\vec{\mu}_i.\vec{r}_{ij})\,(\vec{\mu}_j.\vec{r}_{ij})}{|\vec{r}_{ij}|^5}\right), \tag{5.11}$$

where $\mu_0$ is the void magnetic susceptibility. Since the magnetic dipole $\vec{\mu}$ is at the root of the interaction, a proper understanding of the magnetisation is mandatory. The alloy from which the beads are made has an interesting property. Despite be-

ing ferromagnetic, the alloy has a magnetization curve with almost non hysteresis, as shown in Fig.5.7. Furthermore, this figure shows that the magnetization grows linearly with the amplitude of the magnetic field applied. As a consequence, despite being ferromagnetic, the beads mimic paramagnetic properties. Finally, the spherical shape of the beads gives two other important properties. Firstly, unlike to usual paramagnetic materials, the magnetic susceptibility $\chi$ of the alloy is extremely important. Indeed, since the bulk material is ferromagnetic by nature, its bulk magnetic susceptibility is important with $\chi_{bulk} = 300$ [106]. Because of the spherical shape of the particles, the bulk susceptibility is not the effective susceptibility, which is given by [127]

$$\chi = \frac{3\chi_{bulk}}{3 + \chi_{bulk}} \approx 3 \tag{5.12}$$

which is several order of magnitude larger than any other usual paramagnetic material. This observation explains why this material is often referred to as "superparamagnetic". The value of $\chi$ corresponds to the gray dashed line in Fig.5.7 and is in perfect agreement with the experiments. Second, the beads behave like point-like magnetic dipole thanks to their spherical symmetry [91], whatever their size. As a consequence of all those properties, one can express the magnetic dipole has

$$\vec{\mu}_i = \frac{4\pi a_i^3 \chi \vec{B}}{3\mu_0} + \vec{\mu}_i^r \tag{5.13}$$

where $a_i$ is the beads radius and $\vec{B}$ is the total external magnetic field. Note that the magnetic dipole $\vec{\mu}_i$ and the external magnetic field are collinear. The vector $\vec{\mu}_i^r$ accounts for the remnant magnetic dipole. In terms of equivalent magnetic field, it has been measured at $0.015\ \mathrm{mT}$. It has a very small amplitude compared to magnetic fields used in experiments. Note that the magnetic saturation is never reached in the experiments. The experimental range of magnetic field is given in the red shade area in Fig.5.7, which corresponds to $|\vec{B}| \in [-8, 8]\ \mathrm{mT}$.

Given the two interactions above, a structure can self-organise into a stable configuration. Given the horizontal coils depicted in Fig.5.4, the beads can acquire a vertical magnetic dipole. Those dipoles generate a horizontal repulsion for particles trapped at the interface. This magnetic repulsion is counterbalanced by the capillary attraction which keeps the particles at close. Equilibrium is found when

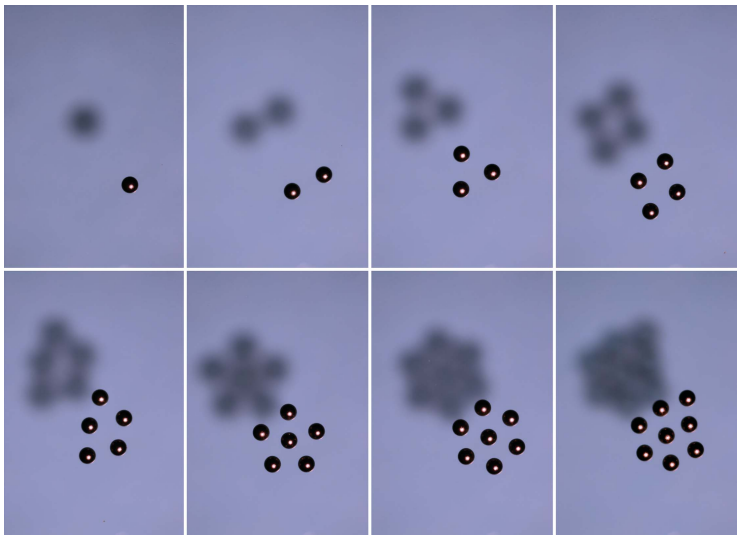

**Figure 5.8:** Structure observed experimentally for beads of diameter $2a = 500\ \mu\mathrm{m}$ pinned at an air-water interface. The capillary attraction between the ferromagnetic beads is conterbalanced by a vertical magnetic field (out of the plane of the picture). The beads being magnetic, the induced magnetic moments (out of the plane of the picture) give a repulsion between the particle. Note the 6-fold symmetry which originates from the interaction potentials. Pictures taken from [111].

the overall potential energy is minimised with

$$\begin{aligned} U &= \frac{1}{2}\sum_{i\neq j} U_m(\vec{r}_{ij}) + U_c(\vec{r}_{ij}), \\ &= \frac{1}{2}\sum_{i\neq j}\left(\frac{4\pi}{9\mu_0}\frac{a_i^3 a_j^3 \chi^2 |\vec{B}_z|^2}{|\vec{r}_{ij}|^3} - 2\pi\sigma q_i q_j K_0\left(\frac{|\vec{r}_{ij}|}{l_c}\right)\right), \end{aligned} \tag{5.14}$$

In this expression, we neglected the remnant contribution to the magnetic dipoles given their small amplitudes. The potential energies involved in the definition above naturally lead to an axisymmetric structure with a 6-fold symmetry, given their mathematical definition. Indeed, only the magnitude of the interdistance $|\vec{r}_{ij}|$ defines them. The structures one observes are illustrated experimentally in Fig.5.8 for a number of beads increasing from 1 to 8. The bead diameter in this figure is $2a = 500\ \mu\mathrm{m}$ and the vertical magnetic field is kept constant.

Adding a horizontal magnetic field can deform the global structure but also lead to new stable ones. The effect of a constant horizontal contribution was investi-

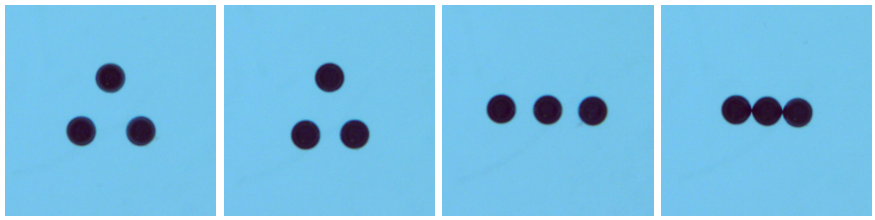

**Figure 5.9:** Possible configurations for a three-beads structure pinned at an air-water interface with a vertical and an horizontal magnetic field. From left to right: increasing magnitude of $\vec{B}_x$. The case $\vec{B}_x = \vec{0}$ is depicted in the far left and gives the regular triangle. For non-zero magnitude of $\vec{B}_x$, the triangle deforms to an isoceles. Above the critical value $\vec{B}_x^\star$, the linear structure can be made stable [27]. Finally, important horizontal field values lead to the collapse of the structure. Credit: Galien Grosjean, ULiege.

gated by Chinomona *et al.* [27]. In their aticle, they demonstrated theoretically that for a "sufficiently strong" horizontal magnetic field $\vec{B}_x$, a rectilinear structure of three beads can be made stable. Their condition has a complex expression but can be approximated by $|\vec{B}_x^\star| \approx |\vec{B}_z|/2$. Later, this work was used and validated by Grosjean *et al* for their experimental realisation of the Najafi-Golestanian microswimmer [75]. The different structures obtained for a three-beads assembly with a horizontal contribution $\vec{B}_x$ to the magnetic field are depicted in Fig.5.9. Four situations are considered. With $\vec{B}_x = \vec{0}$, a regular triangle is found, similarly to the results shown in Fig.5.8. For increasing values of $\vec{B}_x$, the triangle deforms to an isosceles one. The shorter side of the triangle is the one aligned with the horizontal field. When reaching the threshold value $\vec{B}_x = \vec{B}_x^\star$, the linear structure can be observed. Finally, for large values of $\vec{B}_x$, the beads touch each other. The decreasing distance between the beads finds its explanation in the dipole-dipole interaction. Indeed, when a horizontal field is added, the interaction between the horizontal component of the dipoles is attractive, decreasing the relative efficiency of the magnetic repulsion induced by $\vec{B}_z$. Note that the system is bistable once $\vec{B}_x > \vec{B}_x^\star$, the linear and triangular structures can both be observed.

The linear and triangular structures are both able to swim, using different strategies nonetheless. Their swimming dynamics is the core of the second part of this thesis. Before discussing their theoretical studies and numerical modelling, let us first discuss briefly their experimental realization.

### 5.2.2 Time-dependent magnetic fields - Swimming dynamics

The horizontal motion of the assembly is only possible if a non-reciprocal deformation is achieved, as discussed above in this chapter. For this purpose, time-dependent magnetic fields are used. The global magnetic field is therefore made of three contributions. The vertical field $\vec{B}_z$ which gives the dipole-dipole repulsion. The horizontal field $\vec{B}_x$, henceforth referred to as "offset", stabilises the rectilinear structure and gives reproducible initial conditions from an experimental point of view [77]. And finally, the time-dependent magnetic field $\vec{B}_{osc}(t)$, also horizontal, which can give the non-reciprocal deformation. It is worth noticing that thanks to the Helmholtz coils, the magnetic fields applied are spatially homogeneous and therefore no net force of magnetic origin is to consider. The translation of the swimmer is only due to the hydrodynamic interaction and the non-reciprocal deformation.

Let us briefly describe the hydrodynamic interactions involved in the swimming dynamics. When a sphere moves into a fluid, it creates a flow. A second sphere, immobile, would therefore be dragged into the induced flow and set into motion. The force $\vec{F}_h$ exerted from the former sphere to the latter and mediated by the fluid is called *hydrodynamic interaction*. In the case of low Reynolds number flows, the mathematical expression of those forces can be derived. A more complete description is given in Appendix B. In a few words, for the sake of intuition, let us develop further the example discussed a few lines ago. A sphere labelled $j$, with a velocity $\vec{v}_j$, exerts a force $\vec{F}_{h,i}$ on a neighbouring sphere labelled $i$ which reads

$$\vec{F}_{h,i} = \frac{9\pi\eta a_i a_j}{2|\vec{r}_{ij}|}\left(\vec{v}_j + \frac{\vec{r}_{ij}(\vec{r}_{ij}.\vec{v}_j)}{|\vec{r}_{ij}|^2}\right), \tag{5.15}$$

where $\vec{r}_{ij} = \vec{r}_i - \vec{r}_j$ and points from sphere $j$ to sphere $i$. This effect is the means by which systems at low Reynolds number can swim. Indeed, from a dynamical point of view, the forces involved into hydrodynamic interactions break Newton's third law of dynamics: for the force $\vec{F}_{h,i}$ due to $j$ and applied to $i$, there is no opposed force with the same magnitude originating from $i$ and applied to $j$. In the peculiar case of swimming, it means that in a collection of particles the sum of all internal forces can be different from zero and therefore gives an overall motion. The key for such a dynamics is a non-reciprocal deformation.

Non-reciprocal deformation is observed for the triangular and the linear config-

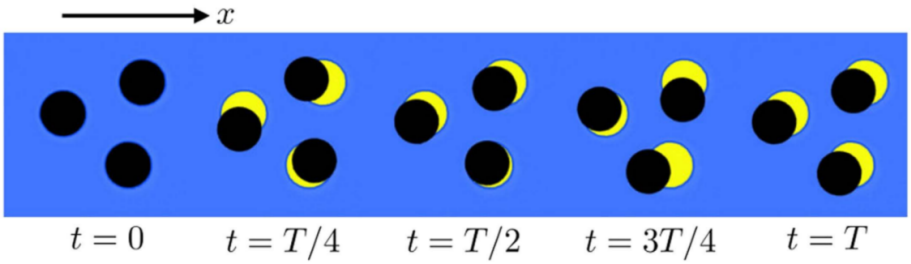


**Figure 5.10:** Non-reciprocity illustrated for the triangular case. Snapshots illustrating the deformation of the triangular swimmer during a period of the magnetic field oscillation for beads of diameter $2a = 500\ \mu\mathrm{m}$. Black disks account for the actual position of each beac while yellow disks correspond to their initial position. Deformation and motion can therefore be tracked. The swimmer starts in an regular configuration. It rotates counterclockwise ($t = T/4$) before being an isosceles ($t = T/2$). The swimmer then rotates clockwise ($t = 3T/4$) before being equilateral again ($t = T$). The swimmer is back at its initial configuration but has moved from its initial position. Adapted from [77].

urations, as shown in Figs. 5.10 and 5.11. For each figure, the non-reciprocal dynamics is illustrated using snapshots during a whole cycle of deformation. For the triangular configuration, Fig.5.10 shows two mains features. Firstly, the structure oscillates around its center, clockwise (see $t = T/4$) and counter-clockwise (see $t = 3T/4$). Secondly, the triangle deforms, oscillating between a regular structure (see $t = 0$) and an isosceles one (see $t = T/2$). Interestingly, both oscillations are in quadrature of phase, fulfilling the condition of non-reciprocity. The dynamics from $t = 0$ to $t = T$ is not the same as the one observed when "rewinding" the dynamics, i.e. when considering the dynamics from $t = T$ to $t = 0$. This observation testifies that the deformation is non-palindromic and therefore non-reciprocal. Since non-reciprocity is achieved, the assembly can swim along the interface, as it can be seen in Fig.5.10. The linear configuration also displays a non-reciprocal deformation. Figure 5.11 gives snapshots of the deformation dynamics for a microswimmer at $f = 2\ \mathrm{Hz}$. One period of the oscillating field is illustrated. The blue vertical dashed lines give points of reference in order to track the deformation over one cycle. One sees that each particle oscillates around its initial position. In particular, the two left particles are at their closest at $t = 0.19\ \mathrm{s}$ approximatively while the two particles of the right are at their closest at $t = 0.31\ \mathrm{s}$. As a consequence, a phase shift exists between each oscillation. Given the theory of Najafi and Golestanian [124, 71], non-reciprocity is achieved. Note that if the swimmer seems motionless, it is only because of its

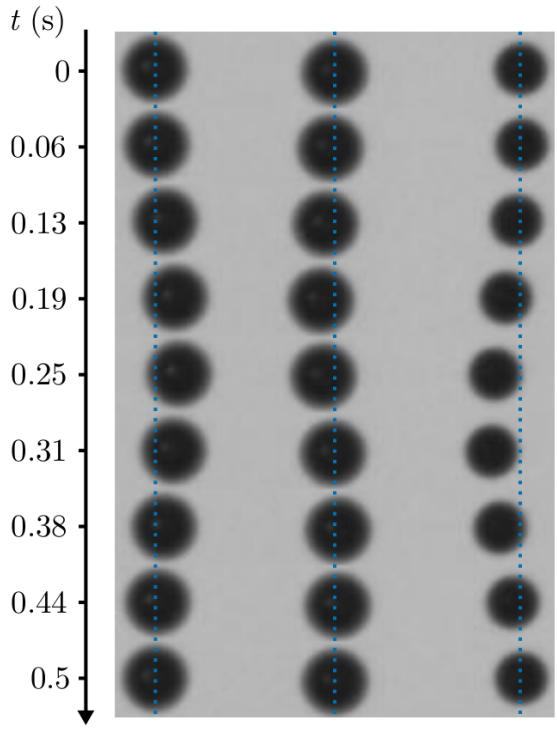


**Figure 5.11:** Non-reciprocity illustrated for the linear case. Snapshots illustrating the deformation of the triangular swimmer during a period of the magnetic field oscilaltion for two beads of diameter $2a = 500\ \mu\mathrm{m}$ and one bead of diameter $2a = 397\ \mu\mathrm{m}$. The magnetic field is applied along the horizontal direction and oscillates at $f = 2\ \mathrm{Hz}$. The two first particles approach until being at their closest at $t = 0.19\ \mathrm{s}$. The two last particles are at their closest for $t = 0.31\ \mathrm{s}$ approximatively. The swimmer is back to its initial configuration at the end of the cycle. Adapted from [75].

low velocity. Indeed the linear configuration swims at $12\ \mu\mathrm{m/s}$ at its best [75] while the triangular configuration swims up to $300\ \mu\mathrm{m/s}$ [77].

### 5.2.3 Applications

Given its efficiency, the triangular swimmer is a candidate of choice for microfluidic applications. Beside its speed reaching values up to one radius per period of oscillation ($v = a/T$), the triangular is shown to be completely and remotely controllable. By changing "slowly" the orientation of the oscillating field, the swimmer can make U-turns, loops and changes of direction [77]. In this context, "slowly" means slower than the period of oscillation of the field. This remote controllabil-

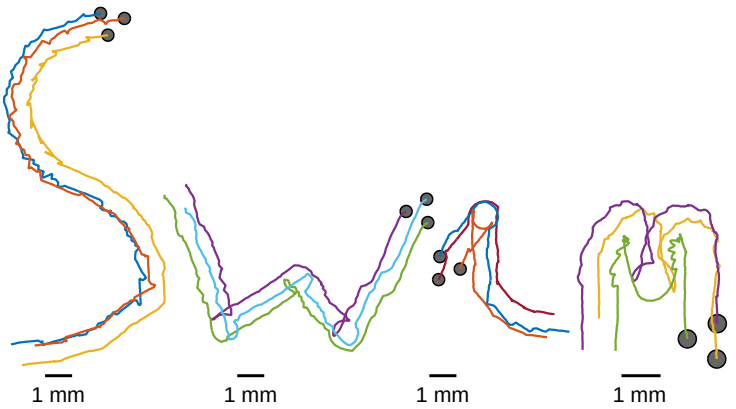


**Figure 5.12:** Remote controllability illustrated. Changing the orientation of the oscillating field $\vec{B}(t)$, the letters **S**, **W**, **I** and **M** can be drawn when tracking the swimmer trajectory. U-turns, loops and curved trajectories are seen. Credit: Galien Grosjean, ULiege.

ity is illustrated in Fig.5.12 where the the swimmer draws the letters S, W, I and M when tracking its trajectory while changing the orientation of the field.

Given its manoeuvrability, the swimmer could, for example, be used for mixing fluid at low Reynolds number. It is worth noticing that mixing at low Reynolds number is a challenging task. Indeed, mixing usually rely on turbulence in the fluid. At low Reynolds number, it is no longer possible. Looking back at Eq.(5.2), one can see that the advection term $(\vec{u}.\vec{\nabla}).\vec{u}$ responsible of turbulence is neglected in this limit. As a consequence, other mechanisms are required. One of those strategies is based on the idea of creating multiple layers of fluids to obtain a complex entanglement mimicking a mixing process. This is the same idea as the baker doing his *croissants* by creating multiple layers of puff pastry. And because pastries have inspired multiples ideas in chaos theory, the principle of creating complex entanglement of layer of fluids is called *chaotic advection* [15]. This process is illustrated with the linear structure in Fig.5.13. Food dyes have been added to water in the experiments to follow the creation of the layers. A linear structure was formed by increasing $\vec{B}_x$ (see Fig.5.13(b)). A horizontal rotating field forces the rod to rotate at its frequency. The induced flow drags the dyes and the layers are created (see Fig.5.13(c)). Because flows are reversible at low Reynolds number, rotating the field backwards bring back the bulk to its initial state (see Fig.5.13(d)). The sole difference observed is the gray shaded area in Fig.5.13(d) which is due

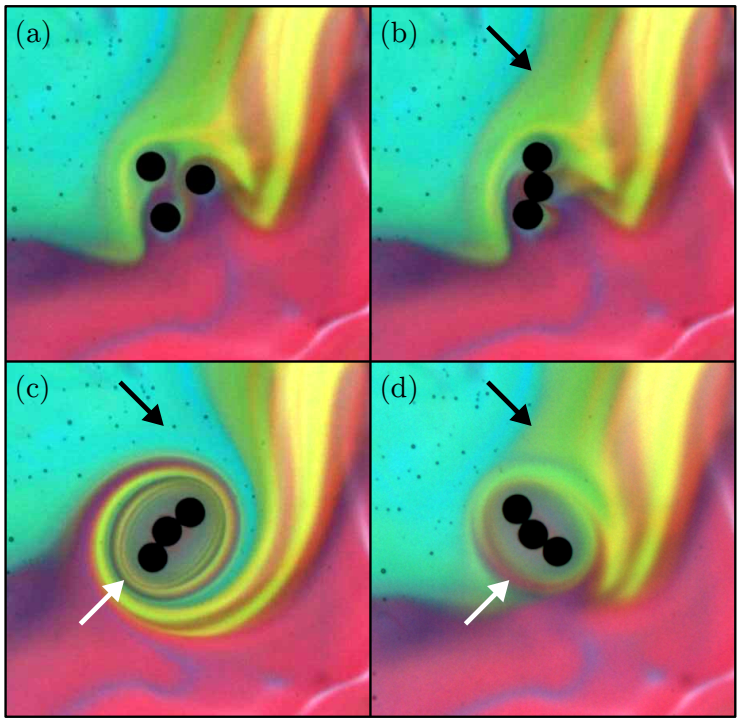


**Figure 5.13:** Mixing food dyes at low Reynolds number using a magnetocapillary swimmer. **(a)** A Swimmer is placed where the mixing is required. (b) The beads are assembled into a linear structure and a rotating magnetic field is applied. (c) After approximately eight turns clockwise, layers of dyes are formed around the rod. (d) After approximately eight turns counter-clockwise, the surface is back at its original state. Only a gray zone is visible where the thermal diffusion of the dyes have occurred. Credit: Galien Grosjean, ULiege.

to the thermal diffusion of the dyes between each layer of fluid.

Finally, this swimmer has been shown to be able to transport cargo of different types along the interface, from polystyrene beads to sesame seeds [76]. The swimmer captures the cargo via capillary interaction. In those cases, manoeuvrability is conserved but the locomotion requires more than 3 beads for propulsion. Indeed, because of cargo attaches to the beads, this cargo restrains their motion. In this situation, restrained beads do no longer participate to the non-reciprocal deformation. As a consequence, more beads are required.

## 5.3 Conclusions

Despite the rich behaviour illustrated in the previous sections, the theoretical description of the dynamics of magneto-capillary swimmers is challenging [27]. The second part of this thesis is dedicated to the investigation of the dynamics in two cases: the case of 3 particles in free space only submitted to time-dependent magnetic fields and the case of 3 confined particles in time-dependent magnetic field. The former case corresponds to the Najafi-Golestanian configuration and gives a proper realization of this swimmer. The latter case investigated is the triangular swimmer. Therefore, in the two following chapter, we ask the question *what is the cooperative dynamics required in this system in order to order to obtain a non-reciprocal deformation?* We will develop the theoretical framework required to understand the cooperative interactions of the beads on the interface and discuss how a global self-propulsive dynamics is achieved.

# 6

# Magnetocapillary linear swimmer

*As stated in the beginning of this part of the manuscript, the three-beads magnetocapillary microswimmer can be stabilised into a linear configuration by adding an offset of high amplitude. This condition is approximately found for* $|\vec{B}_x|/|\vec{B}_z| = 0.586$ [75, 27]. *This geometry corresponds to the one using by Najafi and Golestanian in their seminal study of micro-swimmers* [124, 71]. *As an experimental validation of their work, we managed to move this structure along the interface using time-dependent magnetic fields.*

*This chapter will be divided in two parts. First, we will seek for a way to generate a non-reciprocal deformation of this microswimmer. We show that using beads of different size can lead to non-reciprocity. Second, this system is solved from a dynamical point of view in order to complete Golestanian kinematic study in* [124, 71]. *A linear model for the magnetocapillary microswimmer is proposed and a full theoretical investigation closes this chapter. Especially, the optimisation and miniaturisation of this microswimmer is discussed.*

All the results presented in this chapter can be found in the following articles.

- Lagubeau G., Grosjean G., Darras A., Lumay G., Hubert M. & Vandewalle N. *Statics and dynamics of magnetocapillary bonds*, Phys. Rev. E, **93**, 053117 (2016).

- Grosjean G., Hubert M. & Vandewalle N. *Realization of the Najafi-Golestanian microswimmer*, Phys. Rev. E, **94**, 021101 (2016).

## 6.1 Seeking non-reciprocity

When dealing with low Reynolds number dynamics and locomotion, creating a non-reciprocal deformation is not a trivial task. In the forthcoming sections, we will show how to generate this non-reciprocity using beads of different sizes in the structure. This leads to different interactions between each pair of beads and therefore break the spatial symmetry of the swimmer. Under a time-dependent magnetic field, each pair will oscillate with a different phase shift and therefore fulfil the swimming condition of Najafi and Golestanian in Eq.(5.5) [71].

### 6.1.1 Experimental background

Let us give some experimental background to this section. Experiments has been provided by Galien Grosjean from Liege University. The beads considered through this chapter have a diameter ranging from $2a = 793\ \mu\mathrm{m}$ down to $2a = 397\ \mu\mathrm{m}$. The beads are placed at an air-water interface and float thanks to their wetting properties. Since they have strong ferromagnetic properties as described in Chapter 5, in order to counterbalance the capillary attraction between beads at the interface, a vertical field $\vec{B}_z$ is applied. The amplitude of this field is $|\vec{B}_z| = 4.5\ \mathrm{mT}$. This vertical field is provided by a pair of horizontal electric coils in the Helmholtz configuration as depicted in Fig.5.4. In order to stabilise the three beads assembly into a linear configuration, an intense and constant horizontal field $\vec{B}_x$ is also applied [27] with an amplitude $|\vec{B}_x| = 2.2\ \mathrm{mT}$. The deformation is due to a superimposed oscillating field $\vec{B}_{osc}(t)$ applied parallel to $\vec{B}_x$. The peak amplitude of this field is $|\vec{B}_{osc}| = 0.5\ \mathrm{mT}$ and its frequency $f$ ranges between $0.1\ \mathrm{Hz}$ and $5\ \mathrm{Hz}$. It follows that the global magnetic field writes

$$\vec{B}(t) = \Big(|\vec{B}_x| + |\vec{B}_{osc}|\sin(\omega t)\Big)\,\vec{e}_x + |\vec{B}_z|\vec{e}_z, \tag{6.1}$$

where $\omega = 2\pi f$ is the angular frequency of the oscillating field. All the vector fields and a schematic of the assembly are given in Fig.6.1

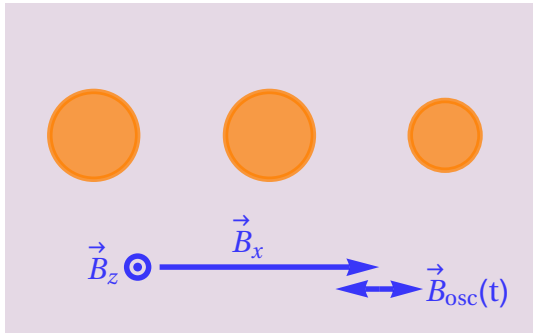


**Figure 6.1:** Schematic of the three beads self-assembly in the collinear case. A vertical field $\vec{B}_z$ magnetises the beads and induces a repulsive dipole dipole interaction. An high intensity horizontal field $\vec{B}_x$ gives a stable linear configuration has described in [27]. Finally, a small amplitude oscillating field $\vec{B}_{osc}(t)$ deforms the structure. Non-reciprocity is obtained by considering beads of different sizes, as shown in this figure.

As it has been discussed previously, beads of different sizes are required for the non-reciprocal deformation of the assembly. The reason is simple: identical beads would create identical forces on each other. Since we are dealing with internal forces for this deformation, identical forces would lead to an immobile bead at the center of the system and two beads oscillating in opposition of phase on the sides. As a consequence, different forces and therefore different beads are required. Using two beads of $500\ \mu\mathrm{m}$ and one bead of $397\ \mu\mathrm{m}$, it has been possible to obtain a swimmer swimming up to $15\ \mu\mathrm{m/s}$. This corresponds to a Reynolds number up to $10^{-1}$. In the next section, the magnetocapillary potential is investigated in the linear regime in order to quantify completely the effect of the size on the interactions.

### 6.1.2 Linear analysis

Let us consider the interaction between a pair of beads. An illustration of the forces acting in the system is given in Fig.6.1. On the one hand, we know from Chapter 5 that the capillary interaction is described by

$$U_c(\vec{r}) = -2\pi\sigma q_1 q_2 K_0\left(\frac{|\vec{r}|}{l_c}\right), \tag{6.2}$$

where $\vec{r}$ lies in the horizontal plane. For the sake of simplicity, we define $\Gamma = 2\pi\sigma q_1 q_2$ which measures the magnitude of deformation of the interface and also

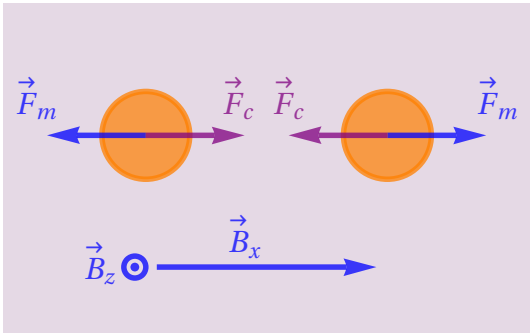


**Figure 6.2:** Schematic for the two beads interaction. Because of the liquid surface deformation, beads attract through the capillary interaction $\vec{F}_c = -\vec{\nabla}U_c$. To prevent the contact between the beads, magnetic fields are applied and leads to a magnetic dipole-dipole interaction $\vec{F}_m = -\vec{\nabla}U_m$.

gives the typical energy stored in the surface deformation. On the other hand, the beads are also submitted to magnetic fields in order to induce dipole-dipole interactions and to stabilize the structure. Given the large amplitudes of magnetic fields considered in this chapter, the remnant contribution of the magnetic dipole can be neglected. As stated in Section 5.2.1, in equivalent field unit, the remnant contribution is measured to be given by $0.015\ \mathrm{mT}$ which is more than ten times smaller than the magnetic fields one uses. For a magnetic field given by $\vec{B} = |\vec{B}_z|\vec{e}_z + |\vec{B}_x|\vec{e}_x$, the magnetic interaction potential is given by

$$U_m(\vec{r}) = \frac{4\pi\chi^2 a_1^3 a_2^3}{9\mu_0}\left(\frac{|\vec{B}_z^2| + |\vec{B}_x^2|\left(1 - 3\cos^2\theta\right)}{|\vec{r}|^3}\right), \tag{6.3}$$

where $\theta$ is the angle between the vector $\vec{r}$ joining the two beads and the horizontal field $\vec{B}_x$.

We can make the magnetocapillary potential dimensionless by considering $\Gamma$ as a unit of energy and by considering the substitution $|\vec{r}| = \overline{r}l_c$. The dimensionless total potential $\overline{U}$ is given by

$$\overline{U} = -K_0\left(\overline{r}\right) + \frac{\left(\mathcal{M}_z + \mathcal{M}_x\left(1 - 3\cos^2\theta\right)\right)}{\overline{r}^3}, \tag{6.4}$$

where $\mathcal{M}_z$ and $\mathcal{M}_x$ are the magnetocapillary numbers and defines as

$$\mathcal{M}_i = \frac{4\pi\chi^2 a_1^3 a_2^3 |\vec{B}_i|^2}{9\mu_0 l_c^3 \Gamma}, \tag{6.5}$$

In this expression, $i = \{x, z\}$. The equilibrium position $(\tilde{r}^\star, \theta^\star)$ is obtained by cancelling the gradient of this potential.

$$\frac{\partial \overline{U}}{\partial \overline{r}}\Big|_{\vec{r}^\star} = K_1(\overline{r}) - 3\frac{\mathcal{M}_z + \mathcal{M}_x\left(1 - 3\cos^2\theta\right)}{\overline{r}^4} = 0, \tag{6.6}$$

$$\frac{1}{\overline{r}}\frac{\partial \overline{U}}{\partial \theta}\Big|_{\vec{r}^\star} = \frac{6\mathcal{M}_x \sin\theta\cos\theta}{\overline{r}^4} = 0. \tag{6.7}$$

The stability, and therefore the natural frequencies, are obtained thanks to the second derivative

$$\frac{\partial^2 \overline{U}}{\partial \overline{r}^2}\Big|_{\vec{r}^\star} = -K_0(\overline{r}) - \frac{K_1(\overline{r})}{\overline{r}} + 12\frac{\mathcal{M}_z + \mathcal{M}_x\left(1 - 3\cos^2\theta\right)}{\overline{r}^5}, \tag{6.8}$$

$$\frac{1}{\overline{r}^2}\frac{\partial^2 \overline{U}}{\partial \theta^2}\Big|_{\vec{r}^\star} = \frac{6\mathcal{M}_x\left(\cos^2\theta - \sin^2\theta\right)}{\overline{r}^5}. \tag{6.9}$$

Equations relative to the azimuthal direction give the equilibrium angles

$$\theta^\star = \frac{n\pi}{2}, \quad n \in \mathbb{N}. \tag{6.10}$$

Stable positions are found for even values of $n$ while unstable positions appear for odd values of $n$ given Eq.(6.9). As a consequence, for the stable azimuthal equilibrium position, the equilibrium distance is given by the transcendental equation

$$\overline{r}^{4\star} K_1(\overline{r}^\star) = 3\left(\mathcal{M}_z - 2\mathcal{M}_x\right). \tag{6.11}$$

This equation predicts a saddle-node bifurcation with $3\left(\mathcal{M}_z - 2\mathcal{M}_x\right)$ being the bifurcation parameter as shown in Fig.6.3. Indeed, the Bessel $K_1(\overline{r})$ function is decreasing as $1/\overline{r}$ for $\overline{r} \ll 1$ and decreasing as $\exp(-\overline{r})$ for $\overline{r} \gg 1$. As a consequence, $\overline{r}^{4\star} K_1(\overline{r}^\star)$ has an unique global maximum, giving an upper bound for $3\left(\mathcal{M}_z - 2\mathcal{M}_x\right) = 3.3408$. Above this critical value, no solution is found. Physically, it means magnetism always overcomes the capillary attraction, bringing the particles infinitely away from each other. Below this critical value, two solutions are found, one stable and one unstable. Indeed, given Eq.(6.11), Eq.(6.8) can be

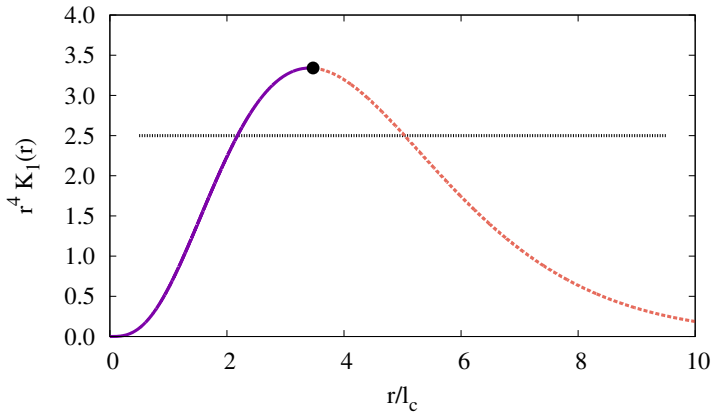


**Figure 6.3:** Illustration of the $r^4 K_1(r)$ function and the corresponding saddle-node bifurcation. The horizontal gray dotted line gives a peculiar value of the constant $3(\mathcal{M}_z - 2\mathcal{M}_x)$. The left-hand side of the curve (plain purple) gives a stable equilibrium interdistance while the right-hand side of the curve (dashed orange) gives the unstable equilibrium interdistance. A saddle-node bifurcation is found for $3(\mathcal{M}_z - 2\mathcal{M}_x) = 3.3408$, above which magnetism always repels the beads infinitely appart. The corresponding highest stable equilibrium interdistance is found for $r/l_c = 3.41387$

rewritten as

$$\frac{\partial^2 \overline{U}}{\partial \overline{r}^2}\Big|_{\vec{r}^\star} = -K_0(\overline{r}) + \frac{3K_1(\overline{r})}{\overline{r}}, \tag{6.12}$$

which gives a positive value for the lowest equilibrium distance and negative for the largest. Note that in this expression, the second derivative depends only parametrically on the magneto-capillary numbers through Eq.(6.11). For the parameters considered experimentally, typical stable distances between the beads give $\overline{r} < 1$. Such a range of values gives the possibility to express the Bessel functions as $K_0(\overline{r}) \simeq \log(\overline{r})$ and $K_1(\overline{r}) \simeq 1/\overline{r}$. In this case, the equilibrium position and stiffness can be expressed in terms of the magneto-capillary numbers. In first approximation, one has

$$\overline{r} = (3\mathcal{M}_z - 6\mathcal{M}_x)^{\frac{1}{3}} \quad \rightarrow \quad |\vec{r}| = \left(\frac{4\pi\chi^2 a_1^3 a_2^3}{3\mu_0\Gamma}\left(|\vec{B}_z|^2 - 2|\vec{B}_x|^2\right)\right)^{\frac{1}{3}}, \tag{6.13}$$

and

$$\overline{k} = \frac{3}{(3\mathcal{M}_z - 6\mathcal{M}_x)^{\frac{2}{3}}} \quad \rightarrow \quad k = \left(\frac{3\mu_0\Gamma^{\frac{5}{2}}}{4\pi\chi^2 a_1^3 a_2^3}\frac{1}{|\vec{B}_z|^2 - 2|\vec{B}_x|^2}\right)^{\frac{2}{3}}. \tag{6.14}$$

Those expressions are only valid if $\bar{r} < 1$ or $|\vec{r}| < l_c$. In this those expressions, the Bessel function $K_0(x)$ has been neglected given its small value compared to $K_1(x)/x$. It is worth noticing that Eq.(6.13) does not depend on the size of the beads since $\Gamma \propto a_1^3 a_2^3$ as it can be seen from Eq.(5.9). This property has been observed experimentally by Vandewalle *et al* in [179]. Contrarily to the distance between the beads, the stiffness does depend on the beads size. Finally, the natural frequency is related to the ratio between the stiffness and the reduced mass of the system $m_r = m_1 m_2/(m_1 + m_2)$, which gives in first approximation

$$\omega_0 = \left(\frac{3\Gamma}{4\pi\rho}\frac{a_1^3 + a_2^3}{a_1^3 a_2^3}\right)^{\frac{1}{2}} \left(\frac{3\mu_0\Gamma}{4\pi\chi^2 a_1^3 a_2^3}\,\frac{1}{|\vec{B}_z|^2 - 2|\vec{B}_x|^2}\right)^{\frac{1}{3}}. \tag{6.15}$$

Note that this formula does not consider the mass of fluid dragged by the beads motion. This mass was estimated in [106] and is given by $m_{fluid} = m_r/16$. In Eq.(6.15), the second factor on the right hand side does not depend on the particle size but the first factor does. Therefore, in order to have different values of $\omega_0$, different radii are necessary. Indeed, $\Gamma$, $\rho$ and $\chi$ cannot be changed since they depend on the magnetic structure of the alloy, the beads wetting properties and density. Given the experimental device, the magnetic fields $\vec{B}_z$ and $\vec{B}_x$ are the same for each particle at the interface. Only remains the radius of the beads in order to generate a difference of natural frequency. Since the natural frequencies $\omega_0$ depend on the radii involved, different pairs of beads do not oscillate with the same phase shift relative to the external field when driven out of equilibrium. This last property is fundamental in swimming systems since it gives the possibility to fulfil the Golestanian condition in Eq.(5.5).

This linear analysis can be verified experimentally. Figure 6.4 gives the distance between two beads compared to the capillary length $l_c$ as a function of the magnetocapillary number $\mathcal{M}_z$. Different bead sizes have been considered. The color code used depends on the ratio $|\vec{r}|/2a$. Finally, the dotted gray line corresponds to Eq.(6.13). No fitting parameter has been used. One sees that the theory captures the experimental data. Only the beads with the lowest ratio $|\vec{r}|/2a$ gives small differences. This difference can come from the expression of the capillary potential which is valid only in the limit $|\vec{r}|/2a \gg 1$ [135].

The natural frequency expression can also be verified. Before verifying the validity of Eq.(6.15), let us consider the method used to obtain this information. Figure

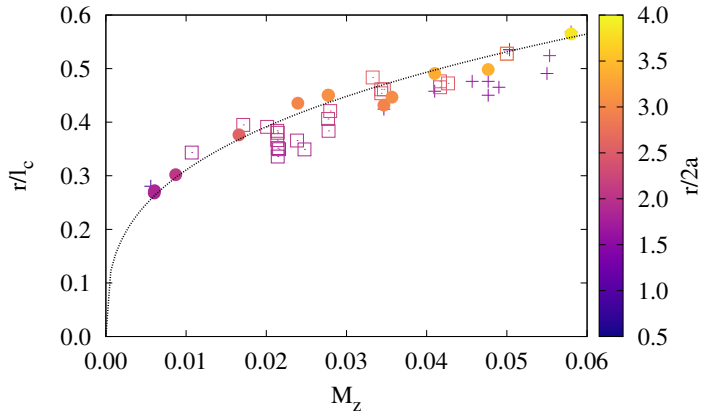


**Figure 6.4:** Interdistance $\bar{r}^{\star} = |\vec{r}|/l_c$ between a pair of identical beads as a function of the magnetocapillary number $\mathcal{M}_z$ for different bead radii $a$. Points account for the experiments and the dotted line to Eq.(6.13): Squares $2a = 500\ \mu\text{m}$, Circles $2a = 397\ \mu\text{m}$ and Crosses $2a = 793\ \mu\text{m}$. The color of each point is directly related to the ratio $|\vec{r}|/2a$ which measure the validity of the capillary potential expression in Eq.(5.10). Experimental data has been provided by G. Grosjean.

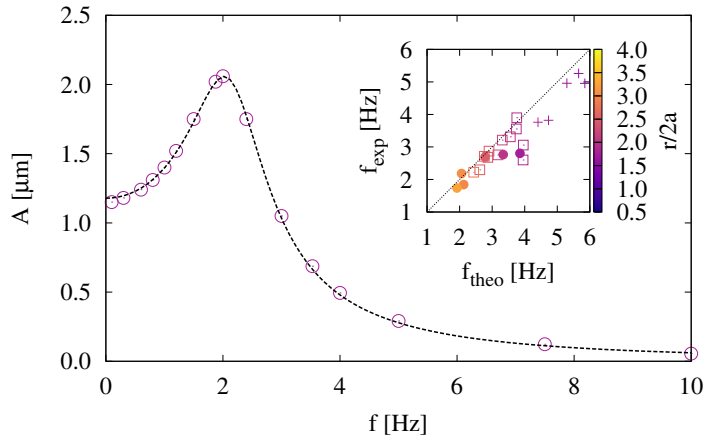


**Figure 6.5:** Amplitude of oscillation of a pair of beads submitted to a weak time-dependent oscillating field as a funciton of its frequency. Points account for experimental data while the dotted line corresponds to a resonant curve. The beads considered have a diameter $2a = 500\ \mu\text{m}$ and the fields are in the ratio $|\vec{B}_z|/|\vec{B}_x| = 2.4$. Errorbars on the amplitude are smaller than the point size. **(Inset)** Comparison between the measured natural frequency and the theoretical natural frequency given by Eq.(6.15). Different bead sizes are considered: Squares $2a = 500\ \mu\text{m}$, Circles $2a = 397\ \mu\text{m}$ and Crosses $2a = 793\ \mu\text{m}$. Points are colored depending on the value of $|\vec{r}|/2a$. Experimental data has been provided by G. Grosjean.

6.5 shows the amplitude of oscillation for a time-dependent fields of fixed amplitude as a function of the frequency. This analysis results in a resonance curve with a peak at $f \approx 2$ Hz. This curve can be fitted using the theory of forced linear oscillator. The result is given by the dotted gray line on the plot. The fitting procedure gives the natural frequency $f_{exp}$ and also the viscous damping time $\tau_v$ of the oscillator. The latter being defined by the ratio of the reduced mass of the system to the Stokes drag. Nevertheless, there is another significant information in this plot. Such a resonant curve is only observed for a linear forced oscillator with a relatively large damping time where the particles inertia plays a role. Indeed, the resonance peak in this case come from the inertia in the system. This observation can be counter-intuitive since we are dealing with low Reynolds number dynamics. The explanation comes from the difference that exists between the particles inertia, measured through the quality factor $Q = \omega_0 \tau_v/2$ and the fluid inertia measured through the Reynolds number defined in Eq.(5.3). Basically, the difference between each dimensionless number comes from the different density involved. As a consequence, one can have a low Reynolds dynamics where the flow inertia is negligible and a relatively high quality factor where the beads inertia becomes relevant. Finally, the inset of Fig.6.5 gives a comparison between the natural frequency measured experimentally and the theoretical frequency computed from Eq.(6.15). One sees that the theory captures correctly the experimental data. Once again, only particles with a small ratio $|\vec{r}|/2a$ deviate from the theory.

This section has given us the main properties of the magnetocapillary interaction. The magnetocapillary potential can be reduced to a linear spring potential with a natural frequency that depends on the radius on the beads involved. We have also seen that the particles inertia plays a significant role in the dynamics. Based on those observations, in the next section, we will try to build a minimal model for the microswimmer.

## 6.2 The inertial Najafi-Golestanian magnetocapillary microswimmer

Let us build a minimalist model. The approach is the following: the condition derived by Najafi and Golestanian (see Eq.(5.5)) was obtained through cinematic hypothesis. Indeed, they assumed the deformation of each arm of the structure without discussing their dynamical origin. Using this kinematic description and

the theory of hydrodynamic interaction, they obtained their formula expressing the speed of the swimmer. We aim here at filling the gap in this approach by discussing the system from a dynamic point of view. This approach will give a more realistic description of the swimmer deformation based on the properties of the magnetocapillary potential. Once the deformation is computed, the result will be used in the Golestanian condition in order to obtain the swimming velocity of the magnetocapillary swimmer. In the forthcoming section, we first develop the model then compare it with the experiments performed by Galien Grosjean at Liege University. The validity of each hypothesis is then discussed and aberrant behaviours are highlighted.

### 6.2.1 A dynamical minimalist model

Given the results of the linear analysis, we can describe the Najafi-Golestanian microswimmer as three beads linked by two different hookian springs of stiffness $k_a$ and $k_b$ and having an identical rest length $L = |\vec{r}|$. The beads are at position $x_1$, $x_2$ and $x_3$ respectively. The asymmetry of the three-beads swimmer is only taken into account in the stiffness of the springs. As a consequence, for the sake of mathematical simplicity, we assume the beads to be identical. Therefore the mass $m$ are identical as well as the Stokes damping factor $\mu = 6\pi\eta a$. Note that three beads are the minimal number required, only two beads won't swim in virtue of the Scallop theorem. Following this idea of a minimal model, the Stokeslet is removed from the analysis, since the hydrodynamic interactions are already integrated in the Golestanian condition. We will seek for the mathematical expressions of the elongation $(x_2 - x_1 - L)$ and $(x_3 - x_2 - L)$ and use them in the Najafi-Golestanian condition in Eq.(5.5). Note that the validity of those approximations will be discussed later in this chapter. The beads are also submitted to an external forcing $F\sin(\omega t)$ which originates from the magnetic dipole-dipole interaction. Given all those assumptions, including the beads inertia observed in Fig.6.5, the Newton equation for each bead writes

$$\begin{aligned} m\ddot{x}_1 + \mu\dot{x}_1 - k_a(x_2 - x_1 - L) &= -F\sin(\omega t), \\ m\ddot{x}_2 + \mu\dot{x}_2 + k_a(x_2 - x_1 - L) - k_b(x_3 - x_2 - L) &= 0, \\ m\ddot{x}_3 + \mu\dot{x}_3 + k_b(x_3 - x_2 - L) &= F\sin(\omega t), \end{aligned} \tag{6.16}$$

It is worth noticing that no net force acts on the fluid. Indeed, each force cancels another in this set of equations. This corresponds to the idea of an actual

swimmer which only moves itself in the fluid by inducing flows in the bulk. As a consequence, there is no Stokeslet generated in average by the swimmer over a cycle of deformation. We now study the oscillators in terms of the elongations $y_a = m\omega^2(x_2 - x_1 - L)/F$ and $y_b = m\omega^2(x_3 - x_2 - L)/F$. In order to suppress redundant parameters, the equations are considered in dimensionless form. Defining $\underline{t} = \omega t$, $\Omega_a^2 = k_a/m\omega^2$, $\Omega_b^2 = k_b/m\omega^2$ and $\beta = \mu/2m\omega$, one has

$$\begin{aligned} \dddot{\overline{y}}_a + 2\beta\ddot{\overline{y}}_a + 2\Omega_a^2\dot{y}_a - \Omega_b^2\dot{y}_b &= \sin(\underline{t}), \\ \dddot{\overline{y}}_b + 2\beta\ddot{\overline{y}}_b + 2\Omega_b^2\dot{y}_b - \Omega_a^2\dot{y}_b &= \sin(\underline{t}). \end{aligned} \tag{6.17}$$

This system can easily be solved in Fourier space. Defining the Fourier transform $\hat{y}_i$, $i = \{a, b\}$ as

$$\begin{aligned} \hat{y}_i &= \int_{-\infty}^{\infty} y_i(\underline{t}) e^{i\underline{\omega}\underline{t}} d\underline{t}, \\ y_i &= \frac{1}{2\pi}\int_{-\infty}^{\infty} \hat{y}_i(\underline{\omega}) e^{-i\underline{\omega}\underline{t}} d\underline{\omega}, \end{aligned} \tag{6.18}$$

one has the following set of algebraic equations

$$\begin{aligned} -\underline{\omega}^2\hat{y}_a + 2i\underline{\omega}\beta\hat{y}_a + 2\Omega_a^2\hat{y}_a - \Omega_b^2\hat{y}_b &= \frac{1}{2i}\left(\delta(\underline{\omega}+1) - \delta(\underline{\omega}-1)\right), \\ -\underline{\omega}^2\hat{y}_b + 2i\underline{\omega}\beta\hat{y}_b + 2\Omega_b^2\hat{y}_b - \Omega_a^2\hat{y}_a &= \frac{1}{2i}\left(\delta(\underline{\omega}+1) - \delta(\underline{\omega}-1)\right). \end{aligned} \tag{6.19}$$

Given the delta functions, only two frequencies remain in the Fourier transform, namely $\underline{\omega} = \pm 1$. The corresponding amplitude are

$$\begin{aligned} \hat{y}_a^{\pm} &= \frac{\left(3\Omega_b^2 - 1\right) \pm 2i\beta}{\Omega_a^2\Omega_b^2 - \left((2\Omega_a^2 - 1) \pm 2i\beta\right)\left(\left(2\Omega_b^2 - 1\right) \pm 2i\beta\right)} = \rho_a e^{\pm i\phi_a} \\ \hat{y}_b^{\pm} &= \frac{\left(3\Omega_a^2 - 1\right) \pm 2i\beta}{\Omega_a^2\Omega_b^2 - \left((2\Omega_a^2 - 1) \pm 2i\beta\right)\left(\left(2\Omega_b^2 - 1\right) \pm 2i\beta\right)} = \rho_b e^{\pm i\phi_b} \end{aligned} \tag{6.20}$$

where $\hat{y}_i^+ = \hat{y}_i^{-\dagger}$. After inverse Fourier transform, the elongation $y_a$ and $y_b$ are given by

$$y_a = \frac{\hat{y}_a^+ e^{i\underline{t}} - \hat{y}_a^- e^{-i\underline{t}}}{2i} = \rho_a \sin\left(\underline{t} - \phi_a\right)$$
$$y_b = \frac{\hat{y}_b^+ e^{i\underline{t}} - \hat{y}_b^- e^{-i\underline{t}}}{2i} = \rho_b \sin\left(\underline{t} - \phi_b\right) \tag{6.21}$$

Given the solutions for the elongation in Eq.(6.21), one can analyse the swimming dynamics of the swimmer. Before computing the swimming speed, we focus on the non-reciprocal deformation of the swimmer by considering its trajectory in the $(y_a, y_b)$ phase space. This result can be found in Fig.6.6 for both the experiments and the theory. The theoretical frequencies $\Omega_a$ and $\Omega_b$ are calculated considering the frequencies extracted at the end of Section 6.1.2. Four frequencies of oscillating field are considered: $f = 0.3$ Hz, $f = 1.5$ Hz, $f = 3.0$ Hz and $f = 4.0$ Hz. One sees that both experimentally and theoretically, an open cycle can be seen, testifying of the non-reciprocal deformation, as discussed in Section 5.1.1. One sees that the cycle is closed for the lowest frequency and open for increasing frequencies. For the highest frequency, the cycle is seen to close again. Beside, the oscillations amplitude is seen to decrease after $f = 1.5$ Hz as expected from the theory of forced oscillator. Finally, one sees that the experimental cycles are well reproduced by the thoery. Only the highest frequency shows some difference which might be due to the effect of the fluid inertia in the experiment because of the high frequency of the oscillating field which is not taken into account in the theory. Given this proof of concept, let us consider the swimming velocity of the magnetocapillary self-assembly.

We know that non-reciprocal deformation is possible. Therefore, let us consider the formula derived by Golestanian [71]. He demonstrated that the velocity of the swimmer is given by

$$\underline{\mathcal{V}} = \lim_{\Delta\underline{t}\to\infty} \frac{\kappa}{2\Delta\underline{t}} \int_0^{\Delta\underline{t}} \left(y_a \overline{y}_b - \overline{y}_a y_b\right) d\underline{t}. \tag{6.22}$$

where $\kappa$ is a geometric factor. In the case of spheres, it expresses as

$$\kappa = \frac{3a_1a_2a_3}{\left(a_1+a_2+a_3\right)^2} \left(\frac{1}{L_a^2} + \frac{1}{L_b^2} - \frac{1}{\left(L_a+L_b\right)^2}\right), \tag{6.23}$$

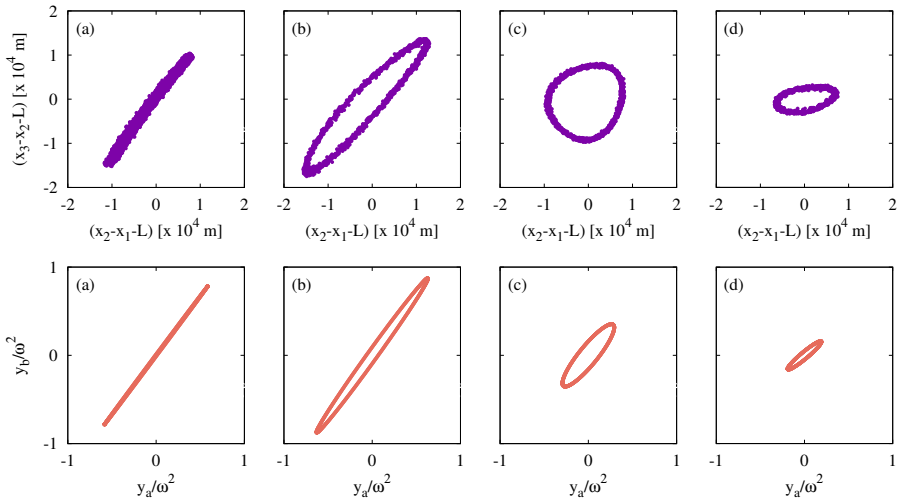


**Figure 6.6:** Deformation of the Najafi-Golestanian microswimmer in the configuration space. Each column accounts for a different frequency: **(a)** $f = 0.3$ Hz, **(b)** $f = 1.5$ Hz, **(c)** $f = 3.0$ Hz and **(d)** $f = 4.0$ Hz. Experiments **(top)** and theory **(bottom)** are considered. Values required for the theoretical curves has been obtained from experiment, leaving no free parameter. Despite differences at high frequency, one sees that the model reproduces correctly the dynamics for low frequency. Experimental data has been provided by G. Grosjean.

where $L_a$ and $L_b$ are the natural length of each oscillator, identical in our case by hypothesis. Injecting the solution obtained previously in Eq.(6.21), one gets

$$\begin{aligned} \underline{\mathcal{V}} &= \frac{\kappa}{4i}\left(\hat{y}_a^+ \hat{y}_b^- - \hat{y}_a^- \hat{y}_b^+\right) \\ &= \frac{\kappa}{2}\underbrace{\mathrm{Im}\left(\hat{y}_a^+ \hat{y}_b^{+\dagger}\right)}_{\mathcal{W}}. \end{aligned} \tag{6.24}$$

This last relation can be developed further in order to recover the condition required for non reciprocity, namely

$$\mathrm{Im}\left(\hat{y}_a^+ \hat{y}_b^{+\dagger}\right) = \rho_a \rho_b \sin\left(\phi_b - \phi_a\right). \tag{6.25}$$

By analogy with Thermodynamics, we refer to the quantity $\rho_a \rho_b \sin\left(\phi_b - \phi_a\right)$ as the "work" $\mathcal{W}$ performed by the system in order to achieve propulsion. This quantity measures the area of the ellipsis in the $(y_a, y_b)$-plane. As it can be seen, the swimming velocity is related to the Fourier coefficients $\hat{y}_a^+$ and $\hat{y}_b^+$.

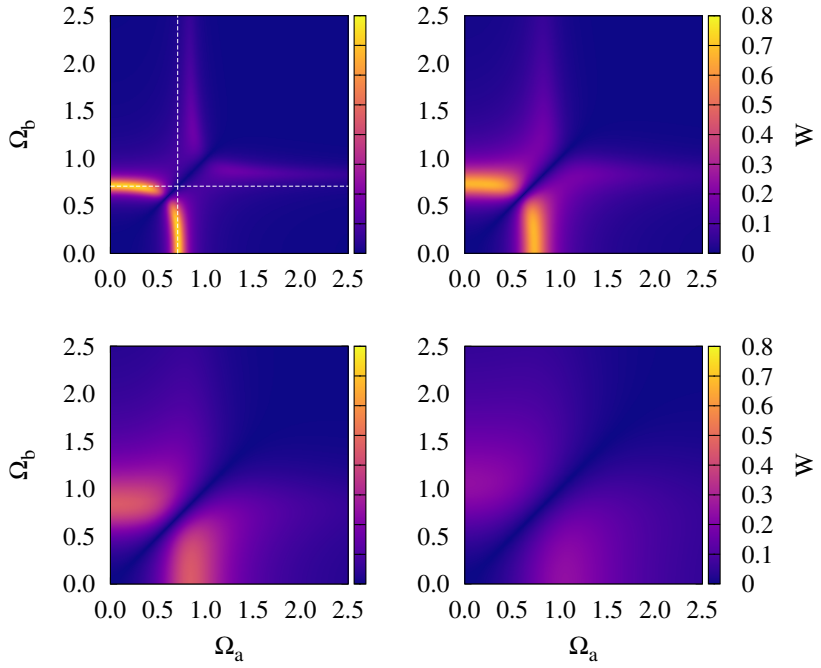


**Figure 6.7:** Work $\mathcal{W}$ as a function of the dimensionless frequencies $\Omega_a$ and $\Omega_b$ for different values of the dimensionless dissipation $\beta$. **(a)** $\beta = 0.1$, **(b)** $\beta = 0.2$, **(c)** $\beta = 0.5$ and **(d)** $\beta = 1.0$. Dashed white lines account for the two resonances observed Eq.(6.26). Note that the bissectrix of each plot corresponds to a line of zero velocity since the swimmer becomes reciprocal. One observes that, as the dissipation increases, the resonance peaks widen and decrease in amplitude.

Developing this expression gives the velocity as a function of the parameters of the Najafi-Golestanian micro-swimmer, namely the dimensionless frequencies $\Omega_a$ and $\Omega_b$ and the dimensionless friction parameter $\beta$

$$\underline{\mathcal{V}} = \frac{\kappa}{2} \frac{6\beta \left(\Omega_b^2 - \Omega_a^2\right)}{\left|\Omega_a^2\Omega_b^2 - \left((2\Omega_a^2 - 1) + 2i\beta\right)\left(\left(2\Omega_b^2 - 1\right) + 2i\beta\right)\right|^2}. \tag{6.26}$$

Restoring dimensioned quantities, one obtains

$$\mathcal{V} = \frac{\kappa}{2} \frac{3\mu F^2 \omega^2 \left(k_b - k_a\right)}{\left|k_a k_b - \left((2k_a - m\omega^2) + i\mu\omega\right)\left((2k_b - m\omega^2) + i\mu\omega\right)\right|^2} \tag{6.27}$$

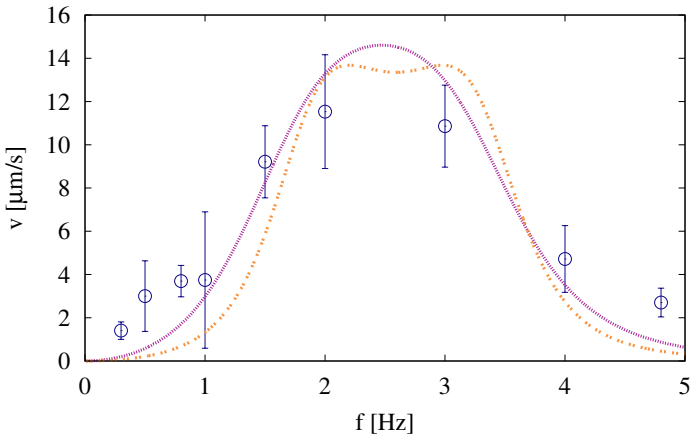


**Figure 6.8:** Speed of the Najafi-Golestanian microswimmer as a function of the frequency of the oscillating field. Both experiment (blue circles) and theory (orange and purple dashed lines) are displayed. Experiments have been done for beads with diameters $2a = 500\ \mu\text{m}$, $500\ \mu\text{m}$ and $397\ \mu\text{m}$ with fields of intensity $|\vec{B}_z| = 4.5\ \text{mT}$ , $|\vec{B}_x| = 2.2\ \text{mT}$ and $|\vec{B}_{osc}| = 0.5\ \text{mT}$. Each point is the average over three independant experiments. Errorbars correspond to the standard deviation around those average values. Theory has been calibrated on Grosjean's experiments, using the value given in Ref.[75]. The two dashed line account for the two damping experienced by the beads given their size. Purple: $2a = 397\ \mu\text{m}$, Orange: $2a = 500\ \mu\text{m}$. Only one fitting parameter is used which is the amplitude of the velocity. Experimental data has been provided by G. Grosjean.

The modulus of Eq.(6.26) is illustrated in Fig.6.7 for four values of $\beta$, and is plotted with a color map as a function of $\Omega_a$ and $\Omega_b$. The same colour code is used for each subplot to allow comparison. One sees that the line $\Omega_a = \Omega_b$ defines a mirror symmetry in the function. It finds its source in the $a \rightleftharpoons b$ anti-symmetry in the $\mathcal{V}$ formula. Changing $\Omega_a$ to $\Omega_b$ and in return changing $\Omega_b$ to $\Omega_a$ simply change the orientation of the swimmer. As a consequence, the swimmer swims at the same speed but in the opposite direction. Resonance curves can also be seen in each subplot. They widen and decrease in amplitude as the damping becomes more important. Those resonance curves are highlighted with white dashed lines in Fig.6.7(a). The position of those curves can be easily found from Eq.(6.26). Cancelling each factor in the denominator leads to the following resonance curves: $\Omega_a = 1/\sqrt{2}$ and $\Omega_b = 1/\sqrt{2}$.

Let us now compare the model to the velocity measured in experiments. Figure 6.8 gives the speed of the Najagi-Golestanian microswimmer as a function of

the frequency of the oscillating field $f = \omega/2\pi$. Experimental data have been provided by Galien Grosjean from Liege University. As a remainder, for the experimental measurements in this figure, the vertical field magnitude is set to $|\vec{B}_z| = 4.5$ mT. The offset field is set to $|\vec{B}_x| = 2.2$ mT while the oscillating field is set to $|\vec{B}_{osc}| = 0.5$ mT. In order to induce the asymmetry required for the non-reciprocal deformation, three beads of different radii are considered. One has two beads of diameter $2a = 500$ $\mu$m and one bead of diameter $2a = 397$ $\mu$m on the extremity of the linear structure in order to assure spatial asymmetry. This leads to two different natural frequencies for the two bonds between each pair of particles. One has experimentally $f_a = 1.810$ Hz and $f_b = 2.093$ Hz, the latter being the natural frequency of the asymmetric pair. In order to fit Eq.(6.27) onto the experimental data, one needs the prefactor $\kappa F^2/m^2$ and the dissipation coefficient $\beta$. The latter can be easily computed given the expression of the Stokes drag. One has for $500$ $\mu$m-beads $\mu/m = 9.195$ and for $397$ $\mu$m-beads $\mu/m = 14.586$. The parameter $\kappa F^2$ will be used as the unique fitting parameter and corresponds to the vertical scaling of the fit. The theoretical model corresponds to the dashed lines in Fig.6.8. Two curves are displayed because of the two values possible for $\beta$. Indeed, the model considers an identical damping acting on each bead for the sake of simplicity. The two curves account for the damping experienced by each type of beads. The "correct" behaviour is expected to be situated in between those two extreme curves. One observes from the figure that the theory is in good agreement with the experimental data. The velocity increases, reaches a plateau where resonance takes place and finally decreases towards zero. One can explain the origin of the plateau from the theoretical curves. Indeed, for the lowest damped case, the plateau shows two maxima which come from the resonance of each oscillator at $\Omega_a = 1/\sqrt{2}$ and $\Omega_b = 1/\sqrt{2}$. In dimensioned units, those two conditions read $f = \sqrt{2}f_a = 2.560$ Hz and $f = \sqrt{2}f_a = 2.960$ Hz which corresponds to the location of the two maxima.

As stated in the beginning of this section, an important assumption has been made in this calculation. The hydrodynamic interaction has been removed from Newton's equation and only considered "artificially" using the Golestanian condition. In order to discuss the validity of this approximation, in the next section, we compare our model with an already existing one.

### 6.2.2 The overdamped limit

To our knowledge, there is no theoretical formalism for the inclusion of the particles inertia in the Najafi-Golestanian microswimmer and, more generally, in any microswimmer model. The only exception is the numerical work done by Pickl *et al.* including numerically the beads inertia in their simulations [143]. In order to justify our approach, we decide to consider our model in the overdamped limit, namely $m \to 0$. This limit was considered by Pande *et al.* in [131]. Solving the dynamics by integrating hydrodynamic interactions through the Oseen tensor (see Appendix B), they computed the swimmer velocity as a function of its parameters. The authors obtained, in the case of forces of same amplitude without phase shift,

$$\mathcal{V}_o = \frac{7a^2\pi\omega^2\eta F^2\left(k_a - k_b\right)}{4L^2\left(k_a^2k_b^2 + 8\pi^2\omega^2\eta^2a^2\left(2k_a^2 + 2k_b^2 + k_ak_b + 18\pi^2\omega^2\eta^2a^2\right)\right)} \tag{6.28}$$

where $\mathcal{V}_o$ refers to their solution, obtained with the Oseen tensor. In this expression, $\eta = \mu/6\pi a$ comes from the Stokes drag coefficient $\mu$ and corresponds to the water dynamical viscosity already defined in Eq.(6.16).

Given this point of comparison, the same analysis is performed with our model. This approach will give a velocity $\mathcal{V}$ which can be compared with $\mathcal{V}_o$. The mismatch between each result is expected to give a measure of the error made. In the $m \to 0$ case, the equations of the dynamics read

$$\begin{aligned}
&\mu\dot{x}_1 - k_a\left(x_2 - x_1 - L\right) = -F\sin\left(\omega t\right),\\
&\mu\dot{x}_2 + k_a\left(x_2 - x_1 - L\right) - k_b\left(x_3 - x_2 - L\right) = 0,\\
&\mu\dot{x}_3 + k_b\left(x_3 - x_2 - L\right) = F\sin\left(\omega t\right).
\end{aligned} \tag{6.29}$$

We define the following dimensionless quantities: $\underline{t} = \omega t$, $\Omega'_a = k_a/\mu\omega$, $\Omega'_b = k_b/\mu\omega$, $y_a = (x_2 - x_1 - L)\omega\mu/F$ and $y_b = (x_3 - x_2 - L)\omega\mu/F$. The dimensionless equations are therefore given by

$$\begin{aligned}
&\overline{y}_a + 2\Omega'_a y_a - \Omega'_b y_b = \sin\left(\underline{t}\right),\\
&\overline{y}_b + 2\Omega'_b y_b - \Omega'_a y_b = \sin\left(\underline{t}\right).
\end{aligned} \tag{6.30}$$

The corresponding Fourier coefficients are found using the same calculus than for

the inertial case and write

$$\hat{y}_a^+ = \frac{3\Omega'_b \pm i}{3\Omega'_a\Omega'_b \pm 2i\left(\Omega'_a + \Omega'_b\right) - 1},$$
$$\hat{y}_b^+ = \frac{3\Omega'_a \pm i}{3\Omega'_a\Omega'_b \pm 2i\left(\Omega'_a + \Omega'_b\right) - 1}. \tag{6.31}$$

Knowing the Fourier coefficients, the velocity is computed using Eq.(6.22). Bringing back dimensioned quantities, the velocity reads

$$\mathcal{V} = \frac{\kappa}{2}\frac{F^2}{\mu^2\omega}\mathrm{Im}\left(\hat{y}_a^+\hat{y}_b^{+\dagger}\right). \tag{6.32}$$

Developing this expression further gives

$$\mathcal{V} = \frac{7a^2\pi\omega^2\eta F^2\left(k_a - k_b\right)}{4L^2\left(k_a^2k_b^2 + 8\pi^2\omega^2\eta^2a^2\left(2k_a^2 + 2k_b^2 + k_ak_b + 18\pi^2\omega^2\eta^2a^2\right)\right)}, \tag{6.33}$$
$$= \mathcal{V}_o. \tag{6.34}$$

It is surprising to observe that the hydrodynamic approach based on the Oseen tensor [131] and our model coincide perfectly. This observation can find some explanation in the article of Felderhof [56]. In his article, he discussed a theory of $N$ beads submitted to one-body forces and two-body forces. As an example, the former would be the $\sin(\omega t)$ force in our model and the latter the spring force acting between two spheres. Felderhof assumed that the motion of each bead around its initial position can be described, in the long term dynamics, by two contributions: a cyclic perturbation $\xi(t)$ and a net translation due to hydrodynamic interactions $\mathcal{V}_o t$. He showed that the time evolution of the perturbation $\xi(t)$ can be made independent of the speed $\mathcal{V}_o$ from a discussion based on the different order of a Taylor expansion. The time evolution of the perturbation $\xi(t)$ belongs to the first order of the expansion while the speed $\mathcal{V}_o$ belongs to the second order. The idea behind his model is to solve the first order of the dynamics and access the $\xi(t)$ before solving the speed $\mathcal{V}_o$. In our model, the idea is essentially the same: the elongation $y_a$ and $y_b$ are solved before considering the velocity and using the Golestanian condition.

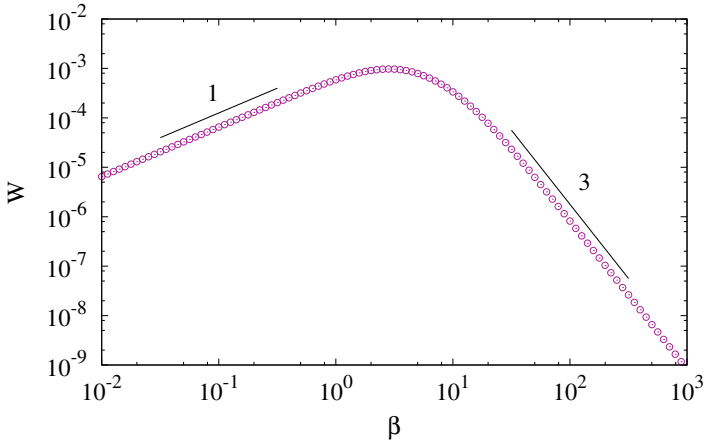


**Figure 6.9:** Evolution of the ``work'' $\mathcal{W}$ as a function of the dissipation coefficient $\beta$ for $f_a = 2.96$ Hz, $f_b = 2.56$ Hz and $f = 1$ Hz. Double logarithmic scale has been used to evidence power laws. For low viscosities, $\mathcal{W}$ increases linearly with $\beta$ as the phase shift increases between the two deformations. For large viscosities, the work $\mathcal{W}$ decreases as $\beta^{-3}$. This is due to the limited deformation of the arms because of viscous effects.

### 6.2.3 Optimisation and aberrant behaviours

Since Pande's model and our approach give the same velocity in the overdamped limit, the properties of the former model are expected to be seen in the latter. Pande's model is known to behave unintuitively when changing the viscosity of the surrounding medium. For high viscosities the swimmer velocity decreases with increasing viscosity while for low viscosities the velocity is seen to increase for increasing viscosity. The former case has been referred to as *conventional regime* while the latter corresponds to the *aberrant regime* [131]. This kind of unintuitive behavior was observed in microbiology with the dynamics of bacteria in viscous, gel-like media [12, 158]. Let us consider the inertial model in Eq.(6.27) to see if the aberrant regime holds.

Considering the case of large viscosity, one obtains

$$\beta \gg 1 \quad \Rightarrow \quad \mathcal{V} \propto \beta^{-3}, \tag{6.35}$$

while low viscosity gives

$$\beta \ll 1 \quad \Rightarrow \quad \mathcal{V} \propto \beta. \tag{6.36}$$

Those limits correspond to the scaling observed by Pande *et al.* [131] in the over-damped limit with the Oseen tensor approach. As a consequence of those two limits, it is expected to observe a global maximum in the function $\mathcal{V}(\beta)$. Pande *et al.* discussed this dynamics in terms of a ratio of time scale. They defined $\Gamma$ as the ratio between the relaxation time scale, which measures the time required for the beads to reach instantaneous equilibrium and the swimming cycle which corresponds to the period of a swimming stroke. They argue that, for $\Gamma \gg 1$, the beads cannot reach equilibrium during a swimming stroke. Increasing $\beta$ in this limit reduces the amplitude of oscillation which, as a consequence, decreases the velocity. For $\Gamma \ll 1$, an increase of viscosity $\beta$ does not change the amplitude since the beads are in equilibrium with the external forcing at each instant. The increase of speed comes from the hydrodynamic coupling which increases with the viscosity (see Appendix B). It is interesting to observe that our approach does not consider explicitly the hydrodynamic interactions but only the condition of non-reciprocity with Eq.(6.22). Yet, the increasing velocity for small increasing viscosity is recovered. Since our model gives easily access to the elongation, let us study this property deeper.

The key to locomotion is the work $\mathcal{W} = \mathrm{Im}(y_a^+ y_b^-) = \rho_a \rho_b \sin(\phi_b - \phi_a)$ which measures the non-reciprocity in the dynamics. Equations (6.20) give the evolution of the amplitude $\rho_a$ and $\rho_b$. The following scaling are observed

$$\begin{aligned} \beta \ll 1 \quad &\Rightarrow \quad \rho_i \propto 1, \\ \beta \gg 1 \quad &\Rightarrow \quad \rho_i \propto \beta^{-1}, \end{aligned} \tag{6.37}$$

where $i = \{a, b\}$. Those two dependencies correspond indeed to the interpretations made by Pande *et al.*. Low viscosities do not alter the amplitude. High viscosities decrease the amplitude since the beads cannot follow the external forcing. Simply considering those last results does not explain neither the conventional nor the aberrant evolution of the velocity $\mathcal{V}$. The last ingredient defining the work $\mathcal{W}$ is the phase shift $\sin(\phi_b - \phi_a)$. One can easily show that

$$\tan(\phi_b - \phi_a) = \frac{6\beta\left(\Omega_b^2 - \Omega_a^2\right)}{\left(3\Omega_a^2 - 1\right)\left(3\Omega_b^2 - 1\right) + 4\beta^2} \tag{6.38}$$

which gives the following asymptotic behaviours

$$\begin{aligned} \beta \ll 1 \quad &\Rightarrow \quad \tan\left(\phi_b - \phi_a\right) \propto \beta, \\ \beta \gg 1 \quad &\Rightarrow \quad \tan\left(\phi_b - \phi_a\right) \propto \beta^{-1}. \end{aligned} \tag{6.39}$$

Since $\sin(x) = \tan(x) + \mathcal{O}(x^3)$, those scalings hold for the sine of the phase shift. As a consequence, the conventional and aberrant dynamics of the swimmer comes from the phase shift induced dynamically in the system. It increases for small increasing viscosity, increasing the swimming efficiency in return. For large increasing viscosities, the phase shift decreases towards zero, breaking the non-reciprocity condition.

## 6.3 Conclusion

This chapter was dedicated to the theoretical investigation of the experimental Najafi-Golestanian microswimmer. We focused on the condition required in order to achieve a non-reciprocal deformation of the microswimmer. Analysing the magnetcapillary potential, a condition has been founds. This microswimmer has to be made of three beads of different radii in order to break the spatial symmetry of the swimmer. Under a time-dependent external field, the two halves of this swimmer does not oscillates identically. Both oscillations occur at the same frequency but not with the same phase shift relative to the external perturbation. As a consequence, non-reciprocity is achieved and a translation of the swimmer can be seen on the interface.

In order to build a minimalist model, we have mixed the Golestanian's kinematic approach with a dynamical investigation of the deformation. This dynamical model considers the beads inertia and no hydrodynamic coupling. The interaction between the beads are made linear. In this hybrid approach, the deformation of the swimmer is solved beforehand and then injected in the Golestanian condition. This method reproduce correctly the experimental findings, both in terms of deformation cycle and swimmer velocity. Our hybrid model have been compared to an exact solution of the dynamics through the Oseen tensor in the overdamped limit. The two approaches gives identical results which testify of the validity of our approach. As a consequence of those results, our hybrid model could lead

to way for the investigation of the role of the particle inertia in microswimmers.

# 7

# Three-beads magnetocapillary microswimmer

*As stated at the beginning of this part, soft ferromagnetic beads pinned at an air-water interface can move spontaneously along the interface once submitted to time dependent magnetic fields. The three-beads dynamics, the simplest magnetocapillary microswimmer able to swim* [111]*, has been largely studied experimentally* [111, 77]*. Yet, it remains a theoretical* [27] *and numerical challenge* [168]*. In this chapter, we will isolate the key mechanism giving rise to the swimming dynamics, namely the individual beads rotation. From this observation, numerical simulations are performed in order to investigate systematically the swimming dynamics. A minimalist model is proposed to explained the observations made from the numerics.*

## 7.1 Seeking non-reciprocity

Before developing a theoretical model for the triangular swimmer presented in Chapter 5, the experiments are briefly described and the main results are discussed. Based on the experiments, numerical simulations are performed.

### 7.1.1 Experimental background

Let us give some experimental background to this section. Experiments involving the triangular swimmer have been performed by Galien Grosjean from Liege Uni-

versity and are fully described in [77]. The beads considered through this chapter have a diameter $2a = 500$ m. They have strong ferromagnetic properties as described previously in chapter 5 and 6. The beads are placed at an air-water interface and float thanks to their wetting properties. Three magnetic fields are applied to the system in order to counterbalance the capillary attraction and in order to generate the non-reciprocal deformation. Those magnetic fields are generated by three sets of Helmholtz coils as depicted in Fig.5.4. The vertical field has an amplitude ranging in $|\vec{B}_z| \in [3, 10]$ mT. The two other fields are horizontal, one is constant and the other is time-dependent. The constant field, named "offset", defines the $x$-axis in the experiments. Its amplitude ranges in $|\vec{B}_x| \in [0, 1]$ mT. Given its small amplitude compared to the vertical field, isosceles triangles are seen instead of linear structures. The purpose of this field is to ensure reproducible experiments [77]. The time-dependent field is applied with an angle $\alpha$ relative to $\vec{B}_x$. This field varies sinusoidally in time with a frequency $f \in [0.1, 3]$ Hz and with a peak amplitude $|\vec{B}_x| \in [0, 2]$ mT. This field is responsible of the non-reciprocal deformation required for low-Reynolds number swimming. All those fields are illustrated in Fig.7.1. Mathematically, the total magnetic field $\vec{B}(t)$ writes

$$\begin{aligned}\vec{B}(t) = &\Big(|\vec{B}_x| + |\vec{B}_{osc}| \cos\alpha \cos(\omega t)\Big)\, \vec{e}_x \\ &+ |\vec{B}_{osc}| \sin\alpha \cos(\omega t) \vec{e}_y \\ &+ |\vec{B}_z| \vec{e}_z, \end{aligned} \tag{7.1}$$

with $\omega = 2\pi f$. A typical experimental result is given in Fig.7.2 for three beads and illustrates the deformation sequence of the swimmer. Two degrees of freedom are involved: the deformation of the triangle and the oscillation of the self-organized structure. Figure 7.2(a) shows the value of the internal angles of the triangle $\alpha_i$ as a function of time. Each colour corresponds to different vertex. Orange areas indicate "platy" isosceles triangles with two angles $\alpha_i < 60$ and one angle $\alpha_i > 60$. Yellow areas account for "pointy" isosceles triangles with two angles $\alpha_i > 60$ and one angle $\alpha_i < 60$. In Fig.7.2(b), the rotation of the structure is recorded as a function of time around its equilibrium angle. It shows a sinusoidal oscillation in quadrature with the oscillation from "platy" to "pointy" isosceles. According the Golestanian condition of non-reciprocity in Eq.(5.5), one might expect those two degrees of freedom to make the non-palindromic sequence of defor-

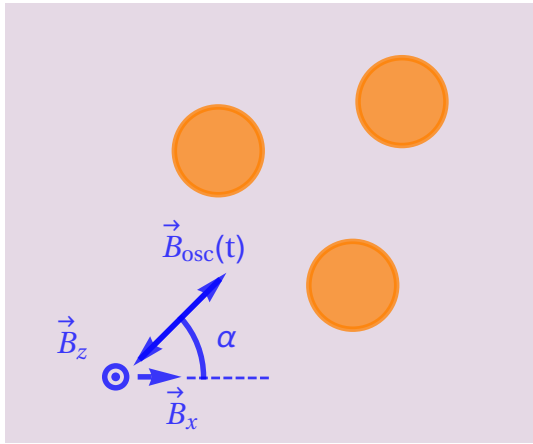


**Figure 7.1:** Schematic of the fields used in the experiments. The three beads are submitted to a vertical constant field $\vec{B}_z$ in order to overcome the capillary attraction. A small amplitude constant field $\vec{B}_x$ ensures the reproductibility of the experiments. Finally a time-dependent field $\vec{B}_{osc}(t)$ is applied with an angle $\alpha$ relative to $\vec{B}_x$.

mation responsible of the swimming dynamics. This non-reciprocal sequence is illustrated schematically in Fig.7.2(c). Under those conditions, the swimmer can reach speed of about one sphere radius per period of the external field ($\mathcal{V} = af$) which leads to Reynolds number $\mathrm{Re} < 10^{-1}$ for a typical frequency $f = 1$ Hz.

## 7.2 Numerical simulations of magnetocapillary swimmers

An attempt of numerical simulations have been made by Harting and his team using Lattice-Boltzmann simulations [168]. This numerical method aims at solving a fluid dynamics using a coarse-grained approach on a given lattice [155]. This method allows for solving the fluid dynamics as well as the particles swimming motion and the surface deformation. Nevertheless, the precision of this method is comparable to the massive amount of numerical resources it requires. In order to allow for an extensive study of the triangular swimmer dynamics, we develop a force-based method where all interactions, even hydrodynamic ones, are described by forces. This method is numerically cheaper and therefore gives the possibility to explore the parameter space extensively. Nevertheless, the information about the flow dynamic is lost in the process.

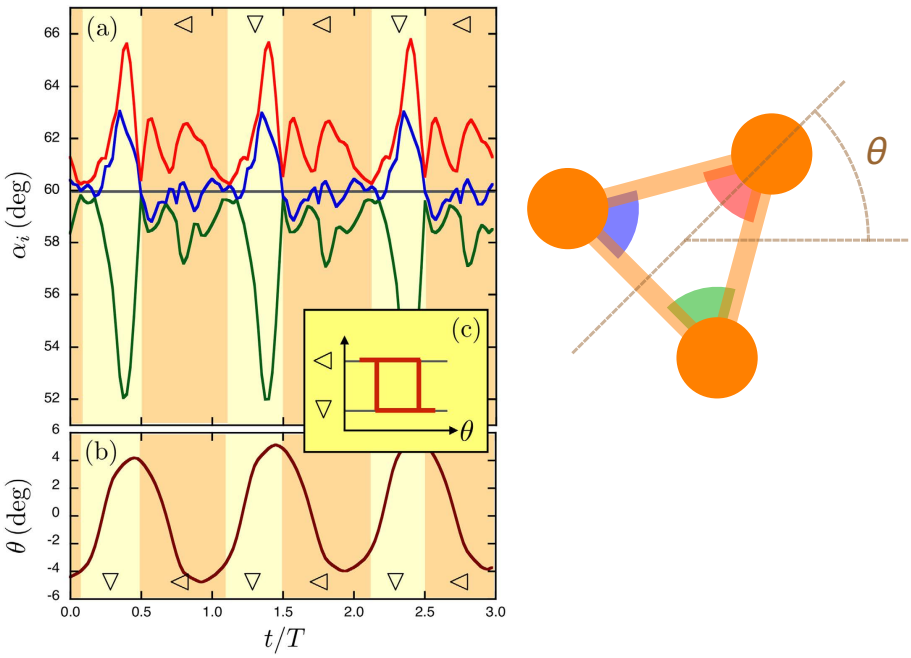


**Figure 7.2:** Experimental investigation of the triangular swimmer dynamics. **(a)** Deformation dynamics. Each colour corresponds to the value of a given vertex of the triangle. The color code is explained in the schematic in the right hand part of the figure. The triangle is seen to deform from a flat isosceles triangle (``platy'' isosceles) to a pointy isosceles triangle (``lepto'' isosceles). **(b)** Orientation of the swimmer as a function of time as defined in the right hand side of the figure. One sees that the deformation and the orientation are in quadrature of phase. **(c)** Schematic representation of the non-reciprocal deformation in the configuration space. An open cycle is clearly visible. Adapted from [77]

In the following, a brief description of the method is presented before giving some results provided by our numerical integration.

### 7.2.1 Building the numerics

Each bead is characterised by this radius $a_i$ and density $\rho$ which give their volume $V_i = 4\pi a_i^3/3$, their mass $m_i = 4\pi a_i^3 \rho/3$ and moment of inertia $I_i = 8\pi a_i^5 \rho/15$. Their capillary charge $q_i$ has been measured experimentally in order to compute the capillary attraction $\vec{F}_c$ between two beads $i$ and $j$ at the interface. The $q_i$'s values are stored in Tab.7.1. The total capillary attraction acting on particle $i$ from

all particles $j \neq i$ derives from the potential in Eq.(5.10) and writes

$$\begin{aligned}\vec{F}_{c,i}(\vec{r}_{ij}) &= -\sum_{i\neq j} \vec{\nabla} U_c(\vec{r}_{ij}), \\ &= -2\pi \frac{\sigma}{l_c} \sum_{i\neq j} q_i q_j K_1 \left( \frac{|\vec{r}_{ij}|}{l_c} \right) \frac{\vec{r}_{ij}}{|\vec{r}_{ij}|},\end{aligned} \tag{7.2}$$

where $\vec{r}_{ij} = \vec{r}_i - \vec{r}_j$ is the vector pointing from particle $j$ to particle $i$. Note that the superposition principle is used here. As already discussed in Chapter 5, this approximation is only valid for large distances between the beads.

The magnetic properties of the beads are known from Fig.5.7. The beads magnetization is given by

$$\vec{\mu}_i = \frac{4\pi a_i^3 \chi \vec{B}(t)}{3\mu_0} + \vec{\mu}_i^r, \tag{7.3}$$

with $\chi = 3$ and $|\vec{\mu}_i^r|$ given in Tab.7.1. The resulting magnetic dipole-dipole interaction derives from Eq.(5.11) and gives

$$\begin{aligned}\vec{F}_{m,i}(\vec{r}_{ij}) &= -\sum_{i\neq j} \vec{\nabla} U_m(\vec{r}_{ij}), \\ &= \frac{3\mu_0}{4\pi} \sum_{i\neq j} \left( \frac{(\vec{r}_{ij} \times \vec{\mu}_i) \times \vec{\mu}_j}{|\vec{r}_{ij}|^5} + \frac{(\vec{r}_{ij} \times \vec{\mu}_j) \times \vec{\mu}_i}{|\vec{r}_{ij}|^5} \right. \\ &\quad \left. - \frac{2\vec{r}_{ij}(\vec{\mu}_i . \vec{\mu}_j)}{|\vec{r}_{ij}|^5} + \frac{5\vec{r}_{ij}(\vec{r}_{ij} \times \vec{\mu}_i).(\vec{r}_{ij} \times \vec{\mu}_j)}{|\vec{r}_{ij}|^7} \right).\end{aligned} \tag{7.4}$$

Beside the magnetic force due to the dipole-dipole interaction, the beads are submitted to an external magnetic torque $\vec{\tau}_m$. It tends to align the remnant magnetic dipole of each bead with the external field. Note that this torque has no effect on the paramagnetic part of the magnetization since it is parallel to the external field $\vec{B}(t)$. Therefore, the torque writes

$$\vec{\tau}_{m,i} = \vec{\mu}_i^r \times \vec{B}(t). \tag{7.5}$$

We assume in this description that the remnant magnetization is fixed in the molecular lattice of the material. As a consequence, a change of orientation of the remnant magnetization will also lead to a rotation of the beads. This effect has been observed experimentally [74] and briefly described in [73]. The forces

and torques here above are the driving mechanisms of the dynamics. They are the means by which energy is injected to the microswimmer. The dissipation of this energy is due to the hydrodynamic interaction with the surrounding medium. Yet, the hydrodynamic interactions are also the means by which the motion of the swimmer is possible. Their description requires a brief discussion. It was shown in the previous chapter that the particle inertia plays a role in the deformation cycle. The hydrodynamic interaction as described in Appendix B does not consider such effect but only a perfectly overdamped regime. Nevertheless, even though the swimmer dynamics shows that inertia plays a role in experiment, we assume that a particle $j$ with velocity $\vec{v}_j$ interacts with a neighbouring particle $i$ at distance $\vec{r}_{ij}$ according to

$$\left(\vec{F}_i, \vec{\tau}_i\right) = \hat{\mu}_{ij}^{-1} \left(\vec{v}_j, \vec{\omega}_j\right), \tag{7.6}$$

where $\hat{\mu}_{ij}$ is the mobility matrix whose full expression is given in Appendix B. This approach describes the hydrodynamic interactions as forces related to the velocity of the other beads on the interface. In the context described in Appendix B, this leads to the following force

$$\begin{aligned}\vec{F}_{h,i} = \sum_{j\neq i} \Bigg\{ & \frac{9\pi\eta a_i a_j}{2|\vec{r}_{ij}|} \left(\hat{\mathbb{I}} + \frac{\vec{r}_{ij}\otimes\vec{r}_{ij}}{|\vec{r}_{ij}|^2}\right).\vec{v}_j \\ & + \frac{3\pi\eta a_i a_j (a_i^2 + a_j^2)}{2|\vec{r}_{ij}|^3} \left(\hat{\mathbb{I}} - 3\frac{\vec{r}_{ij}\otimes\vec{r}_{ij}}{|\vec{r}_{ij}|^2}\right).\vec{v}_j \\ & + \frac{6\pi\eta a_i a_j^3}{|\vec{r}_{ij}|^3} \left(\hat{\epsilon}.\vec{r}_{ij}\right).\vec{\omega}_j + \mathcal{O}\left(\frac{1}{|\vec{r}_{ij}|^4}\right) \Bigg\} \\ & - 6\pi\eta a_i \vec{v}_i \end{aligned} \tag{7.7}$$

where $\left(\hat{\epsilon}.\vec{r}_{ij}\right).\vec{\omega}_j = \vec{r}_{ij}\times\vec{\omega}_j$ and $\left(\vec{r}_{ij}\otimes\vec{r}_{ij}\right).\vec{v}_j = \vec{r}_{ij}(\vec{v}_j.\vec{r}_{ij})$. The two first terms correspond to the Translation/Translation (TT) coupling of the hydrodynamic interactions. The third term corresponds to the Rotation/Translation (RT) coupling. Note that we choose to limit ourselves to $\mathcal{O}(|\vec{r}_{ij}|^{-4})$. Indeed, beyond the third order in $|\vec{r}_{ij}|^{-1}$, triplet of beads are involved [114]. We choose to consider only pair interactions for the sake of simplicity. Regarding rotation, the hydrodynamic torque is simply given by

$$\vec{\tau}_{h,i} = -8\pi\eta a_i^3 \vec{\omega}_i. \tag{7.8}$$

| Diameter $2a$ ($\mu$m) | Cap. charge $q$ ($\mu$m) | Remnant magn. $\lvert\vec{\mu}^r\rvert$ (nA/m) |
|---|---|---|
| 397 | 6 | 1.1732 |
| 500 | 12 | 2.3437 |
| 793 | 45 | 9.3502 |

**Table 7.1:** Summary of the different properties of the beads used. Both the capillary charge $q$ and the remnant magnetization $|\vec{\mu}^r|$ are given

For the rotation dynamics, only the zeroth order in $|\vec{r}_{ij}|^{-1}$ is considered for simplifying further analytical investigations. Given those forces and torques, Newton's equations of motion write

$$m_i\dot{\vec{v}}_i + \vec{F}_{h,i} + \vec{F}_{c,i} + \vec{F}_{m,i} = 0, \tag{7.9}$$

$$I_i\dot{\vec{\omega}}_i + \vec{\tau}_{h,i} + \vec{\tau}_{m,i} = 0. \tag{7.10}$$

Since the beads are trapped at the air interface, the first equation is only considered in the $(x, y)$-plane while the second is only considered in the $z$-direction. In Eq.(7.9), one-body forces and two-body forces are considered. In Eq.(7.10), only one-body torques are taken into account.

Finally, the equations are integrated via a simple self-made Euler integration scheme in C/C++. The numerical stability of the equations has been verified in the case of the 3-beads dynamics, using an integration time step $\delta t_{simu} = 5\,10^{-4}/f$.

### 7.2.2 Results

Using the algorithm described in the previous section, one can now investigate the swimming dynamics numerically. We first show that the deformation of the triangle can be correctly reproduced and that the swimmer indeed swims along the interface. Figure 7.3 gives the deformation and the orientation of the triangle in numerics with parameters close to the one used for Fig.7.2. One sees from Fig.7.3(a) that the triangle again changes periodically from a platy-isosceles triangle to a lepto-isosceles triangle and vice-versa. In the meantime, the structure oscillates as depicted in Fig.7.3(b). Yet, some differences from the experiments are visible. Two angles have exactly the same value and the phase-shift between the deformation and the oscillation is not optimal in contrast with Fig.7.2. Nevertheless, the main features are reproduced. Beside those two ingredients, the

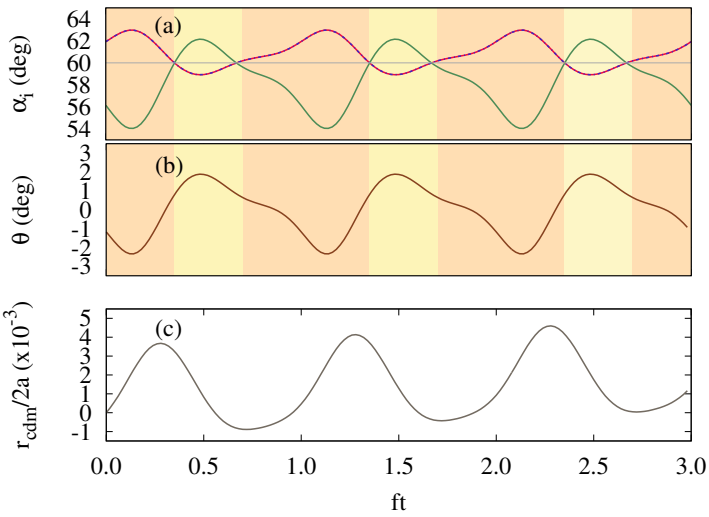


**Figure 7.3:** Swimming dynamics in numerical simulations. **(a)** Deformation as a function of the dimensionless time, **(b)** orientation, **(c)** center of mass translation. The simulation parameters are $|\vec{B}_z| = 3$ mT,$|\vec{B}_x| = 0.5$ mT, $|\vec{B}_{osc}| = 0.75$ mT, $f = 2$ Hz and $\alpha = 0$. The color code used is the same as the one considered in Fig.7.2.

triangle is shown to swim at the interface as testified by Fig.7.3(c) which gives the displacement of the center of mass as a function of time. One indeed sees that onto the oscillation of the center of mass, an overall translation is visible.

The swimmer being able to swim, let us analyse its efficiency. One way to analyse the efficiency of a swimming organism is to measure its dimensionless velocity $\mathcal{V}/2af$. This quantity measures the actual speed of the swimmer and compares its value to $2af$. This speed would be the one of a swimmer travelling a distance $2a$ equal to the size of a bead during a period $1/f$ equal to the swimming strokes period. Let us first analyse the dimensionless speed $\mathcal{V}/2af$ as a function of the amplitude of the oscillating field $\vec{B}_{osc}$. The result is given in Fig.7.4 in double logarithmic scale for several different frequencies. The vertical field is set to $5$ mT while the offset is set to $0.1$ mT. The important value of $|\vec{B}_z|$ is considered in order to remain in the small deformation regime where linear theory is expected to hold. Please note that the oscillating field and the offset are perpendicular which yields $\alpha = \pi/2$. The curves order from the lowest frequency ($f = 0.5$ Hz) to the higher frequency ($f = 5$ Hz) from top to bottom. The speed is seen to increase quadratically with the amplitude of the field, as indicated by the solid

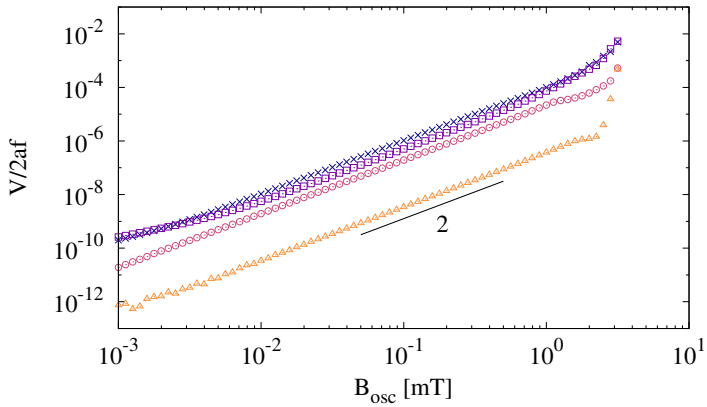


**Figure 7.4:** Dimensionless speed of the swimmer $\mathcal{V}/2af$ as a function of the amplitude of the oscillating field $\vec{B}_{osc}$ in double logarithmic scale. The vertical field amplitude has been set to $|\vec{B}_z| = 5\ \mathrm{mT}$ and the amplitude of the offset is $|\vec{B}_x| = 0.1\ \mathrm{mT}$. Different values of the frequency have been considered: Blue crosses: $f = 0.5$ Hz, Purple squares: $f = 1$ Hz, Pink circles: $f = 2$ Hz, Orange triangles: $f = 5$ Hz. The power law is evidenced by the black solid line.

black line in the plot. Note that other amplitude of $\vec{B}_z$ and $\vec{B}_x$ have been investigated. Identical dependencies are observed for different magnitude of those fields. Differences only appear for important offsets and small intensities of the vertical field. Indeed for those two limits the beads are close to each other and nonlinear behaviours are observed because of the non-linearity of the magneto-capillary potential.

We then choose to study the evolution of the dimensionless speed with the frequency $f$ of the oscillating field. The corresponding result is given in Fig.7.5 in double logarithmic scale. While $\vec{B}_z$ has been fixed to $5\ \mathrm{mT}$ in this analysis, the magnitude of both $\vec{B}_{osc}$ and $\vec{B}_x$ has been varied. Similarly to the previous analysis, the angle $\alpha = \pi/2$ has been considered. The speed evolution is seen to change according to power laws. Several regimes are observed for each set of parameters investigated. For low frequency, the dimensionless speed increases linearly with $f$. The end of this regime depends on $\vec{B}_x$. Above $f = 1$ Hz the dimensionless speed change as $f^{-5}$. The transition to this regimes is seen to be independent of both field intensities. The behaviour described here has been observed for other sets of parameters. Nevertheless, similarly to the previous case, extreme values of the fields give different behaviours. Once again, this is assumed to be

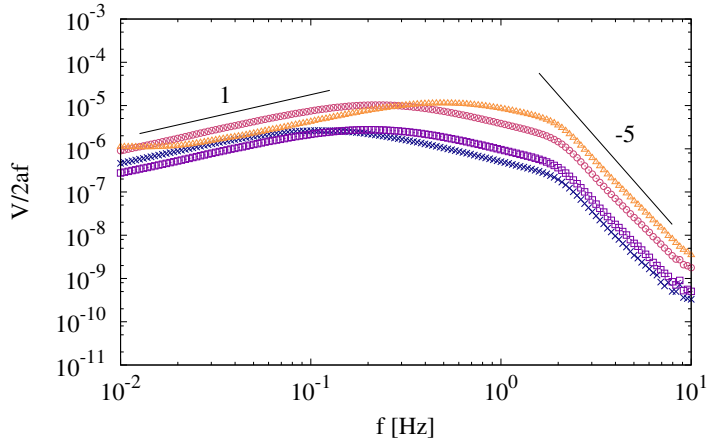


**Figure 7.5:** Dimensionless speed of the swimmer $\mathcal{V}/2af$ as a function of the frequency of the oscillating field $\vec{B}_{osc}$ in double logarithmic scale. The vertical field amplitude has been set to $|\vec{B}_z| = 50\,\mathrm{mT}$. Different values of the offset and oscillating amplitudes have been considered: Blue crosses: $|\vec{B}_x| = 0.1\,\mathrm{mT}$ and $|\vec{B}_{osc}| = 0.1\,\mathrm{mT}$, Purple squares: $|\vec{B}_x| = 0.2\,\mathrm{mT}$ and $|\vec{B}_{osc}| = 0.1\,\mathrm{mT}$, Pink circles: $|\vec{B}_x| = 0.2\,\mathrm{mT}$ and $|\vec{B}_{osc}| = 0.2\,\mathrm{mT}$, Orange triangles: $|\vec{B}_x| = 0.5\,\mathrm{mT}$ and $|\vec{B}_{osc}| = 0.2\,\mathrm{mT}$. The power laws are evidenced by the black solid lines.

due to nonlinear dynamics given the large beads oscillations and close proximities.

The value of the vertical magnetic field can also be changed. Figure 7.6 shows the dimensionless speed as a function of the vertical field magnitude. A unique set of parameters is considered here since the same behaviour has always been observed. The speed is seen to decreases as $f^{-14/3}$. These rather intriguing power laws is justified in the following section thanks to the linear model developed later. Yet, a small explanation can be given. Since all the interactions are shown to decrease with the distance between the spheres, especially the hydrodynamic and magnetic interaction, the motion of the swimmer is expected to be less efficient for large interdistances. Since the interdistance is directly related to the vertical field intensity [179], a decreasing speed is expected.

Finally, we consider the influence of the offset intensity on the dimensionless speed evolution. The corresponding result is given in Fig.7.7 in double logarithmic scale for different values of the oscillating field frequency. Similarly to the previous analysis, the oscillating field and the offset are perpendicular to each other. The curves correspond to different frequencies, which order from left to right from

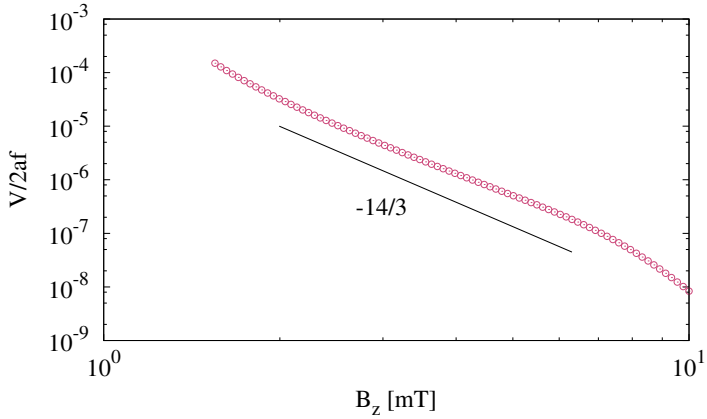


**Figure 7.6:** Dimensionless speed of the swimmer $\mathcal{V}/2af$ as a function of the amplitude of the vertical field $\vec{B}_z$ in double logarithmic scale. The offset field amplitude has been set to $|\vec{B}_x| = 0.1$ mT and the amplitude of the oscillating field is $|\vec{B}_{osc}| = 0.1$ mT. Its frequency is $f = 1$ Hz. The power law is evidenced by the black solid line.

the lowest ($f = 0.2$ Hz) to the highest frequency ($f = 2$ Hz). One observes that no power law is visible on the graphs. A single maximum is seen and moves towards low value of $|\vec{B}_x|$ as the frequency decreases. This observation aligns with the observation already made in Fig.7.5 where the swimming speed peak is seen to displace as the offset intensity is varied. Beside this observation, one can also see that decreasing the field frequency $f$ increases the swimming speed.

Given all the forces presented in the previous section and integrated in the numerical simulation, it becomes difficult to understand which part of the system drives the swimming mechanism. The advantage of numerics over experiments is the choice of the physical ingredients used in the algorithm. Cancelling each force while keeping the other active gives the possibility to evidence the propulsive strategy in the dynamics. Following this idea, we choose to consider the Rotational-Translational hydrodynamic (RT) coupling in the dynamics. This coupling corresponds to the third term in Eq.(7.7), namely

$$\vec{F}_{h,i}^{RT} = \sum_{j \neq i} \frac{6\pi\eta a_i a_j^3}{|\vec{r}_{ij}|^3} \left(\hat{\epsilon}.\vec{r}_{ij}\right).\vec{\omega}. \tag{7.11}$$

Taking this force into account drastically changes the swimming dynamics of the

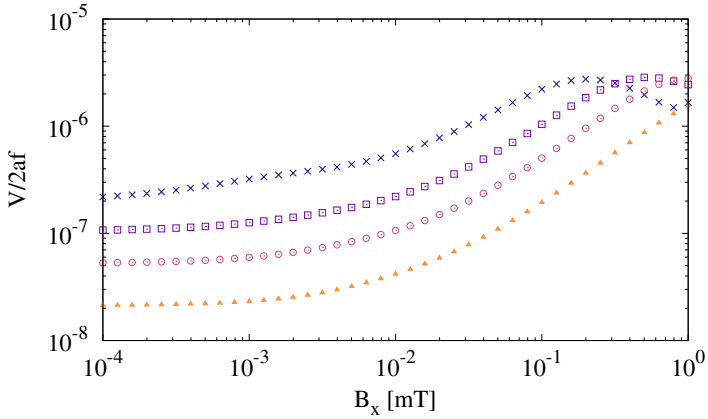


**Figure 7.7:** Dimensionless speed of the swimmer $\mathcal{V}/2af$ as a function of the frequency of the oscillating field $\vec{B}_{osc}$ in double logarithmic scale. The offset field amplitude has been set to $|\vec{B}_x| = 0.1$ mT and the vertical field amplitude is $|\vec{B}_z| = 5$ mT. Different curves account for different frequencies: Different values of the frequency have been considered: Blue crosses: $f = 0.2$ Hz, Purple squares: $f = 0.5$ Hz, Pink circles: $f = 1$ Hz, Orange triangles: $f = 2$ Hz.

assembly, as shown in Fig.7.8. This figure gives the motion of the center of mass as a function of time for the same set of parameters. We have considered $|\vec{B}_z| = 3$ mT, $\vec{B}_{osc} = 1$ mT, $\vec{B}_x = 0.5$ mT and $f = 1$ Hz. The only difference between each panel of the figure is the RT coupling. On the left-hand side of Fig.7.8, the RT coupling has not been considered while being consider in the right-hand side of the figure. The difference is obvious: the inclusion of the RT coupling gives the possibility for the beads assembly to swim along the fluid interface.

Given this last result, in the following section we will develop a toy model which aims at giving some insight of the results we obtain in this section. More specifically, we will justify the power laws observed in each figure already presented.

## 7.3 Gaining insight with a toy model

If the RT coupling is the key force that leads to the displacement of the assembly, it means that the rotation of the beads in the oscillating field is at the core of the swimming dynamics. Let us try to understand how the beads individual rotation can alter the motion of the center of mass. Figure 7.9 illustrates the model. In the

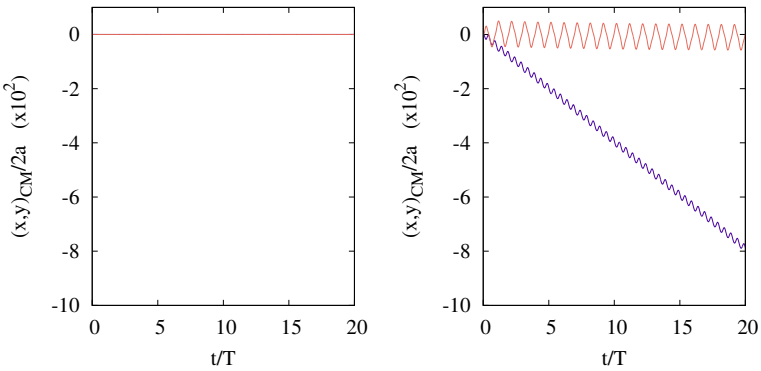


**Figure 7.8:** Evidence of the importance of the Rotational-Tranlational hydrodynamic (RT) coupling in the swimming dynamics. Each plot shows the motion of the center of mass along the $x$ (blue) and $y$ direction (pink) as a function of the dimensionless time $tf$. **(left)** RT coupling disabled, **(right)** RT coupling enabled. The vertical field $\vec{B}_z$ is set to $3\ \mathrm{mT}$, the oscillating field $\vec{B}_{osc}$ has an amplitude of $1\ \mathrm{mT}$ and frequency of $1\ \mathrm{Hz}$. The offset $\vec{B}_x$ is set to an amplitude of $0.5\ \mathrm{mT}$.

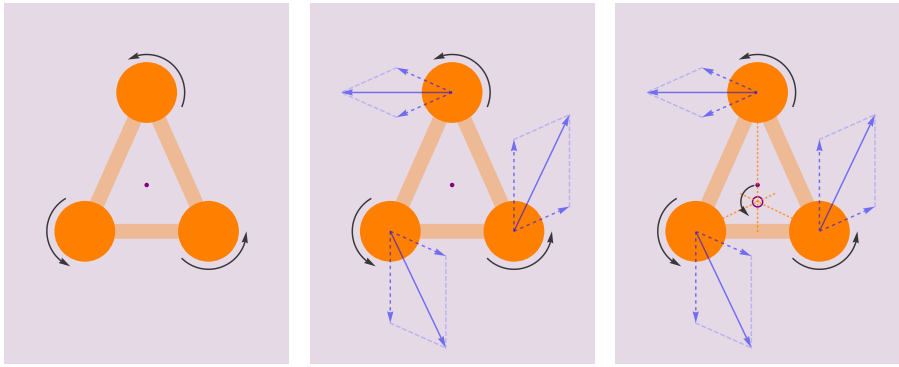

**Figure 7.9:** Finding the hydrodynamic centre of rotation: a step-by-step approach. **(a)** The beads rotates in order to align their remnant magnetization in the external magnetic field. The velocity field around each particle is given by the *rotlet*, as described in App.B. **(b)** The RT coupling between the beads rotation and translation forces the beads to move in the induced flow. The dashed blue arrows give the hydrodynamic force induced by a single neighbouring beads. The solid blue arrow on each bead gives the resulting total hydrodynamic force arising from the RT coupling. **(c)** From the force resulting from the RT coupling, one can find the hydrodynamic centre of rotation. This point is found by tracing the line perpendicular to the resulting total force on each bead. The intersection, the hydrodynamic centre, is indicated by the purple circle at the intersection of the oranged dotted lines.

following, for the sake of simplicity, all beads are supposed identical. As shown in Fig.7.9(a), all beads rotate in the fluid and supposedly identically. The rotation

of each bead is due to the interaction between the remnant magnetization and the external field. As a consequence of this rotation, each bead is the source of a rotlet, a point-like torque, as described in Appendix B. In our example, all beads rotate counter-clockwise, so does the flow around each bead. This flow induces forces, as depicted in Figure 7.9(b). Each blue dashed arrow comes from the interaction of a bead with a neighbouring one. The direction of the arrow is perpendicular to the line joining the pair of beads involved. The total force on each bead can be found by simple geometrical construction. This force is given by the solid blue arrow. Each of these arrows points in the same direction, counter-clockwise in this example, because of the identical rotation of each sphere on the surface. Using again a geometrical construction, one observes that those three solid blue arrows define a center of rotation which is not the center of mass, we name this point the *hydrodynamical center of rotation* of the triangle. It is found by drawing the line perpendicular to each solid blue arrow. The intersection of each line is this hydrodynamic center. This point is indicated by a circle in Fig.7.9(c) and clearly differs from the center of mass of the structure. The center of mass corresponds to the purple point in the figure. Appendix C gives the mathematical expression of the hydrodynamic center. Finally, because of the global rotation of the structure, the center of mass rotates around the hydrodynamic center. In this example, the triangle is a "lepto" isosceles and the hydrodynamic center of rotation is below the center of mass. In the case of a "platy" isosceles triangle, the center of mass is above the hydrodynamic centre.

On the one hand, the hydrodynamic centre is located above or below the center of mass depending on the triangle configuration. On the other hand, the individual rotation of the beads rotates the center of mass around the hydrodynamic centre clockwise and counter-clockwise. The result is the global translation of the center of mass after a cycle of deformation. The translation mechanism is illustrated thanks to Fig.7.10. The cycle begins with a triangle in the "lepto" isosceles configuration and oriented to the right, as depicted in Fig.7.10(a). Because of the beads rotation, the overall structure also rotates in the counter-clockwise direction. Since the hydrodynamic centre and the center of mass do not coincide, the latter moves as indicated by the dashed gray line in Fig.7.10(b). In Fig.7.10(c), the shape of the triangle changes to a "platy" isosceles triangle. As a consequence, the hydrodynamic centre is now below the center of mass. Note that the center of mass has not moved during the deformation. Finally, in Fig.7.10(d) the beads ro-

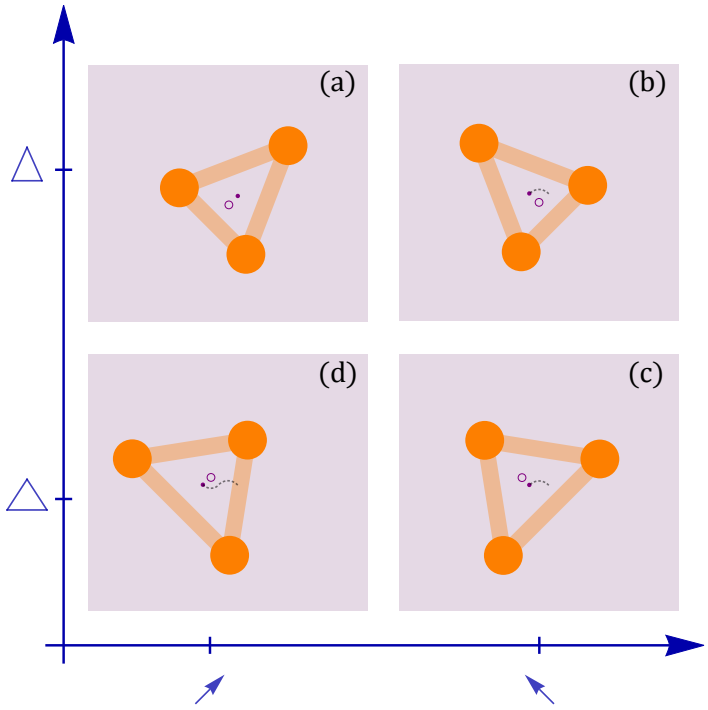


**Figure 7.10:** Non-reciprocal deformation of the triangular swimmer. The center of mass is represented by the purple point. The hydrodynamic centre of rotation is given by the purple circle. The gray dashed curve gives the displacmeent of the center of mass from its starting position. The triangle begins the cycle in the ``lepto'' isosceles configuration and oriented to the right **(a)**. Because of the beads rotation, the triangle orients to the left, moving the center of mass around the hydrodynamic centre **(b)**. Then, the triangle shape-shifts to a ``platy'' isosceles triangle, without moving the center of mass but changing the position of the hydrodynamic centre **(c)**. After this deformation, the beads rotate in the other direction and change the orientation of the triangle back to the right. Meanwhile, the center of mass rotates around the hydrodynamic centre and continues to move **(d)**. Finally, the triangle comes back to its initial shape.

tate in the clockwise direction. Because of the new position of the hydrodynamic centre, this new rotation does not cancel the previous one. On the contrary, one sees that the center of mass moves further away from its starting point. When the triangle comes back in its initial shape, the center of mass is assumed to remain immobile. Therefore, at the end of the cycle, the triangle has moved the distance given with the gray dotted line.

Now that the motion of the triangle has been understood, let us quantify its

displacement as a function of the experimental parameters.

## 7.4 Quantifying the swimming dynamics

Scaling for the swimming dynamics can be extracted from Fig.7.9. First of all, we need to express the deformation of the triangle. A first method considers the angle $\alpha$ which measures the angular deviation from a regular triangle. For example, for an isosceles triangle, the vertex values are $(\pi/3+\alpha, \pi/3-2\alpha, \pi/3+\alpha)$, the second value corresponding to the main vertex. This deformation can be expressed in terms of the sides length of the triangle, which gives a second method. For an isosceles, one can write $(d, d-A_{def}, d)$ where the second value is the side opposed to the main vertex and $A_{def}$ is the amplitude of deformation. As stated in Appendix C, $\alpha$ and $A_{def}$ are related. Given those definitions, the model can be studied more deeply.

In a few words, the translation of one bead comes from the individual rotation of the neighbouring ones. As a result, the structure rotates around the hydrodynamic centre. Assuming a solid rotation of the triangular structure, if one knows the instantaneous velocity of the beads around the hydrodynamic centre, one accesses the velocity of the center of mass through classical mechanics arguments. For this purpose, the only requirement is the distance between the hydrodynamic centre and the center of mass. Indeed, this distance can be seen as a hydrodynamic lever. Therefore, let us first access the individual bead velocity due to the rotlets. The flow field induced by a rotlet is given in Appendix B and scales as

$$|\vec{v}_i| \propto \frac{|\vec{\omega}_j|}{|\vec{r}_{ij}|^2}. \tag{7.12}$$

The translation of the center of mass can be obtained assuming a solid rotation of the structure. Indeed, in such case, the angular velocity of one bead around the hydrodynamic centre is also the angular velocity of the center of mass around the hydrodynamic center. From this property, the translational speed of both the beads and the center of mass can be linked to each other through their distance to the hydrodynamic centre. The details of the calculus giving the distance between the center of mass and the centre of rotation is given in Appendix C. In the small deformation approximation, this distance scales as $A_{def}$ while the distance between the beads and the hydrodynamic centre scales as $\vec{r}_{ij}$. As a consequence,

$$\frac{|\vec{v}_i|}{|\vec{r}_{ij}|} \propto \frac{\mathcal{V}}{A_{def}}. \tag{7.13}$$

Mixing Eqs.(7.12) and (7.13) yields to the scaling

$$\mathcal{V} \propto A_{def} \frac{|\vec{\omega}_j|}{|\vec{r}_{ij}|^3}. \tag{7.14}$$

As we will see later, the beads rotation and the triangle deformation are described dynamically. As a consequence, the phase shift between the rotation of the beads and the deformation of the structure may not be exactly given by $\pi/2$. Instead, the phase shift might be given by the parameter of the experiments, similarly to the Najafi-Golestanian swimmer discussed in the previous chapter. As a consequence, in order to take into account the imperfect non-reciprocity of the global deformation, we choose to include empirically a factor $\sin\Delta\phi$ in the previous formula. Finally, for the sake of simplicity, we choose to relate the velocity $|\vec{\omega}_j|$ to the amplitude of rotation of one bead. It yields $|\vec{\omega}_j| \propto A_{rot}\omega$. The final form of the scaling therefore reads

$$\mathcal{V} \propto \frac{1}{|\vec{r}_{ij}|^3} \omega A_{rot} A_{def} \sin\Delta\phi. \tag{7.15}$$

It is worth comparing this formula to Golestanian's in the case of the linear swimmer. Najafi and Golestanian obtained

$$\mathcal{V} \propto \frac{1}{|\vec{r}_{ij}|^2} \omega A_1 A_2 \sin\Delta\phi. \tag{7.16}$$

Our scaling gives the same result except for the denominator. Indeed, the authors obtained the $|\vec{r}_{ij}|^{-2}$ factor as a result of the Stokeslet. Since the Rotlet has a higher exponent, the $|\vec{r}_{ij}|^{-3}$ in our formula makes sense. As a consequence, both formula express the same dynamics based on the same ingredients. In order to develop further Eq.(7.15), one needs to know how $A_{rot}$ and $A_{def}$ are related to the parameters of the experiments. We will first study the rotation of the beads and then the deformation of the assembly.

### 7.4.1 The beads dynamics

From Eq.(7.10), one can write down the Newton equation describing the beads rotation

$$I|\dot{\vec{\omega}}| + 8\pi a^3 \eta |\vec{\omega}| + |\vec{\mu}^r||\vec{B}_x| \sin(\theta) + |\vec{\mu}^r||\vec{B}_{osc}(t)| \sin(\theta - \alpha) = 0. \quad (7.17)$$

Let us consider this equation in the linear regime, i.e. $\theta \ll 1$. This limit is obtained for a small oscillating field amplitude and an intense vertical field. Let us also consider the case $\alpha = \pi/2$ already considered in the simulations in Section 7.2.2 which greatly simplifies the analysis. With those assumptions, the equation simplifies to

$$I|\dot{\vec{\omega}}| + 8\pi a^3 \eta |\vec{\omega}| + |\vec{\mu}^r||\vec{B}_x|\theta = |\vec{\mu}^r||\vec{B}_{osc}(t)|. \quad (7.18)$$

This is exactly the equation of a damped and forced linear spring. The external forcing comes from the oscillating field. The forcing amplitude is given by $|\vec{\mu}^r||\vec{B}_{osc}(t)|$. Note that being in the linear regime, the beads rotation frequency is given by the external field frequency $f$. The stiffness is given by the interaction potential with the offset $\vec{B}_x$. It means that the offset defines a natural frequency for the rotation. As a consequence of this equation, the angular dynamics can be described using the linear resonance theory. For the temporal evolution of the rotation, one has $\theta(t) = A_{rot} \cos(\omega t - \phi)$ with

$$A_{rot} = \frac{|\vec{\mu}^r||\vec{B}_{osc}|}{\sqrt{\left(|\vec{\mu}^r||\vec{B}_x| - I\omega^2\right)^2 + 64\pi^2\eta^2 a^6 \omega^2}}, \quad (7.19)$$

$$\tan \phi_{rot} = -\frac{8\pi a^3 \eta \omega}{|\vec{\mu}^r||\vec{B}_x| - I\omega^2}. \quad (7.20)$$

Let us extract the scaling of the amplitude $A_{rot}$ for further comparisons with the numerics. The oscillation is linearly proportional to the oscillating field amplitude

$$A_{rot} \propto |\vec{B}_{osc}|. \quad (7.21)$$

The velocity scales differently with the frequency depending on its value compared to the resonant frequency. This leads to

$$A_{rot} \propto \begin{cases} 1 & \text{if} \quad f \ll \sqrt{|\vec{\mu}^r||\vec{B}_x|/I}, \\ f^{-2} & \text{if} \quad f \gg \sqrt{|\vec{\mu}^r||\vec{B}_x|/I}. \end{cases} \tag{7.22}$$

The value for the transition frequency can be estimated and gives $\sqrt{|\vec{\mu}^r||\vec{B}_x|/I} = 0.68$ Hz for the numerical parameters used in the simulations.

### 7.4.2 The triangle dynamics

For the description of the triangle dynamics, we will use the results of the previous chapter. Indeed, the deformation of triangle can be described in terms of variation of the sides length $A_{def}$. The previous chapter has shown that the interaction between a pair of beads can be described by a linear forced spring in the small deformation regime. Its stiffness is directly related to the parameters of the experiment. The relation is given in Eq.(6.14). As a consequence, forced by an external field, the amplitude $A_{def}$ is expected to be given by the theory of resonance

$$A_{def} = \frac{F}{\sqrt{(k - m_r\omega^2)^2 + 36\pi^2\eta^2a^2\omega^2}}, \tag{7.23}$$

$$\tan\phi_{def} = -\frac{6\pi\eta a\omega}{k - m_r\omega^2}, \tag{7.24}$$

where we have assumed a viscous damping given by the Stokes formula. In those expression, $F$ is the amplitude of the forcing and $m_r$ is the reduced mass of the pair, already introduced in the previous chapter. Since the force finds its origin in the magnetic dipole-dipole interaction, its amplitude scales as $|\vec{r}_{ij}|^{-4}$. Furthermore, in the linear regime, $F \propto |\vec{B}_{osc}|$. Therefore, the elongation $A_{def}$ scales as

$$A_{def} \propto \frac{|\vec{B}_{osc}|}{|\vec{r}_{ij}|^{-4}}, \tag{7.25}$$

and for the frequency, one has

$$A_{def} \propto \begin{cases} 1 & \text{if} \quad f \ll \sqrt{k/m_r}, \\ f^{-2} & \text{if} \quad f \gg \sqrt{k/m_r}. \end{cases} \tag{7.26}$$

From Chapter 6, one knows that the transition frequency is given approximately by $\sqrt{k/m_r} = 2$ Hz.

Before mixing all the scaling together, let us consider the phase difference between each oscillation. Given the tangent of $\phi_{def}$ and $\phi_{rot}$, using elementary trigonometric relations, one has

$$\tan \Delta\phi = \frac{\tan \phi_{rot} - \tan \phi_{def}}{1 + \tan \phi_{rot} \tan \phi_{def}}. \tag{7.27}$$

Two scaling arises

$$\tan \Delta\phi \propto \begin{cases} f & \text{if} \quad f \ll 1, \\ f^{-1} & \text{if} \quad f \gg 1. \end{cases} \tag{7.28}$$

Since the limit $f \ll 1$ and $f \gg 1$ gives small values of $\tan \Delta\phi$, the scaling presented here also holds for $\sin \Delta\phi$.

As a consequence, from Eq.(7.15) and mixing all scaling together, one sees that

$$\mathcal{V} \propto |\vec{B}_{osc}|^2, \tag{7.29}$$

which corresponds to the scaling observed in Fig.7.4. Regarding the evolution of the velocity as a function of the frequency, the dependencies of $A_{def}$, $A_{rot}$ and $\sin \Delta\phi$ have to be taken into account. It yields

$$\mathcal{V} \propto \begin{cases} f^2 & \text{if} \quad f \ll \sqrt{|\vec{\mu}^r||\vec{B}_x|/I}, \\ f^{-4} & \text{if} \quad f \gg \sqrt{k/m_r}. \end{cases} \tag{7.30}$$

Once made dimensionless, the two scaling of Fig.7.5 are recovered. One should note the boundaries of each scaling. Indeed, the speed increases as $f^2$ only below $|\vec{\mu}^r||\vec{B}_x|/I$. This boundary is defined by the offset $\vec{B}_x$. This is also the case in Fig.7.5. On the contrary, the last scaling, i.e. $v_0 \propto f^{-4}$, is only valid for $f \gg k/m_r$. From the last chapter, we have derived the expression of $k$ as a function of the experimental parameter. Especially, we have shown that the stiffness $k$ is independent of the value of $f$ and only depends on $\vec{B}_z$ when $\vec{B}_x \ll \vec{B}_z$. In the case described in Fig.7.5, the vertical field $\vec{B}_z$ is always more than ten times more

intense then the offset. As a consequence, in Eq.6.14, $|\vec{B}_x|^2$ can be neglected before $|\vec{B}_z|^2$. This observation explains why the last scaling is independent of each experimental parameter.

Finally, we can describe the speed as a function of the distance between each beads. One has

$$\mathcal{V} \propto |\vec{r}_{ij}|^{-7}. \tag{7.31}$$

Knowing from the previous chapter that $|\vec{r}_{ij}| \propto |\vec{B}_z|^{\frac{2}{3}}$ in the case of small offset magnitude, one has

$$\mathcal{V} \propto |\vec{B}_z|^{-\frac{14}{3}}. \tag{7.32}$$

This scaling, only valid for small values of $\vec{B}_z$ as described in the previous chapter, corresponds to the observation made in Fig.7.6.

The toy model developed in this section, based on the swinging motion of the centre of mass around the hydrodynamic centre, is shown to capture correctly the numerical simulations. Indeed, each scaling is rationalised through the rotational dynamics of each beads and the deformation dynamics of the triangle.

### 7.4.3 Remarks about the Najafi-Golestanian microswimmer

It worth noticing that the beads rotation has been only introduced in this chapter despite the discussion of about the Najafi-Golestanian in the previous chapter. The beads rotation in this case can indeed be neglected when considering Eq.(7.17) and its solution. When a strong offset $\vec{B}_x$ is applied to the system, the individual rotations are highly constrained. Indeed, as we have seen earlier, the offset plays the role of a confining potential and its stiffness is directly related to $\vec{B}_x$. Since, in order to stabilize the linear structure discussed in Chapter 6, an intense offset is required, the rotation are limited. Another limiting effect has to be taken into account. Still because of the offset, the beads are rather close to each other in the linear structure. The amplitude of oscillations, and therefore $\vec{B}_{osc}$, is small to prevent the contact between the beads. Since the rotation is driven by the oscillating field, the rotation are expected to be even more negligible.

## 7.5 Conclusion

The triangular three-beds assembly can swim at an air-water interface thanks to time-dependent magnetic fields. Interestingly, the way the swimmer harnesses power from the external fields is different from the Najafi-Golestanian microswimmer. In the latter case, the non-reciprocal deformation comes from the spatial asymmetry of the linear structure. In the triangular one, the non-reciprocal deformation is driven by the rotation of each bead which adds to the triangle deformation to achieve propulsion. The result is a swinging motion where the centre of mass rotates above and below a peculiar point: the *hydrodynamic centre of rotation*. This centre is determined by the hydrodynamic interaction between pairs of beads. It was shown in this chapter that depending on the isosceles triangle obtained, i.e. lepto or platy isosceles, the centre of rotation is respectively below and above the centre of mass. This is this property that is at the root of the non-reciprocal deformation.

A toy model was developed in order to capture of essence of the dynamic. The speed of the triangular swimmer is shown to scale as $\mathcal{V} \propto \omega A_{rot} A_{def} \sin \Delta\phi / l^3$. This relation resembles Golestanian's which means that despite the very different propulsive mechanisms in each system, the same properties can be observed. Finally, based on a linear analysis where the beads rotation and the triangle deformation were decoupled, the evolution of the swimming speed with each parameter was studied. The toy model captures correctly the numerical results and only needs to be compared to experiments and applied to larger assemblies.

# 8

# General conclusion and future work

## 8.1 Conclusion

In this thesis, we asked the question of the effect of a collection of passive individuals on the net translation of the assembly and especially the effect of the number of individuals. Two systems were investigated: walking droplets and magnetocapillary microswimmers.

In the first system, the walking droplets harness power from the interface thanks to waves produced at each impact. The persistence time of those waves is controlled through the vertical oscillation of the liquid surface. From a mathematical point of view, those wave sources can be seen as images of the particles which affect the horizontal dynamics of the droplet. This property is the *wave memory* of the walker. Given the control over the wave persistence time, the number of images of the surface, and therefore the size of the wave memory, can be controlled. In the first of this thesis, the high memory regime has been studied.

In Chapter 3, we discussed this wave driven dynamics in free space. In this case, when entering the high memory regime, the walking droplet is seen to move randomly on the surface. The walker alternates between straight line motion and sudden changes of orientation, an equivalent of *run and tumble* dynamics. The appearance of this dynamics is due to the positive feedback loop between the wavefield amplification and the walking droplet speed fluctuation. This feedback

loop eventually traps the walker in this own waves over a small period. When the droplet leaves the traps, it enters a new run phase with a fluctuating speed. The alternation between the run phase and the tumble phase appears to last forever resulting in a global diffusive dynamics. The root mechanism is a Shil'nikov type bifurcation leading to a homoclinic chaos. Finally, we showed that the diffusive dynamics of the walker on the interface is controllable through the memory parameter. Indeed, the large number of images of the droplet emitting standing waves in the high memory regime allows the walker to enter the thermodynamic regime and to display a diffusive behaviour. The more images there is, the less efficient is the diffusive process. In a few words, the walking droplet dynamics in the high memory regime gives the first example of a perfectly tunable deterministic run and tumble dynamics.

In Chapter 4, we trapped the walker in an harmonic potential in order to provoke the continuous interaction of the walker which its own wavefield. In this situation, the memory is seen to mimic a thermal bath, a white noise, with an effective temperature related to the memory of the droplet. This observation reinforces the idea that the memory indeed allows the walker to enter the thermodynamic regime. Surprisingly, time correlation is seen to disappear despite the non-markovian process at the root of the dynamics. In order to gain insight on the walker dynamics, the wave dynamics was investigated. The investigation of this unique wave-based thermostat shows two main features. First the energy stored in the wavefield is relatively limited because of favoured destructive interferences. This property is to due the correlation between two impacts on the surface. Second, the energy is stored almost identically in the degrees of freedom of the wavefield. This second property finds its origin in the walker driving mechanism: the interplay between the droplet wave generation and the slope of the global wavefield. As a consequence, the wave dynamics mimics a minimisation principle and an equipartition of energy in the system.

The second system explored in this manuscript, the magnetocapilary microswimmers, uses hydrodynamic interactions and non-reciprocal deformations to achieve propulsion. The non-reciprocal deformation is due to the magnetocapillary interactions between the beads. In this dynamics, the particles are driven out-of-equilibrium thanks to time-dependent magnetic fields. This second part of the thesis was dedicated on the creation of non-reciprocal deformation in a magne-

tocapillary swimmer.

In Chapter 6, we explore theoretically the magnetocapillary three-beads Najafi-Golestanian microswimmer. In order to achieve a non-reciprocal deformation in this linear structure, a deep investigation of the magnetocapillary potential was necessary. A simple method to generate non-reciprocal deformation is to consider different beads sizes in the assembly. This leads to interactions between beads with different natural frequency, which breaks the spatial symmetry of the swimmer. The model developed in this chapter is an hybrid toy model, mixing Golestanian's kinematic swimming condition and a dynamical inertial model. In this hybrid approach, the deformation is computed beforehand and then injected in the Golestanian's condition. The model correctly captures the experiment and is shown to give the same results as exact models in the overdamped limit.

In Chapter 7, the three-beads triangular microswimmer was theoretically investigated. The non-reciprocal deformation in this case is different from the linear structure. The triangle uses two ingredients to swim: the individual rotation of each beads and the oscillation between one isosceles triangle (lepto-isosceles) to another (platy-isosceles). The key mechanism is the swinging motion of the triangle centre of mass around the *hydrodynamic centre of rotation*. This one is the result of the hydrodynamic forces coupling the individual rotations to the beads translation. Based on this idea of swinging dynamics, a toy model has been developed based on geometrical and dynamical arguments. A Golestanian-like condition of swimming as been recovered. This theoretical investigation gives the first step towards the investigation of large swimming assembly of magnetic beads on air-water interface.

Given the limited amount of individuals considered in the dynamics in the case of the magnetocapillary swimmer, analogies between the two systems investigated are limited. Further investigations of the swimming dynamics regarding the efficiency as a function of the number of particles are therefore necessary. We end this thesis by giving a few ideas a further investigations which aims at developing further the question raised in this manuscript.

## 8.2 Future work

### 8.2.1 Walking droplets

Walking droplets make up a quite unique system because of the feedback due to the waves on the particle. News geometries and memory storage can be considered in numerical simulations. For example, one can consider 3D waves. Indeed, in actual experiments, the droplets in compelled to move on the air-oil interface and to be propelled by 2D cylindrical waves. Thanks to numerics, one can extend this dynamics to 3D spherical waves for a droplet bouncing into a fourth dimension. A mental picture of this numerical experiments would be the one of a particle flickering in space and emitting a 3D wave each time it lightens up. This flashings would correspond to the bouncing of the droplet in te 2D case. Following the model of Dubertrand *et al*, the wavefield in this situation is given by

$$\begin{aligned}\zeta_i\left(\vec{r},t;\vec{r}_i,t_i\right) =&\zeta_0\cos\left(2\pi f_F(t-t_i)\right)j_0\left(k_F|\vec{r}-\vec{r}_i|\right)\\ &\times\exp\left(-\frac{t-t_i}{\tau_M}\right)\exp\left(-\frac{|\vec{r}-\vec{r}_i|}{\delta}\right),\end{aligned}\tag{8.1}$$

where $j_0$ is the spherical Bessel function of zeroth order and first kind and the vectors $\vec{r}$ are three dimensional. Since mathematically the ingredients used in the dynamics are similar to the 2D case, self propulsion is observed in numerics. Differences appears in the intermediate memory regime. Figure 8.1 shows the dynamics in a 3D harmonic potential for increasing memory parameters. One sees that the walker initially moves along a circle for low memory. As the memory increases, the motion destabilizes in the direction perpendicular to the initial plane of motion. Finally, for the more important memory parameters, the trajectory self-structures into a spherical shell hollow in the inside. This system could be used to analyse further the analogies between memory driven dynamics and quantum mechanics. Indeed, such trajectories also shows quantification of their macroscopic observables $\langle U\rangle$ and $\langle L\rangle$. But, contrarily to 2D dynamics, the quantification in 3D dynamics is expected to touch other observables ($L_z$ in the case of the electron around a proton).

Back in the 2D experiments considered into this manuscript, new confining potentials can be considered. For example, one can consider double-well harmonic

potentials and investigate how the dynamics in each well couples with the other. Such a potential reads

$$U(\vec{r}) = \frac{U_0}{L^4}\left(x^2 - L^2\right)^2 + \frac{4U_0}{L^2}y^2. \tag{8.2}$$

In this expression, $U_0$ is the high of the energy barrier between the two wells and $2L$ their distance. In the intermediate memory regime, the passage from one well to the other strongly depends on the natural frequency $\omega = 2\pi f = \sqrt{8U_0/L^2}$ associated to the wells. Figure 8.2 gives two examples of the dynamic encountered in numerical simulations. The color in the plot indicates the direction of rotation. The center of the wells are indicated with the black dots. The top figure shows a walker blocked in the right well, in a lemniscate state, despite a barrier lower than its average kinetic energy ($U_0 = 0.8\langle K\rangle$). The bottom figure shows a coupling between a trifolium of the left hand side and a circle in the right hand side. Contrarily to the top figure, the barrier is higher than the kinetic energy of the walker at every instant of the dynamics ($U_0 = 2\langle K\rangle$). Despite this difference of energy, the walker is able to climb the barrier in a stable trajectory. The difference between those two dynamics comes from the eigenstates which seems to possess blocking or transmitting properties. This potential can serve to explore new analogies with quantum mechanics as briefly discussed at the beginning of Chapter 2.

### 8.2.2 Magnetocapillary microswimmers

The systems explored in this manuscript has been made of three floating magnetic beads. Nevertheless, experiments have shown that larger assemblies can still swim with different efficiency depending on the amount of beads on the interface [111]. For example, $4$-beads assemblies where shown to be especially non-efficient. Assemblies of $5$ and $6$ beads where also shown to swim but with increasing efficiency. The model developed in Chapter 7 can only explain the $4$-beads dynamics. Therefore further analysis are necessary. The $4$-assembly is shown to deform back and forth into a rhombus when time-depending magnetic fields are applied. The hydrodynamic center of rotation can be computed in this case. It can be shown that the high level of symmetry of the rhombus makes that the center of mass and the hydrodynamic center coincide. As a result, the swinging mechanisms observed in Chapter 7 and illustrated in Fig.7.10 cannot be observed. Regarding the $5$ and $6$-beads assemblies, such cases give multiple hy-

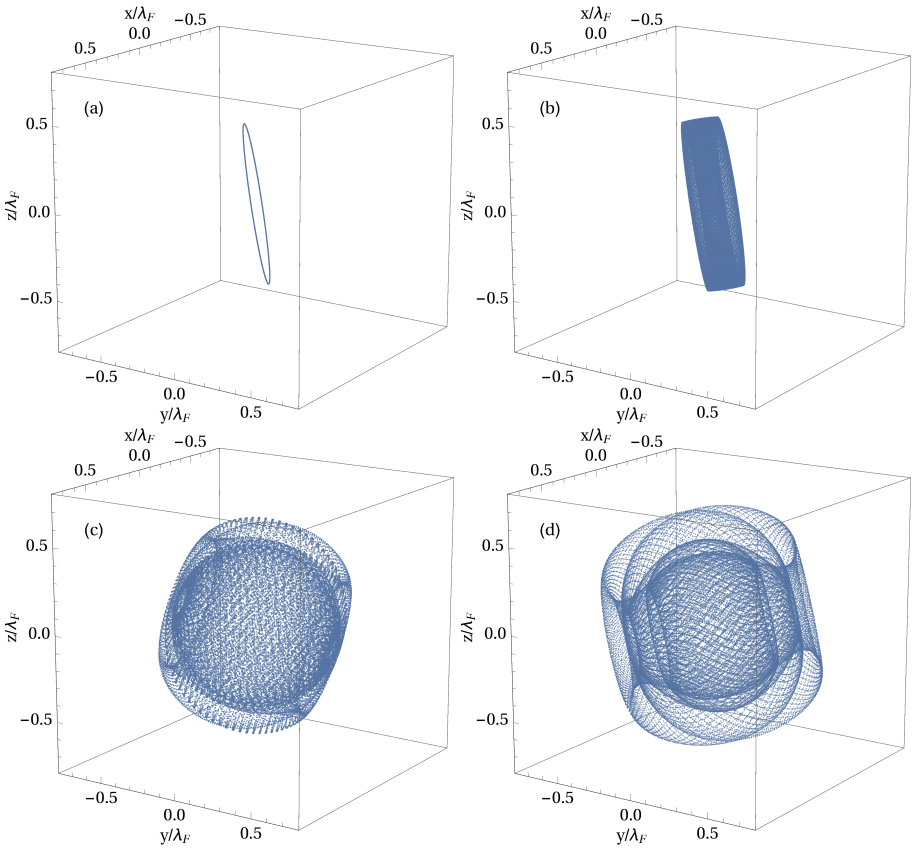


**Figure 8.1:** Dynamics of a walker in a 3D harmonic potential at frequency $f = 1$ Hz for variying memory parameters: (a) $\mathrm{Me} = 10$, (b) $\mathrm{Me} = 20$, (c) $\mathrm{Me} = 30$, (d) $\mathrm{Me} = 40$. All structures have a cylindrical symmetry and are hollow inside. All trajectories display $20000$ flickering in the fourth dimension.

drodynamic centres of rotation. A new description has to be found in order to understand the swimming dynamic observed.

The numerics presented in Chapter 7 does not allow to solve the fluid dynamics along the particle dynamics. A integration of the fluid dynamics in the numerics could allow to investigate further the interaction between the assembly and its environment. This idea could be implemented using another numerical scheme, the lattice-Boltzmann method for example. As a consequence, multiple swimmers dynamics due to hydrodynamic interactions could be explored as well as potential applications in microfluidic such as the mixing process induced by swimmer.

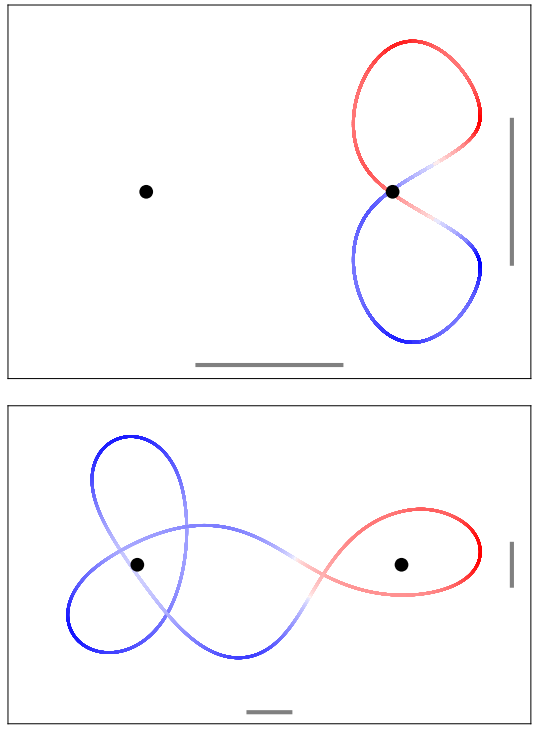

**Figure 8.2:** Dynamics of a walker in a 2D double-wells harmonic potential for varying parmaeters. Top $\mathrm{Me} = 20$, $f = 700$ mHz and $U_0 = 0.8\langle K \rangle$, bottom $\mathrm{Me} = 15$, $f = 300$ mHz and $U_0 = 2\langle K \rangle$. The color code indicates the direction of rotation (blue: clockwise, red: counter-clockwise) and the gray line gives $\lambda_F$ in each direction.

### 8.2.3 Biomimetic self-assembled swimmers

3D printing technologies give the possibility to craft objects of any shape with an extreme ease. Mixing those techniques with magnetic materials can provide objects that can self-assemble and react to external magnetic fields. This idea has been used in our lab using the system depicted in Fig.8.3(a,b). Pieces of ABS a few centimetres long are filled with magnetic cylinders has indicated in the figure. Two cylindrical magnets are placed in the arms with their magnetic moment pointing in the same direction. Two additional magnets are placed in the central part and are anti-parallel. The pieces are also asymmetric. Indeed, the disk at the center has not the radius on each side of the two arms. The purpose of those magnets is double. The two central magnets allow to generate large, centipede-like structures thanks to attractive dipole-dipole interactions (see Fig.8.3(c)). The two

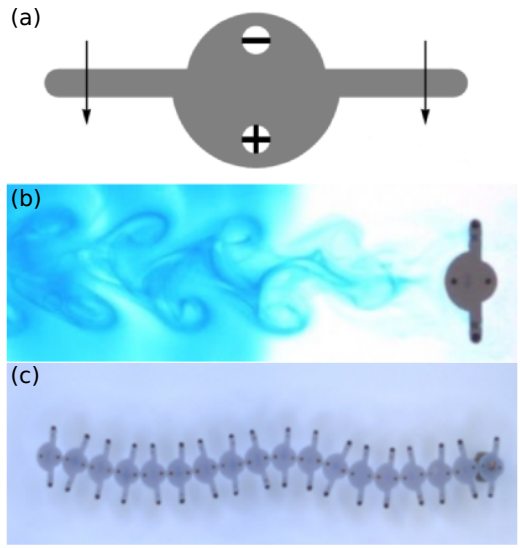


**Figure 8.3:** Biomimetic self-assembled swimmers: (a) Schematic description of the PDMS used in the experiments. Arrows give the direction of the magnets in the arms, plus and minus sign gives the directions of the vertical magnets. (b) Swimming dynamics of this ``swimmer'' at the air interface in presence of blue dye. A small offset field is applied along the direction of motion. The oscillating field is applied perpendicularly to the direction of motion. (c) Assembly of 18 pieces under a unique time-dependant magnetic field applied in the direction perpendicular to the swimmer axis. Credit: Ylona Collard, ULiege.

magnets in the arms tend to align the pieces in external horizontal magnetic fields and therefore deform the structure.

This object has been shown to be able to swim along air-water interfaces, floating also because of its wetting properties. The dynamics being at higher Reynolds number than the dynamics explored in this manuscript ($\mathrm{Re} \approx 200$)), the theory of hydrodynamic interactions does not hold any more. The propulsive mechanism now comes from the vortices emitted by the structure and mainly ejected backward, as evidenced in Fig.8.3(b). Indeed, an oscillating and horizontal magnetic field is applied to the system. The swimmer swims perpendicularly to this oscillating field. Interestingly, adding more and more pieces to the structure completely change the system which mimics sea worms swimming dynamics as shown in Fig.8.3(c). In all case, the system is shown to swim along the interface. Despite those extremely promising experiments, a proper theoretical understand is still lacking. The link between the swimming speed and the vortices emitted has to be

understand. Furthermore, the dynamics of larger assemblies still need to be understood. Nevertheless, given its simplicity, this experiment can assume the role of toy model in order to understand the dynamics of insects and fishes moving in and onto water using similar propulsive mechanisms.

# Appendices

# A

# Numerical simulations of walking droplets

The numerical simulations of walking droplets are made in C/C++. We provide here an exhaustive description of the algorithm we used.

Simulations are made using the assumption that the vertical and the horizontal dynamics are not coupled to each other. The vertical dynamics corresponds to the completely inelastic bouncing ball. The horizontal dynamics is related to the interaction between the droplet and its wavefield.

## A.1 Vertical dynamics

Since the dynamics of an inelastic bouncing ball is periodic and does not show transient behavior [69], this part of the simulation is solved once and for all. The results one obtains are used to compute the horizontal dynamics.

We assume that the surface vertical elevation is given by

$$z_s(t) = A\sin(\omega_s t). \tag{A.1}$$

Because the droplet impacts on the surface are assumed to be inelastic, once the contact occurs, the droplet vertical speed relative to the surface is equal to zero. In other words, the droplet has the same vertical speed as the surface. As a consequence, the droplet only leaves the surface when the surface acceleration

$\ddot{z}_s$ has a magnitude such as

$$\ddot{z}_s = A\omega_s^2 \geq g, \tag{A.2}$$

with $A$ being the forcing amplitude and $\omega_s$ the angular frequency of oscillation. Indeed, in such case, the surface "falls down" with an acceleration higher than the droplet one, i.e. $g$. The take-off instant $t^\star$ can be easily extracted, knowing that it corresponds to the first instant $\ddot{z}_s$ matches $g$

$$t^\star = \frac{1}{\omega_s} \arcsin\left(\frac{g}{A\omega_s^2}\right). \tag{A.3}$$

Therefore, the take-off velocity and the take-off height can be computed. Because the droplet vertical speed is always given by the surface velocity when both are in contact, one has

$$\dot{z}(t^\star) = A\omega_s \sqrt{1 - \left(\frac{g}{A\omega_s^2}\right)^2}, \tag{A.4}$$

and

$$z(t^\star) = \frac{g}{\omega_s^2}. \tag{A.5}$$

The droplet, when leaving the surface, is only submitted to its weight, giving a trajectory and a vertical speed

$$z(t) = z(t^\star) + \dot{z}(t^\star)(t - t^\star) - \frac{g}{2}(t - t^\star)^2, \tag{A.6}$$

$$\dot{z}(t) = \dot{z}(t^\star) - g(t - t^\star). \tag{A.7}$$

The landing instant $t^+$ is found by assuming $z(t^+) = z_s(t^+)$. Numerically, the solution is obtained via the Bisection method with a relative precision of $10^{-6}$. Once $t^+$ has been obtained, the landing velocity $\dot{z}(t^+)$ can be computed.

The knowledge of both $t^\star$ and $t^+$ defines two distinct parts of the motion. During $\Delta t_{fly} = t^+ - t^\star$, the droplet is assumed to have a parabolic trajectory. During $\Delta t_{surf} = 4\pi/\omega_s - t^+ + t^\star$, the droplet is in contact with the surface and interacts with its own wavefield. Knowing $\dot{z}(t^+)$ gives a measure of the amplitude of the standing waves on the surface.

## A.2 Horizontal dynamics

This part of the dynamics is solved by an event-driven algorithm. Only the two instants $t^\star$ and $t^+$ are considered, since one knows the dynamics of the droplet between each.

### A.2.1 Parabolic trajectory

Between $t^+$ and $t^\star$, the only forces acting on the droplet are the external forces, since no contact with the surface occurs. As a consequence, the motion along the $x$ and $y$ directions is given by

$$\Delta x_{fly} = \dot{x}(t^\star)\Delta t_{fly} + \frac{\Sigma F_x}{2m}\Delta t_{fly}^2, \tag{A.8}$$

$$\Delta y_{fly} = \dot{y}(t^\star)\Delta t_{fly} + \frac{\Sigma F_y}{2m}\Delta t_{fly}^2, \tag{A.9}$$

where $\Delta x_{fly} = x(t^+) - x(t^\star)$ (resp. $\Delta y_{fly} = y(t^+) - y(t^\star)$) is the distance travelled between the impact point and the take-off point along the $x$-direction (resp. along the $y$-direction). In this manuscript, we only consider external forces arising from harmonic potentials. This gives

$$\frac{\Sigma F_x}{m} = -\omega^2 x, \tag{A.10}$$

$$\frac{\Sigma F_y}{m} = -\omega^2 y, \tag{A.11}$$

where $(x, y)$ is the distance from the center of the harmonic potential and $\omega$ its natural frequency.

The impact point $(x(t^+), y(t^+))$ is stored in a memory array in order to compute the total wavefield on the surface. Note that trajectories presented in this manuscript are realised considering the impact points.

### A.2.2 Interaction with the surface

At impact, i.e. at $t = t^+$, the droplet loses part of its velocity because of the inelastic interaction with the interface. The vector locally perpendicular to the wavefield is computed as follow. Knowing the position of all previous impact, the

wavefield gradient $\nabla\zeta(\vec{r})(t^+)$ is computed. The wavefield writes

$$\begin{aligned}\zeta(\vec{r},t^+) =& \zeta_0 \sum_{n=1}^{5\mathrm{Me}+1} J_0\left(2\pi\frac{|\vec{r}(t^+)-\vec{r}_n|}{\lambda_F}\right)\times \\ & \exp\left(-\frac{|\vec{r}(t^+)-\vec{r}_n|}{\delta}\right)\exp\left(-\frac{t^+-n\tau_F}{\mathrm{Me}\,\tau_F}\right). \end{aligned} \tag{A.12}$$

The Bessel function $J_0$ as well as the Bessel function $J_1$ discussed below are computed thanks to the algorithm found in the Numerical Recipes [145]. In the equation, the sum over the previous impacts is truncated for practical purpose. Indeed, since the wave amplitude is multiplied by $\exp\left(-(t^+-n\tau_F)/\mathrm{Me}\,\tau_F\right)$, the last sources are negligible compared to the first ones. We choose to truncate the series at the $5\mathrm{Me}+1^{\text{th}}$ term since $\exp(-5) = 6.7\,10^{-3} \ll 1$. The wave amplitude $\zeta_0$ is calibrated via energetic arguments. Assuming that the droplet relative kinetic energy is converted into potential energy for elevating the fluid to the height $\zeta_0$ leads to

$$\zeta_0 = \epsilon\left(\dot{z}(t^+) - A\omega_s\cos\left(\omega_s t^+\right)\right)^2\cos\left(\omega_s t^+\right)^2. \tag{A.13}$$

The third factor in the right-hand side of this equation accounts for a correction to the amplitude because of the phase of the surface oscillation at impacts. The gradient of the field writes

$$\begin{aligned}\nabla\zeta(\vec{r},t^+) =& -\zeta_0 \sum_{n=1}^{5\mathrm{Me}+1} \exp\left(-\frac{t^+-n\tau_F}{\mathrm{Me}\,\tau_F}\right)\times \\ & \left(\frac{2\pi}{\lambda_F}J_1\left(2\pi\frac{|\vec{r}(t^+)-\vec{r}_n|}{\lambda_F}\right)+\frac{1}{\delta}J_0\left(2\pi\frac{|\vec{r}(t^+)-\vec{r}_n|}{\lambda_F}\right)\right)\times \\ & \exp\left(-\frac{|\vec{r}(t^+)-\vec{r}_n|}{\delta}\right)\frac{\vec{r}(t^+)-\vec{r}_n}{|\vec{r}(t^+)-\vec{r}_n|}. \end{aligned} \tag{A.14}$$

Finally, the normal vector $\vec{n}(\vec{r},t^+)$ writes as

$$\vec{n}(\vec{r},t^+) = \left(-\partial_x\zeta(\vec{r},t^+), -\partial_y\zeta(\vec{r},t^+), 1\right). \tag{A.15}$$

Since the amplitude $\zeta_0$ is small compared to the wavelength $\lambda_F$, this expression verifies the condition $|\vec{n}| = 1 + \mathcal{O}\left(\zeta_0/\lambda_F\right)$. We seek for the vector $\vec{p}(\vec{r},t^+) = C_1\vec{n}(\vec{r},t^+) + C_2\left(\dot{\vec{r}}(t^+) - \dot{z}_s(t^+)\vec{e}_z\right)$, perpendicular to $\vec{n}(\vec{r},t^+)$ and

unitary. This vector lies in the plane formed by $\vec{n}(\vec{r},t^+)$ and $\left(\dot{\vec{r}}(t^+)-\dot{z}_s(t^+)\vec{e}_z\right)$. Mathematically, those conditions write

$$\vec{p}(\vec{r},t^+).\vec{n}(\vec{r},t^+)=0, \tag{A.16}$$

$$\vec{p}(\vec{r},t^+).\vec{p}(\vec{r},t^+)=1. \tag{A.17}$$

Since the impact of the droplet with the surface is assumed to be completely inelastic, the relative velocity along the normal vector $\vec{n}(\vec{r},t^+)$ is reduced to zero. As a consequence, the relative speed of the droplet is

$$v_{surf}(t^+)=\left(\dot{\vec{r}}(t^+)-\dot{z}_s(t^+)\vec{e}_z\right).\vec{p}(\vec{r},t^+), \tag{A.18}$$

and this velocity is oriented along $\vec{p}(\vec{r},t^+)$.

Between the instant $t^+$ and $4\pi/\omega_s+t^\star=t^++\Delta t_{surf}$, i.e. the new take-off instant, the droplet is submitted to a lubrication force. This force is assumed to decrease exponentially the speed with

$$v_{surf}\left(4\pi/\omega_s+t^\star\right)=v_{surf}(t^+)\exp\left(-\frac{\Delta t_{surf}}{T_V}\right), \tag{A.19}$$

where $T_v$ is the damping time. The distance travelled on the surface between those two instants is obtained by time integration of the previous equation

$$d_{surf}=v_{surf}(t^+)T_V\left(1-\exp\left(-\frac{\Delta t_{surf}}{T_V}\right)\right). \tag{A.20}$$

Therefore, one has

$$\Delta x_{surf}=d_{surf}\left(\vec{p}(\vec{r},t^+).\vec{e}_x\right), \tag{A.21}$$

$$\Delta y_{surf}=d_{surf}\left(\vec{p}(\vec{r},t^+).\vec{e}_y\right), \tag{A.22}$$

$$\dot{x}\left(4\pi/\omega_s+t^\star\right)=v_{surf}\left(4\pi/\omega_s+t^\star\right)\left(\vec{p}(\vec{r},t^+).\vec{e}_x\right), \tag{A.23}$$

$$\dot{y}\left(4\pi/\omega_s+t^\star\right)=v_{surf}\left(4\pi/\omega_s+t^\star\right)\left(\vec{p}(\vec{r},t^+).\vec{e}_y\right), \tag{A.24}$$

where $\Delta x_{surf}=x(4\pi/\omega_s+t^\star)-x(t^+)$ and $\Delta y_{surf}=y(4\pi/\omega_s+t^\star)-y(t^+)$. The new position $(x(4\pi/\omega_s+t^\star),y(4\pi/\omega_s+t^\star))$ and the new velocity

| Parameter | Value (Unit) |
|---|---|
| Forcing amplitude $A$ | $160\ (\mu\mathrm{m})$ |
| Forcing frequency $f_s$ | $80\ (\mathrm{Hz})$ |
| Forcing angular frequency $\omega_s$ | $502.655\ (\mathrm{rad/s})$ |
| Dimensionless acceleration $\Gamma$ | $4.12\ (-)$ |
| Faraday wavelength $\lambda_F$ | $4.75\ (\mathrm{mm})$ |
| Faraday frequency $f_F$ | $40\ (\mathrm{Hz})$ |
| Faraday angular frequency $\omega_F$ | $251.327\ (\mathrm{rad/s})$ |
| Spatial damping $\delta$ | $2.5\ (\lambda_F)$ |
| Restitution coefficient $\epsilon$ | $0.006\ (-)$ |
| Damping time $T_V$ | $45\ (\mathrm{ms})$ |
| Time above surface $\Delta t_{fly}$ | $14.36\ (\mathrm{ms})$ |
| Time on surface $\Delta t_{surf}$ | $10.64\ (\mathrm{ms})$ |

**Table A.1:** List of the parameters used in the numerical simulations.

$(\dot{x}(4\pi/\omega_s + t^\star), \dot{y}(4\pi/\omega_s + t^\star))$ are used for a new "parabolic trajectory" phase. This algorithm is repeated until a given number of iteration is realised.

### A.2.3 Discussion regarding the algorithm

This numerical scheme of integration has some pros and cons. On the one hand, since the dynamics is integrated via an event-driven algorithm, the simulations are fast, with a duration only proportional to the walker memory. At memory $\mathrm{Me} = 100$, for $2.5\,10^5$ time steps, simulations are completed under 30 seconds on a desktop computer. This allows for long simulations and statistical analysis of the dynamics. Furthermore, since exact equations are considered in the scheme of integration numerical precision is not an issue. On the other hand, some drawbacks exist. Indeed, because the vertical and horizontal dynamics are independent in the numerics, this algorithm does not allow the analysis of chaotic bouncers [189] neither does it consider the relation between $\Gamma$ and $\mathrm{Me}$. This therefore limits the comparison between numerics and experiments. Furthermore, the wave description is not exact but only an approximation as described in [52]. A more precise expression would require a full resolution of Navier-Stokes equations [119].

# B

# Hydrodynamic interactions

The key of low-Reynolds number locomotion lies in the possibility for particles to interact by induced flows and drag forces. On the one hand, a particle moving relative to a fluid induces a flow around itself. On the other hand, when immersed in a flow, particles are submitted to forces dragging them into flow. The consequence are hydrodynamic interactions mediated by the fluid surrounding the particles. The drag force involved here is easy to describe since it is found in most elementary textbooks. For a particle in a flow $\vec{u}(\vec{r})$, the drag force is expressed by

$$\vec{F}_d = 6\pi a\eta\vec{u}(\vec{r}), \tag{B.1}$$

which is the Stokes drag. The flow induced by a moving particle is more complex to describe given the mathematical structure of the Stokes equation.

## B.1 Mathematical background

The demonstration relative to the flow induced by moving objects is inspired by [110], and uses solutions of harmonic and biharmonic equations. In the following development we will need to solve

$$\Delta^2\psi = \delta(\vec{r}). \tag{B.2}$$

This is a biharmonic equation where $\Delta$ is the Laplacian operator and $\delta$ the Dirac delta. This equation can be easily solved in Fourier space. For $\tilde{\psi} = \mathcal{F}(\psi)$, one

has

$$\tilde{\psi} = \frac{1}{|\vec{k}|^4}. \tag{B.3}$$

Therefore, the solution in real space is

$$\psi = \frac{1}{4\pi^2} \int_0^{\pi} \int_0^{\infty} \frac{e^{i\cos\theta|\vec{r}||\vec{k}|}}{|\vec{k}|^2} d|\vec{k}| d\theta, \tag{B.4}$$

which gives

$$\psi = -\frac{|\vec{r}|}{8\pi} \quad \rightarrow \quad \delta(\vec{r}) = -\frac{1}{8\pi}\Delta^2|\vec{r}|. \tag{B.5}$$

Am immediate consequence of this equation are the following relations, originating from classical electromagnetism when studying the electric potential and electric field generated by a point-charge

$$\delta(\vec{r}) = \frac{1}{4\pi}\vec{\nabla}\left(\frac{\vec{r}}{|\vec{r}|^3}\right), \tag{B.6}$$

$$= -\frac{1}{4\pi}\Delta\left(\frac{1}{|\vec{r}|}\right). \tag{B.7}$$

Furthermore, solutions of the equation $\Delta\psi = 0$ have interesting properties. As stated in [94],

Theorem 2 *If $\psi$ is harmonic (i.e. $\Delta\psi = 0$) and continuously differentiable in a closed regular region $\mathcal{R}$, and vanishes at all points of the boundary of $\mathcal{R}$, it vanishes at all points of $\mathcal{R}$*[*].

Theorem 3 *A function, harmonics and continuously differentiable in a closed regular region $\mathcal{R}$, is uniquely determined by its values on the boundary of $\mathcal{R}$*[*].

With those tools, let us study the flow generated by a single point-force and a single point-torque.

## B.2 Point-force and point-torque descriptions

Let us assume a point particle located at the origin and submitted to a force $\vec{f}\delta(\vec{r})$, where $\delta(\vec{r})$ is the Dirac delta and $\vec{f}$ is a constant vector. The equation describing

[*]This theorem holds for an infinite regular region $\mathcal{R}$ (see [94], chap.8, pg.218).

the flow is given by the continuity equation and the Stokes equation

$$\vec{\nabla}.\vec{u} = 0, \tag{B.8}$$

$$\vec{\nabla}p = \eta\Delta\vec{u} + \vec{f}\delta(\vec{r}). \tag{B.9}$$

The Stokes equation being linear, the solution of the fields $p$ and $\vec{u}$ are expected to be linearly proportional to the point force $\vec{f}$,

$$p = \vec{h}.\vec{f}, \tag{B.10}$$

$$\vec{u} = \hat{\mathbb{G}}.\vec{f}, \tag{B.11}$$

where the field $\vec{h}$ (resp. $\hat{\mathbb{G}}$) is a vector field (resp. a second-order tensor field). Taking the divergence of (B.9) and using the continuity equation (B.8), one gets

$$\Delta\left(\vec{h}.\vec{f}\right) = \vec{f}.\vec{\nabla}\delta(\vec{r}). \tag{B.12}$$

This equation can be written as

$$\left(\vec{f}.\Delta\vec{h} - \frac{\vec{f}}{4\pi}\vec{\nabla}\left(\vec{\nabla}.\frac{\vec{r}}{|\vec{r}|^3}\right)\right) = 0. \tag{B.13}$$

Using vector calculus identities and knowing that $\vec{r}/|\vec{r}|^3$ is an irrotationnal vector field, one has

$$\vec{f}.\Delta\left(\vec{h} - \frac{1}{4\pi}\frac{\vec{r}}{|\vec{r}|^3}\right) = 0. \tag{B.14}$$

Finally, assuming that the pressure field cancels at infinity and using Kellogg theorems gives the $\vec{h}$-vector field

$$\vec{h} = \frac{1}{4\pi}\frac{\vec{r}}{|\vec{r}|^3} \quad \rightarrow \quad p = \frac{\vec{f}.\vec{r}}{4\pi|\vec{r}|^3}. \tag{B.15}$$

This scalar field is the same as the one obtained in classical electromagnetism for the electric potential created by a electric dipole, $\vec{f}$ being the "dipole moment" in this analogy. Knowing the pressure field, one can access the velocity field. The equation reads

$$\vec{\nabla}\left(\frac{\vec{f}.\vec{r}}{4\pi|\vec{r}|^3}\right) = \eta\Delta\left(\hat{\mathbb{G}}.\vec{f}\right) + \vec{f}\delta(\vec{r}). \tag{B.16}$$

The force $\vec{f}$ being constant, one has

$$\left(\vec{\nabla} \otimes \frac{\vec{r}}{4\pi|\vec{r}|^3}\right) \vec{f} = \eta \left(\Delta \hat{\mathbb{G}}\right) . \vec{f} + \delta(\vec{r}) \hat{\mathbb{I}} \vec{f}. \tag{B.17}$$

where $\otimes$ is for the dyadic product and $\hat{\mathbb{I}}$ is the unit tensor. Using Eqs.(B.6) and (B.7) gives

$$\left(\eta \Delta \hat{\mathbb{G}} + \frac{1}{4\pi} \left(\vec{\nabla} \otimes \vec{\nabla} - \hat{\mathbb{I}} \Delta\right) \left(\frac{1}{|\vec{r}|}\right)\right) . \vec{f} = 0. \tag{B.18}$$

We would like to use the same strategy used for the computation of the pressure field and place the Laplacian operator before the whole equation. To do so, one could use the equation

$$\Delta |\vec{r}| = \frac{2}{|\vec{r}|}, \tag{B.19}$$

which leads to

$$\Delta \left(\eta \hat{\mathbb{G}} + \frac{1}{8\pi} \left(\vec{\nabla} \otimes \vec{\nabla} - \hat{\mathbb{I}} \Delta\right) |\vec{r}|\right) . \vec{f} = 0. \tag{B.20}$$

Assuming that the velocity field vanishes at infinity and using Kellogg theorems, one gets

$$\hat{\mathbb{G}} = \frac{1}{8\pi\eta|\vec{r}|} \left(\hat{\mathbb{I}} + \frac{\vec{r} \otimes \vec{r}}{|\vec{r}|^2}\right) \quad \rightarrow \quad \vec{u} = \frac{1}{8\pi\eta|\vec{r}|} \left(\vec{f} + \frac{\vec{r}(\vec{r}.\vec{f})}{|\vec{r}|^2}\right). \tag{B.21}$$

The tensor $\hat{\mathbb{G}}$ is referred to as the *Oseen tensor* and the singularities in Eqs.(B.15) and (B.21) correspond to the *Stokeslet*. Those two equations describe the fluid dynamics under the influence of a single external point source. The velocity field generated by a Stokeslet is illustrated in Fig.B.1.

In this manuscript, another useful case is the one involving a single point torque. Such a case is observed for $\vec{f} = \vec{\nabla} \times (\vec{\gamma}\delta(\vec{r}))$ [29]. Indeed, this assertion can be proved by studying the torque exerted on a spherical surface $\mathcal{S}$ centred on the

singularity. One has

$$\vec{\tau} = \oint_{\mathcal{S}} \vec{r} \times \left( \vec{\nabla} p.\vec{n} - \eta \Delta \vec{u}.\vec{n} \right) dr^2, \tag{B.22}$$

$$= \int_{\mathcal{V}} \vec{r} \times \vec{f} dr^3. \tag{B.23}$$

This last integral can be written in terms of the divergence of $\delta(\vec{r})$ thanks to vector calculus identities,

$$\vec{\tau} = \int_{\mathcal{V}} (\vec{r}.\vec{\gamma}) \, \vec{\nabla} \delta(\vec{r}) - \left( \vec{r}.\vec{\nabla} \delta(\vec{r}) \right) \vec{\gamma} dr^3, \tag{B.24}$$

$$= \int_{\mathcal{V}} -\vec{\nabla} \left( \vec{r}.\vec{\gamma} \right) \delta(\vec{r}) + 3\delta(\vec{r}) \vec{\gamma} dr^3, \tag{B.25}$$

where the properties relative to the derivative of the Dirac delta have been used to obtain the last equality. Integrating over the whole enclosed volume gives

$$\vec{\tau} = 2\vec{\gamma}, \tag{B.26}$$

which indeed corresponds to a point torque at the singularity. Considering the point torque, the flow equations are given by

$$\vec{\nabla}.\vec{u} = 0, \tag{B.27}$$

$$\vec{\nabla} p = \eta \Delta \vec{u} + \vec{\nabla} \times \left( \vec{\gamma} \delta(\vec{r}) \right). \tag{B.28}$$

Taking the divergence of the Eq.(B.28) and using the continuity equation (B.27) leads to

$$\Delta p = 0, \tag{B.29}$$

which, using the properties relative to harmonic functions and assuming that the pressure field vanishes at infinity, gives $p = 0$. As a consequence, Stokes equation reduces to

$$\eta \Delta \vec{u} + \vec{\nabla} \times \left( \vec{\gamma} \delta(\vec{r}) \right) = 0. \tag{B.30}$$

This equation being linear and given its mathematical structure, the velocity field is expected to be given by

$$\vec{u} = \vec{g} \times \vec{\gamma}, \tag{B.31}$$

which leads to

$$\left(\eta\Delta\vec{g} + \vec{\nabla}\delta\right) \times \vec{\gamma} = 0. \tag{B.32}$$

Finally, using Eq.(B.6) and that the field $\vec{r}/|\vec{r}|^3$ is irrotationnal, one obtains

$$\Delta\left(\eta\vec{g} + \frac{1}{4\pi}\frac{\vec{r}}{|\vec{r}|^3}\right) \times \vec{\gamma} = 0. \tag{B.33}$$

Again, assuming a vanishing velocity field at infinity, one gets

$$\vec{g} = -\frac{\vec{r}}{4\pi\eta|\vec{r}|^3} \quad \rightarrow \quad \vec{u} = \frac{\vec{\tau}\times\vec{r}}{8\pi\eta|\vec{r}|^3}. \tag{B.34}$$

The singularity described by this corresponds to the *Rotlet*, i.e. the velocity and pressure fields generated by a point-torque at the origin. The velocity field generated by a Rotlet is illustrated in Fig.B.1.

Therefore, neighbouring particles are dragged by this flow and moves along it. The velocity $\vec{v}_i$ of a given particle labelled $i$ is linearly related to the forces $\vec{f}_j$ and torques $\vec{\tau}_j$ applied to all other particles labelled $j$. Mathematically,

$$\vec{v}_i = \hat{\mu}_{ij}.\left(\vec{f}_j, \vec{\tau}_j\right)^T, \tag{B.35}$$

where $T$ denotes the transposed matrix. Here, $\hat{\mu}_{ij}$ is the mobility matrix linking the dynamics of particle $i$ to the dynamics of all particles $j$. The components of this matrix are summarized in the following table, under the "velocity field"-entry. In the case of finite size particle, the mobility matrix gets more complex since the rotational velocity of each particle has to be taken into account.

| Singularity | Velocity field | Pressure field |
|---|---|---|
| Stokeslet | $\vec{u} = \frac{1}{8\pi\eta\|\vec{r}\|}\left(\vec{f} + \frac{\vec{r}(\vec{r}.\vec{f})}{\|\vec{r}\|^2}\right)$ | $p = \frac{\vec{f}.\vec{r}}{4\pi\|\vec{r}\|^3}$ |
| Rotlet | $\vec{u} = \frac{\vec{\tau}\times\vec{r}}{8\pi\eta\|\vec{r}\|^3}$ | $p = 0$ |

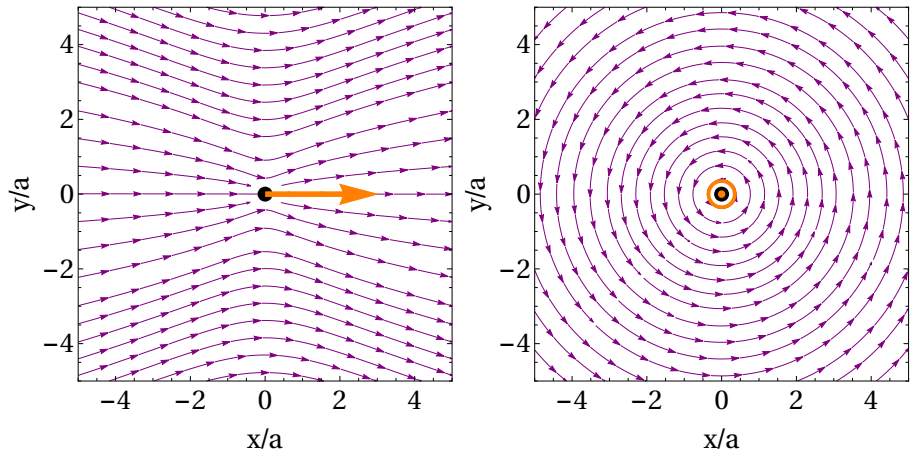


**Figure B.1:** Stokeslet and Rotlet illustrated. **(Left)** Velocity field generated by a single point-force at the origin (orange arrow). **(Right)** Velocity field generated by a single point-torque at the origin (orange point). Note that the field intensity is not related to the density of arrow into the flow. The Stokeslet decreases as $1/|\vec{r}|$ and the Rotlet as $1/|\vec{r}|^2$.

## B.3 Finite-size particles

When considering finite-size particles, the flow generated by moving particles can also exert torques. Indeed, the amplitude of the velocity field is seen to decrease with the distance to the source. As a consequence, the viscous drag on the surface of a neighbouring particle is not symmetric, being more intense on the hemisphere facing the flow source and being less intense on the opposite hemisphere. As a consequence, torques arise and neighbouring particles can experience translational and rotational motion. Mathematically, this leads to the following equation

$$(\vec{v}_i, \vec{\omega}_i) = \hat{\mu}_{ij} . \left(\vec{f}_j, \vec{\tau}_j\right)^T . \tag{B.36}$$

Formally, the mobility matrix is built as follows

$$\hat{\mu}_{ij} = \begin{pmatrix} \hat{\mu}_{ij}^{TT} & \hat{\mu}_{ij}^{TR} \\ \hat{\mu}_{ij}^{RT} & \hat{\mu}_{ij}^{RR} \end{pmatrix}, \tag{B.37}$$

where the submatrice superscripted $TT$ couples the translational motion of two particles (i.e. alike the Stokeslet), $TR$ couples the translation to the torque (i.e. alike the Rotlet), $RT$ couples the rotation to the force and $RR$ couples the

rotational motion of two particles. The expression of each submatrice needs to consider the finite size of each particle since the expression of the Stokeslet and Rotlet in the previous section does not hold any more. To circumvent this issue, a solution is to express the induced flows in a series of powers of $1/|\vec{r}|$. This approach is named the *Rotne-Prager approximation* or the *Method of reflexion*. A full mathematical description can be found in [114]. For a particle labelled $j$ with a radius $a_j$ submitted to a total force and torque $(\vec{f}_j, \vec{\tau}_j)$, at a distance $\vec{r}_{ij}$ of the center of mass of a particle $i$, the inter-mobility submatrices are

$$\hat{\mu}_{ij}^{TT} = \frac{1}{8\pi\eta|\vec{r}_{ij}|}\left(\hat{\mathbb{I}} + \frac{\vec{r}_{ij}\otimes\vec{r}_{ij}}{|\vec{r}_{ij}|^2}\right) + \frac{\left(a_i^2+a_j^2\right)}{24\pi\eta|\vec{r}_{ij}|^3}\left(\hat{\mathbb{I}} - 3\frac{\vec{r}_{ij}\otimes\vec{r}_{ij}}{|\vec{r}_{ij}|^2}\right) + \mathcal{O}\left(\frac{1}{|\vec{r}_{ij}|^4}\right), \tag{B.38}$$

$$\hat{\mu}_{ij}^{TR} = \frac{\hat{\epsilon}.\vec{r}_{ij}}{8\pi\eta|\vec{r}_{ij}|^3} + \mathcal{O}\left(\frac{1}{|\vec{r}_{ij}|^5}\right), \tag{B.39}$$

$$\hat{\mu}_{ij}^{RT} = -\frac{\hat{\epsilon}.\vec{r}_{ij}}{8\pi\eta|\vec{r}_{ij}|^3} + \mathcal{O}\left(\frac{1}{|\vec{r}_{ij}|^5}\right), \tag{B.40}$$

$$\hat{\mu}_{ij}^{RR} = -\frac{1}{16\pi\eta|\vec{r}_{ij}|^3}\left(\hat{\mathbb{I}} - 3\frac{\vec{r}_{ij}\otimes\vec{r}_{ij}}{|\vec{r}_{ij}|^2}\right) + \mathcal{O}\left(\frac{1}{|\vec{r}_{ij}|^6}\right), \tag{B.41}$$

where $\vec{r}_{ij} = \vec{r}_i - \vec{r}_j$. The corrections correspond to three-particles interactions. The factor $\hat{\epsilon}.\vec{r}_{ij}$ is the dot-product with the Levi-Civita third-order tensor which gives a cross product once multiplied with another vector. For the self-mobility submatrices, one has

$$\hat{\mu}_{ii}^{TT} = \frac{1}{6\pi\eta a_i} + \mathcal{O}\left(\frac{1}{|\vec{r}_{ij}|^4}\right), \tag{B.42}$$

$$\hat{\mu}_{ii}^{TR} = 0 + \mathcal{O}\left(\frac{1}{|\vec{r}_{ij}|^7}\right), \tag{B.43}$$

$$\hat{\mu}_{ii}^{RT} = 0 + \mathcal{O}\left(\frac{1}{|\vec{r}_{ij}|^7}\right), \tag{B.44}$$

$$\hat{\mu}_{ii}^{RR} = \frac{1}{8\pi\eta a_i^3} + \mathcal{O}\left(\frac{1}{|\vec{r}_{ij}|^6}\right), \tag{B.45}$$

where the corrections are due to pair interactions with neighbouring particles. Note that, in the case of only two particles interacting via hydrodynamic interactions, the corrections $\mathcal{O}(1/|\vec{r}|^n)$ in the submatrices listed above are of higher

order.

# C

# Determining the hydrodynamic centre

In order to find the hydrodynamic centre of rotation, let us begin by describing parametrically the triangle. The position of each vertex relative to the center of the reference frame is

$$\vec{p}_1 = d\cos\left(\frac{\pi}{6} - \alpha\right)\vec{e}_y, \tag{C.1}$$

$$\vec{p}_2 = -d\cos\left(\frac{\pi}{3} + \alpha\right)\vec{e}_x, \tag{C.2}$$

$$\vec{p}_3 = d\cos\left(\frac{\pi}{3} + \alpha\right)\vec{e}_x. \tag{C.3}$$

The case $\alpha = 0$ gives the equilateral triangle. This parametrisation gives immediately the length of each side of the triangle. The two equal sides of the triangle have a length $d$. The side parallel to the $x$-axis has a length

$$d' = 2d\sin\left(\frac{\pi}{6} - \alpha\right). \tag{C.4}$$

This equation allows to link the angular deformation $\alpha$ to the side length variation $A_{def} = d - d'$. Assuming small values of $\alpha$, one has

$$\begin{aligned}\frac{d - A_{def}}{2d} &= \sin\left(\frac{\pi}{6} - \alpha\right), \\ &= \sin\left(\frac{\pi}{6}\right) - \alpha\cos\left(\frac{\pi}{6}\right) + \mathcal{O}(\alpha^3).\end{aligned} \tag{C.5}$$

This relation gives

$$A_{def} = \sqrt{3}d\alpha + \mathcal{O}(\alpha^3). \tag{C.6}$$

Let us now imagine that the particles rotate counter-clockwise, all in the same direction, and let us assume that they all have the same diameter. All particles are therefore submitted to hydrodynamic forces which write

$$\begin{aligned}
\vec{F}_{p_1} &= -\frac{12\pi\eta a^4}{d^2}|\vec{\omega}|\cos\left(\frac{\pi}{6}-\alpha\right)\vec{e}_x, \\
\vec{F}_{p_2} &= \frac{6\pi\eta a^4}{d^2}\cos\left(\frac{\pi}{6}-\alpha\right)|\vec{\omega}|\vec{e}_x \\
&\quad -\left(\frac{6\pi\eta a^4}{d'^2}+\frac{6\pi\eta a^4}{d^2}\sin\left(\frac{\pi}{6}-\alpha\right)\right)|\vec{\omega}|\vec{e}_y, \\
\vec{F}_{p_3} &= \frac{6\pi\eta a^4}{d^2}\cos\left(\frac{\pi}{6}-\alpha\right)|\vec{\omega}|\vec{e}_x \\
&\quad +\left(\frac{6\pi\eta a^4}{d'^2}+\frac{6\pi\eta a^4}{d^2}\sin\left(\frac{\pi}{6}-\alpha\right)\right)|\vec{\omega}|\vec{e}_y.
\end{aligned} \tag{C.7}$$

Those three forces lead to a global rotation around a unique point which, given $\vec{F}_{p_1}$, is located along the $y$-axis. Given the similarities between $\vec{F}_{p_2}$ and $\vec{F}_{p_3}$, only one of the two is required to obtain the hydrodynamic centre. The hydrodynamic centre is located at the intersection between the $y$-axis and the line perpendicular to $\vec{F}_{p_2}$. The parametric equation of this line is given by

$$y(x) = \frac{4\cos\left(\frac{\pi}{6}-\alpha\right)\sin^2\left(\frac{\pi}{6}-\alpha\right)}{1+4\sin^3\left(\frac{\pi}{6}-\alpha\right)}\left(x+d\sin\left(\frac{\pi}{6}-\alpha\right)\right), \tag{C.8}$$

which is purely geometric and does not depend on physical ingredient such as the speed, viscosity, etc. Therefore, the hydrodynamic centre of rotation is located at

$$\vec{p}_{hcr} = \frac{4d\cos\left(\frac{\pi}{6}-\alpha\right)\sin^3\left(\frac{\pi}{6}-\alpha\right)}{1+4\sin^3\left(\frac{\pi}{6}-\alpha\right)}\vec{e}_y. \tag{C.9}$$

Knowing that the center of mass is located at

$$\vec{p}_{cm} = \frac{1}{3}d\cos\left(\frac{\pi}{6}-\alpha\right)\vec{e}_y, \tag{C.10}$$

the distance between the hydrodynamic centre and the center of mass is

$$\begin{aligned} \vec{p}_{cm} - \vec{p}_{hcr} &= d\alpha\vec{e}_y + \mathcal{O}(\alpha^2) \\ &= \frac{A_{def}}{\sqrt{3}}\vec{e}_y + \mathcal{O}(A_{def}^2) \end{aligned} \tag{C.11}$$

# References


[1] Andersen, A., Madsen, J., Reichelt, C., Ahl, S. R., Lautrup, B., Ellegaard, C., Levinsen, M. T., & Bohr, T. (2015). Double-slit experiment with single wave-driven particles and its relation to quantum mechanics. *Phys. Rev. E*, 92, 013006.

[2] Argoul, F., Arneodo, A., & Richetti, P. (1987). Experimental evidence for homoclinic chaos in the belousov-zhabotinskii reaction. *Phys. Lett. A*, 120, 269.

[3] Barrio, R., Blesa, F., Serrano, S., & Shilnikov, A. (2011). Global organization of spiral structures in biparameter space of dissipative systems with shilnikov saddle-foci. *Phys. Rev. E*, 84, 035201.

[4] Bartumeus, F., Catalan, J., Fulco, U. L., Lyra, M. L., & Viswanathan, G. M. (2002). Optimizing the encounter rate in biological interactions: Lévy versus brownian strategies. *Phys. Rev. Lett.*, 88, 097901.

[5] Bazazi, S., Buhl, J., Hale, J. J., Anstey, M. L., Sword, G. A., & Simpson, S. J. (2008). Collective motion and cannibalism in locust migratory bands. *Current biology*, 18, 735.

[6] Becco, C., Vandewalle, N., Delcourt, J., & Poncin, P. (2006). Experimental evidences of a structural and dynamical transition in fish school. *Physica A*, 367, 487.

[7] Bechinger, C., Leonardo, R. D., Löwen, H., Reichhardt, C., Volpe, G., & Volpe, G. (2016). Active particles in complex and crowded environments. *Rev. Mod. Phys.*, 88, 045006.

[8] Bénichou, O., Loverdo, C., Moreau, M., & Voituriez, R. (2011). Intermittent search strategies. *Rev. Mod. Phys.*, 83, 81.

[9] Benjamin, T. B. & Ursell, F. (1954). The stability of the plane free surface of a liquid in vertical periodic motion. *Proc. R. Soc. Lond. A*, 225, 505.

[10] Berg, H. C. (2004). *E. coli in Motion*. Springer.

[11] Berg, H. C. & Brown, D. A. (1972). Chemotaxis in escherichia coli analysed by three-dimensional tracking. *Nature*, 239, 500.

[12] Berg, H. C. & Turner, L. (1979). Movement of microorganisms in viscous environments. *Nature*, 278, 349.

[13] Bonabeau, E., Dorigo, M., & Theraulaz, G. (1999). *Swarm Intelligence: From Natural to Artificial Systems*. Oxford University Press.

[14] Borghesi, C., Moukhtar, J., Labousse, M., Eddi, A., Fort, E., & Couder, Y. (2014). Interaction of two walkers: Wave-mediated energy and force. *Phys. Rev. E*, 90, 063017.

[15] Boyland, P. L., Aref, H., & Stremler, M. A. (2000). Topological fluid mechanics of stirring. *J. Fluid Mech.*, 403, 277.

[16] Briand, G. & Dauchot, O. (2016). Crystallization of self-propelled hard discs. *Phys. Rev. Lett.*, 117, 098004.

[17] Brown, A. & Poon, W. (2014). Ionic effects in self-propelled pt-coated janusswimmers. *Soft Mat.*, 10, 4016.

[18] Budrene, E. O. & Berg, H. C. (1995). Dynamics of formation of symmetrical patterns by chemotactic bacteria. *Nature*, 376, 49.

[19] Bush, J. W. M. (2010). Quantum mechanics writ large. *PNAS*, 107(41), 17455.

[20] Bush, J. W. M. (2014). Pilot-wave hydrodynamics. *Annu. Rev. Fluid Mech.*, 47, 269.

[21] Bush, J. W. M., Oza, A. U. ., & Moláček, J. (2014). The wave-induced added mass of walking droplets. *J. Fluid Mech.*, 755, R7.

[22] Buttinoni, I., Bialké, J., Kümmel, F., Löwen, H., Bechinger, C., & Speck, T. (2013). Dynamical clustering and phase separation in suspensions of self-propelled colloidal particles. *Phys. Rev. Lett.*, 110, 238301.

[23] Campuzano, S., Orozco, J., Kagan, D., Guix, M., Gao, W., Sattayasamitsathit, S., Claussen, J. C., Merkoçi, A., & Wang, J. (2012). Bacterial isolation by lectin-modified microengines. *Nano Lett.*, 12, 396.

[24] Chan, D. Y. C., Henry, J. D., & White, L. R. (1981). The interaction of colloidal particls collected at fluid interfaces. *J. Colloid Interface Sci.*, 79, 410.

[25] Chaudhuri, D. (2014). Active brownian particles: Entropy production and fluctuation response. *Phys. Rev. E*, 90, 022131.

[26] Chin, D. D. & Lentink, D. (2016). Flapping wing aerodynamics: from insects to vertebrates. *J. Exp. Biol.*, 219, 920.

[27] Chinomona, R., Lajeunesse, J., Mitchell, W. H., Yao, Y., & Spagnolie, S. E. (2015). Stability and dynamics of magnetocapillary interactions. *Soft Mat.*, 11, 1828.

[28] Chupeau, M., Bénichou, O., & Voituriez, R. (2015). Cover times of random searches. *Nature Phys.*, 11, 844.

[29] Chwang, A. T. & Wu, T. Y.-T. (1974). Hydromechanics of low-reynolds-number flow. part 1. rotation of axisymmetric prolate bodies. *J. Fluid Mech.*, 63, 607.

[30] Couceiro, M. S., Ferreira, N. M. F., & Mechado, J. A. T. (2010). Modeling and control of a dragonfly-like robot. *J. of Control Sci. and Eng.*, 2010, 1.

[31] Couder, Y. & Fort, E. (2006). Single-particle diffraction and interference at a macroscopic scale. *Phys. Rev. Lett.*, 97, 154101.

[32] Couder, Y., Fort, E., Gauthier, C.-H., & Boudaoud, A. (2005a). From bouncing to floating: Noncoalesence of drops on a fluid bath. *Phys. Rev. Lett.*, 94, 177801.

[33] Couder, Y., Fort, E., Protière, S., & Boudaoud, A. (2005b). Walking and orbiting droplets. *Nature*, 437, 208.

[34] Crespi, A. & Ijspeert, A. J. (2006). Amphibot ii: An amphibious snake robot that crawls and swims using a central pattern generator. *Proc. of the 9th Int. Conf. on Climbing and Walking robots*, (pp.19).

[35] Cressoni, J. C., da Silva, M. A. A., & Viswanathan, G. M. (2007). Amnestically induced persistence in random walks. *Phys. Rev. Lett.*, 98, 070603.

[36] Cressoni, J. C., Viswanathan, G. M., Ferreira, A. S., & da Silva, M. A. A. (2012). Alzheimer random walk model: Two previously overlooked diffusion regimes. *Phys. Rev. E*, 86(4), 042101.

[37] da Silva, M. A. A., Viswanathan, G. M., Ferreira, A. S., & Cressoni, J. C. (2008). Spontaneous symmetry breaking in amnestically induced persistence. *Phys. Rev. E*, 77, 040101.

[38] Deneubourg, N. R. F. G. G. L. (1991). The blind leading the blind in army ant raid patterns: Testing a model of self-organization (hymenoptera: Formicidae). *J. of Insect Behavior*, 4, 583.

[39] Dervaux, J., Resta, M. C., & Brunet, P. (2016). Light-controlled flows in active fluids. *Nat. Phys.*, 13, 306.

[40] Deseigne, J., Dauchot, O., & Chaté, H. (2010). Collective motion of vibrated polar disks. *Phys. Rev. Lett.*, 105, 098001.

[41] Deseigne, J., Léonard, S., Dauchot, O., & Chaté, H. (2012). Vibrated polar disks: spontaneous motion, binary collisions, and collective dynamics. *Soft Mat.*, 8, 5629.

[42] Dettmann, C. P. (2014). Diffusion in the lorentz gas. *Commun. Theor. Phys.*, 62, 521.

[43] Dombrowski, C., Cisneros, L., Chatkaew, S., Goldstein, R. E., & Kessler, J. O. (2004). Self-concentration and large-scale coherence in bacterial dynamics. *Phys. Rev. Lett.*, 93, 098103.

[44] Dorbolo, S., Terwagne, D., Vandewalle, N., & Gilet, T. (2008). Resonant and rolling droplet. *New J. Phys.*, 10(11), 113021.

[45] Dreyfus, R., Baudry, J., Roper, M. L., Fermigier, M., Stone, H. A., & Bibette, J. (2005). Microscopic artificial swimmers. *Nature*, 437, 862.

[46] Dubertrand, R., Hubert, M., Schlagheck, P., Vandewalle, N., Bastin, T., & Martin, J. (2016). Scattering theory of walking droplets in the presence of obstacles. *New J. Phys.*, 18(11), 113037.

[47] Durey, M. & Milewski, P. A. (2017). Faraday pilot-wave dynamics: discrete-time analysis. *J. Fluid Mech.*, 821, 296.

[48] Earl, D. J., Pooley, C. M., Ryder, J. F., Bredberg, I., & Yeomans, J. M. (2007). Modeling microscopic swimmers at low reynolds number. *J. Chem. Phys.*, 126, 064703.

[49] Ebata, H. & Sano, M. (2015). Swimming droplets driven by a surface wave. *Sci. Rep.*, 5, 8546.

[50] Ebeling, W. (2004). Nonlinear brownian motion - mean squared displacement. *Cond. Mat. Phys.*, 7, 539.

[51] Eddi, A., Fort, E., Moisy, F., & Couder, Y. (2009). Unpredictable tunneling of a classical wave-particle association. *Phys. Rev. Lett.*, 102(24), 240401.

[52] Eddi, A., Sultan, E., Moukhtar, J., Fort, E., Rossi, M., & Couder, Y. (2011). Information stored in faraday waves: the origin of a path memory. *J. Fluid Mech.*, 674, 433.

[53] Erneux, T. (2009). *Applied Delay Differential Equations*. Springer.

[54] Faraday, M. (1831). On a peculiar class of acoustical figures; and on certain forms assumed by a group of particles upon vibrating elastic surfaces. *Phil. Trans. R. Soc. Lond. A*, 52, 319.

[55] Farutin, A., Rafaï, S., Dysthe, D. K., Duperray, A., Peyla, P., & Misbah, C. (2013). Amœboid swimming: A generic self-propulsion of cells in fluids by means of menbrane deformations. *Phys. Rev. Lett.*, 111, 228102.

[56] Felderhof, B. U. (2006). The swimming of animalcules. *Phys. Fluids*, 18, 063101.

[57] Ferreira, A. S., Cressoni, J. C., Viswanathan, G. M., & da Silva, M. A. A. (2010). Anomalous diffusion in non-markovian walks having amnestically induced persistence. *Phys. Rev. E*, 81, 011125.

[58] Feynman, R. P. (1959). There's plenty of room at the bottom. *Caltech Enginering and Science*, 23, 22.

[59] Fort, E., Eddi, A., Boudaoud, A., Moukhtar, J., & Couder, Y. (2010). Path-memory induced quantization of classical orbits. *PNAS*, 107(41), 17515.

[60] Freund, H. & Grassberger, P. (1992). The red queen's walk. *Physica A*, 190, 218.

[61] Gao, W., B. Estanban-Fernández de Ávila, L. Z., & Wang, J. (2018). Targeting and isolation of cancer cells using micro/nanomotors. *Adv. Drug Delivery Rev.*, 125, 94.

[62] Gao, W., Sattayasamitsathit, S., Orozco, J., & Wang, J. (2011). Highly efficient catalytic microengines: Template electrosynthesis of polyaniline/platinum microtubes. *J. Am. Chem. Soc.*, 133, 11862.

[63] Garfinkel, A., Shevtsov, J., & Guo, Y. (2017). *Modeling Life: The Mathematics of Biological Systems*. Springer.

[64] Gauger, E. & Stark, H. (2006). Numerical study of micoscopic articifial swimmer. *Phys. Rev. E*, 74, 021907.

[65] Gazzola, M., Argentina, M., & Mahadevan, L. (2016). Scaling macroscopic aquatic locomotion. *Nat. Phys.*, 10, 758.

[66] Gerdes, J. W., Gupta, S. K., & Wilkerson, S. A. (2012). A review of bird-inspired flapping wing miniature air vehicle designs. *J. Mechanisms Robotics*, 4, 021003.

[67] Gilet, T. (2014). Dynamics and statistics of wave-particle interactions in a confined geometry. *Phys. Rev. E*, 90(5), 052917.

[68] Gilet, T. (2016). Quantumlike statistics of deterministic wave-particle interactions in a circular cavity. *Phys. Rev. E*, 93(4), 042202.

[69] Gilet, T., Vandewalle, N., & Dorbolo, S. (2009). Completely inelastic ball. *Phys. Rev. E*, 79(5), 055201.

[70] Ginot, F., Theurkauff, I., Detcheverry, F., Ybert, C., & Cottin-Bizonne, C. (2018). Aggregation-fragmentation and individual dynamics of active clusters. *Nat. Comm.*, 9, 696.

[71] Golestanian, R. & Ajdari, A. (2008). Analytic results for the three-sphere swimmers at low reynolds number. *Phys. Rev. E*, 77, 036308.

[72] Gray, J. & Hancock, J. (1955). The propulsion of sea-urchin spermatozoa. *J. Exp. Biol.*, 32, 802.

[73] Grosjean, G. (2014). Nageurs magnétocapillaires auto-assemblés.

[74] Grosjean, G., Hubert, M., Collard, Y., Pillitteri, S., & Vandewalle, N. (2018). Surface microswimmers, harnessing the interface to self-propel. *arXiv:1806.01090*.

[75] Grosjean, G., Hubert, M., Lagubeau, G., & Vandewalle, N. (2016). Realization of the najafi-golestanian microswimmer. *Phys. Rev. E*, 94, 021101.

[76] Grosjean, G., Hubert, M., & Vandewalle, N. (2017). Magnetocapillary self-assemblies: Locomotion and micromanipulation along a liquid interface. *Adv. Coll. Int. Sci.*, 255, 84.

[77] Grosjean, G., Lagubeau, G., Darras, A., Hubert, M., Lumay, G., & Vandewalle, N. (2015). Remote control of self-assembled microswimmers. *Sci. Rep.*, 5, 16035.

[78] Guix, M., Mayorga-Martinez, C. C., & Merkoci, A. (2014). Nano/micromotors in (bio)chemical science applications. *Chem. Rev.*, 114, 6285.

[79] H. P. Zhang, A. Be'er, R. S. S. E.-L. F. & Swinney, H. L. (2009). Swarming dynamics in bacterial colonies. *EuroPhys. Lett.*, 87, 48011.

[80] Harris, D. M., Moukhtar, J., Fort, E., Couder, Y., & Bush, J. W. M. (2013). Wavelike statistics from pilot-wave dynamics in a circular corral. *Phys. Rev. E*, 88(1), 011001.

[81] Harshey, R. M. (1994). Bee's aren't the only ones: swarming in garm-negative bacteria. *Mol. Microbiol.*, 13, 389.

[82] Henry, R. J., Masoud, Z. N., Nayfeh, A. H., & Mook, D. T. (2001). Cargo pendulation reduction on ship-mounted cranes via boom-luff angle actuation. *J. Vibr. Cont.*, 7(8), 1253.

[83] Hu, D. L. & Bush, J. W. M. (2005). Meniscus-climbing insects. *Nature*, 437, 733.

[84] Hu, D. L. & Bush, J. W. M. (2010). The hydrodynamics of water-walking arthropods. *J. Fluid Mech.*, 644, 5.

[85] Hu, D. L., Chan, B., & Bush, J. W. M. (2003). The hydrodynamics of water strider locomotion. *Nature*, 424, 663.

[86] Hubert, M. & Dubertrand, R. (2017). Wkb approach to evaluate series of mathieu functions in scattering problems. *arXiv:1708.03195*.

[87] Hubert, M., Ludewig, F., Dorbolo, S., & Vandewalle, N. (2014). Bouncing dynamics of a spring. *Physica D*, 272, 1.

[88] Hubert, M., Perrard, S., & Labousse, M. (2017). Self-propulsion and crossing statistics under random initial conditions. *Phys. Rev. E*, 95(6), 062607.

[89] Hubert, M., Robert, D., Caps, H., Dorbolo, S., & Vandewalle, N. (2015). Resonant and antiresonant bouncing droplets. *Phys. Rev. E*, 91(2), 023017.

[90] I. Karamouzas, B. S. & Guy, S. J. (2014). Universal power law governing pedestrian interactions. *Phys. Rev. Lett.*, 113, 238701.

[91] Jackson, J. D. (1998). *Classical Electrodynamics*. Wiley.

[92] Jurado-Sánchez, B. & Escarpa, A. (2016). Milli, micro and nanomotors: Novel analytical tools for real-world applications. *Trends Anal. Chem.*, 84, 48.

[93] Kasai, T. (2009). *Encyclopedia of Molecular Mechanisms of Disease*. Springer Berlin Heidelberg.

[94] Kellogg, O. D. (1929). *Foundations of Potential Theory*. Springer.

[95] Kerner, B. S. (1999). The physics of traffic. *Phys. World*, 12, 8.

[96] Köhler, S., Schaller, V., & Bausch, A. R. (2011). Structure formation in active networks. *Nat. Materials*, 10, 462.

[97] Kralchevsky, P. A. & Denkov, N. D. (2001). Capillary forces and structuring in layers of colloid particles. *Curr. Opin. Colloid Interface Sci.*, 6, 383.

[98] Kralchevsky, P. A. & Nagayama, K. (2000). Capillary interactions between particles bound to interfaces, liquid films and biomembranes. *Adv. Coll. Int. Sci.*, 85, 145.

[99] Kumar, K. (1996). Linear theory of faraday instability in viscous liquids. *Proc. R. Soc. Lond. A*, 452(1948), 1113.

[100] Kurianski, K. M., Oza, A. U., & Bush, J. W. M. (2017). Simulations of pilot-wave dynamics in a simple harmonic potential. *Phys. Rev. Fluids*, 2, 113602.

[101] Kuznetsov, Y. A., Feo, O. D., & Rinaldi, S. (2001). Belyakov homoclinic bifurcations in a tritrophic food chain model. *SIAM J. Appl.. Math.*, 62, 462.

[102] l. Wang, Q., Wang, C., f. Dong, R., q. Pang, Q., & p. Cai, Y. (2018). Steerable light-driven $tio_2$-fe janus micromotor. *Inorg. Chem. Comm.*, 91, 1.

[103] Labousse, M. & Perrard, S. (2014). Non-hamiltonian features of a classical pilot-wave dynamics. *Phys. Rev. E*, 90(2), 022913.

[104] Labousse, M., Perrard, S., Couder, Y., & Fort, E. (2014). Build-up of macroscopic eigenstates in a memory based constrained system. *New J. phys.*, 16, 113207.

[105] Labousse, M., Perrard, S., Couder, Y., & Fort, E. (2016). Self-attraction into spinning eigenstates of a mobile wave source by its emission back-reaction. *Phys. Rev. E*, 94(4), 042224.

[106] Lagubeau, G., Grosjean, G., Darras, A., Lumay, G., Hubert, M., & Vandewalle, N. (2016). Statics and dynamics of magnetocapillary bonds. *Phys. Rev. E*, 93, 053117.

[107] Lauga, E. & Powers, T. R. (2009). The hydrodynamics of swimming microorganisms. *Rep. Prog. Phys.*, 72, 096601.

[108] Lavy, I., Piel, M., Lennon-Dumémil, A.-M., Voituriez, R., & Gov, N. S. (2016). Deterministic patterns in cell motility. *Nat. Phys.*, 12, 1146.

[109] Leulmi, S., Chauchet, X., Morcrette, M., Ortiz, G., Joisten, H., Sabon, P., Livache, T., Hou, Y., Carrière, M., Lequien, S., & Dieny, B. (2015). Triggering the apoptosis of targeted human renal cancer cells by the vibration of anisotropic magnetic particles attached to the cell membrane. *Nanoscale*, 7, 15904.

[110] Lisicki, M. (2013). Four approaches to hydrodynamic green's functions – the oseen tensors. *arXiv:1312.6231*.

[111] Lumay, G., Obara, N., Weyer, F., & Vandewalle, N. (2013). Self-assembled magnetocapillary swimmers. *Soft Mat.*, 9, 240.

[112] Mackey, M. C. & Glass, L. (1977). Oscillation and chaos in physiological control systems. *Science*, 197(4300), 287.

[113] Marchetti, M. C., Joanny, J. F., Ramaswamy, S., Liverpool, T. B., Prost, J., Rao, M., & Simha, R. A. (2013). Hydrodynamics of soft active matter. *Rev. Mod. Phys.*, 85, 1143.

[114] Mazur, P. & van Saarloos, W. (1982). Many-sphere hydrodynamic interactions and mobilities in a suspension. *Physica A*, 115, 21.

[115] Medina-Sánchez, M. (2017). Medical microbots need better imaging and control. *Nature*, 545, 406.

[116] Medina-Sánchez, M., Schwarz, L., Meyer, A. K., Hebenstreit, F., & Schmidt, O. G. (2016). Cellular cargo delivery: Toward assisted fertilization by sperm-carrying micromotors. *Nano Lett.*, 16, 555.

[117] Medrano-T., R. O., Baptista, M. S., & Caldas, I. L. (2006). Shilnikov homoclinic orbit bifurcations in the chua's circuit. *Chaos*, 16, 043119.

[118] Mendelson, N. H., Bourque, A., Wilkening, K., Anderson, K. R., & Watkins, J. C. (1999). Organized cell swimming motions in bacillus subtilis colonies: Patterns of short-lived whirls and jets. *J. of Bacteriology*, 181, 600.

[119] Milewski, P. A., Galeano-Rios, C. A., Nachbin, A., & Bush, J. W. M. (2015). Faraday pilot-wave dynamics: modelling and computation. *J. Fluid Mech.*, 778, 361.

[120] Minorsky, N. (1935). Problems of anti-rolling stabilization of ships by the activated tank method. *Journal of the American Society for Naval Engineers*, 47, 87.

[121] Moláček, J. & Bush, J. W. M. (2013a). Drops bouncing on a vibrating bath. *J. Fluid Mech.*, 727, 582.

[122] Moláček, J. & Bush, J. W. M. (2013b). Drops walking on a vibrating bath: towards a hydrodynamic pilot-wave theory. *J. Fluid Mech.*, 727, 612.

[123] Nachbin, A., Milewski, P. A., & Bush, J. W. M. (2017). Tunneling with a hydrodynamic pilot-wave model. *Phys. Rev. Fluids*, 2, 034801.

[124] Najafi, A. & Golestanian, R. (2004). Simple swimmer at low reynolds number: Three linked spheres. *Phys. Rev. E*, 69, 062901.

[125] Nawroth, J. C., Lee, H., Feinberg, A. W., Ripplinger, C. M., McCain, M. L., Grosberg, A., Dabiri, J. O., & parker, K. K. (2012). A tissue-engineered jellyfish with biomimetic propulsion. *Nat. Biotechnology*, 30, 792.

[126] Orozco, J., Pan, G., Sattayasamitsathit, S., Galarnyk, M., & Wang, J. (2015). Micromotors to capture and destroy anthrax simulant spores. *Analyst*, 140, 1421.

[127] Osborn, J. A. (1945). Demagnetizing factors of the general ellipsoid. *Phys. Rev.*, 67, 351.

[128] Oza, A. U., Harris, D. M., Rosales, R. R., & Bush, J. W. M. (2014a). Pilot-wave dynamics in a rotating frame: on the emergence of orbital quantization. *J. Fluid Mech.*, 744, 404.

[129] Oza, A. U., Rosales, R. R., & Bush, J. W. M. (2013). A trajectory equation for walking droplets: hydrodynamic pilot-wave theory. *J. Fluid Mech.*, 737, 552.

[130] Oza, A. U., Wind-Willassen, Ø., Harris, D. M., Rosales, R. R., & Bush, J. W. M. (2014b). Pilot-wave hydrodynamics in a rotating frame: Exotic orbits. *Phys. Fluids*, 26, 082101.

[131] Pande, J., Merchant, L., Krüger, T., Harting, J., & Smith, A.-S. (2017). Setting the pace of microswimmers: when increasing viscosity speeds up self-propulsion. *New J. Phys.*, 19, 053024.

[132] Pande, J. & Smith, A.-S. (2015). Forces and shapes as determinants of microswimming: effect on synchronisation and the utilisation of drag. *Soft Mat.*, 11, 2364.

[133] Paranjape, A. A., Dorothy, M., & Lee, K. D. (2012). A flight mechanics-centric review of bird-scale flapping flight. *Int. J. of Aeronautical and Spacial Sci.*, 13, 267.

[134] Paul, W. & Baschnagel, J. (2013). *Stochastic Processes*. Springer.

[135] Paunov, V. N., Kralchevsky, P. A., Denkov, N. D., & Nagayama, K. (1993). Lateral capillary forces between floating submillimeter particles. *J. Colloid Interface Sci.*, 157, 100.

[136] Pearson, K. (1905). The problem of the random walk. *Nature*, 72, 294.

[137] Pearson, K. (1906). *A mathematical theory of random migration*. Dulau and co.

[138] Perrard, S., Labousse, M., Fort, E., & Couder, Y. (2014a). Chaos driven by interfering memory. *Phys. Rev. Lett.*, 113(10), 104101.

[139] Perrard, S., Labousse, M., Miskin, M., Fort, E., & Couder, Y. (2014b). Self-organization into quantized eigenstates of a classical wave-driven particle. *Nature Comm.*, 5, 3219.

[140] Petroff, A. P., Wu, X.-L., & Libchaber, A. (2015). Fast-moving bacteria self-organize into active two-dimensional crystals of rotating cells. *Phys. Rev. Lett.*, 114, 158102.

[141] Pickl, K., Götz, J., Iglberger, K., Pande, J., Mecke, K., Smith, A.-S., & Rüde, U. (2012). All good things come in threes—three beads learn to swim with lattice boltzmann and a rigid body solver. *J. Comp. Science*, 3, 374.

[142] Pickl, K., Pande, J., Köstler, H., Rüde, U., & Smith, A.-S. (2017). Lattice boltzmann simulations of the beads-spring microswimmer with a responsive stroke - from an individual to swarms. *J. Phys.: Cond. Mat.*, 29, 124001.

[143] Pickl, K., Pande, J., Köstler, H., Smith, A.-S., & Rüde, U. (2016). When do microswimmers exit the stokes regime? *arXiv:1603.04633*.

[144] Potts, W. K. (1984). The chorus-line hypothesis of manoeuvre coordination in avian flocks. *Nature*, 309, 344.

[145] Press, W. H., Jeukolsky, S. A., Vetterling, W. T., & Flannery, B. P. (2007). *Numerical Recipes*. Cambridge University Press.

[146] Prigogine, I. & Nicolus, G. (1967). On symmetry□breaking instabilities in dissipative systems. *J. Chem. Phys.*, 46, 3542.

[147] Protière, S., Boudaoud, A., & Couder, Y. (2006). Particle-wave association on a fluid interface. *J. Fluid Mech.*, 554, 85.

[148] Pucci, G., Harris, D. M., Faria, L. M., & Bush, J. W. M. (2017). Walking droplets interacting with single and double slits. *J. Fluid. Mech.*, 835, 1136.

[149] Purcell, E. M. (1977). Life at low reynolds number. *Am. J. Phys.*, 45, 3.

[150] Rahman, A. & Blackmore, D. (2016). Neimark-sacker bifurcations and evidence of chaos in a discrete dynamical model of walkers. *Chaos, Solitons and Fractals*, 91, 339.

[151] Richard, J.-P. (2003). Time-delay systems: an overview of some recent advances and open problems. *Automatica*, 39, 1667.

[152] Romanczuk, P., Bär, M., Ebeling, W., & Lindner, B. (2012). Active brownian particles. *Eur. Phys. J. Special Topics*, 202, 1.

[153] Roper, M., Dreyfus, R., Baudry, J., Fermigier, M., Bibette, J., & Stone, H. A. (2006). On the dynamics of magnetically driven elastic filaments. *J. Fluid Mech.*, 554, 167.

[154] Rössler, O. E. (1976). An equation for continuous chaos. *Phys. Lett. A*, 57, 397.

[155] Rothman, D. H. & Zaleski, S. (1994). Lattice-gas models of phase separation: interfac, phase transitions and multiphase flow. *Rev. Mod. Phys.*, 66, 1417.

[156] Sáenz, P. J., Cristea-Platon, T., & Bush, J. W. M. (2018). Statistical projection effects in a hydrodynamic pilot-wave system. *Nat. Phys.*, 14, 315.

[157] Schaller, V., Weber, C., Semmrich, C., Frey, E., & Bausch, A. R. (2010). Polar patterns of driven filaments. *Nature*, 467, 73.

[158] Schneider, W. R. & Doetsch, R. N. (1974). Effect of viscosity on bacterial motility. *J. Bacteriol.*, 117(2), 383696.

[159] Scholz, C., Engel, M., & Pöschel, T. (2018). Rotating robots move collectively and self-organize. *Nat. Comm.*, 9, 931.

[160] Schütz, G. M. & Trimper, S. (2004). Elephants can always remember: Exact long-range memory effects in a non-markovian random walk. *Phys. Rev. E*, 70, 045101.

[161] Sfakiotakis, M., Lane, D. M., & Davies, B. C. (1999). Review of fish swimming modes for aquatic locomotion. *IEEE J. Oceanic Engineering*, 24, 237.

[162] Shil'nikov, A., Nicolis, G., & Nicolis, C. (1995). Bifurcation and predictability analysis of a low-order atmospheric circulation model. *Int. J. Bifur. Chaos*, 6, 1701.

[163] Shyy, W., Aono, H., k. Kang, C., & Liu, H. (2013). *An Introduction to Flapping Wing Aerodynamics*. Cambridge University Press.

[164] Shyy, W., k. Kang, C., Chirarattananon, P., Ravi, S., & Liu, H. (2016). Aerodynamics, sensing and control of insect-scale flapping-wing flight. *Proc. R. Soc. A*, 472, 20150712.

[165] Silva, C. P. (1993). Shil'nikov's theorem - a tutorial. *IEEE Transactions on Circuits and Systems I: Fundamental Theory and Applications*, 40, 675.

[166] Singh, V. V., Kaufmann, K., Orozco, J., Li, J., Galarnyk, M., Arya, G., & Wang, J. (2015). Micromotor-based on–off fluorescence detection of sarin and soman simulants. *Chem. Comm.*, 51, 11190.

[167] Stevens, J. M., Galyov, E. E., & Stevens, M. P. (2006). Actin-dependent movement of bacterial pathogens. *Nat. Rev. Microbiol.*, 4, 91.

[168] Sukhov, A., Ziegler, S., Xie, Q., Trosman, O., Pande, J., Grosjean, G., Hubert, M., Vandewalle, N., Smith, A.-S., & Harting, J. (2018). Resonant motion of triangular magnetocapillary swimmers. *In preparation*.

[169] Sumino, Y., Nagai, K. H., Shitaka, Y., Tanaka, D., Yoshikawa, K., Chaté, H., & Oiwa, K. (2012). Large-scale vortex lattice emerging from collectively moving microtubules. *Nature*, 483, 448.

[170] Takatori, S. C., Dier, R. D., Vermant, J., & brady, J. F. (2016). Acoustic trapping of active matter. *Nat. Comm.*, 7, 10694.

[171] Tambasco, L. D., Harris, D. M., Oza, A. U., Rosales, R. R., & Bush, J. W. M. (2016). The onset of chaos in orbital pilot-wave dynamics. *Chaos*, 26(10), 103107.

[172] Terwagne, D., Gilet, T., Dorbolo, S., & Vandewalle, N. (2009a). Metastable bouncing droplets. *Phys. Fluids*, 21, 054103.

[173] Terwagne, D., Ludewig, F., Vandewalle, N., & Dorbolo, S. (2013). The role of deformations in the bouncing droplet dynamic. *Phys. Fluids*, 25, 12.

[174] Terwagne, D., Mack, N., Dorbolo, S., Gilet, T., Raty, J.-Y., & Vandewalle, N. (2009b). The mayonnaise droplet. *Chaos*, 19(4), 041105.

[175] Theurkauff, I., Cottin-Bizonne, C., Palacci, J., Ybert, C., & Bocquet, L. (2012). Dynamic clustering in active colloidal suspensions with chemical signaling. *Phys. Rev. Lett.*, 108, 268303.

[176] Tierno, P., Golestanian, R., Pagonabarraga, I., & Sagués, F. (2008). Controlled swimming in confined fluids of magnetically actuated colloidad rotors. *Phys. Rev. Lett.*, 101, 218304.

[177] Tobalske, B. W. (2007). Biomechanics of bird flight. *J. Exp. Biol.*, 210, 3135.

[178] Vandewalle, N., Clermont, L., Terwagne, D., Dorbolo, S., Mersch, E., & Lumay, G. (2012). Symmetry breaking in a few-body system with magnetocapillary interactions. *Phys. Rev. E*, 85(4), 041402.

[179] Vandewalle, N., Obara, N., & Lumay, G. (2013). Mesoscale structures from magnetocapillary self-assembly. *Eur. Phys. J. E*, 36, 127.

[180] Vella, D. & Mahadevan, L. (2005). The "cheerios effect". *Am. J. Phys.*, 73, 817.

[181] Vicsek, T. & Zafeiris, A. (2012). Collective motion. *Phys. Rep.*, 517, 71.

[182] Viswanathan, G. M., Afanasyev, V., Buldyrev, S. V., Murphy, E. J., Prince., P. A., & Stanley, H. E. (1996). Lévy flight search patterns of wandering albatrosses. *Nature*, 381, 413.

[183] Vizsnyiczai, G., Frangipane, G., Maggi, C., Saglimbeni, F., Bianchi, S., & Leonardo, R. D. (2017). Light controlled 3d micromotors powered by bacteria. *Nat. Comm.*, 8, 15974.

[184] Volfson, D., Cookson, S., Hasty, J., & Tsimring, L. S. (2008). Biomechanical ordering of dense cell populations. *PNAS*, 105, 15346.

[185] von Hippel, P. H. (2007). From "simple" dna-protein interactions to the macromolecular machines of gene expression. *Annu. Rev. Biophys. Biomol. Struct.*, 36, 79.

[186] Wang, C., Wang, Q., Dong, R.-F., & Cai, Y.-P. (2018). Dynamic self-assembly of micro-nanomotor. *Inorg. Chem. Comm.*, 91, 8.

[187] Ward, A. J. W., Sumpter, D. J. T., Couzin, I. D., Hart, P. J. B., & Krause, J. (2008). Quorum decision-making facilitates information transfer in fish shoals. *PNAS*, 105, 6948.

[188] Williams, B. J., Anand, S. V., Rajagopalan, J., & Saif, M. T. A. (2014). A self-propelled biohybrid swimmer at low reynolds number. *Nat. Comm.*, 5, 3081.

[189] Wind-Willassen, O., Moláček, J., Harris, D. M., & Bush, J. W. M. (2013). Exotic states of bouncing and walking droplets. *Phys. Fluids*, 25, 082002.

[190] Wu, Y., Jiang, Y., Kaiser, D., & Alber, M. (2007). Social interactions in myxobacterial swarming. *PLOS Computational Biology*, 3, 2546.

[191] Xu, H., Medina-Sánchez, M., Magdanz, V., Schwarz, L., Hebenstreit, F., & Schmidt, O. G. (2018). Sperm-hybrid micromotor for targeted drug delivery. *ACS Nano*, 12, 327.

[192] Yamada, D., Hondou, T., & Sano, M. (2003). Coherent dynamics of an asymmetric particle in a vertically vibrating bed. *Phys. Rev. E*, 67, 040301.

[193] Yomosa, M., Mizuguchi, T., Vásárhelyi, G., & Nagy, M. (2015). Coordinated behaviour in pigeon flocks. *PLOS One*, 10, e0140558.